CRANFIELD INSTITUTE OF TECHNOLOGY

SCHOOL OF INDUSTRIAL AND MANUFACTURING SCIENCE

PhD THESIS

ACADEMIC YEARS 1990-1993

BRYAN. W. ALLCOCK

HYDROGEN CONCENTRATION MEASUREMENTS USING A GEL-FILLED ELECTROCHEMICAL PROBE.

SUPERVISOR   M. J. ROBINSON

DECEMBER 1993

To Rebecca, and to my father who lacked nothing
but the opportunity.

ACKNOWLEDGEMENTS.

The author would like to express his gratitude and thanks to Dr. Mike Robinson, who in a supervisory capacity offered his support and guidance throughout the research period. Both technical and academic support were gratefully received from Kees Smitt[1] and Dr. Rob Brouwer[2] whose enthusiasm for the project fuelled its progress.

Special thanks must be relayed to my partner Rebecca for her forbearance and understanding over the past years. Finally thanks to my parents Ralph and Margaret whose encouragement and financial support over the years have been greatly appreciated.

ABSTRACT

A novel gel-filled electrochemical hydrogen probe was developed and used to measure hydrogen concentrations in carbon-manganese steels. The results were compared with those from an electrochemical permeation technique and a volumetric method. The probe was used to determine the distribution of hydrogen in 5mm steel plates cathodically charged on one side to represent the wall of a pipe or pressure vessel used in hydrogen service. The concentration measurements obtained by the three techniques were in good agreement with each other and with those predicted from diffusion equations and this permitted the precise boundary conditions on the charged metal surface to be determined. Surface reaction kinetics were investigated to model the hydrogen distribution and these were solved using solutions to Fick's diffusion equations. After long charging times the hydrogen concentration on the efflux surface of the plate approached that on the influx side, indicating that an almost uniform hydrogen distribution had been established. Rather than rapid loss of hydrogen from the free surface, as had been assumed previously, it was clear that there was a large resistance to hydrogen transport across the metal/air interface. Microstructural damage was examined both optically and using the scanning electron microscope. Separate investigations were carried out to help understand the effect that reversible and irreversible trapping had on the diffusion of hydrogen through the steel.

CONTENTS

LIST OF FIGURES.

LIST OF TABLES.

LIST OF PLATES.

1.0 INTRODUCTION

There is a need for determining localised hydrogen concentrations so that mechanical degradation effects attributed to hydrogen can be evaluated and understood. Localised conditions in the material are generally responsible for degradation, and bulk measurements are not sensitive to localised variations.

High temperature methods of hydrogen determination, which frequently employ vacuum extraction, measure the total hydrogen content of the steel, including that which is trapped at grain boundaries and inclusions within the microstructure. These methods are generally destructive and unsuitable for use in the field. By contrast, low temperature electrochemical methods, which rely on the oxidation of hydrogen as it emerges from the metal surface, detect only the lower concentration of the mobile lattice hydrogen. It is this hydrogen, however, that is more significant as it can diffuse to defect sites within the material and cause embrittlement. Electrochemical methods of hydrogen determination generally employ a cell containing an electrolyte of NaOH solution or concentrated H_2SO_4. These cells can be troublesome to set up and consequently are unsuitable for rapid testing. The probe described in this work is a further development of the electrochemical probe in which the electrolyte has been immobilised in the form of a gel.

In the following survey, an overview of the processes relating to hydrogen in metals is given. The study has essentially been divided into three main areas of interest. In the first, the way in which hydrogen is generated on a metal substrate and the subsequent diffusion of this hydrogen into the metal is considered. In the second section a study of the transport of hydrogen in metals has been made. Microstructural effects; trapping of hydrogen in steel; and proposed mechanisms for hydrogen embrittlement and hydrogen induced failure will also be considered. Finally, a review the techniques available for predicting the hydrogen concentration accumulated in these materials and the

subsequent problems involved in interpreting these data, will be made.

Hydrogen monitors have many advantages over other more conventional monitoring devices such as acoustic emission and ultrasonic techniques; primarily the possibility to relate a series of surface hydrogen concentration measurements to the structural soundness of a pipe or vessel. Hydrogen monitors can also be used to detect hydrogen permeation and the effectiveness of inhibitors to stop this permeation. Used with a complete corrosion monitoring system, hydrogen monitors can give meaningful data that will allow the corrosion engineer or technician to make decisions to optimise the successful operation of a potentially corrosive system.

The three year research programme at Cranfield set out with the intention to develop a technique to measure the surface hydrogen concentration of steel exposed to specific corrosive environments which might simulate those found in operating plants. In particular, it was intended to simulate the rate of hydrogen charging that was typical of the overhead lines of catalytic crackers, where significant hydrogen damage was expected. The programme would also endeavour to provide a better understanding of the interaction of hydrogen with defects in the microstructure.

The results obtained with this technique would subsequently be compared with those from a conventional electrochemical hydrogen probe. The programme of research in the laboratory would then be used to assess the potential applications of the technique as a tool for assessing the life expectancy of a working vessel in the petrochemical and petrochemical related industries.

2.0 LITERATURE SURVEY.

2.1 Current Hydrogen Related Problems in the Petro-Chemical Industry.

Numerous failures of sour gas pipelines and associated vessels have occurred around the world as a direct or indirect effect of hydrogen. Processes used for fuels upgrading provide environments where practically all types of hydrogen deterioration of the structural steel may take place. An example of an integrated flow scheme for crude oil processing is shown in Figure 1[1]. Special problems arise during operation at elevated temperatures and pressures such as the effect of hydrogen sulphide (H_2S) above 250°C.

Some of the more important processes in current refinery practice which give rise to hydrogen related problems are[2]:

1. **Hydrotreating.** This removes by reaction with hydrogen those parts of heavy gasoline which poison the catalyst in reformers.

2. **Catalytic Reforming.** This improves the octane of motor gasoline produced by the hydrotreater by reacting the treated gasoline with hydrogen in the presence of a catalyst such as platinum.

3. **Hydrodesulphurisation.** This removes sulphur from gas oil by reacting with hydrogen at high temperatures.

4. **Hydrocracking.** This performs a similar task to a Fluid Catalytic Cracker. Lubricating oil is converted from vacuum distillation units to gasoline by cracking large hydrocarbon molecules to lighter ones in the presence of a catalyst.
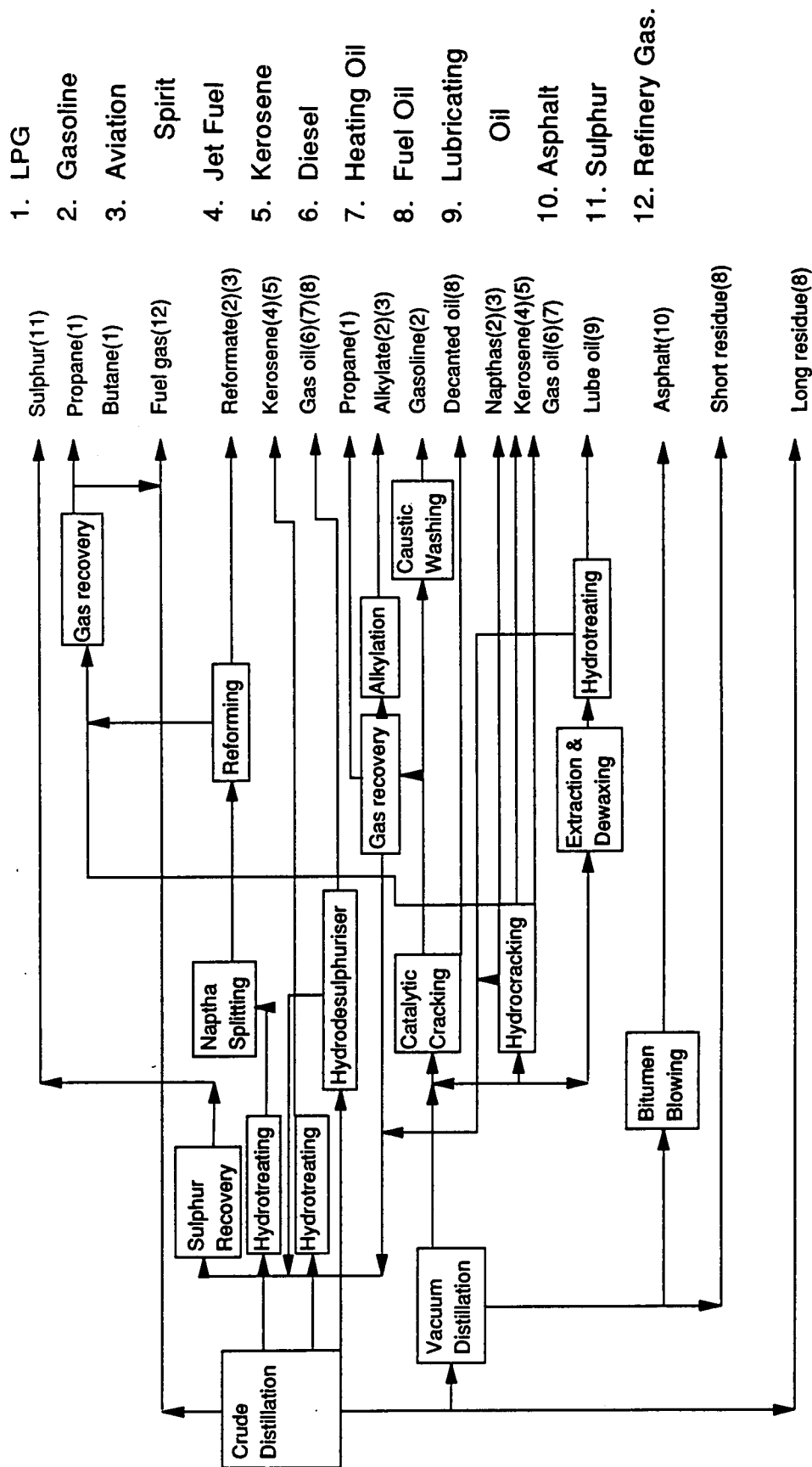
Figure 1. Example of Integrated Flow Scheme for Crude Oil Processing, A. J. Turnell[2]

1. LPG
2. Gasoline
3. Aviation Spirit
4. Jet Fuel
5. Kerosene
6. Diesel
7. Heating Oil
8. Fuel Oil
9. Lubricating Oil
10. Asphalt
11. Sulphur
12. Refinery Gas.

Sulphur(11)
Propane(1)
Butane(1)
Fuel gas(12)
Reformate(2)(3)
Kerosene(4)(5)
Gas oil(6)(7)(8)
Propane(1)
Alkylate(2)(3)
Gasoline(2)
Decanted oil(8)
Napthas(2)(3)
Kerosene(4)(5)
Gas oil(6)(7)
Lube oil(9)
Asphalt(10)
Short residue(8)
Long residue(8)

Gas recovery
Reforming
Caustic Washing
Alkylation
Gas recovery
Extraction & Dewaxing
Hydrotreating
Naptha Splitting
Hydrodesulphuriser
Catalytic Cracking
Hydrocracking
Bitumen Blowing
Sulphur Recovery
Hydrotreating
Hydrotreating
Vacuum Distillation
Crude Distillation

4

The hydrocracker can also produce gasoline from heavier stocks such as bitumen. In each of these processes the equipment is exposed to a wet hydrogen sulphide environment, usually at elevated temperatures. Not only is the plant equipment affected but usually the pipes which carry flue gasses such as H_2S, methane, and various cyano-compounds away from the processing area are also subjected to the aggressive corrosive environments.

Considerable study has been made of the effect of environmental variables in order to provide a basis for deciding when it is necessary to use special materials, and to provide a guide for those situations where it is possible to change the environment to avoid embrittlement or hydrogen induced failures. In the field, it may not only be the working process environment which generates considerable quantities of diffusible hydrogen. Periodically, the plant must be shut down and operations suspended while the equipment and pipes are cleaned. Bursts of hydrogen, in considerable concentrations, may arise as a result of such cleaning processes.

On a laboratory scale, it is impractical to utilize a real working environment due to volume, temperature, pressure and time factors. Consequently, simulated environments are used which accelerate the deleterious effects of hydrogen that are observed in the field.

There are numerous ways to combat hydrogen problems, the actual choice usually being controlled by economic as well as technical limitations. Fortunately hydrogen damage at atmospheric temperatures can often be largely circumvented by careful attention to material selection and fabrication practices. Moreover, the additional cost is often relatively minor.

Even if a system is fabricated in the proper manner from suitable materials, problems may arise in service. Additionally the problems associated with vessels which are presently in service need to be addressed. Often it is not

5

economically viable to shut down and replace a complete working plant on the presumption that the construction material or fabrication practices are susceptible to hydrogen damage. In this situation it is imperative that meticulous monitoring of the structure is maintained to determine the point at which it becomes unsafe.

2.2 Generation and Diffusion of Hydrogen in Materials.

2.2.1 Hydrogen Absorption Media.

In order to study the deleterious effects of hydrogen in ferrous materials one must first provide a source of hydrogen which will then penetrate and diffuse through the steel. Generally, there are two categories which describe the method of artificially charging a steel sample with hydrogen. The first method is absorption due to charging from the gas phase. This usually involves a pure hydrogen atmosphere or mixed gas atmosphere, of for example, hydrogen and hydrogen sulphide[3], bought into contact with the steel at elevated temperatures and pressures. The second method is absorption from an aqueous electrolyte either by cathodic polarization or as a result of a corrosion process. There are numerous electrolytes which are commonly used to generate hydrogen at the electrode surface. A review of the more common solutions is shown in Table 1.

Often it is the aim of the researcher to recreate conditions as closely as possible to those found in the field. In order to simulate field conditions on a laboratory scale, aggressive solutions, often containing "hydrogen promoters" are used which accelerate the hydrogen adsorption process. A vessel which has been in service for 30 years, exposed to a hydrogen generating environment may have sustained considerable damage. A charging electrolyte used in the laboratory must simulate the equivalent damage in a matter of days or months rather than years. This, however, may not be possible when concerned with the diffusion of hydrogen in materials such as steel.

When cathodically charging mild steel in an acidic electrolyte, various problems can arise. Pumphrey[4] and later, Ford et al.[5], observed that during measurements of hydrogen permeation rates through mild steel containing

7

elongated (FeMn)S inclusions, H_2S was produced at the metal surface by dissolution of the inclusions. This may seem advantageous from the point that the H_2S further promotes the absorption of hydrogen into the steel. However, Ateya and Pickering[6] observed that the void or pit created by the dissolution of the inclusion provided an ideal site for the anodic dissolution of the steel. This, coupled with the possibility of crevice corrosion around the inside of the charging vessel may lead to quite severe corrosion of the steel specimen. As the specimen is cathodically charged to liberate hydrogen at its surface it would be considered to be protected from such anodic dissolution. This observation prompted careful design of test rigs ensuring good "throwing power" or current distribution over the whole of the sample surface.

Apart from the artificial methods of hydrogen generation, there are situations during the fabrication or maintenance of iron and steel products during which hydrogen is generated as a result of, or as a by-product of a given process. Other such sources of hydrogen include:

1. Steel Making, heat treatment and hot working,
2. Welding,
3. Chemical pickling, de-scaling (for the removal of corrosion products), paint stripping and etching,
4. Electroplating and
5. Cathodic protection.

Table 1. Review of Hydrogen Charging Electrolytes.

Electrolyte	Temperature	Mode of Charging	Author and Reference
1N H_2SO_4 + H_2S [as Na_2S(aq)]	2°C, 50°C and ambient	Galvanostatic 20 µA mm^{-2}	P. H Pumphrey[4, 7] E. Sunami et al.[8] D. L. Dull[9] P. Amiott et al.[10]
0.1N H_2SO_4	25 ± 0.5°C	Galvanostatic & Potentiostatic	B. S. Chaudhari et al.[11]
1N H_2SO_4 / 1N D_2SO_4	-60 to 100 °C	Galvanostatic & Potentiostatic	M. Boes et al.[12]
0.1N H_2SO_4	Ambient	Galvanostatic 2.5 mA cm^{-2}	J. Brogan et al.[13]
0.2M NaOH	22°C	Galvanostatic 0.22 to 4.34 mA cm^{-2}	L. Nanis et al.[14]
NACE Sol. (TM-02-84*) Buffered Brine◆ HIC Test Sol.ſ NACE Sol. (TM-01-77)¢			M. G. Hay [15]
0.05M H_2SO_4 + thiourea	21 ± 1°C	Galvanostatic 6.4 mA cm^{-2}	D. Noël et al[16]
Saturated $Ca(OH)_2$	25°C	Galvanostatic 10 A m^{-2}	T. Zakroczymski[17]

* Synthetic sea water to ASTM D1141. Initial pH 4.8 to final pH 5.4 saturated to 1 atm. with H_2S.

◆ 5 wt% NaCl, 0.98 wt% acetic acid, 0.51 wt% sodium acetate, pH 4.1 saturated to 1 atm. with H_2S.

ſ Synthetic sea water to ASTM D1141 and acetic acid to pH 3.5 ± 0.05.

¢ 5 wt% NaCl, 0.5 wt% acetic acid, initial pH 2.8 final pH 2.8 to 3.5.

Steel Making.

In steel making, the principal source of hydrogen contamination is the reaction of iron with moisture in the charge or in the humid atmosphere to produce hydrogen and iron oxide. This process can result in several parts per million of hydrogen left in the steel, which is an amount sufficient to produce permanent damage. An apparent solution to this problem has been to pour or cast the steel under vacuum.

Welding.

In arc welding, moisture in the atmosphere can act as a source of hydrogen. However, the primary source of hydrogen is the high-temperature decomposition of the electrode coating and the reaction of the molten metal with these by-products. The principal source of hydrogen in the molten weld pool stems from the arc atmosphere. This ionized column of gas is responsible for the dissociation of hydrogenous compounds in the arc, be they water vapour, dirt or grease. The principal sources of hydrogen in welding consumables are:

- Absorbed moisture in the flux coating of the electrodes.
- From the breakdown of organic materials such as cellulose in coated electrodes where the hydrogen will form a larger portion of the shielding gas.
- Any other hydrogenous compounds in the flux coating.
- Oil, dirt or grease contamination of the electrode coating.
- Hydrated oxides, for example rust on the surface of the welding wires.

De-scaling and Pickling Processes.

Small parts and structures, particularly of high strength steels, probably pick up the majority of hydrogen from chemical pickling or cleaning operations used to remove scale and oxides from the steel surface. Often such

processes operate at elevated temperatures where the absorption of hydrogen is dramatically increased. The processing, contaminant vessels and equipment of the petroleum and chemical industries are prime examples of this. During cleaning and de-scaling, relatively short bursts of hydrogen generated by the cleaning process can penetrate the steel causing quite extensive damage.

Electroplating.

In electroplating processes, hydrogen ions in the electrolyte act effectively as metal ions and are consequently deposited on the substrate surface along with the desired plate. If there is a high rate of co-deposition the hydrogen in the plate diffuses into the substrate and the result is the embrittlement of the base metal. The embrittlement problem is further complicated by the slow rates of diffusion through most of the metal plates. This tends to "trap" the hydrogen and make its elimination much more difficult.

Cathodic Protection.

Cathodic protection is widely used to prevent the general corrosion of non-stainless, carbon and carbon manganese steels. Properly designed, installed and maintained, cathodic protection systems when applied to appropriate structures and components exposed to suitable environmental conditions, achieve these objectives efficiently. With application of a poorly implemented system, especially with over protection, the structure is polarized to a sufficiently negative potential which reduces the aqueous electrolyte and hydrogen is liberated on the steel surface[18]. This can result in localised hydrogen embrittlement of the structure.

Corrosion Processes.

In industries where hydrocarbons are handled, the most common source of hydrogen occurs when sulphide ions and water are present. This occurs in systems containing hydrogen sulphide, H_2S. When steel, such as pipes or

11

vessels, is subject to an environment which contains wet H_2S, then the following chemical reaction occurs on the steel surface:

$$2Fe + 2H_2S \rightarrow 2FeS + 4H_{adsorbed} \qquad [1]$$

The iron is removed from the surface of the steel and iron sulphide is formed; this removal of iron is weight loss corrosion. Hydrogen is then produced as atomic hydrogen which is absorbed into the metal surface. At the steel surface the following reaction occurs:

$$4H_{adsorbed} \rightarrow 2H_{absorbed} + H_2(g) \qquad [2]$$
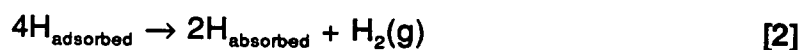
The absorbed hydrogen diffuses into the steel while the hydrogen gas moves into the process medium. A detailed evaluation of the mechanism by which hydrogen enters the steel through the hydrogen evolution reaction will be discussed in section 2.2.2.

2.2.2 The Kinetics of Hydrogen Absorption into Steel.

A basic, quantitative understanding of the hydrogen embrittlement of steel will only be possible if we know the characteristics and parameters associated with the entry of hydrogen into steel. Equation [1] shows the reaction occurring on steel in the presence of H_2S which results in the evolution of hydrogen. There is then a further reaction as shown in equation [2] where absorbed hydrogen diffuses into the steel and the hydrogen gas moves into the process medium.

Other substances can cause hydrogen evolution on a steel surface, in addition this process can be accelerated by cathodic poisons such as arsenic. On a laboratory scale, solutions of mineral acids such as sulphuric acid can be used to generate the diffusible hydrogen. Once a source for the generation of hydrogen has been established, the kinetics of the evolution and absorption of hydrogen can be investigated.

Bockris and Roch[19] concluded from their studies of the comparative rates of hydrogen and deuterium evolution on iron cathodes that the rate determining step for the hydrogen evolution reaction was slow discharge of a proton to an adsorbed hydrogen atom. It has been shown in several instances[20, 21], that the determination of the degree of surface coverage with hydrogen enables the identification of the subsequent steps in the mechanism. From the point of view of mechanism diagnosis alone, it is not necessary to know the absolute value of the coverage, but only its variation with potential and consequently current density. Such information can be readily obtained from the studies of the rate of permeation of hydrogen through a steel plate.

On closer examination of the hydrogen evolution reaction, the following steps should be considered:-

1. Transport of a hydrated proton H_3O^+ to the double layer.

2. Loss of the water of hydration shield in the vicinity of the double layer.

3. Adsorption of the proton to the electrode surface.

4. Discharge (electronation) of the proton to an adsorbed hydrogen atom.

5a. Chemical combination of two adjacent hydrogen adatoms to form a hydrogen molecule - possibility of surface migration between site of discharge and site of recombination.

5b. Electrodic combination of an adatom and a proton to form a hydrogen molecule.

6. Desorption of hydrogen gas as H_2.

7. Bubble formation as H_2 molecules coalesced, and evolution of bubbles.

This sequence is illustrated schematically in Figure 2.[22]

In accordance with Devanathan and Stachurski[23], the overall mechanism for the hydrogen evolution reaction on a steel surface is one of rate determining discharge (step 4 in Figure 2), followed by Tafel recombination at low overpotential, step 5 and electrochemical desorption at high overpotentials (>600 mV NHE), as step 6 in Figure 2. Steps 1 and 7 of the reaction mechanism are rarely limiting and in addition, step 2 and 3 are thought not to affect the overall reaction rate.

From the view point of the hydrogen absorption reaction, the rate of the reaction in equation [3] is the critical factor, and depends simply on the

14
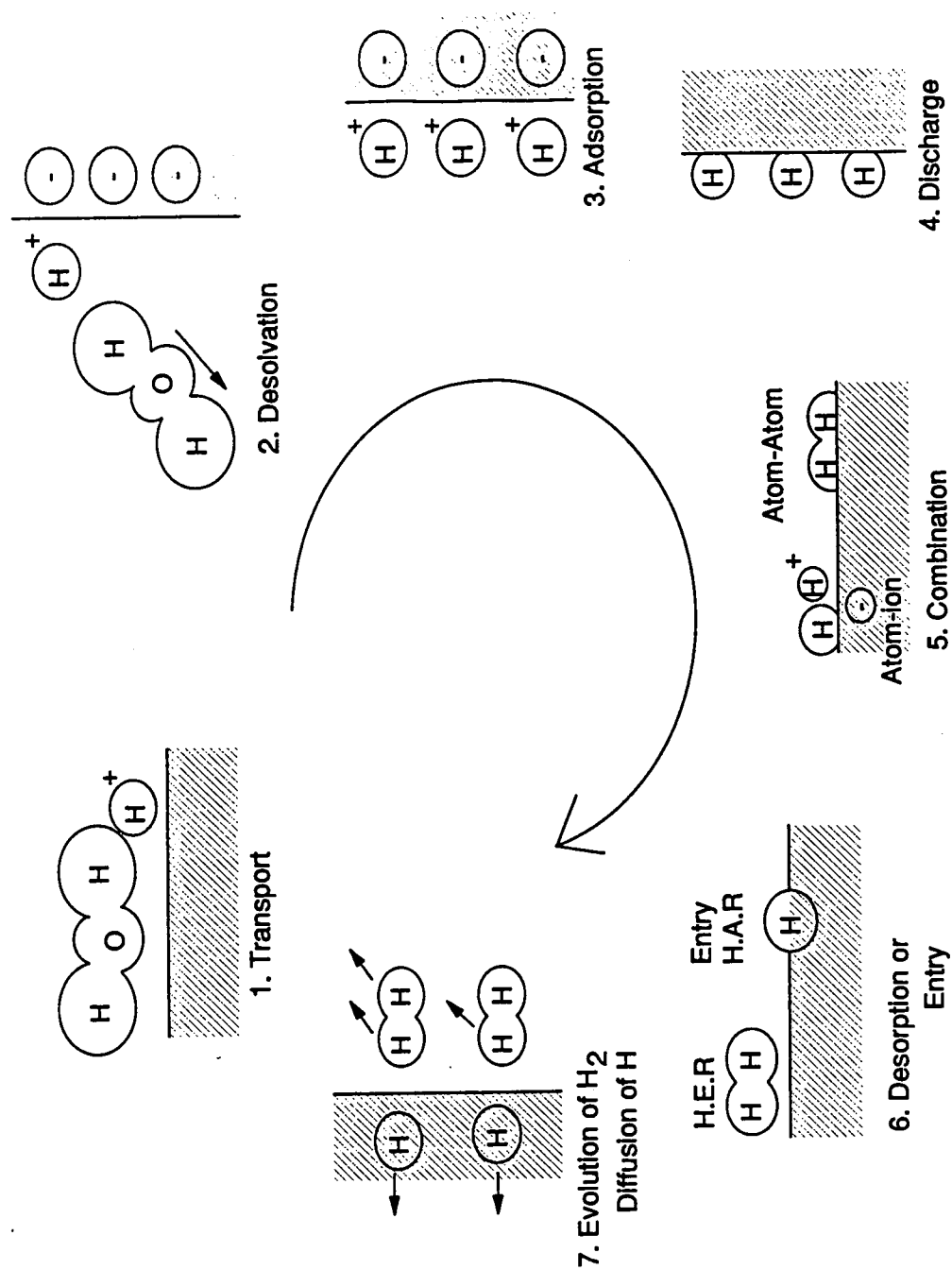
Figure 2. Mechanistic Steps Involved During the Hydrogen Evolution Reaction. R. D. McCright[22]

15

specific rate constant K_{abs} and the steady-state concentration or surface coverage of hydrogen atoms on the surface, θ_H[24].

$$H_{adsorbed} \underset{k_{des}}{\overset{k_{abs}}{\rightleftharpoons}} H_{absorbed} \qquad [3]$$

Numerical evaluation of these constants may be estimated from the experimental measurement of such parameters as the steady state hydrogen permeation current, for a series of different cathodic charging currents. The hydrogen overvoltage and the hydrogen diffusivity may also be evaluated during cathodic hydrogen charging and it is possible to evaluate the kinetic parameters involved in the Hydrogen Adsorption Reaction and the Hydrogen Evolution Reaction by manipulation of a basic model such as the IPZ model[20, 25], developed by Iyer, Pickering and Zammanzadeh. The model enables computation of the hydrogen discharge and recombination reaction rate constants and the more important hydrogen adsorption and absorption rate constants. The latter two parameters respectively, quantitatively describe the sub-surface kinetic properties of the metal-hydrogen interaction leading to quantitative characterisation of the hydrogen coverage at the metal surface, θ_H.

The model considers a subsurface reaction (as a result of proton tunnelling) that is quite fast and constitutes a transition layer of a thickness that could range upwards from approximately 1 nm[24]. This establishes a sub-surface hydrogen concentration of C_0. As hydrogen is generated on the charging surface an equilibrium will be established between the surface covered (adsorbed hydrogen atoms) and hydrogen just below the surface (in the absorbed state, with concentration C_0)[25]. By manipulation of the model one can estimate approximate values for the finite rate constants, K_{abs} and K_{des}, for the absorption and desorption processes.

16

2.2.2.1   The Role of Hydrogen Promoters

A number of species have the effect of increasing the kinetics of the hydrogen entry into steel. The significant feature is that, in many cases, very small additions of these substances bring about a substantial increase in the hydrogen entry kinetics. The generic terms "cathodic poison" and "cathodic promoter" are applied to these species because they are said to poison the evolution reaction and therefore promote hydrogen absorption.

Prominent among the species which have been found to promote the hydrogen entry are certain compounds and elemental forms of Group V-A and VI-A elements of the Periodic Table. These are phosphorus, arsenic[26], antimony, and bismuth (V-A)[27] and sulphur, selenium, and tellurium (VI-A)[27]. Other species which increase the hydrogen permeation are the halide ions (particularly iodine) in acid solutions, cyanide ion in alkaline solutions and hydrocarbons such as naphthalene[28], thioureas and triazoles[29]. Salts of heavy metals such as mercury, tin and lead have also been reported as enhancing hydrogen entry.

McCright and Staehle[26] reported the effect of arsenic upon the entry of hydrogen into mild steel at a constant electrochemical potential. It was noted that the extent of hydrogenation depended on the electrochemical potential. Only when the species was polarised to sufficiently cathodic potentials was there noticeable entry and permeation of hydrogen in the steel. The arsenic compound was most efficient as a hydrogen promoter below a potential of -400 mV_H, the reversible potential of the As/AsH_3 system as in equation [4].

$$AsH_3 \rightleftharpoons As + 3H^+ + 3e^- \qquad \text{[4]}$$

The effect of arsenic on the permeation efficiencies of 1010 steel as a function of applied cathodic potential in sulphuric acid solutions is shown in Figure 3

17
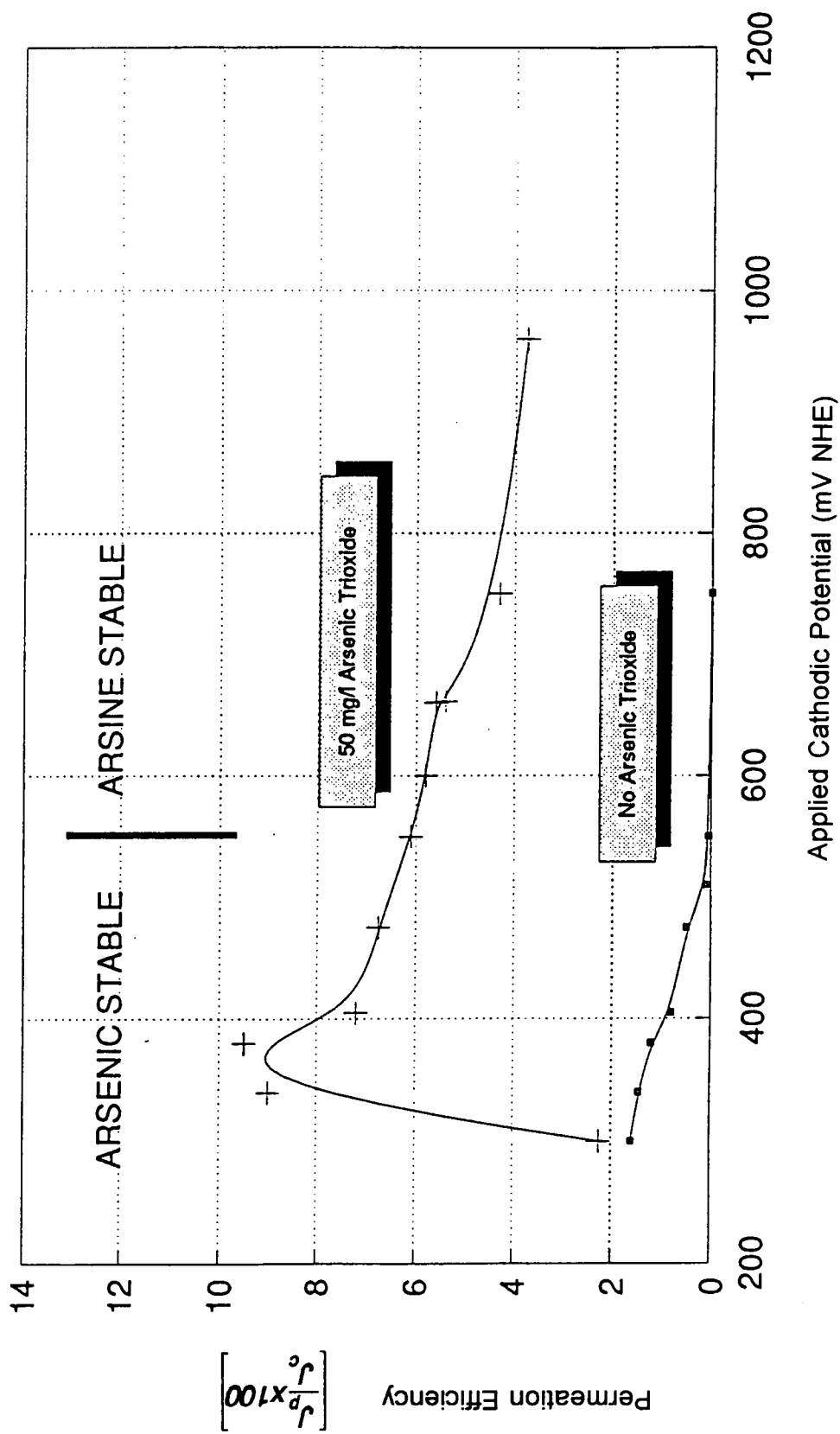
Figure 3. Effect of Arsenic Trioxide Additions on Permeation Efficiency[26]

18

taken from reference (26). It was concluded that efficintet cathodic poisoning could be achieved if during charging, the potential at the steel surface was maintained at a value more cathodic than -400mV$_H$.

Unfortunately no clear cut general explanation can be given why certain species act as hydrogen promoters. Possible considerations such as adsorption strength of the species, structure of the double layer, surface and bond energies, should be made. The most pronounced effects for Group V and VI elements appear most generally where the hydrides of these elements are stable. These hydrides appear to adsorb strongly and compete with hydrogen for available sites. Adsorption of the hydride phase can result in an increase in the surface concentration of hydrogen by such a scheme as:

$$2Fe + AsH_3 \rightarrow FeAsH_2 + FeH \qquad\qquad [5]$$

The experiments cited on charging from the gas phase emphasize the uniqueness of the hydride phase in catalyzing the hydrogen entry[31].

It is well known that additions of H_2S to the charging media promote hydrogen induced cracking of steels in aqueous media, especially when the media are acid[32,33]. In acid media the active species is H_2S and in alkaline solutions the active species is HS^- and S^- [30,34,35]. Measurements of both hydrogen permeation rates[8] and hydrogen uptake[30,34] have shown that the addition of H_2S increases the hydrogen concentration.

2.2.3 Fickian Diffusion and Boundary Conditions Arising from Electrochemical Hydrogen Charging.

Electrochemical methods for the investigation of metal-hydrogen systems are superior to other techniques, e.g., gas-volumetric, because of their simple procedure and their flexibility towards variation of experimental conditions. Moreover, these techniques allow measurements at very low hydrogen equilibrium pressures which occur, for instance, in metal-hydrogen systems associated with group V(a) elements of the periodic table[22] in the concentration range for ideal dilute solutions at normal temperatures.

Often conventional laboratory hydrogen permeation studies are carried out using similar apparatus to those first used by Devanathan and Stachurski[36] as shown schematically in Figure 4. The arrangement is such that a metal membrane is fixed between two glass compartments. On one side the cathodic cell provides a source of mobile hydrogen, of which a small fraction absorbs into the membrane and diffuses through the steel, under a concentration gradient to the opposite side. On the opposite side, in the anodic cell, the atomic hydrogen emerging from the steel is oxidised to water and the associated oxidation current used as a direct indication of the amount of hydrogen diffused through the steel. The surface hydrogen concentration of the steel on the anodic side is maintained at zero thus allowing calculation of the surface hydrogen concentration on the cathodic or input side once steady state conditions have been achieved.

Electrochemical methods for the investigation of the permeability of metal membranes to atomic hydrogen are carried out using a potentiostatic or galvanostatic mode of charging. Each of these modes of charging give rise to a separate set of boundary conditions at the charging surface. Conditions at the exit surface are usually such that the surface hydrogen concentration is held at a minimum value relative to the background hydrogen concentration in

20
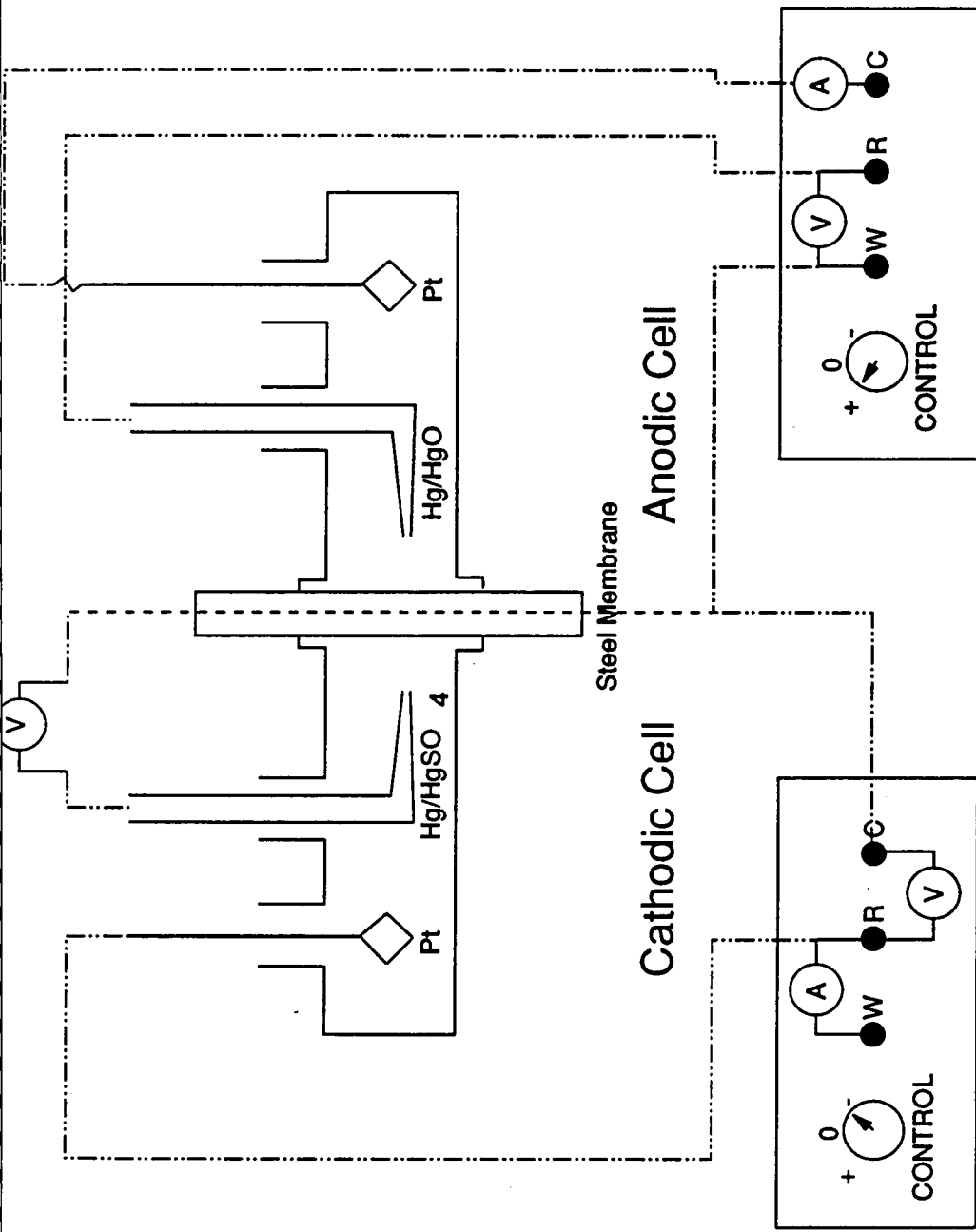
Figure 4.   Conventional Cell Arrangement for Hydrogen Permeation Experiments Based on the Work of M. A. V Devanathan and Z. Stachurski[36].

21

the steel. Traditionally it was assumed that the two modes of hydrogen charging yield simple static boundary conditions. The potentiostatic, or constant potential, mode of charging would induce a step-wise jump in the surface hydrogen concentration at the charging surface and thereafter this would remain constant. The galvanostatic mode of charging would induce a state of constant hydrogen flux at the charging surface thus resulting in an increase in surface hydrogen concentration until at infinite times, when steady state conditions are reached, a maximum value is achieved.

Since these initial postulations as to the achievable boundary conditions at the entrance surface of a steel membrane during cathodic hydrogen charging, there has been much speculation as to their validity. Pumphrey[7] and later Archer and Grant[37] gave clear evidence supporting a third model which described more accurately the boundary conditions arising as a result of cathodic hydrogen charging.

It is pointed out that the widespread assumptions that the use of a potentiostatic technique guarantees the constant surface hydrogen concentration boundary conditions, and that the galvanostatic mode of charging guarantees boundary conditions based on a constant flux of hydrogen at the charging surface, are incorrect. The boundary conditions actually established depends on the relative rates of the various steps involved in the hydrogen evolution reaction at the entrance face and its subsequent diffusion through the membrane.

During electrochemical hydrogen permeation experiments, whether performed potentiostatically or galvanostatically the anodic current density at the exit side $(x = L)$ is measured as a function of time (t) from the onset of hydrogen generation at the entrance side $(x = 0)$. The current is related to the concentration (C) of hydrogen in the plate by the first Fick law[38], where D is the apparent diffusion coefficient of hydrogen in the steel, J is the flux and F is

the Faraday constant.

$$J_{(t)} = -DF \left(\frac{\delta c}{\delta x} \right)_{(x=1)}$$ [6]

This is based on the assumption that in the plate interior the unidirectional diffusion of hydrogen is far greater from the influx to efflux side than the flux of hydrogen escaping from the influx side, this being governed by the second Fick law[38], as shown in equation [7]. This is not necessarily the case, however, for a slow coupled discharge mechanism as observed with the hydrogen absorption reaction and consequently compensation for this assumption has to be made.

$$\frac{\delta C_{(x)}}{\delta t} = D \frac{\delta^2 C_{(x)}}{\delta x^2}$$ [7]

In order to derive quantitative expressions for parameters such as the apparent diffusion coefficient and the surface hydrogen concentration of the membrane solutions to equations [6] and [7] with the appropriate boundary conditions must be found. The solutions to equation [7] are derived either by a Laplace or Fourier Transform method. Due to the complex nature of such expressions it is more convenient to express them in terms of dimensionless variables which are defined by equations [8-11].

$$\tau = \frac{Dt}{L^2}$$ [8]

$$\chi = \frac{x}{L}$$ [9]

$$\sigma_{(\chi, \tau)} = \frac{C_{(x, t)}}{C_o}$$ [10]

23

$$J_{(\tau)} = \frac{[J_t - J_0]}{[J_\infty - J_0]} \qquad \text{[11]}$$

In [10], C_0 is the constant surface concentration at the entrance side, established at all times for the constant concentration case and at infinite times for the constant flux case and the case where the flux is limited by surface reaction rates. In [11], J_∞ is the steady state permeation current density and J_0 is the steady state permeation current at t < 0 where J_0 may or may not be zero but in general represents the background hydrogen concentration in the steel. Consequently equation [7] may be rewritten in its dimensionless form as:

$$\frac{\delta\sigma(\chi)}{\delta\tau} = \frac{\delta^2\sigma(\chi)}{\delta\chi^2} \qquad \text{[12]}$$

Tables 2- 5 show a series of diffusion coefficients, taken from the literature, calculated for various carbon-manganese steels.

For steels of similar composition to those used in this work, described in section 3.1, the diffusion coefficients published in the literature, range from between 7.2×10^{-6} cm^2 s^{-1} [16] and 4.0×10^{-7} cm^2 s^{-1} [105,121].

Table 2.   Diffusion Coefficients From the Work of J. Brogan et al.[13]

Material	Diffusion Coefficient D cm^2 s^{-1}
Steel Type: Pipe line (no analysis given)	9.2×10^{-7} 1.32×10^{-6}

Table 3. Diffusion Coefficients From the Work of M. G. Hay[15]

Steel Type: Pipe line steel	Diffusion Coefficient D cm^2 s^{-1}
Z245.3 CatIII	2.4×10^{-6}
Z245.1 CatII$^{\$*}$	2.2×10^{-6}
Z245.1 CatII*	2.4×10^{-6}

Composition %	Z245.3 CatIII	Z245.1 CatII$^{\$*}$	Z245.1 CatII*
C	0.15	0.04	0.09
Mn	1.02	0.8	0.77
Si	<0.01	0.21	0.1
S	0.012	0.001	0.001
P	0.01	0.01	0.009
Cu	0.02	0.18	0.01
Ni	0.01	0.18	0.02
Cr	0.01	0.02	0.02
Mo	<0.01	-	0.002

$^{\$}$ Heat treated

* Calcium treated for sulphide shape control.

Table 4.   **Diffusion Coefficients From the Work of D. Noël et al.[16]**

Steel Type: Pipe line steel	Diffusion Coefficient D cm^2 s^{-1}
120	5.9×10^{-6}
27	6.3×10^{-6}
77	7.2×10^{-6}
142	7.0×10^{-6}
43	6.4×10^{-6}
D2	0.49×10^{-6}

	120	27	77	142	43	D2
Composition. (%)						
C	0.06	0.05	0.06	0.05	0.08	0.009
Mn	0.36	0.29	0.32	0.3	0.37	0.36
P	0.006	0.006	0.008	0.007	0.009	0.003
S	0.008	0.006	0.01	0.007	0.021	0.014
Si	0.03	0.03	0.03	0.03	0.03	0.004
Cu	0.03	0.01	0.04	0.01	0.16	0.009
Ni	0.01	0	0.02	0.01	0.05	0.008
Cr	0	0	0	0	0.05	0.007
Mo	0.001	0.001	0.001	0.001	0.012	0.002
V	0.002	0.001	0.001	0.001	0.002	0.006
Al	0.033	0.042	0.051	0.036	0.051	0.003
N$_2$(ppm)	78	71	83	54	77	29

Table 5. Diffusion Coefficients From the Work of DeLuccia and D. A. Berman[105,121]

Steel Type: Mild Steel. (No analysis given)	Diffusion Coefficient D cm^2 s^{-1}
4340	4.0×10^{-7}

2.3 HYDROGEN IN MATERIALS.

2.3.1 The Effect of Microstructure on Hydrogen Transport.

Introduction

Hydrogen Embrittlement is a mechanical-environmental failure process that results from the initial presence or absorption of excessive amounts of hydrogen in metals, usually in combination with residual or applied tensile stress. It occurs most frequently in high-strength steels and certain other high strength alloys.

Embrittlement by hydrogen damage manifests itself as a decrease in tensile ductility (reduction in area in laboratory testing), a decrease in notched tensile strength, particularly in slow strain rate tests but not in rapid or impact tests and delayed failure by fracture under static loading. Yield strength is not significantly affected. In the absence of a sharp initial crack, hydrogen-induced fracture caused by the diffusion of hydrogen into the metal often initiates at subsurface sites where triaxial stress is highest. When the critical stress is exceeded, a crack initiates and propagates through the region of high hydrogen concentration. If a sharp crack is already present, such as a fatigue or stress-corrosion crack, the hydrogen cracking may initiate at the tip of the pre-existing crack[39]. In quenched-and-tempered steels, hydrogen cracking usually follows prior austenite grain boundaries[39].

2.3.1.1 Classification of Hydrogen Damage Processes.

It is necessary to categorize the specific types of hydrogen damage in order to enhance the understanding of the factors that affect this behaviour in alloys and provide a basis for development and analysis of theories regarding different hydrogen damage mechanisms. The first three classes are grouped

28

together and designated as hydrogen embrittlement because these are the failure modes that typically exemplify classical hydrogen embrittlement[40].

Hydrogen Embrittlement

(i) *Hydrogen environment embrittlement* occurs during the plastic deformation of alloys in contact with hydrogen-bearing gases or a corrosion reaction and is therefore strain rate dependent. The degradation of the mechanical properties of the ferritic steels, nickel-base alloys, titanium alloys, and metastable austenitic stainless steels is greatest when the strain rate is low and the hydrogen pressure and purity are high.

(ii) *Hydrogen stress cracking* is characterised by the brittle fracture of a normally ductile alloy under sustained load in the presence of hydrogen. Most often, fracture occurs at sustained loads below the yield strength of the material. This cracking mechanism depends on the hydrogen fugacity, strength level of the material, heat treatment/microstructure, applied stress, and temperature. For many steels, a threshold stress exists below which hydrogen stress cracking does not occur. This threshold is a function of the strength level of the steel and the specific hydrogen-bearing environment. Therefore, threshold stress or stress intensity for hydrogen stress cracking is not considered a material property. Generally the threshold stress decreases as the yield strength and tensile strength of an alloy increases[40]. Hydrogen stress cracking is associated with absorption of hydrogen and a delayed time to failure (incubation time) during which hydrogen diffuses into regions of high triaxial stress.

29

(iii)   *Loss in tensile ductility* was one of the earliest recognised forms
of hydrogen damage. Significant reductions in elongation and
reduction in area are observed for steels, stainless steels, nickel-
base alloys, aluminium alloys and titanium alloys exposed to
hydrogen. This mode of failure is most often observed in lower-
strength alloys, and the extent of loss in tensile ductility is a
function of hydrogen content of the material[41]. Loss in tensile
ductility behaviour is strain rate sensitive and becomes more
pronounced as the strain rate decreases.

(iv)   *Hydrogen attack and Decarburization* are high-temperature forms
of hydrogen damage which occur in carbon and low-alloy steels
exposed to high-pressure hydrogen at high temperatures for
extended time. Hydrogen enters the steel and reacts with
carbon either in solution or as carbides to form methane gas; this
may result in the formation of cracks and fissures or may simply
decarburize the steel, resulting in a loss in strength of the alloy.
This form of damage is temperature dependent, with a threshold
temperature of approximately 200°C.

(v)   *Blistering* occurs predominantly in low-strength alloys when
atomic hydrogen diffuses to internal defects, such as laminations
or non-metallic inclusions, and then precipitates as molecular
hydrogen (H_2)[42]. The pressure of molecular hydrogen can attain
such high values that localised plastic deformation of the alloy
occurs, forming a blister that often ruptures[43]. Blisters are often
found in low-strength steels that have been exposed to
aggressive corrosive environments (such as H_2S) or cleaned by
pickling.

(vi)   *Shatter cracks, flakes, and fish eyes* are features common to
         hydrogen damage in forgings, weldments, and castings. They
         are attributed to hydrogen pick up during melting operations
         when the melt has a higher solubility for hydrogen than the solid
         alloy. During cooling from the melt, hydrogen diffuses to and
         precipitates in voids and discontinuities, producing the features
         that result from the decreased solubility of hydrogen in the solid
         metal. In many aspects these features are comparable to
         blistering, and this could be considered a special case of that
         class.

(vii)   *Micro-perforation* by high-pressure hydrogen occurs at extremely
         high pressures of hydrogen near room temperature. Micro-
         perforation occurs predominantly in steels. This form of
         hydrogen damage manifests itself as a network of small fissures
         that allow permeation of the alloy by gases and liquids.

(viii)   *Degradation in flow properties* in hydrogen environments has
         been found at ambient temperatures for iron and steel and at
         elevated temperatures for several alloy systems[44]. The steady-
         state creep rate under constant load has been observed to
         increase in the presence of hydrogen for some nickel base
         alloys.

(ix)   *Hydride formation* produces loss of ductility in magnesium,
         tantalum, niobium, vanadium, uranium, thorium, zirconium,
         titanium, and their alloys, as well as many other less common
         metals and their alloys. The degradation of mechanical
         properties and the cracking of these metals and their alloys are
         attributable to the precipitation of metal hydride phases.
         Hydrogen pick up often results from welding, heat treating,

31

charging from corrosion processes, or during melting of the alloy. Hydride formation is enhanced for some metal-hydrogen systems by the application of stress, the co-called stress-induced hydride formation. Alloy systems that form hydrides are generally ductile at high (>300 K) and low (<100 K) temperature. This temperature dependence is comparable to that observed for the hydrogen embrittlement of ferrous and nickel alloys. Some of these alloys are also susceptible to failure in hydrogen by mechanisms other than hydride formation. Some evidence exists that nickel and aluminium alloys may also form a highly unstable hydride that could contribute to hydrogen damage of these alloys; however, this possibility has not been confirmed.

2.3.1.2 Hydrogen Induced Cracking (HIC)

Mechanism of Crack Initiation.

In process environments containing wet hydrogen sulphide, or a combination of constituents which lead to the presence of significant amounts of absorbed hydrogen on the surface of the component, then substantial amounts of hydrogen will diffuse into the steel. The magnitude of the sulphide concentration will determine the percentage of surface coverage of hydrogen formed on the metal surface and will define the extent of the problem associated with the internal diffusion of hydrogen into the metal.

As the hydrogen diffuses into the steel it will be arrested by the free surfaces generated by discontinuities, such as sulphide and oxide inclusions in the steel[41]. At these surfaces some degree of combination will take place forming molecular hydrogen, which will be unable to escape. This will generate internal pressure at the inclusions and cause cracking or blistering (if defects are close to the surface) in the steel. As the stresses build up on neighbouring inclusions, coalescence of the cracks by localised shear can occur and the phenomena of step-wise cracking is observed[45]. This is illustrated in Plates 1 and 2.
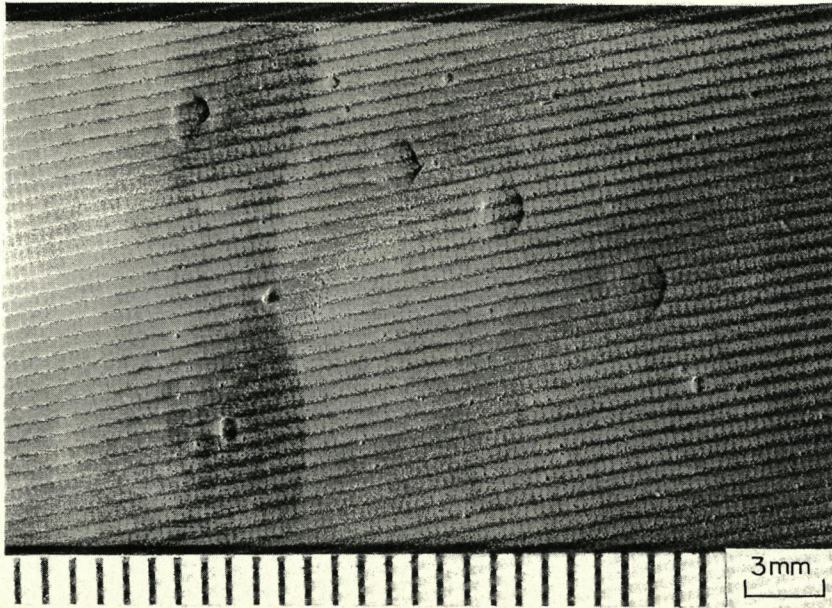
Plate 1. Typical Hydrogen Blistering in Pipe-Line Steel[46].
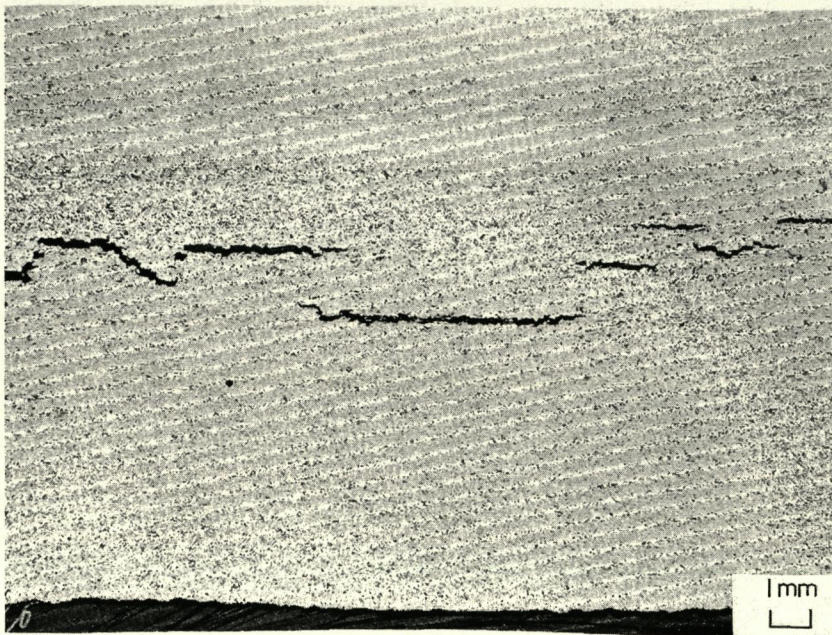
Plate 2. Typical Hydrogen Induced Cracking in Pipe-Line Steel[46].

The possibility of crack initiation into the matrix depends upon the internal pressure generated at the inclusion/matrix interface and also upon the inclusion morphology. The internal pressure in any such defect will depend upon the hydrogen content adsorbed by the steel from the environment C_0. The value of C_0 will depend upon both the chemical and surface properties of the steel. The value of C_0 must be compared with the minimum hydrogen content necessary to initiate a crack C_{th}[40]. However, C_{th} will depend only upon the properties of the steel and the properties and geometry of its inclusions. Hence by comparing C_0 with C_{th} a model for hydrogen induced cracking can be devised as shown in Figure 5[47].

Factors that Influence HIC

The factors that influence hydrogen induced cracking can be conveniently considered in terms of the above model. If the problem is to be avoided, steps should obviously taken either to reduce C_0, the amount of hydrogen entering the steel or alternatively increase C_{th}, which can be considered as the tolerance level in the steel before cracking occurs.

Modes of hydrogen uptake have been considered in detail in section 2.2.1 of this work. One of the best ways to reduce the hydrogen uptake of the steel is to reduce the degree of corrosion. This can be achieved with the use of corrosion inhibitors. Amine inhibitors form a film on the steel and are commonly used, but to rely on inhibition means that the system has to be constantly monitored.

It would be beneficial to remove the H_2S and ensure that the pH of the system does not fall too low, but for practical installations both of these routes may not be applicable. It has been shown that a local sulphidising environment can be formed by reaction of the environment with sulphide inclusions at the surface of the steel and hence reducing the sulphur in the steel may be

35
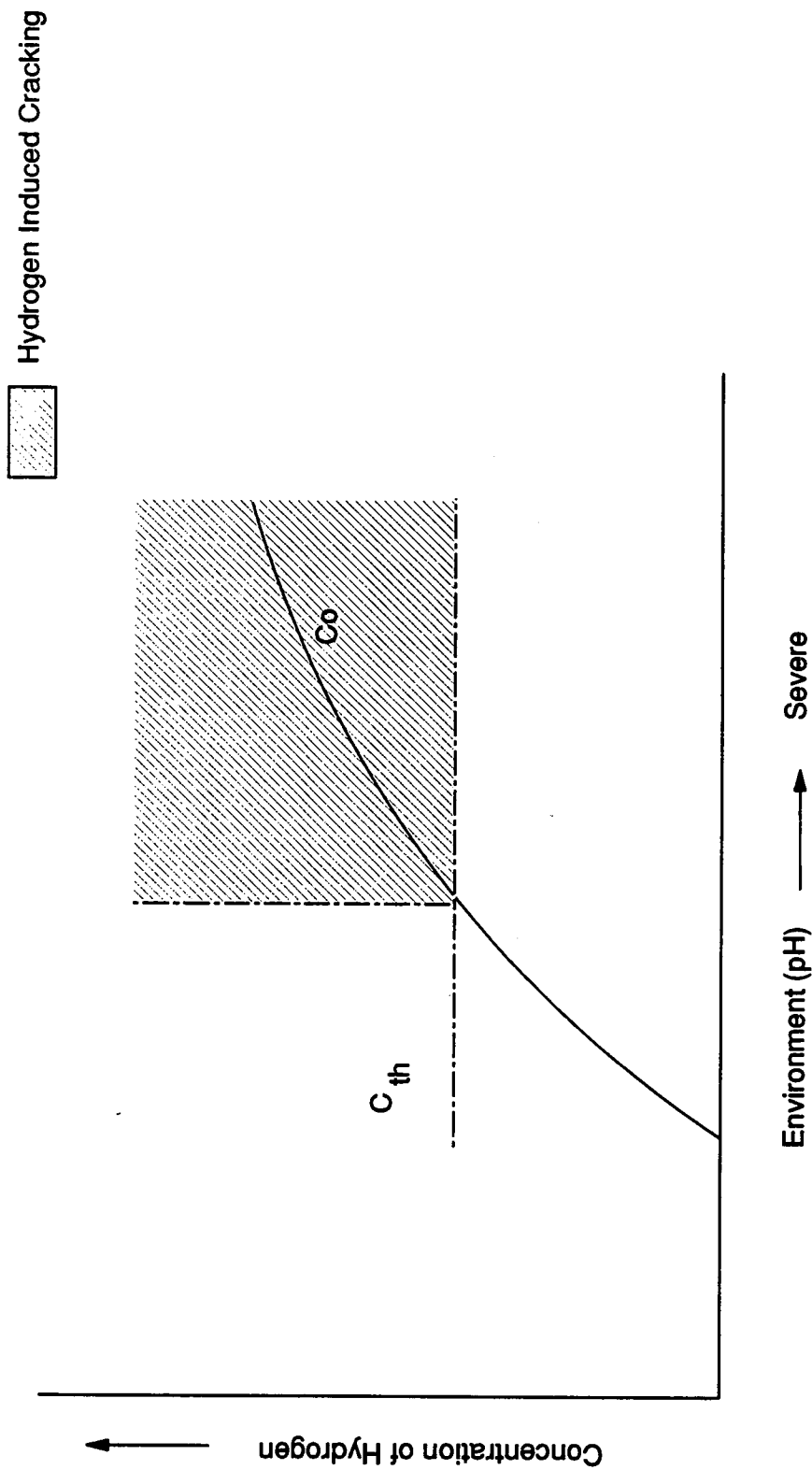
Figure 5. Schematic Illustration of the Relation Between C_0 and C_{th} [47].

36

beneficial. The additions of copper to steel has been shown to be beneficial in certain circumstances in reducing the uptake of hydrogen in the steel[48,49]. The exact mechanism is not clear but it is reasonable to assume that the copper precipitates on the surface of the steel acting as a nucleation site for the hydrogen recombination reaction and hence reduces the amount of hydrogen available for diffusion into the steel. Alternatively copper precipitates as a copper sulphate film on the surface of the steel which is partially protective. Various levels of copper have been proposed to eliminate the problem of HIC. These are mainly based on standard exposure tests where steels are subjected to immersion in artificial sea water saturated with H_2S and containing acetic acid which lowers the pH to around 3.5[47].

A value of 0.25% Cu is suggested to be sufficient to prevent HIC in seamless pipes, whereas levels of 0.3% are claimed to be required for submerged arc welded pipe. The efficiency of the copper additions depends upon the acidity of the solution. Copper is shown to be beneficial in sea water saturated with H_2S, but its influence is nullified in more acidic conditions. This is probably because in the highly aggressive conditions, produced by acidifying with acetic acid, the rate of hydrogen production is so fast that even if Cu reduced the amount of diffusible hydrogen there would still be sufficient to cause damage. Small additions of chromium and nickel to the melt are also thought to be beneficial to the reduction in HIC susceptibility of the steel[49].

Factors that Influence the Tolerance Level of Hydrogen in the Steel.

If the hydrogen has to nucleate inside the steel at discontinuities formed by inclusions then an obvious way to increase C_{th} is to remove all inclusions. It has been observed that decreasing the sulphur content of the steel, markedly reduces the amount of HIC. Further, if the inclusions present are highly elongated then this will increase the problem of HIC, as the hydrogen pressure inside these defects will have a more significant effect as the defects get

37

longer and sharper. In summary it would appear that controlled-rolled steels are more susceptible to HIC than quenched and tempered steels and the effect increases as the sulphur content increases. Type II manganese sulphide inclusions are particularly harmful as they deform plastically during rolling and elongate in the rolling direction.

It would be beneficial if the form of the inclusions could be changed. Additions of calcium and cerium to the steel alter the surface energies of the inclusions causing them to spheroidise[49]. Hence their influence on fracture behaviour is reduced and the influence of the internal hydrogen pressure is minimised. This is shown in Table 6 for API steels X42 → X65 treated with calcium[45]. Generally the level of Ca added to kill the sulphides is such that the ratio Ca/S ≥ 2.5. Note that in Table 6 the effect of clean steel is also demonstrated, i.e., that the level of hydrogen permissible before cracking is larger from the Rim of the ingot (higher purity) than from the core where the segregation influence is strongest. This means that continuous cast steel offers an advantage over normal billet processing for resistance to HIC.

Table 6 C_{th} Values for Some Carbon-Manganese Steels.

Steel	Mn content	Location	C_{th} cc/100gr at NTP
Ordinary steel X42 → X65 API Steels.	>1.2	Core Portion	0.6 → 1.1
		Rim Portion	1.6 → 1.8
	<1.0	Core Portion	0.9 → 1.3
		Rim Portion	1.6 → 1.8
Ca-treated Steel	-	Core Portion	1.8 → 2.0
		Rim Portion	1.8 → 2.0

Local segregation of alloying elements and impurity can also lead to problems in HIC. Local Mn and P segregation can produce localised low temperature transformation products and cracks occur as these localised regions are subjected to tests in synthetic sea water saturated with H_2S. As the manganese content increases the volume of transformation product increases and hence for resistance to HIC it is advisable to restrict the Mn limit, but this adversely affects the weldability of the steel and the preferred route is to reduce the amount of carbon, sulphur and phosphorus in the steel.

2.3.1.3 Occurrence of Manganese Sulphide Inclusions in Steel.

In cast material manganese sulphide occurs as small isolated globules, as thin films or chains along grain boundaries, or as massive irregular inclusions randomly distributed throughout the matrix. In American literature these are classified as Type I. Type II and Type III respectively[50]. Type I is found in steels killed completely with silicon or incompletely with aluminium, zirconium, or titanium. Type II results if a critical amount of aluminium is added, this being just sufficient to lower the oxygen content of the steel and leave no excess of aluminium. This has also been observed in steels strongly deoxidised with zirconium or titanium. Type III results when an excess of aluminium is used for deoxidation. Magnesium when used to deoxidise the steel gives rise to Type III manganese sulphide inclusions. Massive spherical inclusions can also be encountered in high-sulphur free-cutting steels. In this type of steel, low silicon contents give inclusions with high length/width ratio, to result in good machinability. At steel-working temperatures all types of MnS inclusions deform easily, but there is evidence to suggest that the plasticity of the inclusions in the high-sulphur steel (free cutting) can vary depending on the silicon content[50]. The higher the silicon content, the greater the plasticity, and it has been suggested that silicon probably reduces the solubility of oxygen in the sulphide phase. MnS inclusions can contain up to 75% FeS in solid solution at the MnS/FeS eutectic temperature (1170°C), but this

decreases to around 25% at room temperature. Thus FeS can be precipitated with a decrease in temperature or on annealing material containing MnS inclusions for a long time. From the point of view of properties, Type I or Type III are preferred, since Type II has been associated with low ductility. MnS inclusions can be mistaken for FeO but distinction can be made with silver nitrate solution which whitens MnS but leaves FeO unaffected[50].

In most structural steels the inclusions take the form of isolated oxides or sulphides distributed throughout the matrix as shown typically in Plates 3 and 4. Their volume fraction is closely related to composition and there has been an increased tendency in recent years to reduce impurity levels giving rise to so called "clean steels". The morphology and distribution of the inclusions is dependent on the both composition and processing procedure and has a marked effect on mechanical properties, particularly toughness, for a pipeline steel.

Over the past 30 years the importance of inclusions in modifying the fracture behaviour of steels has been recognised[51,52] and theoretical models have been developed[53] to explain the observed effect. The general mechanism of ductile failure is one of void nucleation, void growth and finally void coalescence. Voids may nucleate either by decohesion of the metal particle interface or by cracking of second phase particles. Growth of the voids follows and is enhanced by strain concentrations caused by the presence of voids or cracks. If decohesion is the feature controlling fracture then it can be seen that the ductility decreases exponentially as the volume fraction of particles increases. In addition, the morphology of the inclusions is important because increasing the length/width ratio of the second phase particles gives a higher tensile ductility when the long axis of the inclusion is parallel to the tensile axis compared with plate-like inclusions tested parallel to their minor axis. Relationships such as these indicate that in order to obtain improved performance from steels then either the volume fraction of inclusions must be
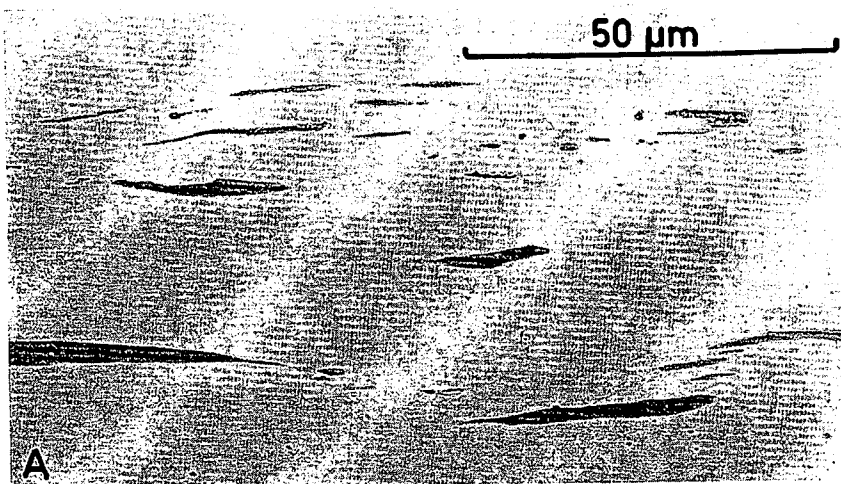
Plate 3. Typical Type (III) MnS Inclusions, Viewed in the Longitudinal Direction[54].
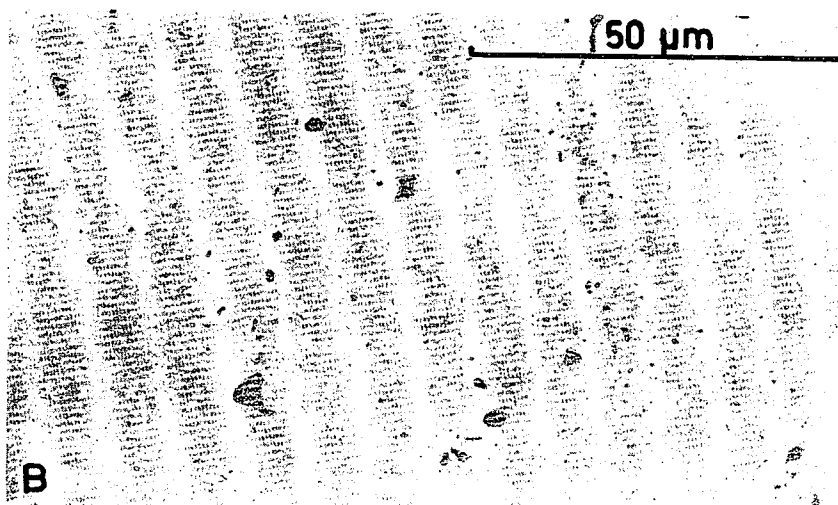
Plate 4. Typical Type (III) MnS Inclusions, Viewed in the Transverse Direction[54].

41

reduced or their morphology must be modified to avoid the formation of long elongated particles.

2.3.1.4 Development of Steels Resistant to Hydrogen Induced Cracking.

The methods discussed earlier for reducing HIC in steel suggest that low sulphur steel should be used to reduce the number of inclusions available for HIC nucleation. To ensure minimum surface area of any inclusions that may occur, Ca should be used in the melt to cause spheroidisation. To reduce hydrogen diffusion in the steel additions of copper, chromium and nickel would be beneficial. Figure 6[47] shows a detailed schematic representation for the production of a modern pipeline steel, which illustrates the above points.

In recent years, two concurrent changes in the steel making practice used to produce line pipe steel have influenced the sulphide shape in the final product. The first was the use of aluminium additions to refine the ferrite grain size in order to lower the ductile-to-brittle transition temperature and increase the yield strength. The second was the use of controlled rolling at temperatures near the critical temperature to further refine the grain size. Unfortunately, both processes are conducive to the formation of Type II manganese sulphide inclusions.

Sims[55] has explained how deoxidation increases the solubility of sulphur in the melt, and how increasing deoxidation results in a conversion from Type I to Type II MnS inclusions. In semi-killed steels the sulphides solidify before the rest of the melt and consequently form a globular shape. In fully-killed steels, the sulphides are among the last products to solidify. They freeze as thin films in austenitic grain boundaries and between dendrites.

Controlled rolling is conducive to the formation of elongated MnS stringers because the deformability of MnS increases with increasing temperature.

42

Also, Type II MnS is softer than Type I MnS[55,56]. Work has showed a positive correlation between hydrogen cracking sensitivity and the total length of inclusions in a unit cross-sectional area. There appears to be no doubt that Type II MnS stringers strongly sensitize a steel to hydrogen cracking.

Corrosive gas transmission line pipe

H2S
CO2

(High pressure line pipe with lowered pH value by increasing P_{CO_2} and P_{H_2S})

Corrosion rate control

(1)   Prevention of Hydrogen infiltration

Addition of Ni, Cr, Cu, W

(2)   Stabilization of corrosion products

Prevention of hydrogen-induced cracking caused by infiltrated hydrogen

(1)   Cleaner steel and sulphide shape control
- $S \le 10 \sim 30$ ppm
- $O \le 30 \sim 40$ ppm
- Ca treatment (Ca $15 \sim 35$ ppm)

(2)   Prevention of segregation
- Lower C
- Lower P
- Magnetic stirrer in continuous casting
- Prevention of bulging in continuous casting

(3)   Floatation of inclusions and inclusion control
- Ar bubbling in ladle
- Large tundish
- Ar shrouding
- Straight mold

Prevention of hydrogen stress corrosion cracking caused by infiltrated hydrogen

(1)   Lowered HAZ hardness
- H_v max : $260 \sim 240$
- Lower C and lower $C_{(eq)}$

(2)   Low-$C_{(eq)}$ high tensile steel
- Low C, High Mn, bainite steel
- 2-phase rolling
- Controlled cooling after rolling.

Figure 6. Control Items in Steel Making for Manufacturing Corrosive Gas Transmission Line Pipes[47].

2.3.2 Trapping of Hydrogen in Steels.

Introduction

Random solid solutions of hydrogen in metals might exist if the metal were a single crystal free of defects, and if the dissolved hydrogen were in dilute enough solution. However, all real solids contain defects which may trap hydrogen, and the mutual interaction of dissolved hydrogen atoms may permit clusters to form. Therefore, all real solutions are non-random, and hydrogen may be trapped in a variety of sites. The same is true, of course, of all atoms dissolved in a solid, but the rapid diffusion of hydrogen in metals, even at low temperatures, permits the trapping to take place at much lower temperatures than is true of any other dissolved atom. Furthermore, the presence of trapped hydrogen may be associated with the many striking mechanical effects; especially forms of hydrogen induced damage discussed in the previous section. Therefore, it is important to examine the nature of trapped hydrogen from a practical point of view, as well as studying trapping for its fundamental influence on hydrogen diffusion in metallic materials.

Hydrogen traps are sites within the material matrix that are identified by a deepening of the associated potential well. These obstacles, present in the material, affect several important parameters which are fundamental to the understanding of the transport of hydrogen in steel:

1. The hydrogen distribution in the microstructure.
2. The hydrogen diffusion coefficient.
3. The quantity of hydrogen desorbed from the steel at room temperature.
4. The hydrogen embrittlement and hydrogen induced cracking susceptibility of the material.

45

The consequence of trapping is to decrease the rate of transport of hydrogen through the metal because there is a finite probability of the hydrogen atoms entering into traps and because the residence time in the trap site will be longer than in a normal lattice diffusion site.

There are two distinct kinds of traps, present to a varying extent in materials such as steel. These are reversible and irreversible traps. A reversible trap is one at which hydrogen has a short residence time at the temperature of interest with a corresponding low interaction energy. On the other hand for the same conditions an irreversible trap is one with a negligible probability of releasing its hydrogen. A schematic representation of these traps in terms of their energy levels is shown in Figure 7.[57]

The energy levels of interstitial sites, A, and trapping sites, B, are where hydrogen resides. The evolution rate of hydrogen from a trapping site is a function of the trap activation energy E_T. E_N and E_S are the energy levels associated with absorption from the surface to the bulk and from the bulk to a trapping site respectively. The energy E_B represents the potential well which accompanies a trapping site. The magnitude of E_B, determines the nature of the trapping site. If $[E_T] >> [E_B]$ then the trap is said to be irreversible.

2.3.2.1 General Features of Trapping.

Embrittlement or hydrogen induced damage of steel, has historically been associated with the view that hydrogen could be trapped in voids in highly strained regions around crack tips, at dislocations, or in a variety of places where its effects might be deleterious to mechanical soundness of the material. Later on, such measurements of solubility at high pressure and diffusion anomalies at low temperature permitted more detailed description of trapping in steels. Consequently, several groups examined the trapping from a theoretical point of view. An important step was made by McNabb and

46

Increasing Energy ◄—

Distance —►

47
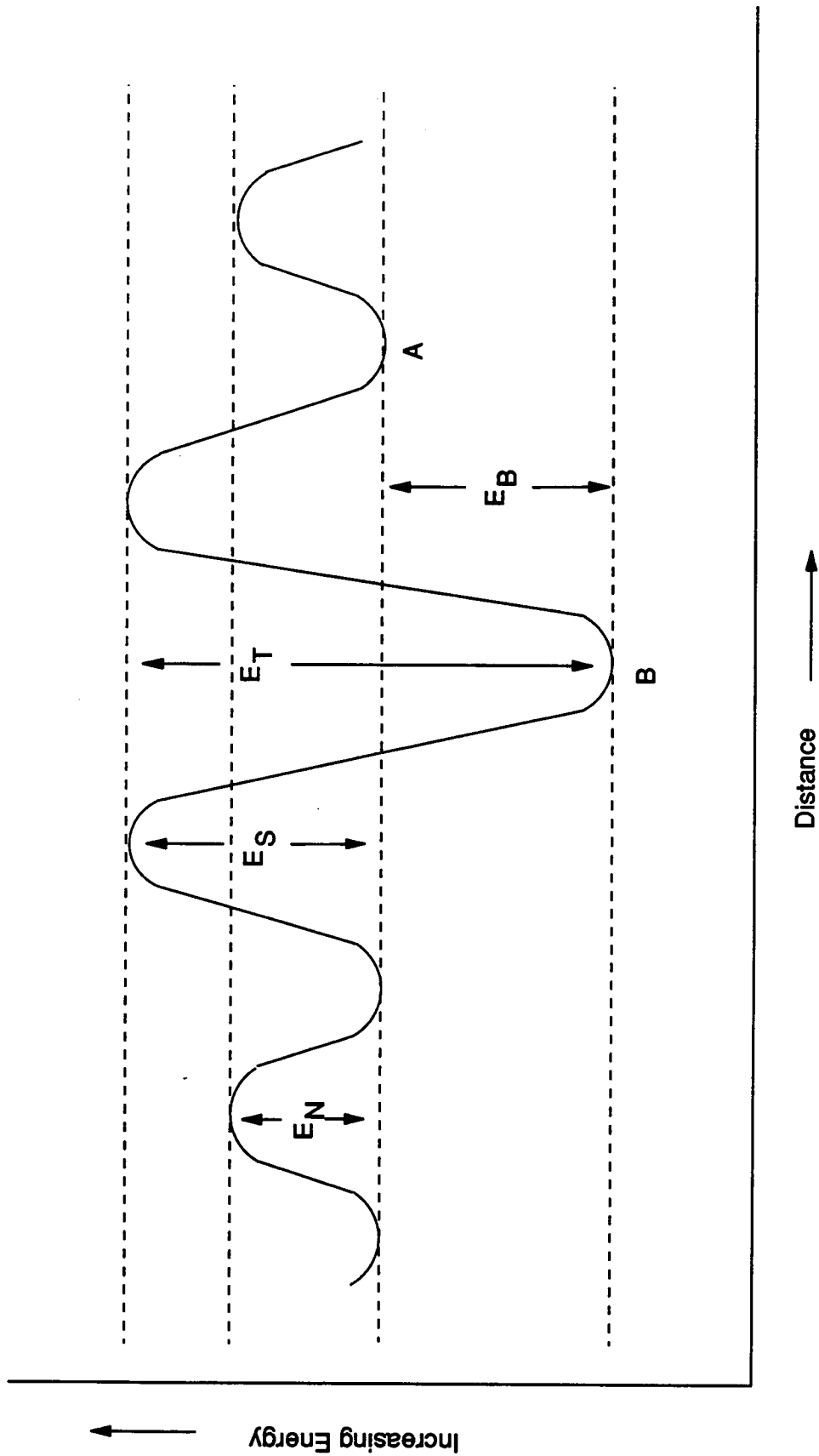
Figure 7.   Model for Trapping Site, Showing Energy Level of Hydrogen in the Vicinity of the Trap[57].

Foster[58], who described solutions of the diffusion equation, detailed in section 2.2.3, for various conditions of trapping. Their equation for the diffusion coefficient D in terms of the trap free lattice diffusion coefficient D_{latt} is the following:

$$D=D_{latt} \left(1+\frac{Nk}{p}\right)^{-1} \qquad [13]$$

Here p and k are release rate and trapping parameters, respectively. N is the number of trap sites per unit volume of material.

The general formulation of McNabb and Foster was applied to diffusion and trapping in steel by Oriani[59] under certain conditions of local equilibrium. He furthermore evaluated the relevant trapping parameters from previous experiments. He concluded that traps at interfaces were more important for trapping of hydrogen in steel (which had not been cold worked) than were the traps at dislocations. His expression for the effective diffusion coefficient D is given by:

$$D=D_{latt}C \left[C+C_{trap}(1-\phi)\right]^{-1} \qquad [14]$$

In this equation C is the lattice concentration of hydrogen, C_{trap} is the concentration of hydrogen in trapped sites, and Φ is the fraction of trapping sites which are occupied.

The analysis of Oriani was based on constancy of the activation energy for diffusion right up to the trapping site. Modification of this treatment was made by Koiwa[60], who considered the expression for the effective diffusion coefficient in terms of a model which permitted attention to the effect of a change in activation energy for diffusion near the traps. His expression for the apparent activation energy is really the same as those of Oriani, McNabb and Foster. Koiwa also examined differences in trapping and escape parameters when tetrahedral or octahedral site occupancy is assumed in a body centred

48

cubic (bcc) lattice.

2.3.2.2 Trapping Sites in Materials Pervious to Hydrogen.

Accumulation in Voids.

Voids in bcc metals have not been easy to observe, the difficulty of quenching vacancies into bcc metals has hindered experiments performed on such metals. However, Luppo and Ovejero-Garcia[61] described such experiments showing retardation of hydrogen diffusion in bcc metals in terms of trapping in micro-voids. The hypothesis that voids containing hydrogen could be produced by annealing or by deformation in iron and steel was examined by von Ellerbrook and co workers[62]. Von Ellerbrook observed that the solubility of hydrogen in iron and steel at lower temperatures, showed considerable departure from the familiar high temperature behaviour. He also noted the departure from Arrhenius behaviour of diffusion of hydrogen in iron below 150°C. Von Ellerbrook proposed that both effects could be explained by assuming that hydrogen could be reversibly trapped in small voids in steels. Von Ellerbrook analyzed observations on hydrogen outgassing at room temperature previously published by a number of investigators. Von Ellerbrook was able to adequately fit the data by calculating the release rate of hydrogen from micro-voids.

The trapping of hydrogen in micro-voids induced by deformation in a more pure material, Armco iron, was deduced by Kumnick and Johnson[63]. From transient effects in the permeation of hydrogen through annealed iron, they postulated that these transients were caused by trapping of hydrogen in micro-voids which had been introduced during the annealing following a rolling operation by means of which they had produced their thin foils. They observed no similar transients for foils thinned by chemical reduction prior to annealing.

Accumulation of Hydrogen in High Strain Fields.

Hydrogen has been assumed to segregate preferentially in dilatational strain fields. Thus, it has been assumed to segregate in the strain field near the tip of a crack and thereby assist in crack growth. Many hypotheses of this type of segregation have been proposed, but few experiments have succeeded in showing this segregation directly.

The interaction of interstitials with strain fields about dislocations has been addressed by many people. Cottrell and Bilby[157] described the way in which atmospheres of interstitials might form under edge dislocations. Later, Cocharat and co workers[64] calculated the interaction energies of interstitials with the strain fields about both edge and screw dislocations. The calculations for the large local strains near interstitials and applying appropriate boundary conditions is extremely difficult. Even for an interstitial such as carbon in iron, where the local strains about the carbon atom can be inferred from the strain associated with carbon-martensite systems, the results are often erroneous.

Changes in permeability of hydrogen through deformed Armco iron measured by Kumnick and Johnson were also interpreted in terms of trapping of hydrogen by dislocations[63]. However, they apparently found the trapping efficiency of a dislocation to be about one or two atoms of hydrogen per atom plane of dislocation length, which was very similar to that predicted by Cotterell and Bilby's model[157].

Grain Boundary Traps.

Grain boundaries in metals have long been known to be sinks for impurities. Hydrogen may be absorbed on the interfaces between precipitates and the metal lattice. Podgurski and Oriani showed that hydrogen is absorbed on the surfaces of aluminium nitride particles in iron-aluminium alloys[65]. The

interface can reversibly absorb hydrogen at room temperature, but prior absorption of nitrogen at the interface at somewhat higher temperatures (500°C) appears to block surface sites from subsequent hydrogen absorption. Other examples of hydrogen absorption at interfaces between iron and metallic carbides in steels are described at length in the review paper of Bernstein and Thompson[66].

Dislocation Trapping.

A standard method of detecting trapping of hydrogen by dislocations in iron is observation of the absorption and evolution of hydrogen from a gaseous medium. The study of Kumnick and Johnson was noted earlier. To eliminate certain surface problems, they coated the exit surface of their specimens with a thin palladium plate. They estimated that about one atom of hydrogen was trapped per atom plane of dislocation length. They were not, however, able to deduce the trapping energy from their measurements. Transient deviations in hydrogen permeability were assumed to be caused by two types of traps. One was a deep trap assumed to be micro-voids which were considered to be similar to the voids postulated by von Ellerbrock and co workers[62]. The second type of trap was assumed to be dislocations, which they deduced from annealing studies, were probably not isolated, but were in the form of cell walls.

One should note that steady-state permeation of hydrogen through materials is unaffected by the presence of traps, providing that the traps are filled prior to equilibrium. Permeation of hydrogen in alpha-iron was reviewed by Gonzales[67] whose collection of data showed remarkable consistency of values of permeation rate from different investigators even though the iron must have had widely varying density of traps of various kinds.

51

Accelerated evolution of hydrogen from metals during plastic flow has also been examined. One example is that of Donovan's[68] work on the evolution of tritium from iron, nickel, and several alloys. Tritium was used as a radioactive tracer to permit use of low release rates. By noting release rate as a function of strain, Donovan showed that excellent correlations could be made with yield phenomena, uniform flow, fracture, serrated stress-strain regions, etc. Furthermore, measurements made as a function of temperature permitted activation energies to be calculated for tritium diffusion. Good correlation of the measured diffusion energies was obtained for iron and nickel, the only materials for which Donovan produced consistent data.

Impurity Trapping

When concerned with the trapping of hydrogen on a large scale by voids, dislocations, boundaries and strained regions, the geometry cannot be specified completely, and because hydrogen can be trapped in a variety of sites with different binding energies, it is difficult to specify the trapping in quantitative terms. Impurity trapping, however, has simpler and more easily specified geometry, so the thermodynamics and kinetics of hydrogen bound to impurities are much easier to specify.

Makio lino[69] described the precipitates or second phases in steel as trap sites for hydrogen, possibly controlling hydrogen induced embrittlement. In particular he described the relationship, in terms of binding energies, between hydrogen and substitutional foreign atoms.

Table 7 shows a summary of some of the binding energies associated with hydrogen, which was compiled and elaborated by Hirth[43].

Table 7. Data for Hydrogen Trap Binding Energies in Iron.

Trap Site	Binding Enthalpy (eV)
H-perfect lattice	0
H-H	0.044
H-N	≥0.13
H-Ti	0.27
H-½H$_2$, vapour phase or in void.	0.30
H-AlN (Aluminium Nitride) interface.	0.67
H-FeC interface.	≥0.87
H-TiC interface.	0.98

Hydrogen traps which are shallow or reversible in the diffusion process at ambient temperature might be analyzed to yield satisfactory values for the binding energy by permeation, absorption, or evolution experiments on the assumed basis of thermodynamic equilibrium of hydrogen in normal lattice sites and in abnormal trap sites. As for hydrogen traps which are not shallow and behave as sinks at ambient temperature, high temperature hydrogen evolution experiments must be attempted.

2.3.2.3 Prediction of Trapping Parameters.

Turnbull and co workers[70] made a theoretical analysis of the combined effects of reversible and irreversible trapping, with varying degrees of occupancy, on hydrogen transport in metals. The analysis was coupled with repetitive electrochemical permeation experiments to characterise the diffusion and trapping parameters associated with a 13% Cr martensitic stainless steel

53

commonly used for oil production tubing. The density of reversible and irreversible traps was measured along with the binding energy of the reversible traps and the capture rate constant for the irreversible traps. In the light of this work it was concluded that it would be erroneous to use an effective diffusion coefficient as a quantitative parameter for characterising hydrogen transport in systems which were dominated by irreversible trapping.

2.3.3 Mechanisms of Hydrogen Embrittlement and Hydrogen Induced Failure.

Introduction.

Hydrogen embrittlement (H.E.) is defined as the hydrogen assisted reduction of the load-bearing and/or the mechanical energy absorption ability of a metallic alloy. Theories and models used to describe cracking associated with hydrogen atoms, have to account for the electrochemical kinetics of hydrogen atom generation, the absorption of hydrogen atoms, transport and localisation of hydrogen atoms in the metal and the interaction of the material with the absorbed hydrogen atoms under localised conditions of stress and strain. All of these factors have to be considered in predicting the response of a material to a particular environmental and mechanical condition.

The transport and localisation (or trapping) of hydrogen atoms in the metal are discussed in detail in sections 2.3.1 and 2.3.2 respectively. Failure due to absorbed hydrogen atoms generally requires localisation, or trapping of the hydrogen atoms. Localisation of hydrogen atoms can occur at trap sites such as dislocations, grain boundaries, interfaces between different phases, or voids and cracks within the material where hydrogen atoms can surface absorb and recombine[71]. Localisation can also occur through the effect of stress on the chemical potential of hydrogen atoms. Regions of hydrostatic stress are regions of low chemical potential and thus diffusion of hydrogen atoms will occur to this region, thereby raising the local concentration of hydrogen atoms. During steady-state conditions, where the flux of hydrogen atoms is independent of time, the local chemical potential will be that of hydrogen atoms in the bulk material since the system would come to equilibrium but the local hydrogen atom concentration would be elevated in relation to the surrounding unstressed matrix.

A range of mechanisms have been proposed to explain the effect of hydrogen on the materials behaviour and there are several theories concerning the mechanism of hydrogen embrittlement. It appears, however, that there is no single mechanism applicable to all systems. Some broad classifications have evolved, as described by Birnbaum[72], within which these individual mechanisms may be grouped.

1. Hydrogen Related Phase Change Mechanisms;
   - Hydride Induced Cracking

2. Hydrogen Enhanced Local Plasticity Mechanisms;
   - Hydrogen Induced Slip Softening
   - Enhanced Plastic Flow

3. Mechanisms Related to Hydrogen Effects on the Cohesive Energy;
   - Lattice Decohesion.
   - Hydrogen Adsorption (Surface Energy)

In addition to the above, there are several other mechanisms which are not described adequately by the general classifications offered by Birnbaum. These describe hydrogen embrittlement as a function of internal hydrogen pressure (Pressure theory) and as a function of hydrogen dislocation interactions.

2.3.3.1 Hydrogen Related Phase Change Mechanisms.

The most common example of a hydrogen related phase change mechanism is the stress induced formation of hydrides and the subsequent brittle fracture of these phases. The metals which form hydrides are primarily group V

56

metals of the periodic table including Nb, V and Ta and also Zr, Ti, Mg, Pd and their alloys. The fracture proceeds by hydride formation in the stress concentrated region of the crack tip, cracking of the hydride, crack arrest at the hydride-matrix interface and a cyclic repartition of the above events. The hydrides have an increased volume and the triaxial tensile field at a crack tip promotes hydride formation under conditions where they would be thermodynamically unstable. The hydrides exhibit limited ductility because of restricted dislocation mobility and cracking of the hydrides is by a brittle cleavage mode.

Westlake[73] suggested that hydrides could form ahead of a crack tip which would result in lattice embrittlement as the hydride is of lower strength than the surrounding matrix. After such a phase has contributed to crack propagation it redissolves. Brittle hydrides could conceivably be formed by contact of hydrogen with metal and thus provide a constantly mobile cracking medium. However, despite the wide range of modern surface analysis techniques, no positive evidence exists verifying the presence of an iron hydride phase. Gilman[74] proposed that it was thermodynamically possible for the formation of a surface hydride near the tip of a crack in iron which would suppress the glide of dislocations which, in turn, would suppress crack blunting enabling crack propagation. Crack propagation would be possible as the presence of the hydride phase would tend to prevent stress relaxation and thus provide favourable conditions for embrittlement.

2.3.3.2 Hydrogen-Enhanced Local Plasticity Mechanisms.

The term hydrogen embrittlement commonly refers to the loss of macroscopic ductility and the brittle appearance of failed surfaces when viewed at a low magnification. Cleavage resulting from decohesion is an obvious example where both microscopic and macroscopically brittle behaviour are observed.

Birnbaum[72] claimed that hydrogen-enhanced local plasticity was a viable mechanism for a large number of metals and alloys including nickel-base, iron-base and aluminium-base alloys.

Birnbaum's description of the cracking process involves localisation of hydrogen atoms at the crack tip, reduction in flow stress, slip localisation in the vicinity of the tip and continued localisation of shear leading to fracture by the various plastic failure processes, although the exact mechanism by which shear localisation causes fracture is not known.

Beachem[75,76] gave evidence of a model which described hydrogen embrittlement as a function of hydrogen induced slip softening. He proposed four interactions which could account for many phenomena encountered in stress corrosion cracking and hydrogen induced cracking:

1. On evolution of hydrogen it is either absorbed at the surface of the metal where it diffuses to defects during electrolytic charging, or it becomes part of a corrosion reaction and enters the metal at a crack tip.

2. Pure molecular hydrogen gas dissociates at clean forming surfaces and enters the metal. Some of the hydrogen will immediately form molecules again but some atoms will be absorbed before recombination.

3. Hydrogen diffuses to regions of high triaxial stress within the metal.

4. The presence of hydrogen dissolved in the ferrite matrix aids the deformation of the matrix.

Beachem[75] supported the first three points with experimental evidence and suggested that they were more concerned with the supply of hydrogen to the critical regions, whereas the final point is the crucial interaction determining the susceptibility to cracking. By observing the increases of plasticity and the lowering of torsional flow stress in material degraded by hydrogen, Beachem[75] suggested that the role of hydrogen is to increase the movement of dislocations along the slip planes. He argued that the formation, growth and coalescence of micro-voids as the fracture mode during hydrogen assisted cracking distracts the attention away from embrittlement mechanisms and towards microscopic plasticity.

Enhanced plastic flow is associated with hydrogen dislocation interactions and is primarily based on fractographic observations[77]. This approach proposes that atomic hydrogen enhances dislocation motion, generally screw dislocations, and the creation of dislocations at surfaces and/or crack tips, leading to softening of the material on a localised scale. Although this behaviour has been observed in certain steels, hardening by hydrogen has also been found. Careful high-resolution electron microscopy of what appears to be brittle cleavage or inter-granular fracture surfaces has revealed evidence of crack tip plasticity in support of this mechanism[78].

2.3.3.3 Hydrogen Effects on the Cohesive Energy.

The basis for the decohesion model for hydrogen embrittlement is that dissolved hydrogen atoms at high local concentrations in the lattice, grain boundary or interphase boundaries lower the local maximum cohesive force acting against the collinear separation of the metal atoms[79]. The requirement for cracking is a local tensile stress which is sufficiently high to equal the hydrogen-decreased maximum local cohesive force. The decohesion model postulates that the cohesive force is lowered by hydrogen but does not attempt to provide an explanation for that effect.

59

Troiano[80,81] suggested that the existence of large elastic stresses in the vicinity of the crack tip implies conditions which are thermodynamically favourable for the accumulation of hydrogen and that the hydrogen would produce a weakening of the cohesive Fe-Fe bond. This theory was further investigated by Oriani and co workers[82]. It was postulated that hydrogen concentrated at regions which were able to support elastic stresses approaching those of the cohesive strength of the iron lattice and reduce the Fe-Fe bond strength such that the maximum cohesive force is lowered. He suggested that this only occurs when the highly stressed regions are within a few atomic spaces of the crack tip. Oriani assumed that a critical concentration of hydrogen was required below which no cracking occurred. If this was the case, the experimental evidence would suggest that such concentrations could only be achieved within a few atom spacings of the crack tip.

The most direct investigation of the validity of the decohesion model is that of Vehoff and Rothe[83]. They could conceive of only two candidates for the observed fracture mechanism; micro-cleavage (hydrogen aided decohesion) and hydrogen aided micro-void formation ahead of the crack tip[83]. The latter was dismissed due to lack of evidence relating to the existence of micro-voids. In general it was concluded[83] that it would be very difficult to devise a feasible experiment to measure the cohesive force between iron atoms within which a very large amount of hydrogen was dissolved (with a H:Fe ratio >1:10). Oriani[82] concluded that competent theoretical investigations allow one to be confident that dissolved hydrogen does increase the force resisting the co-linear separation of iron atoms so that the basic postulate of the decohesion model is supported by theory.

The hydrogen Adsorption or surface energy theory is based on the Griffith theory that when a crack grows, strain energy is released but new surface energy is created. This implies that a crack will grow when the strain energy

released is greater than the new surface energy. Petch and Stables[84] suggested that the adsorption of hydrogen by a newly formed fracture surface lowers the surface energy and, in turn, the Griffith stress required for brittle fracture. Fast fracture is not affected by hydrogen but, where crack propagation is slow, hydrogen adsorption can take place and lower the stress intensity necessary for fracture. The crack will be unstable and will propagate at the rate determined by the supply of hydrogen.

The evidence suggesting hydrogen assisted cracking is a surface or near-surface effect is contrary to the slip theory of Beachem[75] but Hirth[43] suggested that adsorption could still occur as a crack tip mechanism in a more complex over-all process although he disputed a completely brittle surface energy controlled crack process since Lynch[85] showed that it greatly underestimated the work of fracture. Hirth also stated that the model was unaccountable for discontinuous cracking as indicated by acoustic emission spectroscopy, and it could not explain why the tendency for delayed failure could be reversed on stress removal[43].

2.3.3.4 The Pressure Theory.

The pressure theory of hydrogen damage, or more specifically, hydrogen embrittlement, is one of the oldest models for hydrogen damage[44]. This theory attributes hydrogen embrittlement to the diffusion of atomic hydrogen into the metal and its eventual accumulation at voids or other internal surfaces in the alloy. The underlying concept of the pressure theory is that recombination of hydrogen atoms at these internal voids or fissures can result in a high pressure of hydrogen gaseous molecules sufficient to enlarge the internal cavity thus causing progressive failure. For example, under conditions of high charging, such as for relatively low strength line-pipe steels in H_2S containing environments, internal voids and fissures can develop (usually associated with MnS inclusions) and in some cases surface blistering

61

can be observed. The basic concept implies that there is some degree of pre-existing or deformation-induced interfacial separation since only the growth of these cavities is considered explicitly. Step-wise cracking is often observed in the absence of external stress but with applied stresses fracture extends by linking blisters formed in stacked arrays in a plane perpendicular to the stress axis. This is known as stepwise hydrogen induced cracking.

The proton-dislocation interaction model was proposed by Bastein and Azou[86], and follows on from the pressure theory of Zappfe and Sims[44]. The model considers that hydrogen is transported by interstitial proton diffusion, or by dislocations through proton-dislocation interaction. Hydrogen then collects at defects as super-saturated hydrogen gas which exerts high pressure. The high pressure causes tri-axial stress around the defect which, in turn, assists crack development, despite there being no plastic deformation which would be necessary in the lattice decohesion model.

The proton-dislocation model was investigated by Tien and co workers[87] along with Johnson and Hirth[88] and more recently by Nair and co workers[89] who developed a quantitative model which required the exact binding energies associated with hydrogen and various forms of localisation or traps. This was necessary as the interest was predominantly in the number or concentration of hydrogen atoms that could be transported by dislocations to areas of high tri-axial stress. It was suggested that hydrogen would exist as anions in strong trapping sites and as atomic hydrogen in weaker trapping sites. Consequently in strong trapping sites hydrogen would destroy metal bonds by absorbing dissociated electrons. The destruction of these metal bonds would lead to a weakening of the lattice in the vicinity of the trap and consequently embrittle the material.

2.4 MEASURING THE HYDROGEN CONTENT OF MATERIALS.

2.4.1 Types of Hydrogen Probes and Monitors

There are three basic categories of hydrogen probe available at present. These are

1. Pressure type hydrogen probes. (PHP)
2. Vacuum type hydrogen probes. (VHP)
3. Electrochemical hydrogen probes. (EHP)

2.4.1.1 Pressure Hydrogen Probes.

The pressure hydrogen probe (PHP) determines the existence of hydrogen by measuring the hydrogen pressure generated in a steel tube or void. These probes have been used extensively in the petroleum industry[90]. There are two common configurations of the PHP[91], the Finger Pressure Probe and the Patch Pressure Probe. The Finger Pressure Probe is inserted into the environment to be studied and measures hydrogen diffusion on the surface of the sensing portion of the probe. The Patch Pressure Probe is affixed to the outside of the pipe or vessel and measures hydrogen diffusion through the wall itself.

The Finger type pressure hydrogen monitor is usually constructed of stainless steel with a sensing element made from the material under test, as shown in Figure 8[92]. The end of the probe inserted into the environment is sealed, and the opposite end contains a pressure gauge, a temperature gauge and a bleed-off valve. The "finger" itself is hollow, with some models having a filler rod to cut down the internal volume. When the low carbon steel is exposed to a corrosive environment with hydrogen present, the surface corrodes and atomic hydrogen is generated. It is then absorbed through the sensing skin

PRESSURE GAUGE

HOLLOW PLUG

ACCESS FITTING

ANNULAR ELEMENT
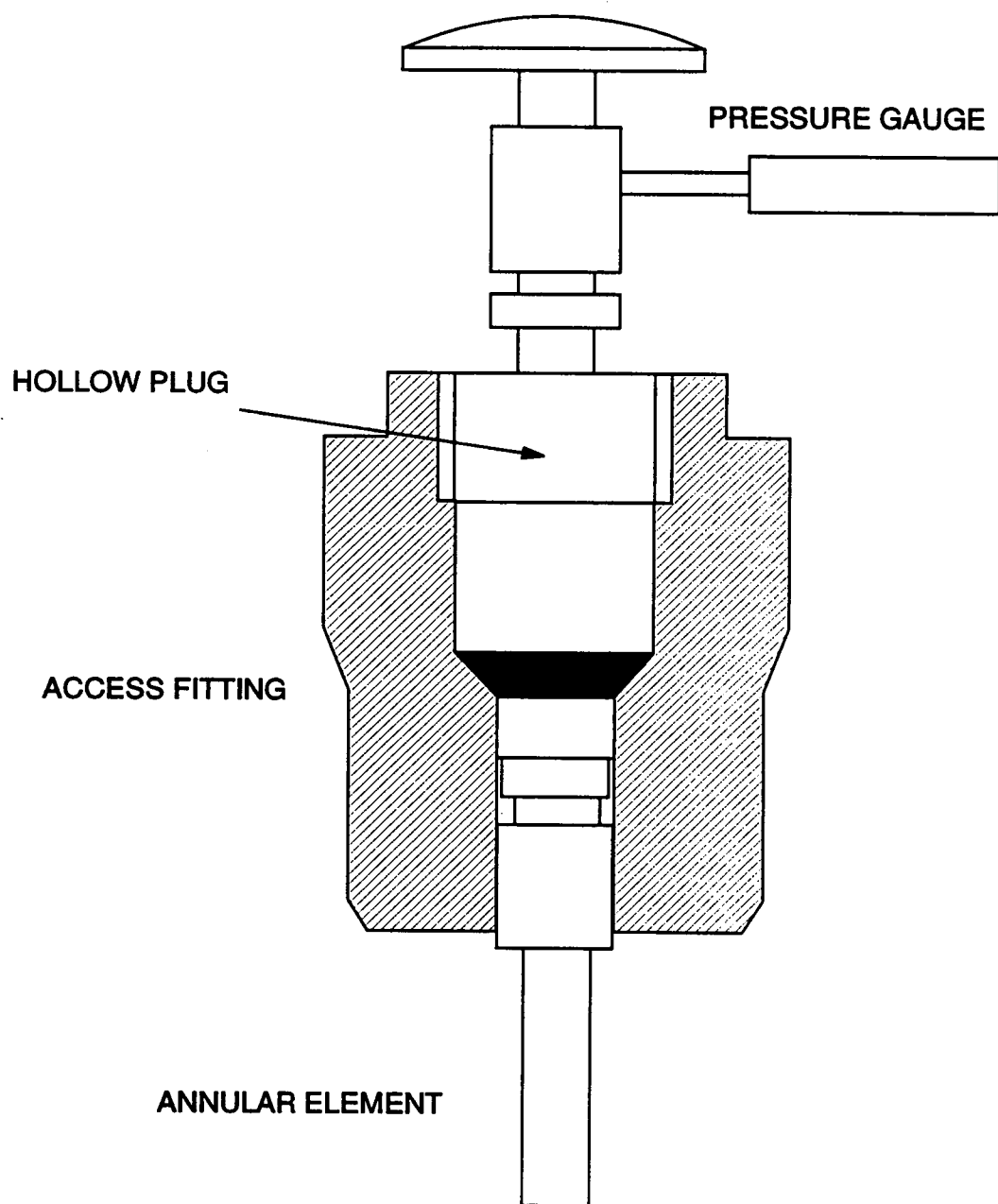
Figure 8   Schematic of the Finger Type Pressure
Hydrogen Probe[92].

64

reaching the void or annulus, after which it combines to form molecular hydrogen and is then trapped within the chamber. Since it can no longer pass through the steel, there is a build up in pressure. After temperature compensations, the pressure increase is recorded. This record will correlate with the amount of atomic hydrogen being absorbed in the corrosion process on the surface of the sensing portion of the probe[93].

The Patch configuration pressure hydrogen monitor is constructed of any material, usually the same as that being monitored[91]. It is approximately the same diameter as the pipe and is usually fixed to the pipe by welding. A pressure gauge, temperature gauge and bled-off valve, as in the Finger probe, is attached and sealed to the hole in the patch. As hydrogen absorbs through the wall it combines to form molecular hydrogen in the annulus between the pipe wall and the patch. The pressure build up is then monitored as with the Finger probe.

The most recent modifications to these types of monitors has been to eliminate the mechanical gauges and replace them with a solid state electrical sensing unit[93]. This unit usually consists of a pressure transducer and a thermocouple which are potted into an epoxy resin sealed unit. The signal is transmitted to an instrument where a liquid crystal read out is obtained showing the hydrogen transmission rate in cubic centimetres per day.

2.4.1.2 Vacuum Hydrogen Probes.

There are essentially two types of Vacuum hydrogen monitors, the first was developed by Lawrence and co workers[94,95] and the second by Radd, Oertle and Vennett[96-98].

The instrument originally designed by Lawrence was reported to perform the following functions.

1. Measure the bulk hydrogen content in a metal in the range from around 50 wppb to several hundred wppm;

2. Detect surface hydro-carbon contaminations;

3. Measure hydrogen concentration gradients and;

4. Be operated under routine laboratory conditions.

A schematic of the hydrogen analyzer is shown in Figure 9[99]. The system essentially consists of an air tight specimen holder, an energy source, for extracting hydrogen from the test specimen, a micro-quantitative gas-metering system (MGM) or hydrogen generator, a palladium-gold semi-permeable membrane (SPM), a vacuum pump, a high purity argon gas source and an electrical signal conditioning system. Hydrogen present as water or organic material is released from a metal by one of the three extraction modes

1. Low energy spark (for surface analysis);

2. Quartz muffle furnace or an induction furnace (for bulk hydrogen analysis) and;

3. Laser (for measuring hydrogen concentration gradients).

The hydrogen thus librated is directed toward the activated SPM by the flowing argon. The SPM lets only hydrogen permeate through it while remaining impermeable to other gases. The hydrogen passes through the SPM into a high vacuum where it is detected by an increase in the ion current reading as seen by the ion pump.

The earlier work of Radd, Oertle and Vennett[96-98] used a high vacuum in a cavity into which hydrogen permeates. The vacuum was maintained by a magnetic ion pump, whose electrical current requirement was proportional to the rate at which hydrogen was being captured by the pump. This particular design was intended to run along side a Finger or Patch pressure hydrogen probe and was consequently welded directly on to the pressure probe.

66
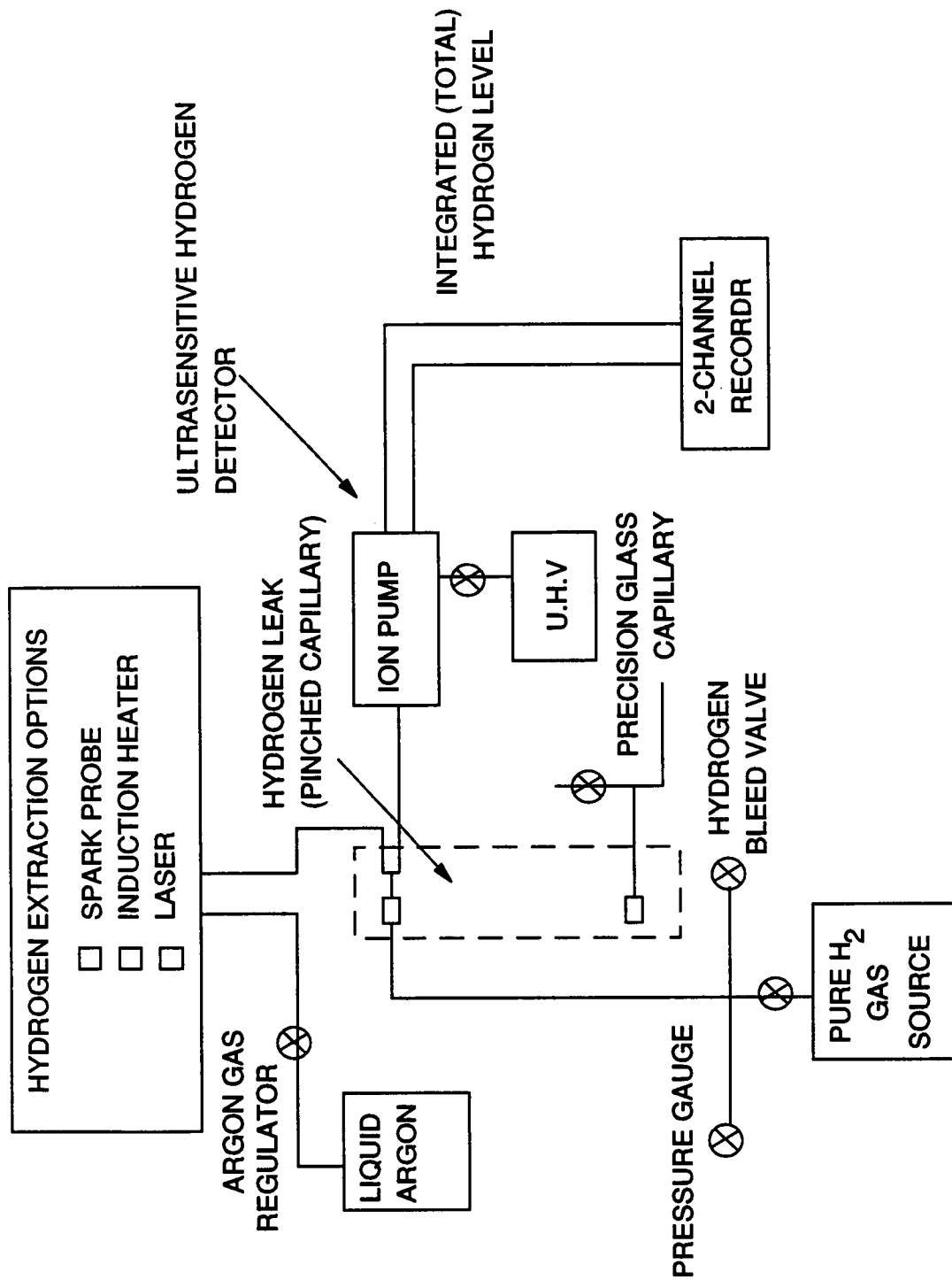
Figure 9.   Schematic of the Ultra-sensitive Hydrogen Analyzer[99]

2.4.1.3. Electrochemical Hydrogen Probes.

The Electrochemical hydrogen probe consists of a cell, usually made of either glass or Teflon, into which hydrogen will permeate. The cell is filled with an electrolyte into which an auxiliary electrode is inserted and used to oxidise hydrogen atoms that enter the cavity. The electrochemical current required to sustain this oxidation reaction is proportional to the rate at which hydrogen atoms enter the cell.

Two general types of Electrochemical hydrogen permeation probes (EHP) are in common use at present. The first is a commercial probe[100] which places a palladium foil at the steel surface where hydrogen emerges and then forms a cavity over the foil. A Teflon reservoir with auxiliary and reference electrodes form the cavity. Concentrated sulphuric acid is used as the electrolyte and the palladium foil as an anode. Hydrogen exiting the steel readily permeates the palladium foil, due to its high solubility and is then oxidised yielding a hydrogen permeation current.

The second type uses a dilute sodium hydroxide electrolyte, and the steel surface contacted by the electrolyte serves as the anode in the driven electrochemical reaction,[101-104] as shown in Figure 10[101]. The hydrogen atoms permeate through the steel, reach the electrolyte/steel interface and are then oxidised to form hydrogen ions (H^+) which enter the solution. The current required to support this reaction is a measure of the number of hydrogen atoms that are emerging from the steel.

Both electrochemical hydrogen permeation probes described here function according to the electrochemical method of hydrogen permeation developed by Devanathan and Stachurski[36].

This method requires that a diffusion gradient exists within the metal, i.e. a

high concentration of hydrogen on the influx side, due to the hydrogen promoting environment, and a zero concentration on the efflux, or exit, side, due to anodic polarisation with a potentiostat, shown schematically in Figure 11(a). By keeping the exit surface at zero concentration in this manner, the oxidising current may be taken as a direct measure of the rate of permeation of hydrogen. Analysis of the build up and decay transients can then be used to give diffusivity or concentration information.

An alternative electrochemical method for determining the surface hydrogen concentration of a metal is in the form of the Barnacle Electrode[101]. The barnacle electrode technique makes use of only the extraction side of the permeation cell, since the hydrogen is assumed to be already uniformly distributed throughout the specimen. A schematic diagram of the boundary conditions arising from this arrangement is shown in Figure 11(b). The probe disturbs the hydrogen concentration just below the metal surface oxidising the hydrogen under a potential gradient. Fick's Laws of diffusion are then used to evaluate the surface hydrogen concentration. A major simplification of the barnacle electrode is the use of the nickel/nickel oxide electrode to replace the potentiostat and act as an allegedly stable, non-polarising power electrode (cathode) that lowers the hydrogen concentration at the exit surface of the steel (anode) by oxidising the emerging hydrogen atoms to water.

2.4.1.4. Miscellaneous Hydrogen Monitors.

The Lithium Nuclear Micro-probe.

The Lithium Nuclear Micro-probe (LNM) was developed by Padawer and Schneid[105] and was designed to provide a quantitative means of hydrogen concentration-depth profile analysis within the first few microns of a materials surface. The LNM works essentially on the basis of Lithium - 7 (^{7}Li) ions at a kinetic energy of 3.075 MeV reacting with hydrogen nuclei in the surface of the
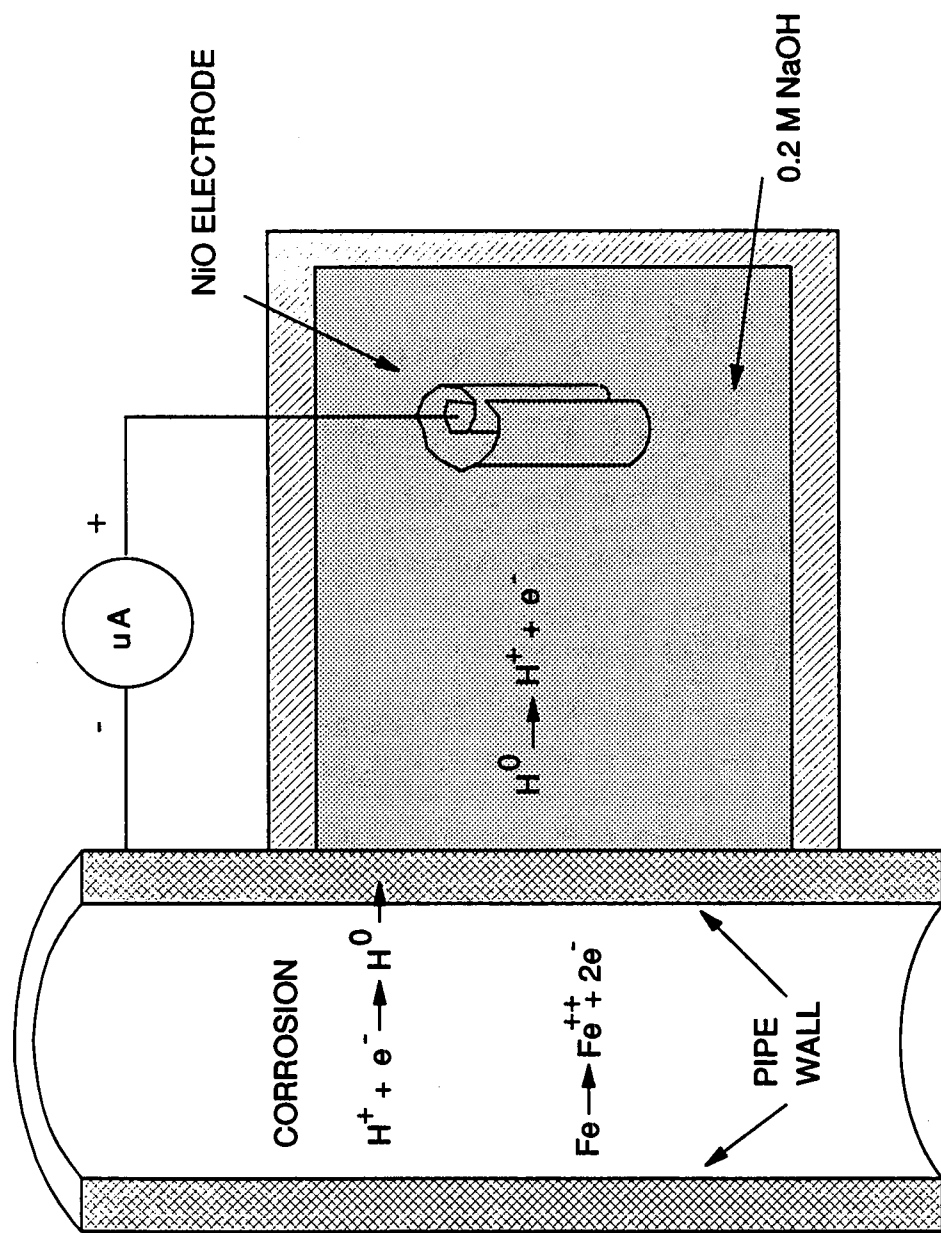
Figure 10. Schematic of Typical "Barnacle" Type Electrochemical Hydrogen Probe[101].

70
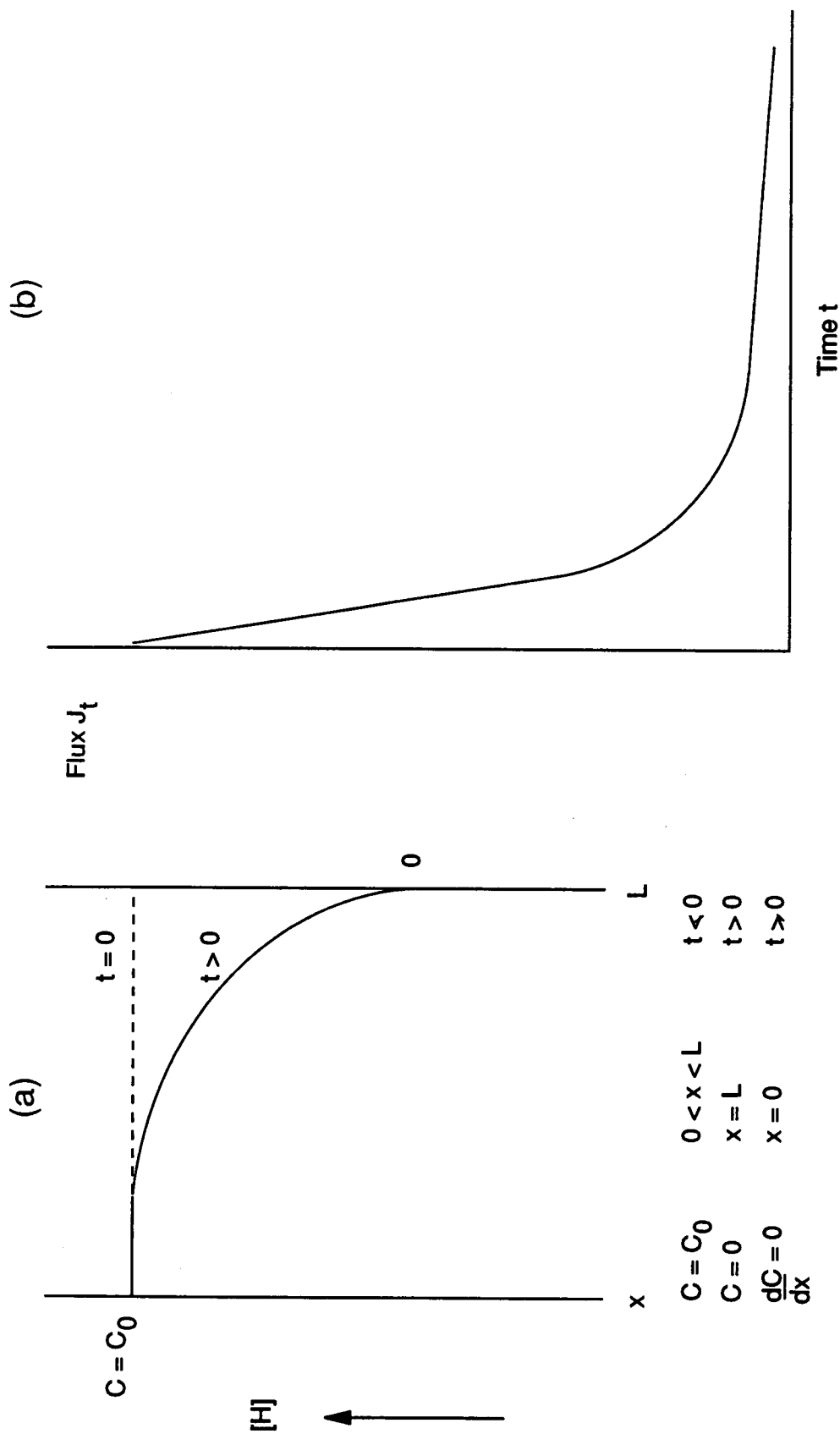
Figure 11.   Boundary Conditions Arising from (a) Electrochemical Hydrogen Permeation Probe Measurements, (b) The Barnacle Electrode Type Hydrogen Probe.

71

substrate to form the fifth excited state of ^8Be, which decays promptly by emitting either a 17.64 or 14.74 MeV gamma ray. The number of gamma rays emitted is directly proportional to the number of hydrogen nuclei at that particular depth probed. By control of the energy of the incident ^7Li beam, probing depth can be varied. This depth can be determined accurately by knowing the incident beam energy and the stopping power or absorption properties of the target material. Measurements can be made to several microns depth with an approximate resolution of 0.1 μm.

The LNM has been successfully employed by Padawer and Alder[106] to investigate the hydrogen concentration in steels during various stages of electroplating. In particular detailed studies were carried out on the hydrogen uptake of steel structures during cadmium and chromium plating[106]. The LNM proved to be a very sensitive and accurate laboratory tool for determining surface and sub-surface hydrogen concentrations. Due to the physical constraints of the probes design, however, the instrument was not suitable for field use[105].

The Solid Ionic Conductor Electrolyte Probe[106].

This method of hydrogen detection uses a solid proton conductor electrolyte of hydrogen uranyl phosphate tetra-hydrate ($UO_2HPO_4.4H_2O$) or (HUP). This is a yellow plastic compound which responds to changes in hydrogen concentration to maintain a constant hydrogen partial pressure on one side of the electrolyte[107].

The probe was reported[107] to have a Nernstian response according to the expression:

$$-zEF=RT \ln\left[\frac{p\dot{H}_2}{p\ddot{H}_2}\right]$$
[15]

where   z = charge carried   F = Faraday constant

E = potential across electrolyte

R = gas constant

T = Temperature.

$p\dot{H}_2$ and $p\ddot{H}_2$ are the partial pressures of hydrogen on

either side of an electrolyte membrane.

Generally, a perspex tube, approximately 10 mm in diameter, is stuck onto the corroding structure which has previously been palladium coated (necessary due to the corrosive nature of HUP). The HUP electrolyte is placed on top of the palladium coated surface and a stainless steel ram, whose face had been coated with the WO_3 slurry, is pressed against the electrolyte at 20 MPa for about 1 hour. A schematic of the assembled device is shown in Figure 12[106]. The probe responds due to a change in the hydrogen concentration at the electrolyte/palladium interface caused by dissolution of hydrogen into the palladium. To improve the response, the palladium layer was replaced by palladium powder pressed into the surface of the electrolyte as shown in Figure 13[107]. This change in hydrogen concentration is indicated by a change in the probe potential which is then monitored with a voltmeter.

The output from the device is logarithmically proportional to the ambient hydrogen concentration at the working electrode. Measurement is made relative to the hydrogen partial pressure of the reference electrode which is maintained at a constant value. In this way, the device is able to provide a quantitative measure of the ambient hydrogen concentration.

HUP ELECTROLYTE

REFERENCE ELECTRODE

WORKING ELECTRODE
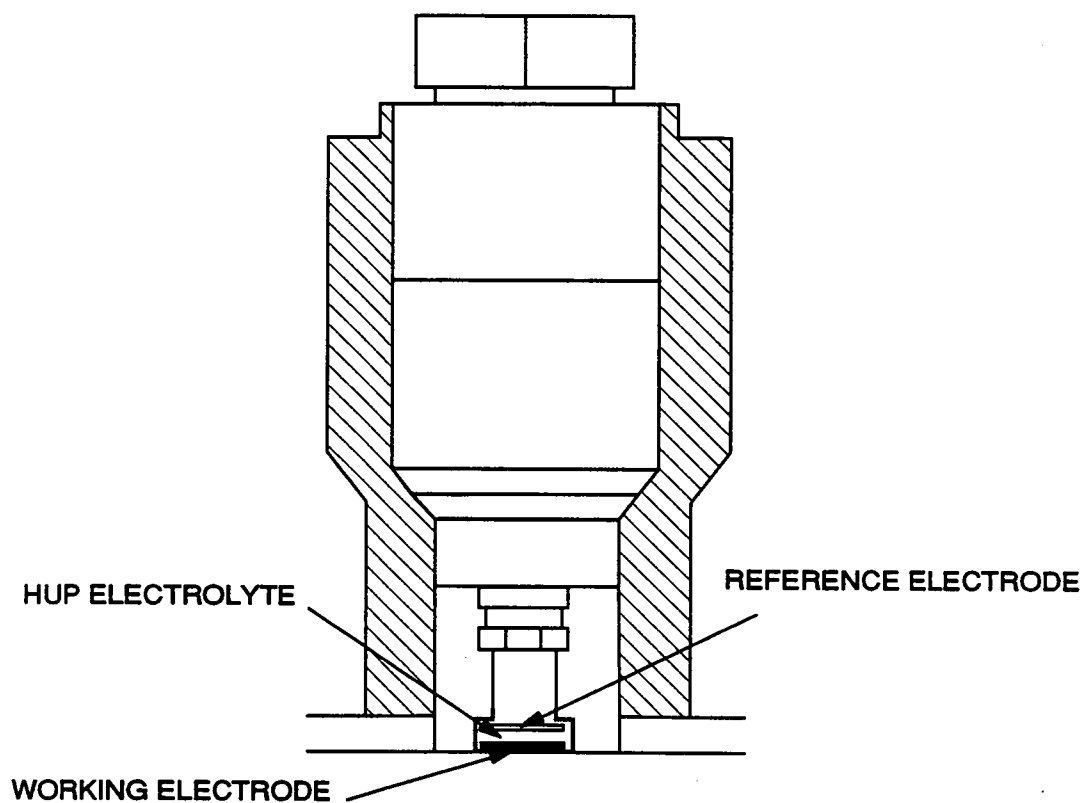
Figure 12.   Solid Ionic Conductor Electrolyte Hydrogen
Uranyl Phosphate Probe[106].

74
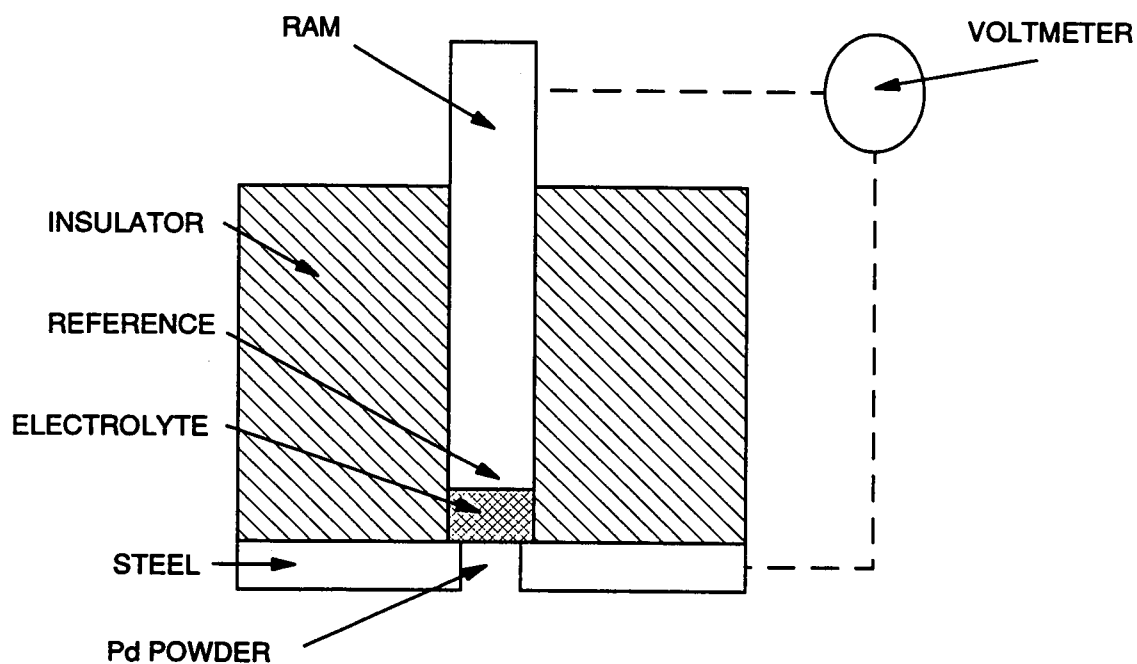
Figure 13.   Improved Solid Ionic Conductor Electrolyte
Hydrogen Uranyl Phosphate Probe[107].

75

This device is particularly useful in that the probe may be configured in any geometric design. Additionally, there is no requirement to maintain or service the unit, as the electrolyte is not consumed. As the measurement of the hydrogen concentration takes place in ionic form, rather than in gas phase, there is no need for a hydrogen bleed valve to release built up hydrogen pressure.

The probe may be used in two ways. Firstly, it may be configured inside a sacrificial housing which may corrode, liberating the hydrogen to be monitored. This mode of operation is similar to that used for the finger-type pressure hydrogen probe. Alternatively, the probe may be attached to the outside of a pipe wall or vessel and used to monitor the permeation of hydrogen through the steel. This method has the advantage of real time monitoring and functions in a similar manner to the Barnacle-type electrochemical hydrogen probe. The probe has been successfully used in corrosion monitoring systems and for monitoring hydrogen uptake in steel during cathodic protection studies[106].

2.4.1.5. Hydrogen Extraction Over Mercury[108]

This method of hydrogen extraction was published by British Standards in conjunction with the Welding Standards Committee[108]. The BS 6693[108] standards describe methods for the determination of hydrogen in several types of welds and weld metal. The metal to be tested is used to deposit a single weld bead which is rapidly quenched. Both the welding and quenching procedures are carefully controlled. The specimen, so produced, is maintained at room temperature for a sufficient time to release its content of diffusible hydrogen, which is collected over mercury and measured by a volumetric method. The parent plate material test piece should be prepared from a semi-killed grade of steel containing not more than 0.2% Carbon and not more than 0.05% Sulphur. Prior to use, the test piece should be

76

degassed at 650°C for 1 hour. After the sample has been welded and dried it is arranged in the apparatus shown in Figure 14[108]. The main stipulations of the standard are that:

1.   Mercury should be used as the confining liquid.
2.   It should be possible to maintain the sample under vacuum for a brief period to remove any traces of foreign gasses trapped on the fractured surfaces of the sample.
3.   The volume of collected gas should be measured to an accuracy of at least 0.05ml (s.t.p.).

Once assembled, the sample should be maintained under reduced pressure at 25 ± 5°C (298 ± 5K) for a period of 72 hours when the final volume is measured. After the experiment, the barometric pressure should be measured, the sample removed, brushed to remove any oxide films and weighed to the nearest 10 mg. The results, which must be repeated four times, are then expressed as a volume, in mm^3 at standard temperature and pressure, of diffusible hydrogen per 100 g of deposited weld metal.

The method for determination of diffusible hydrogen on weld metal has been modified in the past and high quality grade liquid paraffin has been used instead of mercury[109]. The experiment is performed at ambient or slightly elevated temperatures and the results are interpreted in the same way as for mercury. Some work in the past has been carried out using glycerol as the collection medium[110]. There does, however, appear to be some evidence[110] that the hydrogen is sparingly soluble in the glycerol and consequently the mercury or liquid paraffin extraction is favoured.

9 mm spherical joint

High vacuum hollow key single oblique
stopcock 4 mm bore

Atmosphere

Vacuum

0 to 10 mL burette
graduated to 0.05 mL,
approximately 30 mm
in length per mL,or
10 to 11 mm o.d.

High vacuum hollow key
double oblique stopcock
4 mm bore

300
approx.

34/35 joint

Weld specimen

Rubber band

75

Straight
section
120

o.d. 30

140

Permanent
magnet

Mercury

R 50

R 80

Borosilicate glass
throughout

All linear dimensions are in millimetres.

Figure 14.   Example of diffusible Hydrogen Collecting
Apparatus[108].

78

2.4.2 Comparison of Hydrogen Probes and Monitors.

The Electrochemical hydrogen probe (EHP) has the advantage of being a rate measuring device. Its sensitivity is greater than that of the Pressure probe but somewhat less than that of the Vacuum hydrogen monitors. The sensitivity of the Pressure Hydrogen Probe (PHP) is limited by the sensitivity of the pressure gauge. The Finger PHP is rugged and suitable for such applications as oilfield use, where no external power supply is required, although field experience with the Patch probe is limited. Vacuum hydrogen probes are much more sensitive than pressure probes and can be constructed in Finger and Patch configurations.

Vacuum hydrogen probes use the same principle as the Pressure type probes but they are far more sensitive to changes in the hydrogen charging characteristics of the environment, consequently they are more suitable for laboratory and plant environments than they are for more hostile applications such as oilfields etc. The electronics and other hardware required for their running are expensive and fragile by field operation standards. Electrical power is also required to run these monitors. These obstacles, however, can be overcome when the special capabilities of the vacuum type hydrogen probes are required.

The ion gauge can be transported to various locations where a chamber has been made, inserted in the chamber, and then used to measure hydrogen partial pressure that accumulates after a period of time. The VHP of Radd and Oertle[97] has a high sensitivity and has the advantage of measuring the hydrogen entry rate directly, rather than by calculating it from a hydrogen pressure which has built up over a period of time.

The construction of a Finger or Patch probe can be readily handled in work shop conditions, but mounting a Patch in the field is difficult. The Patch is

usually attached by welding and a good mechanical vacuum pump (10^{-1} Pa) is required to achieve the initial vacuum. Once operational, the vacuum hydrogen probe requires no further maintenance. The Finger probe, although most commonly used, has not had a successful past history[91]. Several disadvantages are apparent, the hydrogen permeation at the pipe surface may not be the same as that through the different material in the Finger probe, also constant maintenance is required to bleed-off accumulated hydrogen. Early models often allowed hydrogen to leak giving inaccurate data or no data at all[91]. More recent models are much more reliable. Units fit into most existing access systems and can be moved from one access point to another. The measurements of the Finger probe are direct readings of permeation of a known surface, consequently, data is easy to interpret.

Hydrogen entry rates (and correlation to corrosion rates) must be computed for PHP and VHP type hydrogen probes from the pressure build up per unit of time. The pressure build up in the PHP may be used to determine the solubility, C_0, of hydrogen corresponding to the pressure, P, of hydrogen gas as given by Sieverts Law[93]:

$$C_0 = Kp^{1/2} \qquad [16]$$

Where K is the Sievert's constant and, in magnitude, is equal to the solubility of H in metal at a pressure of 1.0 atm. of H_2. The dependence of the square root of pressure originates from the atomic nature of dissolved hydrogen. The Sievert's law constant is equal to the square root of the equilibrium constant K_{eq}. K_{eq}, may be determined from its thermodynamic relationship with the free energy change, ΔG, associated with the dissolution of hydrogen in metal:

$$-\Delta G = RT \ln K_{eq} \qquad [17]$$

The vacuum hydrogen probe relates the electrical current required by an ion pump to maintain a high vacuum in the chamber and is proportional to the rate at which hydrogen is captured by the pump. This again is converted to a

80

difference in pressure and is interpreted by use of Sievert's law[111].

Electrolytic type hydrogen monitors have been commercially available for some time and failures have been few[91]. More diverse applications have been made with the electrochemical hydrogen probe than the pressure and vacuum hydrogen probes[91]. The probe has been used in corrosion monitor systems and for assessing the effectiveness of inhibitor films[91]. There are several advantages with the Electrochemical hydrogen probe. Attachment to the pipe is not permanent, a hole is not required and consequently the unit can be moved and the technique is essentially non-destructive. Accurate instant readings are available as the unit records the actual permeation of hydrogen through the steel. Consequently the probe is a real time monitoring device which can be used to calculate the surface hydrogen concentration on the inside of the pipe or vessel. The versatility of the probe makes it ideal for field use, which overrides any disadvantages such as cost. One of the most significant aspects of electrochemical hydrogen probes over those previously described is that they determine mobile, or damaging hydrogen which can then be related to actual service conditions.

2.4.3 Surface Effects and Passivity.

Introduction.

The electrochemical permeation technique described previously in section 2.4.1.3 is used to study hydrogen diffusion and trapping in metals. The technique, however, poses several problems. Firstly the problem of surface film formation on the hydrogen exit side. If there is a film on the evolution side, most likely an oxide, then some hydrogen will be utilized reducing it. A delay time will occur before the hydrogen diffusion commences. Consequently this leads to a lower than expected value for the quantity of hydrogen diffusing through the specimen. Secondly, problems arise from anodic dissolution of the metal on the exit surface under the probe. In some systems, the potential at which hydrogen is completely oxidised at the exit surface is more anodic than the potential for anodic dissolution for the metal. This is sometimes the situation with iron, depending on the applied potential and anolyte. A review showing the range of potentials used to oxidise the hydrogen to protons at the exit surface and modes of sustaining that potential are shown in Table 8. In each case, unless otherwise stated, the electrolyte used in the anodic compartment was 0.1M NaOH.

Passive Oxide Films.

Anodic dissolution of the steel specimen on the exit surface can be controlled by careful selection of the anolyte. As shown by Table 8, the most commonly used electrolyte, in conjunction with steel specimens, in the anodic compartment of the double cell arrangement[36] is an aqueous solution of sodium hydroxide. Carbon Manganese and Stainless Steel, when oxidised in caustic solutions, will form a thin and dense passive film on the surface, consisting of γ-Fe_2O_3, according to the Pourbaix diagram shown in Figure 15[112].

Table 8. A Review of Hydrogen Oxidation Potentials.

Potential mV(N.H.E)	Mode	Author
+95	Ni/NiO	J. J. DeLuccia and D. A. Berman[113]
+200	Potentiostatic	J. Brogan, I. M. Austin and E. F. Walker[114]
+308	Ni/NiO	M. G. Hay[115]
0.00	Potentiostatic	D. Noël[116]
-330 to -150	Potentiostatic	T. K. G. Namboodhiri and L. Nanis[117]
+50	Potentiostatic	C. L. Yu and T. p. Perng[118]
-30	Potentiostatic	B. S. Chaudhari and T. P. Radhakrishnan[119]
+325	Potentiostatic	T. Zakroczymski[120]
+390	Potentiostatic	P. Mandatos and C. Duret[121]
+125	Potentiostatic	K. Van Gelder[122]

Several workers, in particular Manolatos and Duret[123] and earlier Bockris[124] acknowledged that this passive oxide film could form a barrier to hydrogen permeation.

Mandatos and Duret[123] proposed modifications to the hydrogen permeation technique and in particular, the interpretation of their results to minimise the effect a passive film may have on diffusible hydrogen. This was achieved primarily by controlling the growth conditions (environment and time) of the passive oxide layer.

Figure 15.   Potential-pH Diagram for the Iron-Water
System[112].
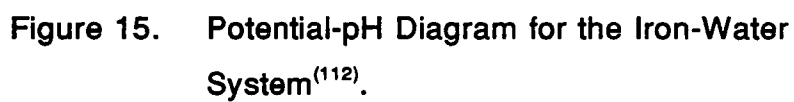
Pyun and Oriani[125] studied permeation transients for passivated iron and nickel measured at room temperature as a function of applied anodic potential and electrolyte composition. They proposed a model which described the permeation of hydrogen through the passivated metals as being controlled chiefly by the kinetic processes in the passivating films. They concluded that hydrogen permeation could be described by Fickian diffusion in the metal coupled with diffusion and migration in the oxide layer[125]. It was also suggested that the system could be treated as for diffusion in laminated layers.

An alternative approach to overcoming the effect of a passive film formed on iron and steel during hydrogen oxidation in permeation experiments was to coat the exit surface with a thin layer of palladium[124-126]. Zakroczymski[126] claimed that the application of a fine palladium film to the steel specimen, accelerated the hydrogen ionisation reaction and was effective against the anodic dissolution of the metal.

2.4.3.1. The Kinetics of Steel Passivation.

In experiments involving relatively short term hydrogen determinations, as with the gel-filled hydrogen probe described in this work, it is necessary to determine the time it takes for a passive film to grow on a bare steel surface. As the passive film grows, the resulting passivation current decays rapidly to a very low steady-state equilibrium value, representing slow dissolution and repair of the film.

A range of methods have been used to produce bare metal for transient electrochemical studies and these have been extensively reviewed by Newman[127]. One of the most common methods for determining the kinetics of passive film formation is the scratched electrode test[128]. In this test, bare steel was produced by impinging a diamond stylus upon a rotating disc

specimen under potentiostatic conditions. A scrape was made by momentarily activating a solenoid which causes the tool to briefly impact on the rotating specimen surface. The solenoid was connected to the scraping arm via two leaf springs, capable of absorbing any excess energy. Independent setting of the rest and activated position of the arm, as well as the return spring energy are all possible, providing good control over scrape characteristics.

The validity of the scratch technique has been questioned due to possible over estimation of the initial current measurements and the distribution of initial current between bare and filmed surfaces. Wei and Geo[129] questioned the technique's validity and suggested that the magnitude of the initial current may be better attributed to charging of the double layer rather than a reaction on the bare metal surface.

Several other techniques have been suggested in preference to the scratch test technique. Song and Cao[130] utilised a linear response model after subjecting a passivated metallic electrode to small amplitude potential step perturbations. Their results were used to compare this technique with the results obtained from impedance measurements.

Hashimoto and co workers[131] examined potential fluctuations on an iron substrate during repassivation. In their experiments, the specimen was first cathodically polarized at the potential of -1.1 V(SCE) to remove the air formed passive film. Then the potential was changed to 0.1 V(SCE). When there was no passive film, the iron dissolution was around 2 mAcm^{-2}. After about 1 second, the anodic current started to decrease rapidly, and the current showed a linear relationship on log current / log time axes. The anodic current decay in NaCl free 200 ppm $NaNO_2$ solution is shown in Figure 16[131].

The plateau at the start of the measurement represents the initial, large current which appears truncated due to its dependence on the impedance of

the polarization circuit. This current seems to carry mainly the actively dissolving iron ions before the film starts to form[131]. When the equilibrium between active dissolution of iron and the formation of the passive film, γFe_2O_3, has shifted almost totally in favour of the passive film formation, the current decays rapidly, at a rate of approximately $1/t$, to a low background, equilibrium value.

Bardwell[132] also examined the formation of a passive film on iron and iron-chrome alloys. The materials were examined in pH 8.4 borate buffer solutions using electrochemical and surface analytical techniques. Figure 17(a)[132] shows the current transient observed when the potential of an oxide free Fe-6Cr electrode is stepped to various potentials in the passive region. The Fe-6Cr electrode was cathodically reduced for 3 minutes at -1.7 V before the borate buffer solution was changed, the sample re-immersed on open circuit, the potential stepped back to -1.7 V for 1 second. Subsequently, the potential was stepped into the passive region and the current transient recorded. The corresponding integrated anodic charge is shown in Figure 17(b)[132]. Bardwell and MacDougall and Graham[133] observed that, as with the case of pure iron[134], the charge increased linearly with anodic potential over the range -0.7 to 0.4 V. From Figure 17(a) the gradient of the linear portion of the graph, at times greater than 1 second, the gradient was approximately -1.02. Consequently the rate of passive film formation can be considered to decay inversely with respect to time on log axes.

87
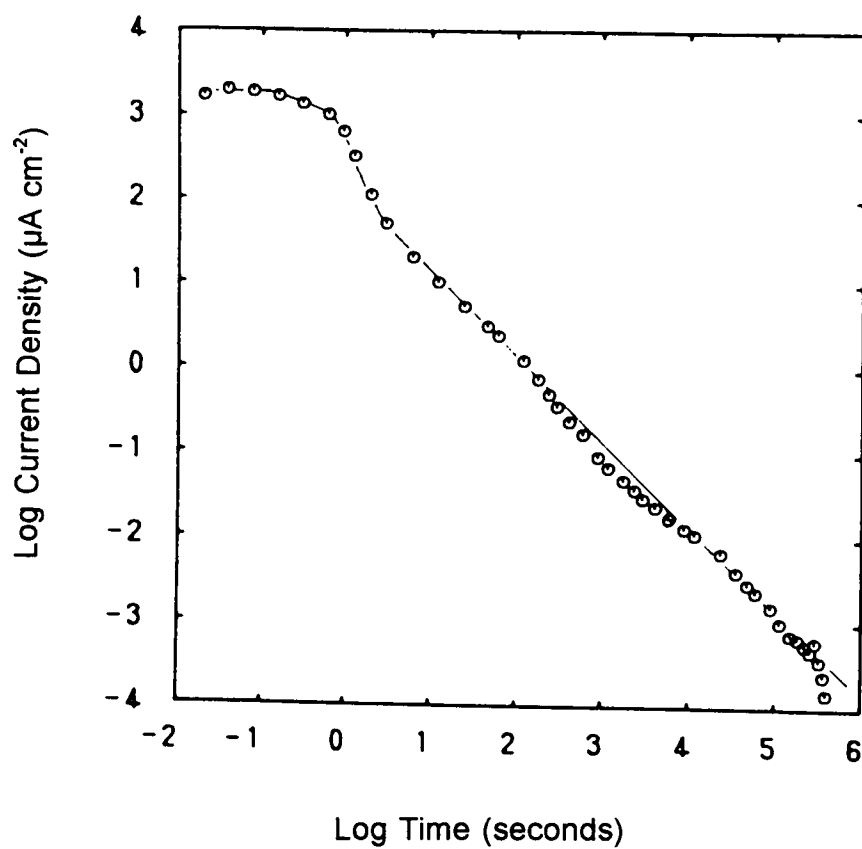
Figure 16. Anodic Current Decay Due to Passive Film Growth in a NaNO$_2$ Solution at a Potential of 0.1 V (SCE)[131].

88
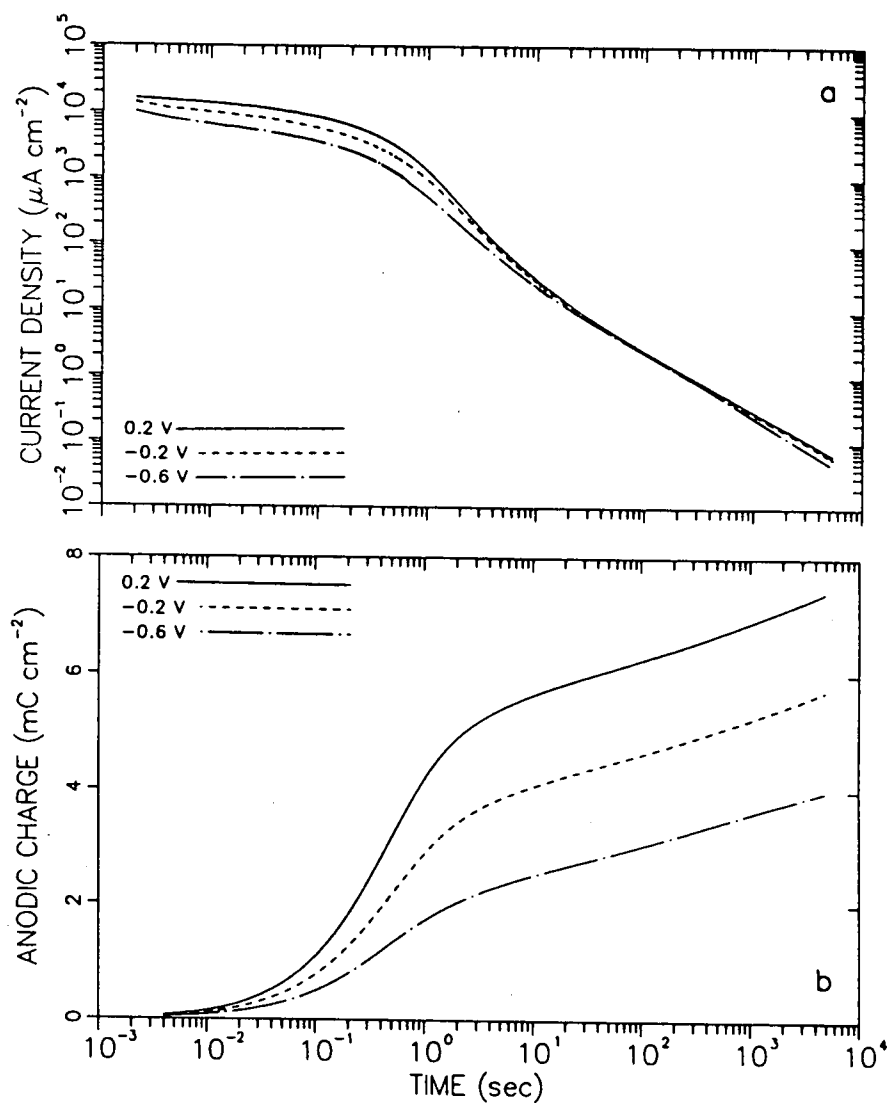
Figure 17.   (a) Current Density and (b) The Anodic
               Charge Transients for a Potential Step
               Experiment to Study Passive Film Formation
               of Steel[132].

89

3.0 METHODS

3.1 Materials

Two carbon-manganese steels have been studied in this research programme. The first was a 35 mm thick plate which was known to be susceptible to HIC and was identified as NAM plate. The second steel was supplied by British Steel as normalised 19 mm thick plate which was selected for its good through thickness properties. This was identified as BS Z25 plate. The chemical analysis for each steel is given in Table 9. Optical micrographs of the materials, etched in 2% Nital, are also shown in plates 5 to 7.

In general, each micrograph exhibits a banded microstructure of pearlite and ferrite, the ratios of which were consistent with percentage carbon content as shown in Table 9. Plates 5 and 6 show the BS Z25 plate which has the lower carbon content (0.12% wt. element) and consequently exhibits the lower proportion of pearlite. The BS Z25 plate exhibits the finer grain size of the two materials with little banding and grains that are generally equiaxial. In conjunction with corresponding sulphur contents, shown in Table 9, a relatively low population of manganese sulphide inclusions were observed in the BS Z25 materials microstructure. Of the two materials, the BS Z25 was considered to be the "cleaner" and hence more suitable for characterisation of the electrochemical aspects of this work. The NAM steel, shown in plate 7, had a large population of elongated manganese sulphide inclusions. This particular steel was known to be susceptible to hydrogen induced cracking. This material was used to characterise the microstructural aspects of this work, particularly for observing any microstructural damage which may have arisen due to cathodic hydrogen charging.

90
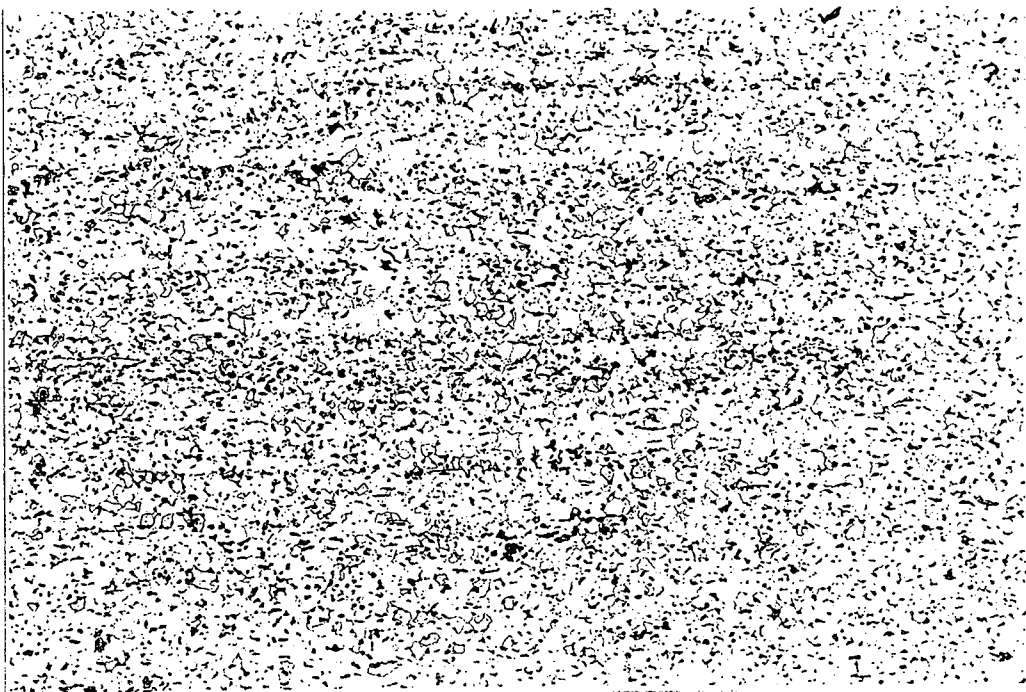
Plate 5.   BS Z25 Plate, Etched. Magnification x50.
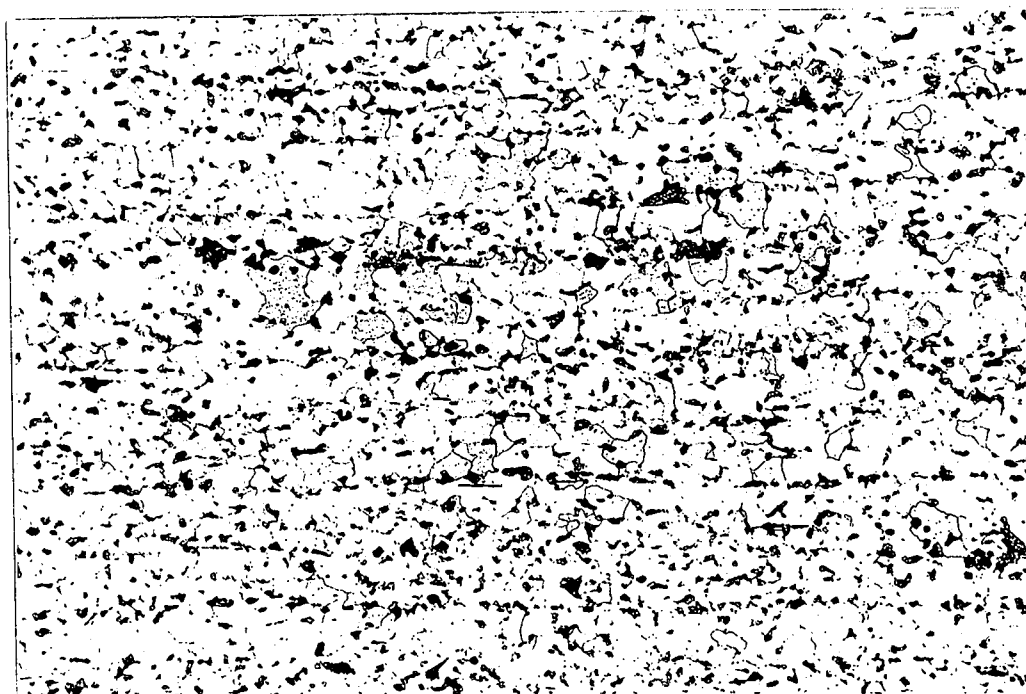
Plate 6.   BS Z25 Plate. Etched. Magnification x100.

Plate 7.   NAM Plate. Etched. Magnification x50.

Table 9. Chemical Composition of Materials.

WEIGHT PERCENTAGE ELEMENT

IDENTITY	C	Si	Mn	P	S	Cr	Mo	Ni	Al	B
BS Z25	0.12	0.30	1.49	0.016	0.009				0.048	
NAM	0.25	0.23	1.10	0.02	0.03	<0.01	<0.03	<0.01	0.03	<0.0005

WEIGHT PERCENTAGE ELEMENT

IDENTITY	Co	Cu	Nb	Ti	N	V	W
BS Z25			0.043		0.006	0.065	
NAM	<0.01	0.01	<0.10	<0.01		<0.01	<0.04

Figures 18 and 19 show optical micrographs of the two steels, each taken at x100 optical magnification. These show the shape of inclusions relative to the surface, longitudinal and transverse sections. The NAM plate and the BS Z25 plate both show elongated type III manganese sulphide inclusions.

Longitudinal
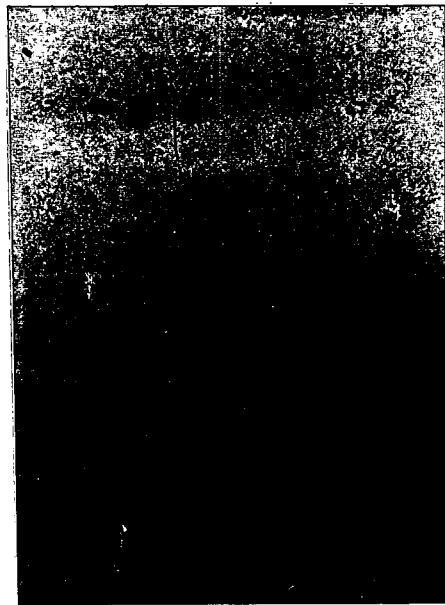
Transverse
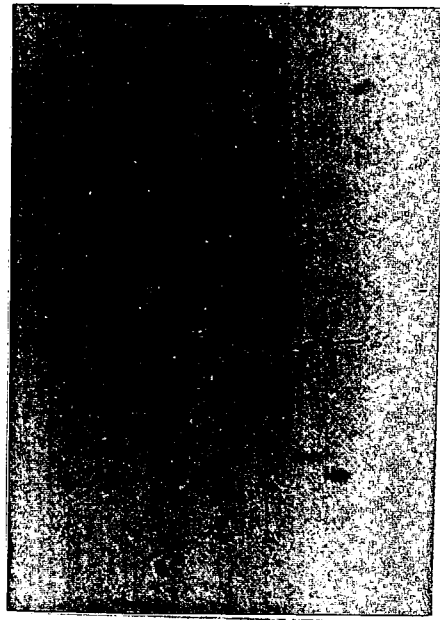
Surface
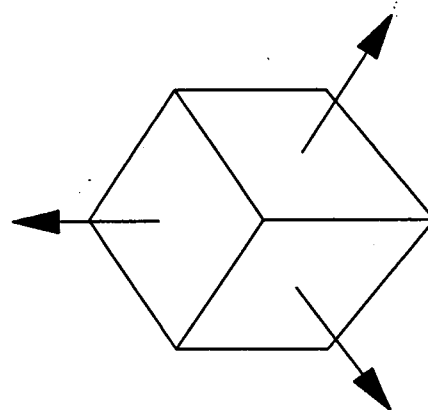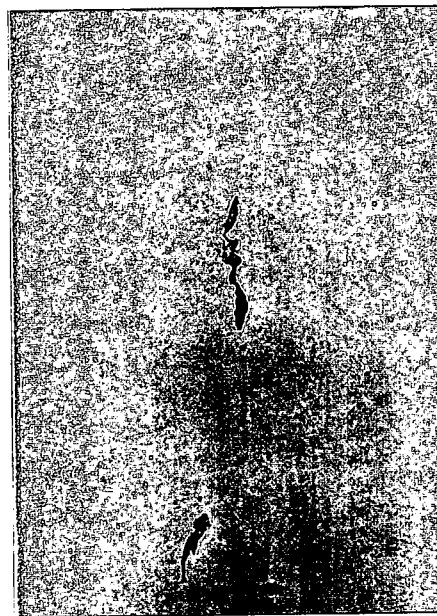
Figure 18.   Inclusion Distribution Within the NAM Plate.

95

Transverse

Longitudinal
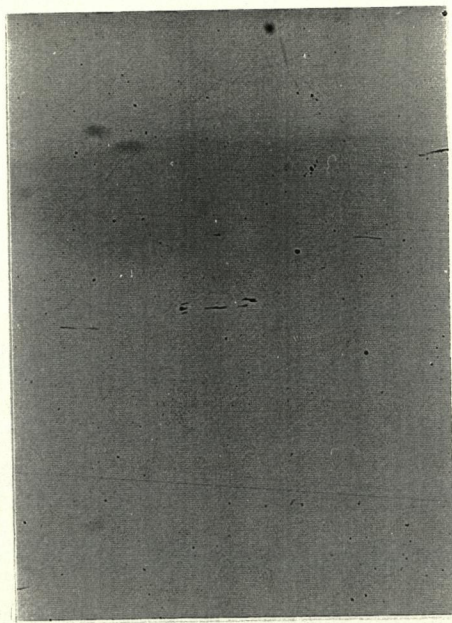
Surface
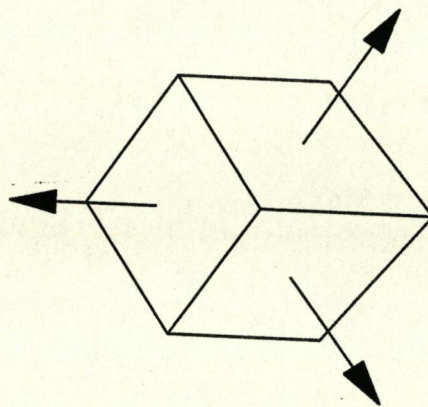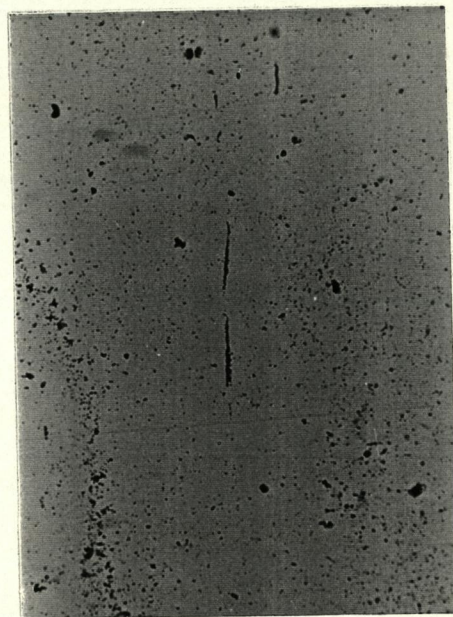
Figure 19.   Inclusion Distribution Within the BS Z25 Plate.

96

3.2   The Gel-Filled Hydrogen Probe.

Introduction

Construction of the gel-filled hydrogen probe was first reported by Robinson and Hudson[104] and is shown schematically in its original form in Figure 20. The body of the hydrogen probe was constructed from a 5ml syringe, from which the nozzle was removed. A Nickel/Nickel Oxide cathode was then formed into a cylinder and held firmly at the inner wall of the syringe. The gel electrolyte was contained in the body of the syringe and the plunger allowed the gel to be extruded from the body, ensuring freedom from air bubbles and allowing good contact with the metal sample. An annular ferrite magnet was fitted around the end of the syringe body which enabled the probe to be firmly attached to the metal surface under investigation. The Nickel/Nickel Oxide auxiliary electrode was manufactured from 98% purity, 500 μm thick poly-crystalline nickel foil. The nickel foil was lightly abraded using 1200 grit carborundum paper and then cleaned in an ultrasonic bath using an Inhibisol solvent (inhibited tri-chloro-ethylene).

Prior to anodizing, the foils were electrochemically polished using 57% by volume H_2SO_4 for 2 minutes at a current density of 0.5 Acm^{-2}. This removed the air formed oxide layer (which was reported to be typically 6-8 Å thick[133]) and activated the surface. The foils were then anodised for 1 hour using a platinum foil counter electrode. The foils were turned through 90° every 15 minutes to ensure an even distribution of charge. After 1 hour the foils were removed from the anodising solution, washed with distilled water and carefully dried in warm air. They were then stored in a desiccator until required.
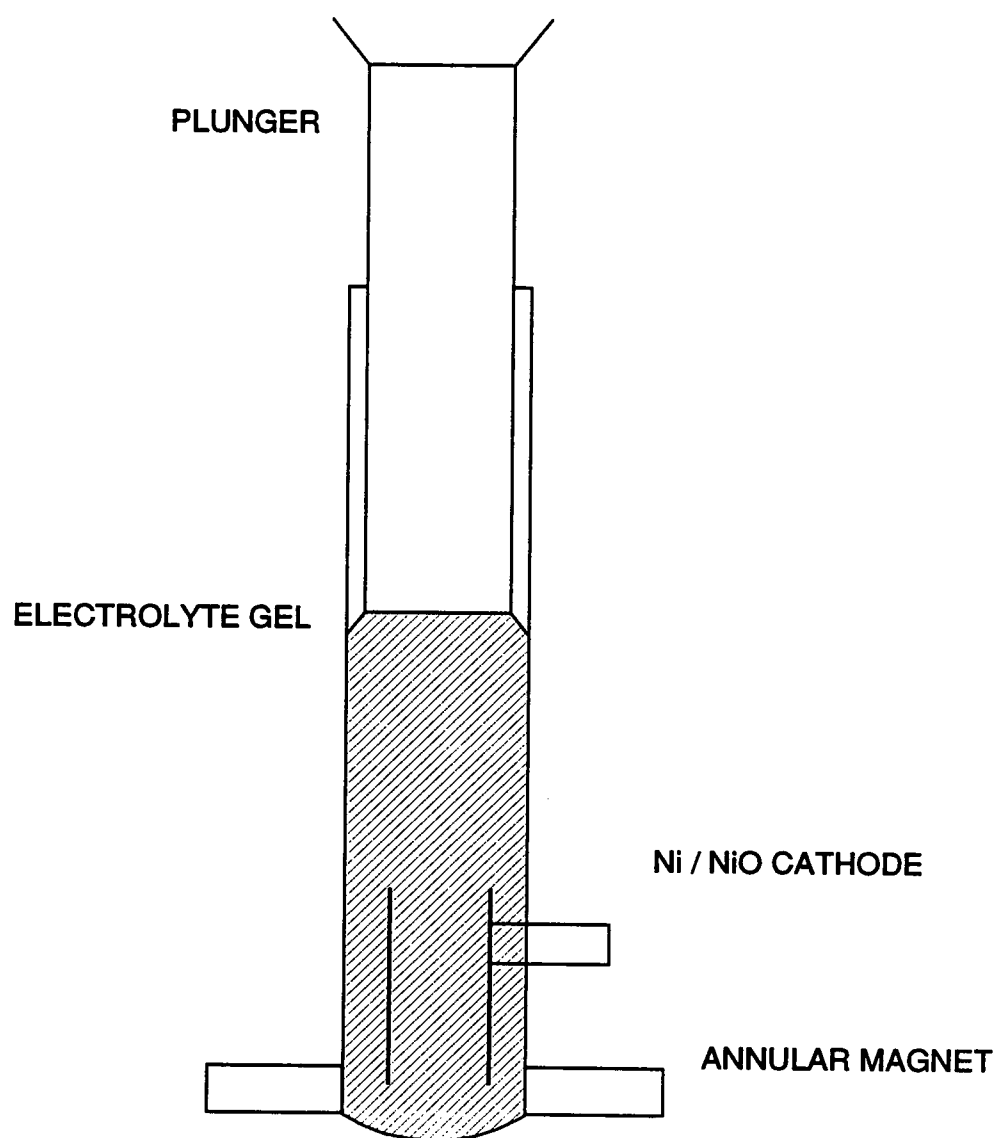
Figure 20.   Original Construction of the Gel-Filled
Hydrogen Probe[104].

The gel-electrolyte was produced using 0.2M NaOH solution made from analar grade sodium hydroxide pellets. The solution was heated to between 60° and 75°C when 31 gl⁻¹ of standard purity agar powder was gently stirred into the solution until dissolved. The mixture turned to a straw colour and care was taken not to over heat it. The mixture was then removed from the heat and allowed to cool to around 50°C. The clean syringe, with its plunger fully extended, was inverted and the gel-solution carefully poured into it along a glass rod to avoid any air bubbles being trapped. The probe was filled to a convex meniscus, which would accommodate any shrinkage of the gel as it cooled to room temperature. Before a measurement was taken using the probe, the convex meniscus was cut off to produce a flat surface ensuring good electrical contact of a known surface area between the metal and gel surfaces.

3.2.1 Modifications to the Gel-Filled Hydrogen Probe.

Experiments performed using the original gel-filled hydrogen probe suggested that the nickel/nickel oxide electrode was not particularly suitable for the probe's applications as it was prone to polarization at high current densities. The nickel/nickel oxide electrode also had a limited life[36]. As a result of this finding a series of experiments were performed to establish the most favourable electrode to suit the probe's applications.

3.2.1.1 Manufacture of the Auxiliary Electrodes.

Work was carried out to assess the stability of the nickel/nickel oxide electrode produced with different anodizing solutions and conditions according to Table 8. A number of nickel/nickel oxide electrodes with different surface morphology and varying degrees of porosity were subsequently produced. Surface analysis using the scanning electron microscope and X-ray diffraction techniques revealed a variety of complex hydroxides and oxy-hydroxides. In

conjunction with mixed potential measurements in 0.2M NaOH solution, these results were used to categorise the nature of the surface oxide film on the nickel substrate.

Table 10.   Anodizing Solutions and Conditions for Manufacture of Auxiliary Electrodes.

Electrode	Solution	Conditions	Current Density $(mA\ cm^{-2})$	Time (hours)
1	10% (vol.) H_2SO_4	Galvanostatic	150	1
2	0.15M Na_2SO_4	Galvanostatic	150	1
3	pH 7.61 Borate Buffer Solution	Galvanostatic	150	1
4	10% (vol.) H_2SO_4	Potentiostatic +1.5V NHE	___	1
5	Sintered Nickel Plaque	As Received	___	___
6	Hg/HgO Element	As Received	___	___
7	Blank Nickel Foil	As Received	___	___

3.2.1.2 Surface Analysis of Anodic Oxide Films on Nickel.

A Cambridge 250(III) Scanning Electron Microscope was used to evaluate the surface condition of each electrode shown in Table 10. Thin window light element analysis of the electrode surfaces was also conducted using the same instrument. This was to determine the $Ni:O_2$ ratio in the surface film. The molecular structure of the films was characterised using Energy Dispersive X-

Ray Analysis on the LINK Compact X-Ray Diffractometer (PW 1840). The path lengths associated with the main peaks obtained by X-Ray diffraction were calculated from a solution to the Bragg equation[134]:

$$\lambda = 2d \sin\theta \qquad [19]$$

where λ = wave length of incident X-Rays.

d = Path length or inter-plainer spacing

θ = glancing angle of incidence between X-ray and reflecting planes.

3.2.1.3 Mixed Potential Measurements.

Freshly anodised electrodes were degreased with iso-propanol and immersed in a 0.2M NaOH solution which simulated the environment within the body of the gel-filled hydrogen probe. The equilibrium potential of the electrodes was measured with respect to a mercury/mercury oxide electrode during a period of 80 hours.

3.2.2 Construction of the Modified Gel-Filled Hydrogen Probe.

Figure 21 shows a schematic representation of the gel-filled hydrogen probe. The mercury/mercury oxide element provided a reference for the steel, which was held anodically at +150 mV relative to the normal hydrogen scale. The reference element was well suited to the strongly alkaline electrolyte which had a pH of around 13.3. The measured rest potential of the reference electrode was around -300 mV on the normal hydrogen scale, in a 0.2M sodium hydroxide solution. The steel sample, reference electrode and platinum auxiliary electrode formed the three electrode system required to operate the device potentiostatically. The auxiliary and reference electrodes were housed in a PTFE tube which rested above the electrolyte. A seal was maintained using a rubber "O" ring. The unit was then fixed to the specimen during the determination using an annular magnet which is secured to the cell body approximately 1 mm above the test surface.

A fresh gel surface was required for each surface hydrogen concentration determination to avoid contamination. Consequently by depressing the PTFE tube a small amount of gel was exuded and could be removed and discarded. Good electrical contact between probe and sample could be tested by depressing the PTFE tube while the probe was attached to the sample. Complete contact by the probe ensured no permanent deviation in the current reading after depressing the tube.

The electrolyte was the only consumable part of the probe. Provided the probe was covered and stored under clean, moist, conditions, it was found to last indefinitely. At present, the probe houses sufficient gel to facilitate approximately twenty measurements. The volume of gel used is not fundamental to the probe's operation, the physical size of the probe may be adjusted to accommodate more electrolyte depending on the application. Due to the high conductivity of the gel-electrolyte, approximately equal to that of

the 0.2M NaOH, it was found that there was no significant IR drop (due to metal-film reactions on surface) arising from the separation between the working and counter electrodes. The gel-electrolyte was produced using 0.2M NaOH solution made from laboratory grade sodium hydroxide pellets in the same manner as that for the original gel-filled hydrogen probe construction. The conductivity of the gel was measured using a standard conductivity meter.

3.2.2.1 Additional Requirements

In addition to the probe, a potentiostatic circuit was used to facilitate the oxidation of hydrogen atoms as they diffused to the efflux surface. This provided a decaying current transient from which the surface hydrogen concentration was calculated. Suitable equipment to record the decaying transient was also used, in the form of either a chart recorder or an interactive data logger.

3.2.3 Surface Preparation

Careful surface preparation of the substrate was of great importance. Due to the generally low magnitude of the current measured in these experiments, of the order of micro-amps, the presence of surface films or impurities could drastically influence the results. A portable polishing device was used in these experiments (the Suhner Rotoset). The polishing unit had a flexible shaft and rotating hand set making it versatile enough to facilitate all the probe's applications. It was found that an adequate surface finish could be achieved using a 17 μm abrasive wheel or equivalent. After polishing, the surface was washed with distilled water and then thoroughly washed with iso-propyl alcohol to remove any grease from the surface.
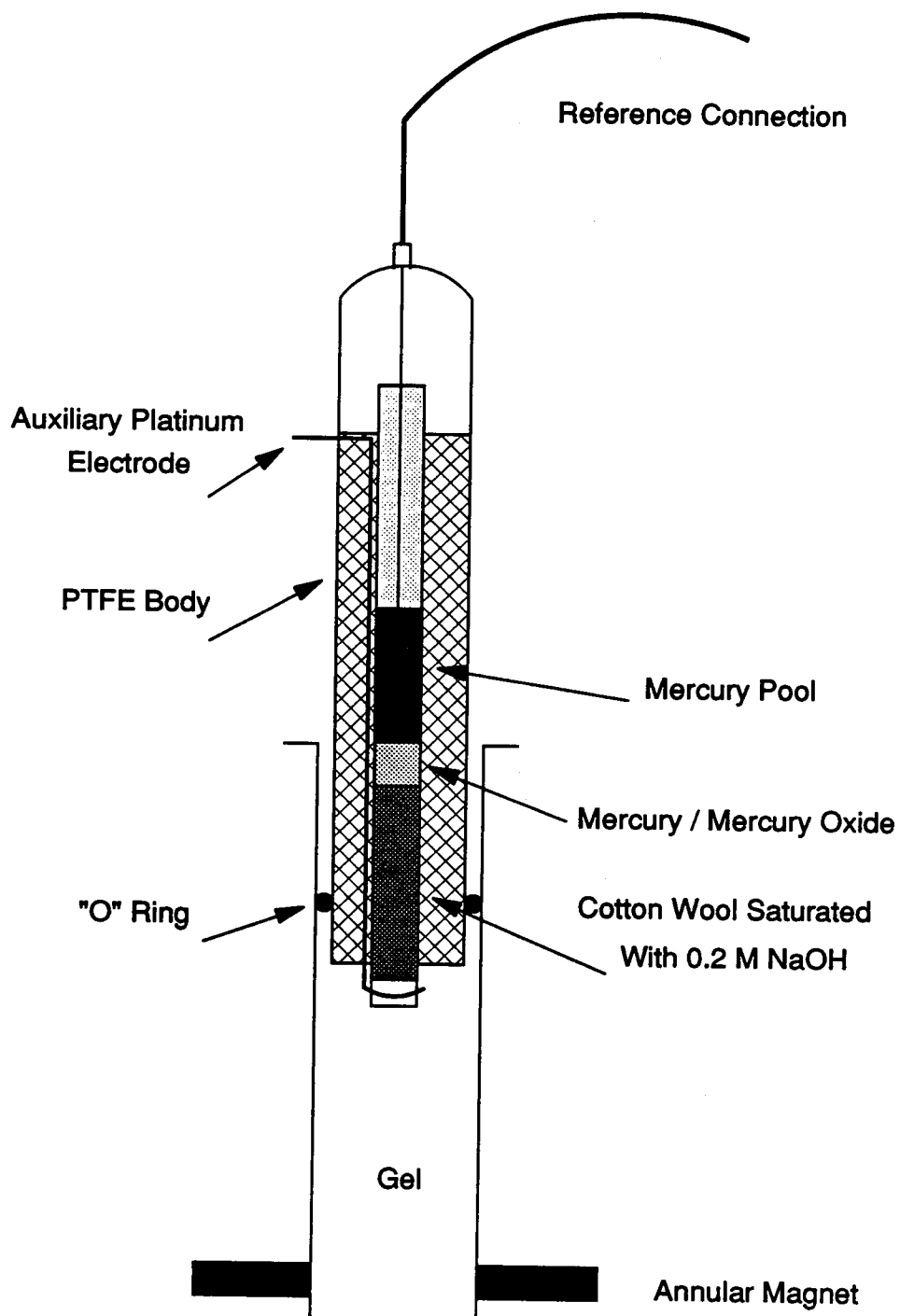
Figure 21.   Schematic Representation of the Modified
Gel-Filled Hydrogen Probe.

3.2.4 Mode of Operation and Calibration of the Gel-Filled Hydrogen Probe

Figure 22 shows a schematic representation of the experimental arrangement required for the determination of the surface hydrogen concentration of a test specimen. Before the probe was used, a series of readings was made on a standard test piece to ensure consistent results. After thorough surface preparation the probe was placed on the test sample and a constant potential of +150 mV (NHE) was applied to the steel. The decaying oxidation current was then recorded every minute for 15 minutes. After the final measurement the probe was removed and covered with a plastic film to prevent the gel from drying out. The sample was finally wiped to removed any residual gel left on the surface. It was found that the probe should be left to equilibrate for around 5 minutes between each complete run.

3.3 Evaluation of the Kinetics of Passive Oxide Film Formation on Steel.

The experimental arrangement, shown in Figure 23, was designed to reproduce the instant when the gel-filled probe was first placed on the steel sample, and passivation of the steel, due to the caustic environment, occurred. The magnitude of the current required to form the passive film and its subsequent decay was measured by disturbing the already passivated steel surface by means of a scratch and monitoring the current required to repair this damage.

A glass cell was attached to a piece of clean, abraded low carbon steel shim, 57 μm thick. The cell contained a solution of standard purity 0.2M NaOH. A platinum auxiliary electrode and mercury/mercury oxide reference electrode were used to maintain a constant potential of +150 mV (NHE) on the membrane surface. The steel, held at this potential, was depleted of residual hydrogen for approximately 18 hours until the recorded current reached a very low background value. When the background current was constant, the
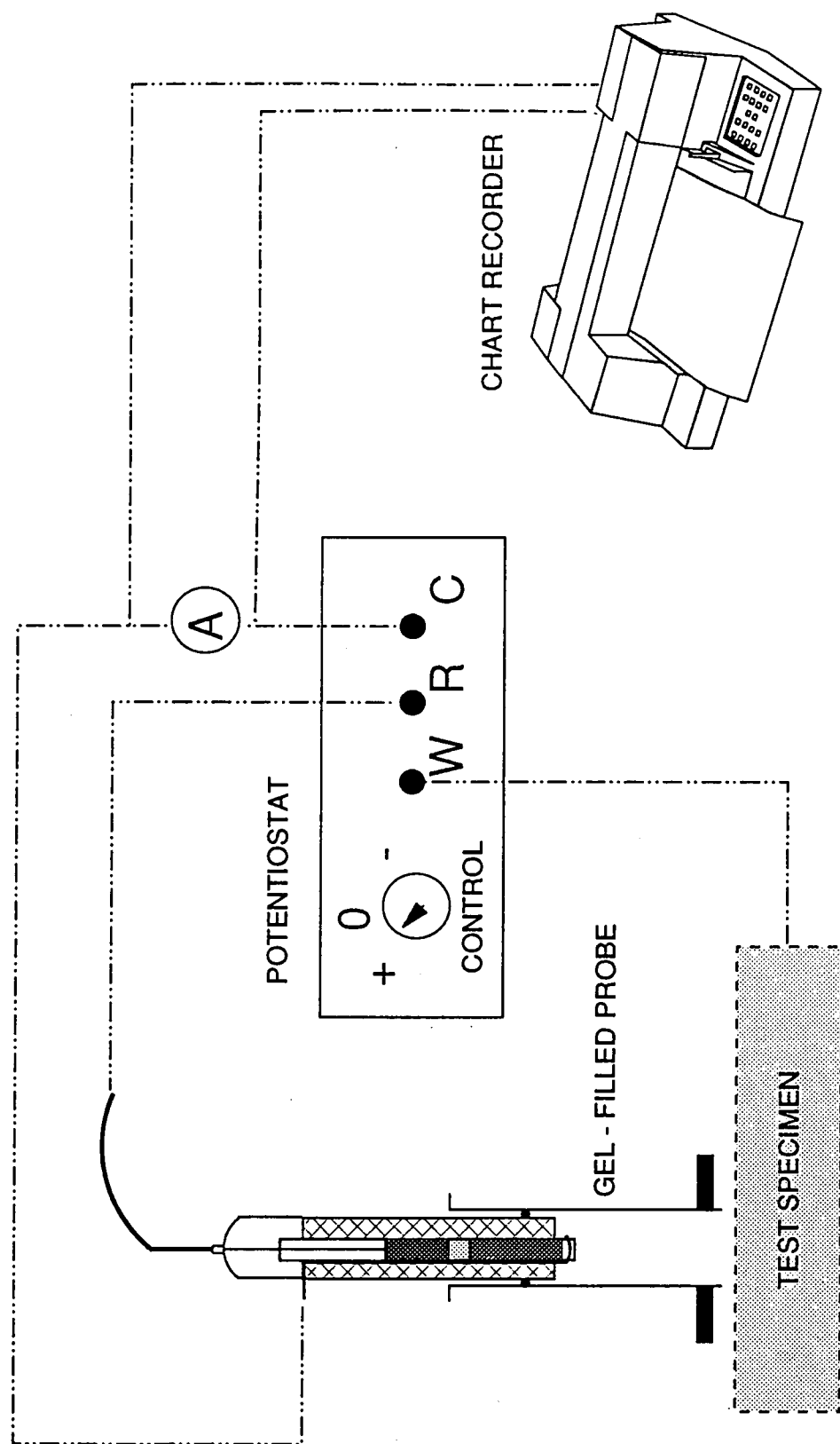
Figure 22. Experimental Arrangement for Gel-Filled Hydrogen Probe Determinations.

106
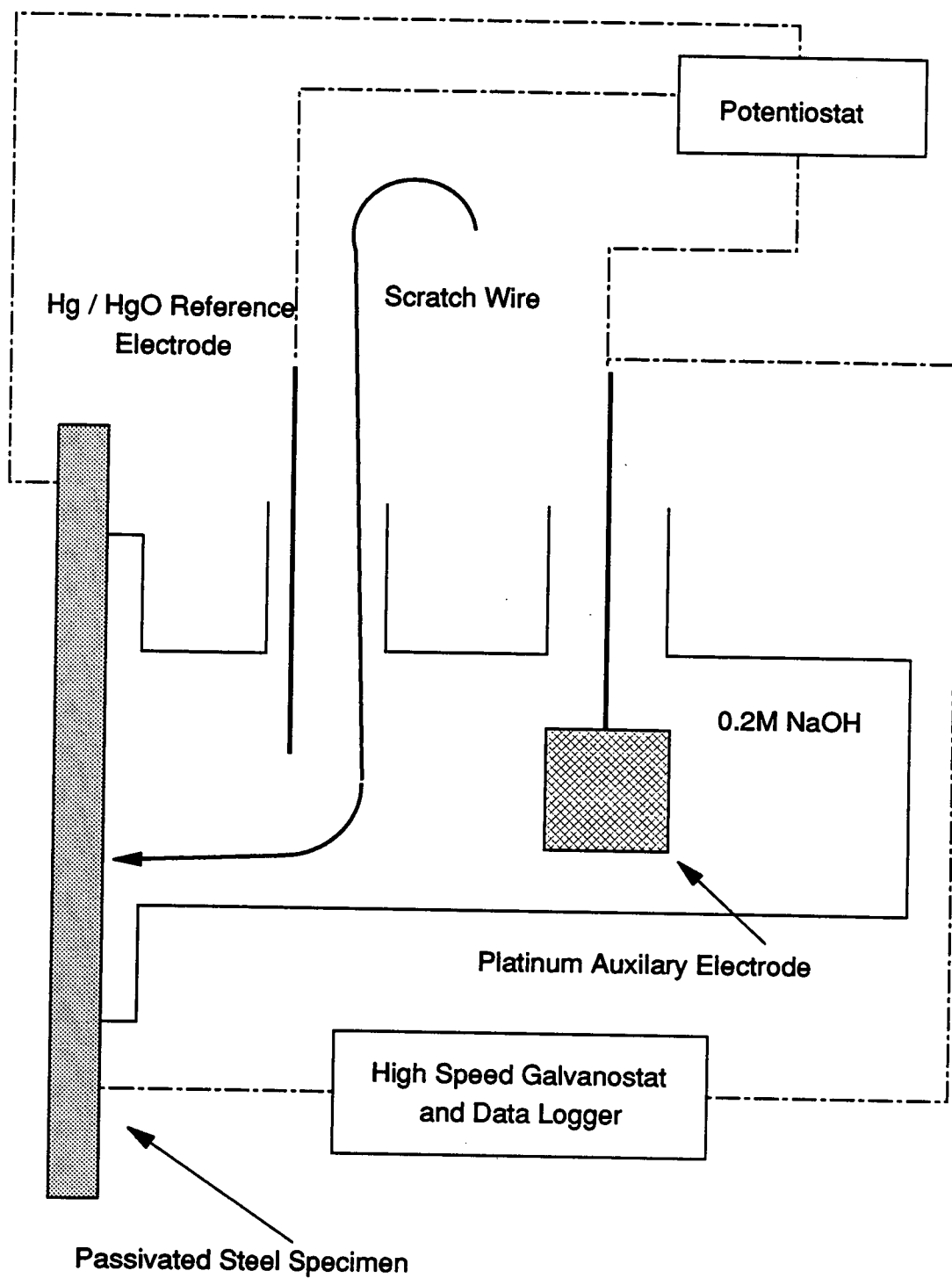
Figure 23.   Arrangement for Scratch Test Experiments.

passivated steel shim was rapidly scratched using a piece of steel wire and the resulting oxidation current, arising from repassivation of the ruptured film, was recorded. The recording device was a fast response galvanometer linked to a cathode ray oscilloscope and chart recorder. Readings were taken every 10 mS until the decaying current transient appeared to return to a uniform background value.

3.3.1 Delayed Probe Readings.

In this series of experiments an attempt was made to passivate the steel surface prior to evaluation of the surface hydrogen concentration using the gel-filled hydrogen probe. The gel-filled probe was attached to the freshly abraded steel sample as with previous determinations illustrated in Figure 22. The probe was allowed to stand on the steel surface at open circuit, for a period of time allowing the steel to passivate before the anodic potential was applied and the current transient recorded to measure the surface hydrogen concentration in the usual way. By varying the delay time, the contribution of the repassivation current made to the total current and to the hydrogen measurement could be assessed. Five consecutive hydrogen concentration measurements were made. A further five replicate readings were taken after time delays of 1, 5, 10, 15 and 20 minutes.

3.4   Preliminary Hydrogen Charging Experiments

Introduction

In the preliminary charging experiments two specimens were machined from the BS Z25 and NAM plates with the dimensions 20x20x19 mm and 20x20x35 mm respectively. Two faces of each specimen were ground to a flat surface and five of the six sides were then coated with an acid resistant lacquer. Electrical contact was made by means of steel studding, drilled and tapped into the sample. The two samples from each material were then cathodically charged for 24 and 96 hours respectively at a current density of 150 mAcm^{-2} in 10%, standard grade sulphuric acid, with the addition of 50 mg/l stannous chloride to promote hydrogen adsorption. Hydrogen concentrations were recorded using the gel filled hydrogen probe in the as-received and charged state.

3.4.1. Comparison of Hydrogen Permeation Measurements with Gel-Filled Hydrogen Probe Readings.

Initially a perspex cell was designed as illustrated in Figure 24. This was designed to facilitate the in-situ monitoring of the hydrogen concentration during cathodic hydrogen charging of the steel sample. The cell was machined from 15 mm perspex to house the electrolyte; 10% standard grade sulphuric acid and 50 mgl^{-1} stannous chloride, a platinum auxiliary electrode, a standard reference electrode, and one face of the working electrode, i.e a 100x100x19 mm steel coupon. The mounting face of the perspex cell, containing the steel coupon contained two counter-sunk stainless steel studs with which to clamp the conventional hydrogen permeation cell in place. The sides of the cell were secured by tapped screws and the inner edges were sealed with a "Dow Corning 781" multipurpose silicone sealant to prevent seepage of the electrolyte.

109
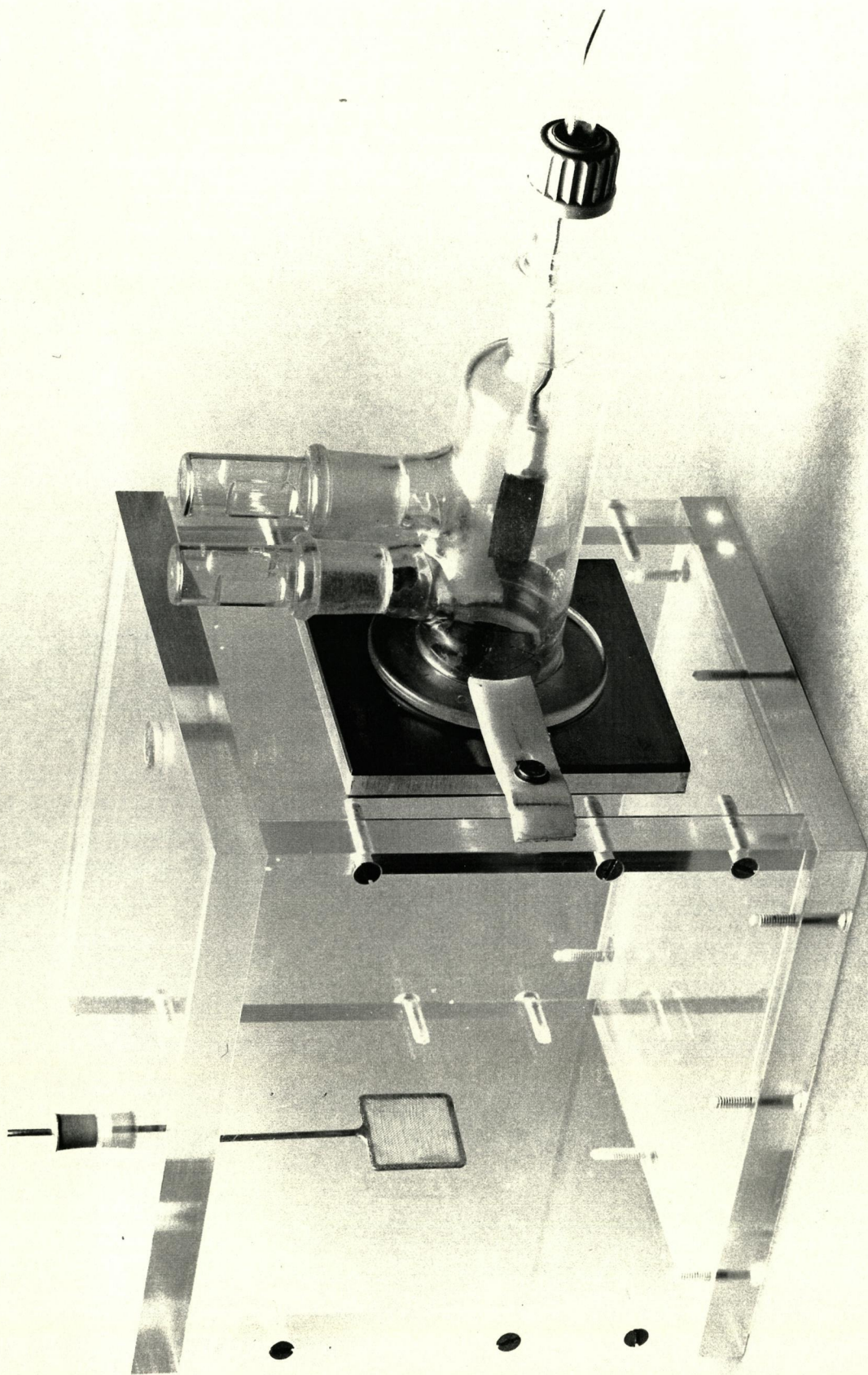
Figure 24.   Perspex Charging Cell Fitted with a Conventional Hydrogen Permeation Cell.

110

The conventional hydrogen permeation cell containing 0.2 M NaOH solution was attached to the uncharged side of the plate and the surface was held at a potential of +150 mV to ensure efficient oxidation of emerging hydrogen. The probe current was measured using a zero resistance ammeter and was recorded on a data logger. Before charging commenced, the steel samples were depleted of hydrogen using the conventional hydrogen permeation cell, until the measured oxidation current reached a low, uniform, value representing the background surface hydrogen concentration of the steel. This initial depletion was carried out for up to 72 hours prior to charging.

The gel-filled hydrogen probe was used at intervals during the permeation experiments described above to measure the concentration of hydrogen at the uncharged surface of the steel plate. The probe was located at the edges of the plate adjacent to the conventional probe and the steel was carefully prepared by abrading with silicon carbide paper and degreasing with iso-propanol before each measurement.

3.5 Modifications to the Hydrogen Charging Experiments.

In the following experiments the gel filled hydrogen probe was used to measure the concentration of surface hydrogen at the charged (influx) and the uncharged (efflux) surfaces in continuation of the preliminary work described above.

In this work the conventional permeation cell, initially used for comparison purposes, was omitted to allow more easy access to the uncharged surface. Some modifications were made to the original cell. A gland consisting of a 4 mm diameter 'O' ring was used to reduce leaks between the sample and the cell and allow longer charging times to be used. A schematic representation of the modifications is shown in Figure 25.

111

CHARGING FACE

RETAINING SCREWS

PERSPEX

STEEL SAMPLE
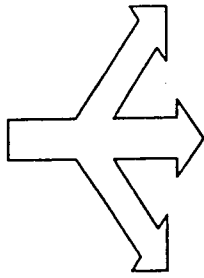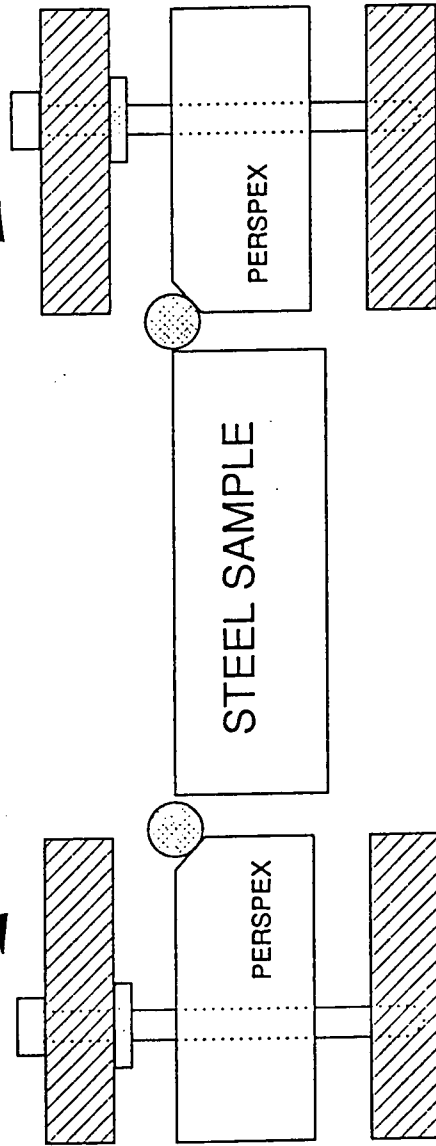
PERSPEX

STAINLESS STEEL GLAND

RUBBER "O" RING

Figure 25.   Modifications to the Perspex Cell.

112

Before determination of the surface hydrogen concentration, fresh probes were constructed as described in section 3.2. The charging was carried out using 10% sulphuric acid with 50mg l^{-1} stannous chloride cathodic poison at a current density of 75 mA cm^{-2}. The charging was interrupted at suitable time intervals in order to make gel-filled hydrogen probe readings on the charged face. The need for careful and thorough surface preparation was very important. Initially, the steel surface was washed with distilled water and then abraded with 1200 grit carborundum paper. This was then wiped with a 0.2M sodium hydroxide solution to neutralise any acid remaining on the steel. Finally the surface was again thoroughly washed with distilled water. The probe was then carefully placed on the steel surface and gently pressed to exude a small quantity of gel. The readings were then recorded over 15 minutes using a data logger. After the probe readings had been made, the charging solution was replaced and hydrogen charging was resumed. This process was repeated throughout the duration of the charging experiment at suitable charging intervals.

Due to the excessive charging times required for the original plate thickness, samples were machined to a thickness of 5 mm. The 5 mm plate was machined from one side of the original 19 mm BS Z25 plate and 35 mm NAM plates respectively. The resulting plates were consequently free of any centre line segregation. The charging apparatus shown in Figure 24 was further modified to facilitate the cathodic hydrogen charging of the reduced thickness plate. The modified charging apparatus was constructed, as shown in Figure 26, based on the double cell apparatus of Devanathan and Stachurski[36]. With this arrangement, a combination of cells could be fixed to the efflux surface. In Figure 26, both the gel-filled hydrogen probe and a modified form of the conventional glass permeation cell were fixed to the efflux surface.
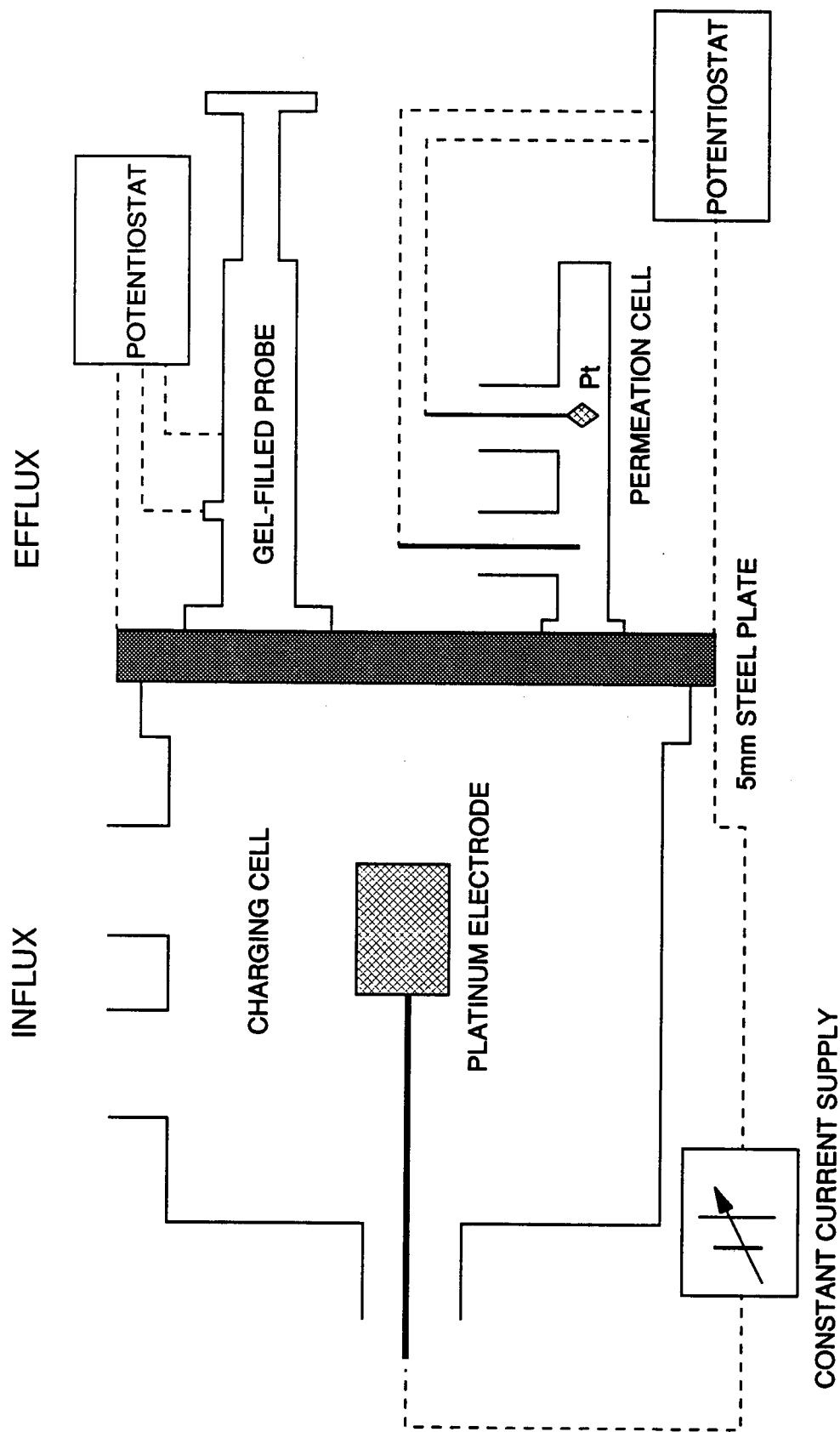
Figure 26. Arrangement for Permeation and Gel-Filled Hydrogen Probe Measurements on 5 mm Plate.

114

The cathodic compartment or influx side was enlarged to incorporate the maximum area of steel to be charged. With this arrangement, a uniform flux of hydrogen through the bulk of the steel would be maintained thus allowing measurements to be made using the glass cell and the gel-filled probe. By minimizing the area of the anodic cell compartment on the efflux surface, a relatively large area remained available for intermittent gel probe readings. The extra space on the efflux side allowed better surface preparation, and a larger area was available for probe readings which might indicate if there was any difference in surface hydrogen concentration relative to position on the efflux surface.

The charging electrolyte contained in the glass cell on the hydrogen influx surface was the same as that used previously, and consisted of 10% H_2SO_4, with the addition of 50 ppm of stannous chloride as a cathodic poison. The sample was charged galvanostatically with a current density of 75 mA cm^{-2}. The depletion electrolyte contained in the glass cell on the hydrogen efflux surface consisted of 0.2M NaOH. The efflux surface was held potentiostatically at +150 mV with respect to the normal hydrogen scale using a mercury/mercury oxide reference electrode and a platinum counter electrode. The modified gel-filled probe was intermittently placed on the efflux surface to monitor the concentration of hydrogen diffused through the thickness of the plate. Prior to application of the gel-filled probe, the surface was prepared using the Schuner Rotaset polisher which gave approximately a 17 μm surface finish.

3.6 The Kinetics of Hydrogen Absorption into Steel

The aim of this experiment was to evaluate approximate values of the finite rate constants, K_{abs} and K_{des}. Figure 27 shows the experimental arrangement of the bipolar cell[36] apparatus used in these experiments. The cathodic cell, contained a 10% sulphuric acid catholyte free of cathodic poison additives.
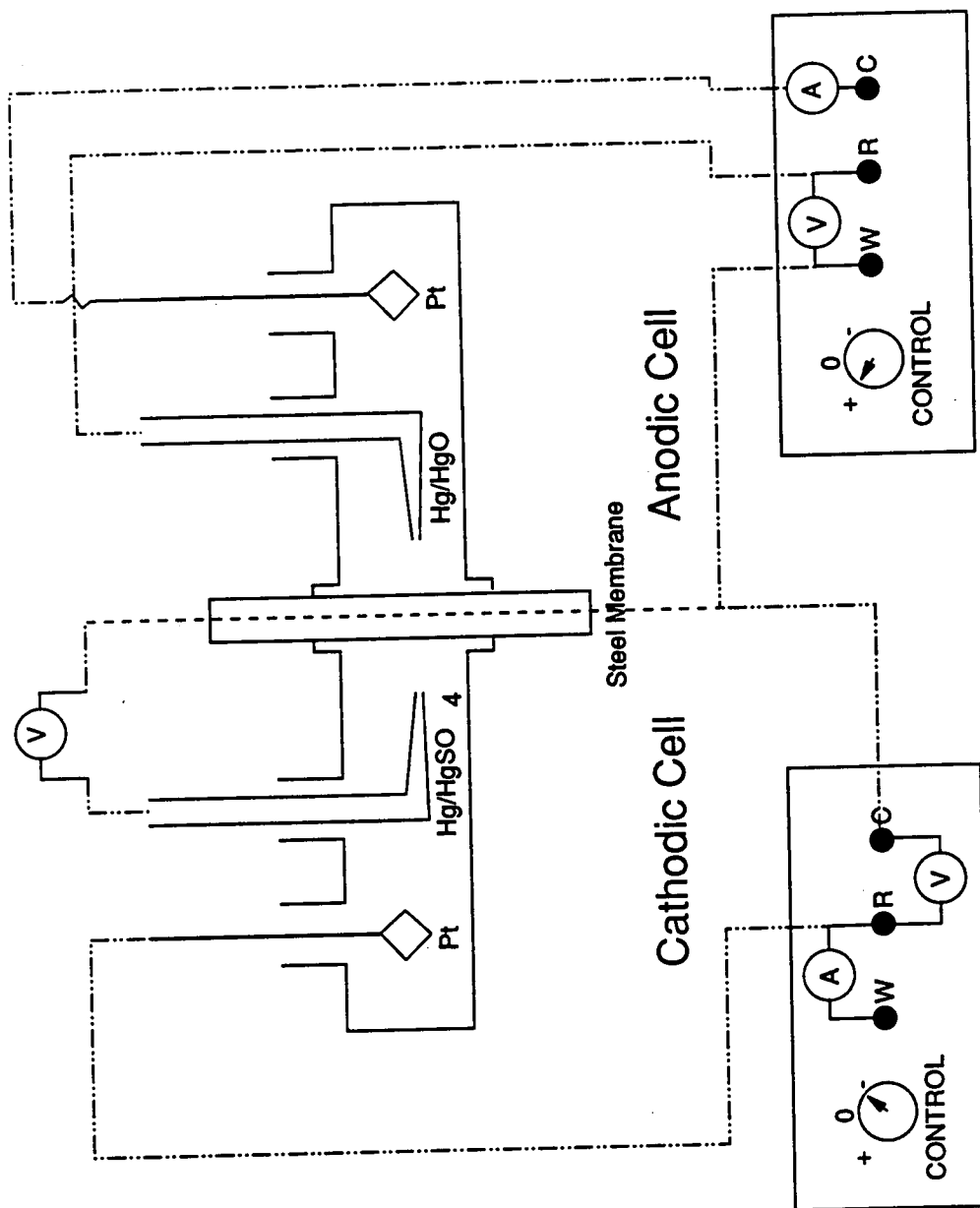
Figure 27. Bi-polar Cell Arrangement Used to Study the Kinetics of Steel Passivation.

116

The steel membrane was charged galvanostatically with a range of current densities using a platinum counter electrode. When the steady state current had been achieved, i.e. when the current at the membrane surface in the anodic cell was independent of time, the steady state potential at the membrane hydrogen influx surface was measured using a Hg/HgSO$_4$ reference electrode. The anodic cell contained a 0.2 M solution of analytical grade sodium hydroxide. The steel membrane was held potentiostatically at +150 mV with respect to the hydrogen scale in this compartment. This was achieved with a Hg/HgO reference electrode and a platinum counter electrode. The permeation current was measured using a zero resistance ammeter arrangement.

Prior to charging, the anodic side of the membrane was subjected to a 24 hour depletion of hydrogen, after which time the background hydrogen concentration throughout the membrane had been reduced to a very low, constant value which was subtracted from the measured permeation current. The temperature in the immediate vicinity of the experimental arrangement was monitored and was found not to fluctuated more than ± 3°C.

3.7 Determination of the Hydrogen Diffusion Coefficient.

Apparent hydrogen diffusion coefficients were calculated from the data collected during hydrogen permeation experiments using the conventional permeation cell shown in Figure 26. Diffusion coefficients were calculated using the breakthrough time, time lag and rise time constant methods[36].

3.8 Volumetric Permeation Experiments.

This experiment was performed to compare the surface hydrogen concentrations measured using the gel-filled hydrogen probe with the volume of hydrogen escaping from the efflux surface in a given time. The method was adapted from the British Standards 6693: Parts 1-5: 1988[108] using the apparatus shown in Figure 28.

Hydrogen diffusing through a steel plate, 1mm thick, was collected at ambient temperature in a glass cell which had a surface area of 35 cm^2 and contained a chemically inert silicone oil (dimethicone polydimethylsiloxane). After 24 hours cathodic charging, the volume of hydrogen that had diffused through the steel plate and into the cell was determined by measuring the length of the gas column accumulated in a 1mm diameter capillary tube using a travelling microscope. The volume of hydrogen measured was then corrected to a volume at standard temperature and pressure.

A conventional electrochemical permeation cell was also attached to the efflux surface to monitor the diffusion of hydrogen through the steel. Values of the diffusion coefficient and surface hydrogen concentration on the influx surface were also calculated from the conventional permeation transient.

3.9 Preparation of Samples for Metallographic Examination

A standard metallographic preparation technique was adopted in these experiments. However, contact with an aqueous phase was avoided as this was found to cause some degree of etching on the sample surface, particularly around cracks caused by hydrogen charging. Table 11 shows the polishing steps used during sample preparation.

118
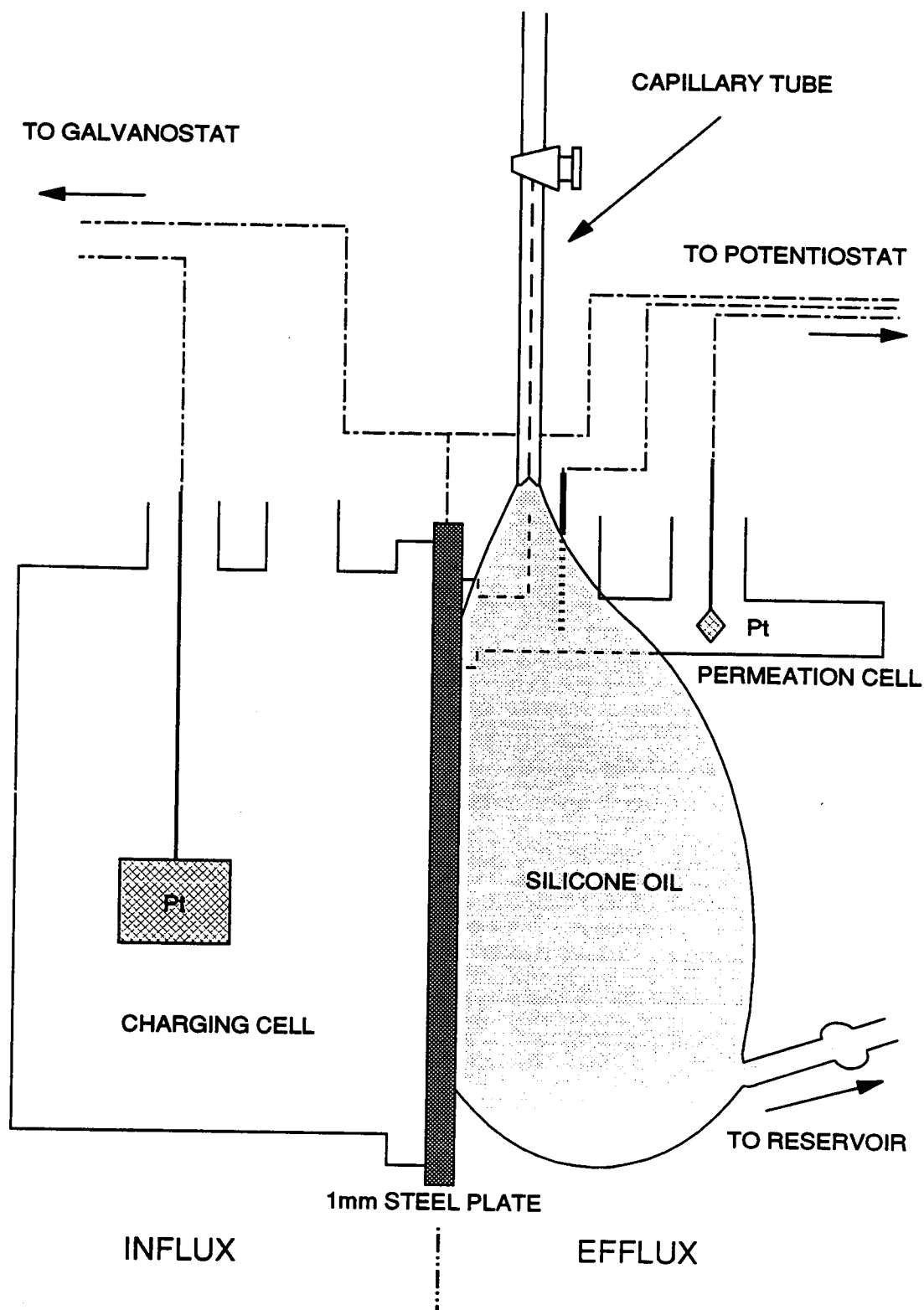
Figure 28.   Experimental Arrangement for Hydrogen
Collection Over Silicone Oil.

Table 11.   Metallographic Preparation of Samples.

Step	Grinding Size (µ)	Pressure (bar)	Time (seconds)	Cloth Type	Lubricant	Cleaning Stage.
1	17	4	240	Carbide Paper	Ethanol	Ethanol/tri-Chloroethane
2	9	4	240	Pan	Hyprez Oil Based	Ethanol/tri-Chloroethane
3	3	4	240	Struers Cloth	Hyprez Oil Based	Ethanol/tri-Chloroethane

3.10   Repeated Charging Experiments to Determine the Effect of Trapping on the Permeation of Hydrogen.

The experimental arrangement shown in Figure 28A for the repeated charging experiments was essentially the same as that shown in Figure 26. The samples, however, were charged under potentiostatic conditions rather than galvanostatic conditions. Samples of the BS Z25 and NAM plates were machined to 1 mm in width from the as-received materials. The reduced thickness specimens were expected to give breakthrough times of around 26 minutes in the case of the BS Z25 material and 17 minutes in the case of the NAM material. The experiments were performed in duplicate for each of the steels. The cathodic compartment of the cell arrangement was filled with 10% sulphuric acid containing 50 ppm stannous chloride which acted as a cathodic poison to promote hydrogen entry. The steel was polarized potentiostatically to -1 V on the normal hydrogen scale. The anodic compartment contained a
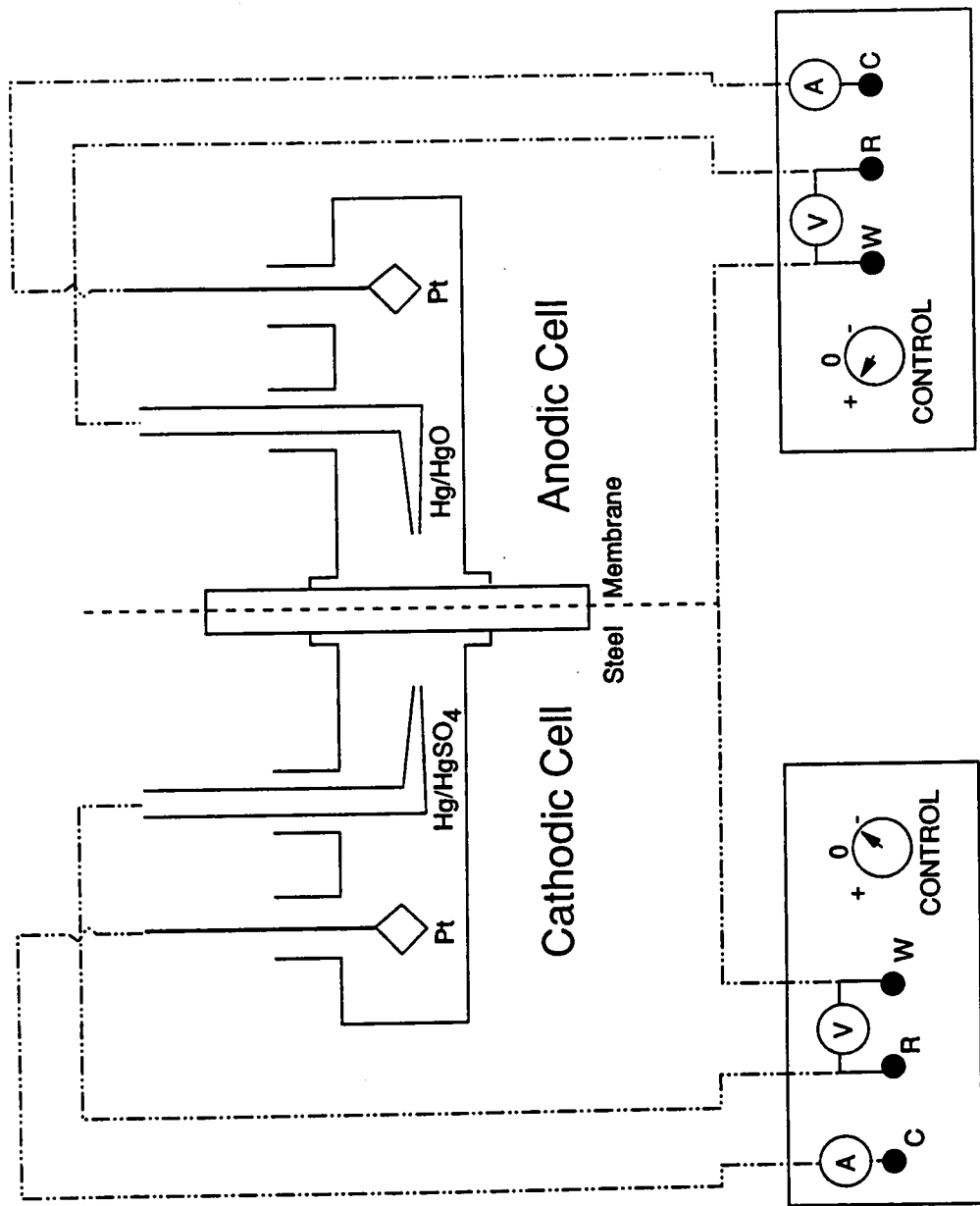
Figure 28A. Bi-polar Cell Arrangement to Determine the Effect of Trapping on the Permeation of Hydrogen.

121

0.2 M sodium hydroxide electrolyte, with the steel held at a potential of +150 mV (NHE), which was sufficient to oxidise any hydrogen diffusing through the steel.

The hydrogen oxidation current was recorded until apparent steady state conditions were achieved i.e. when there was no significant variation in current with respect to time. At this point, the charging electrolyte was removed from the cathodic compartment and a subsequent depletion transient recorded. When the depletion current had reached a steady, low value the procedure was repeated for second and subsequent transients. For successful repetitive permeation transients it was essential that the current was reduced to its previous steady state background value which should be uniform before charging commenced.

4.0 RESULTS.

4.1 Gel-Filled Hydrogen Probe Readings.

Figure 29 shows typical gel-filled hydrogen probe readings taken over 15 minutes using the unmodified gel-filled hydrogen probe arrangement which incorporated a nickel/nickel oxide auxiliary electrode. Calibration data for the probe is summarised in Figure 30. A narrow band of surface hydrogen concentration values formed the upper and lower boundaries of acceptance for each standardisation. If the probe's reading on the standard block conformed to these boundaries then the probe was functioning as expected.

4.2 Selection of the Auxiliary Electrode.

Figure 31 shows an anodic polarization profile for an electro-polished poly-crystalline nickel electrode. The scan was recorded with a scan rate of 0.05 V min^{-1} between 0 and +1.6 V (NHE) in a 10% sulphuric acid solution.

Table 12 shows the main peak path length values (d) obtained using the X-Ray diffraction technique. The values in round brackets "()" show the experimental peak heights as a percentage of the largest peak obtained between an angle of rotation of 10 and 120° to the horizontal plane. The value in square brackets "[]" show the corresponding literature peak heights[140] for the proposed crystalline structures.

Plates 8 and 9 show the surface condition of the sintered nickel plaque at two distinct areas on the electrode surface. Plate 8 shows an area representing the bulk of the electrode surface, seen as a dark grey area, characteristic of a conducting oxide such as ß-NiOOH[141]. At higher magnification, the surface appears to consist of a flaky, plate like structure. The surface appears to be very rough, and suggests a high degree of inhomogeneity.

123
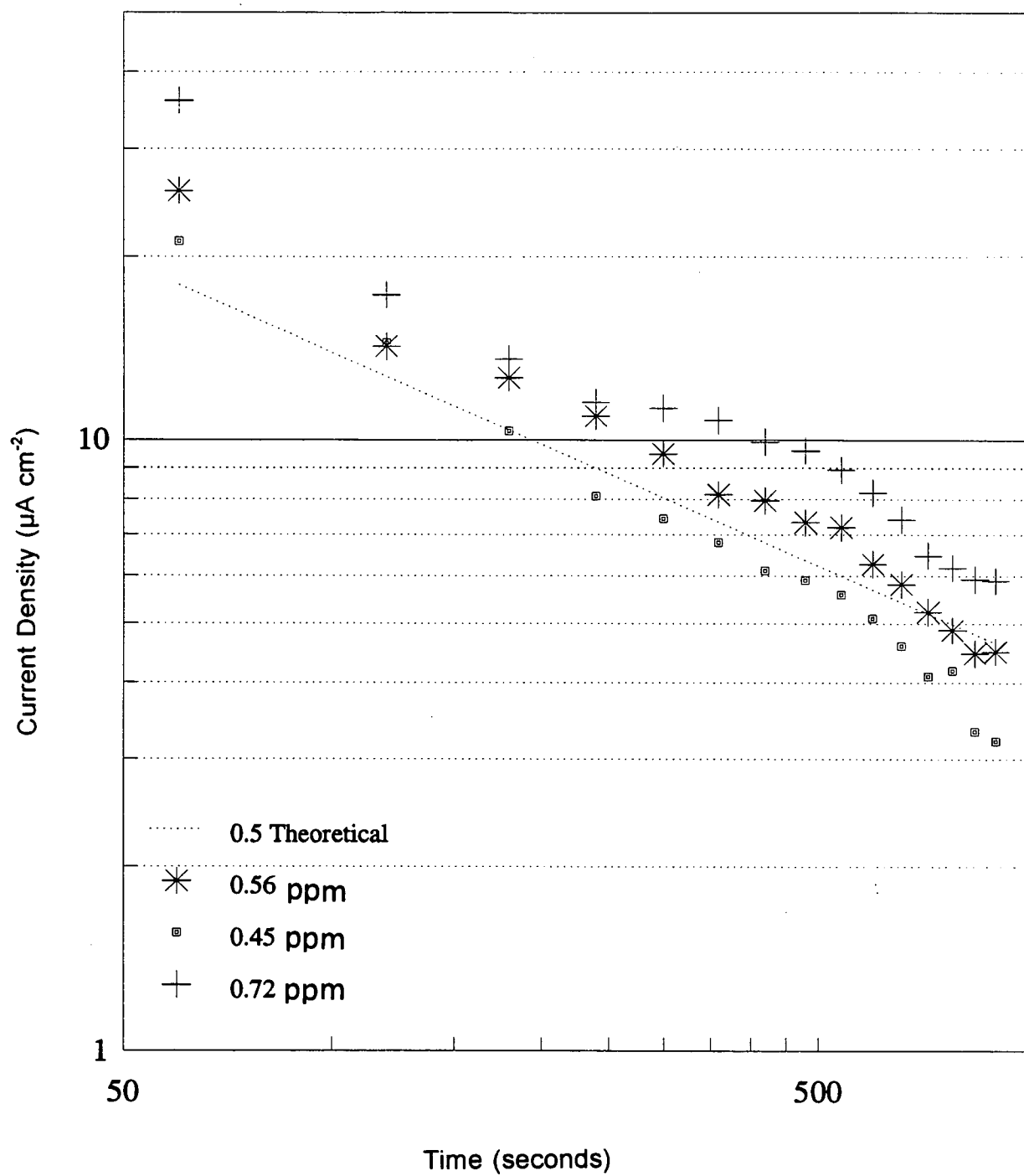
Figure 29.   Typical Gel-Filled Probe Readings Using
Nickel/Nickel Oxide Auxiliary Electrode.

124
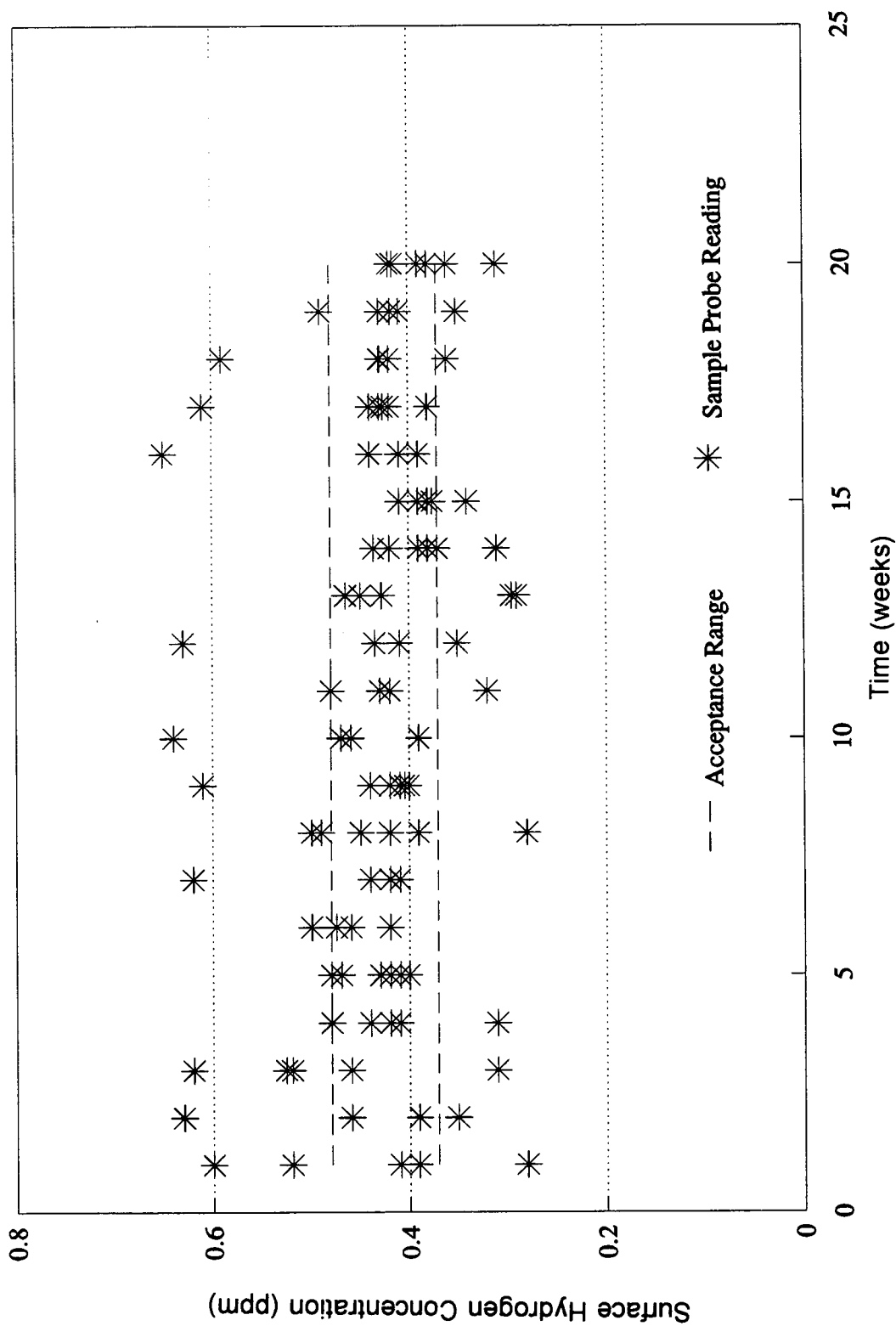
Figure 30. Plot to Show Scatter of Data on Standard Block Using Gel-Filled Probe with Nickel/Nickel Oxide Auxiliary Electrode.

125
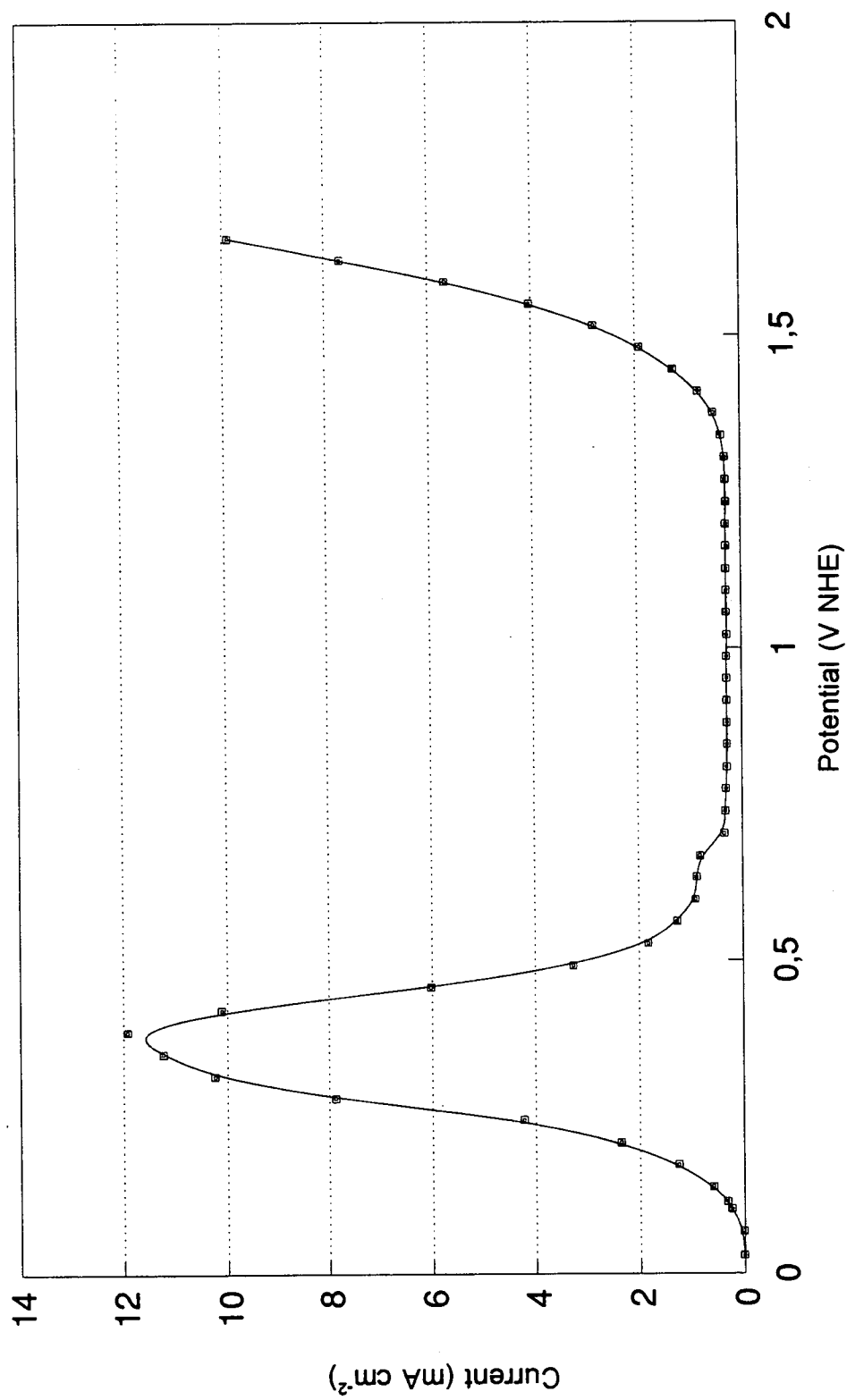
Figure 31.   Anodic Polarization Profile for Poly-Crystalline Nickel Foil.

126
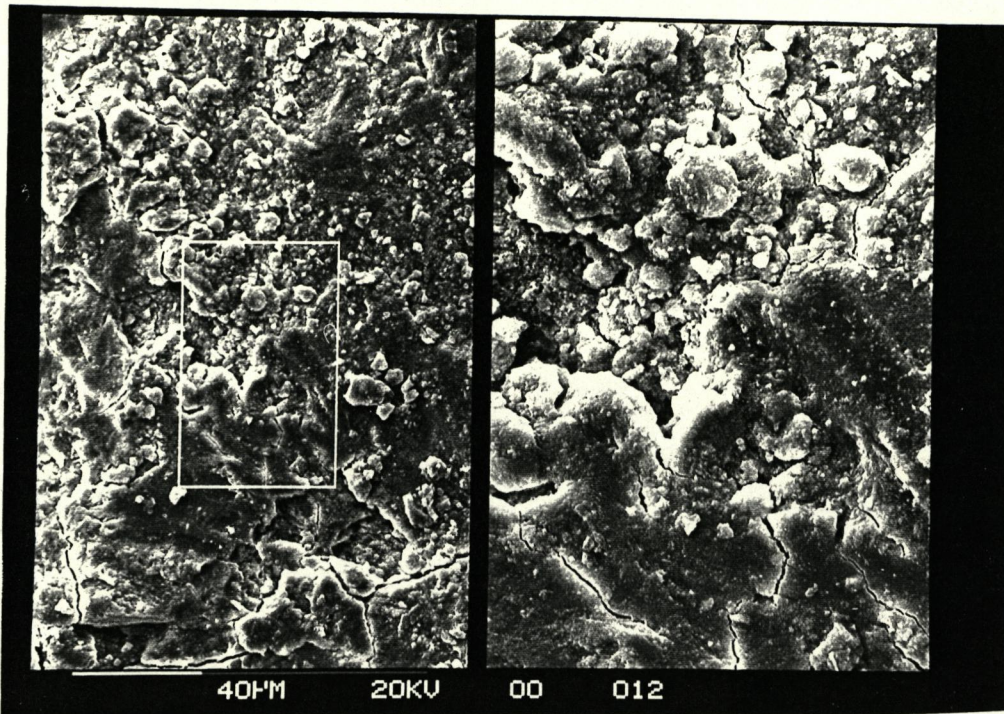
Plate 8.   Sintered Nickel Plaque Showing Dark Area
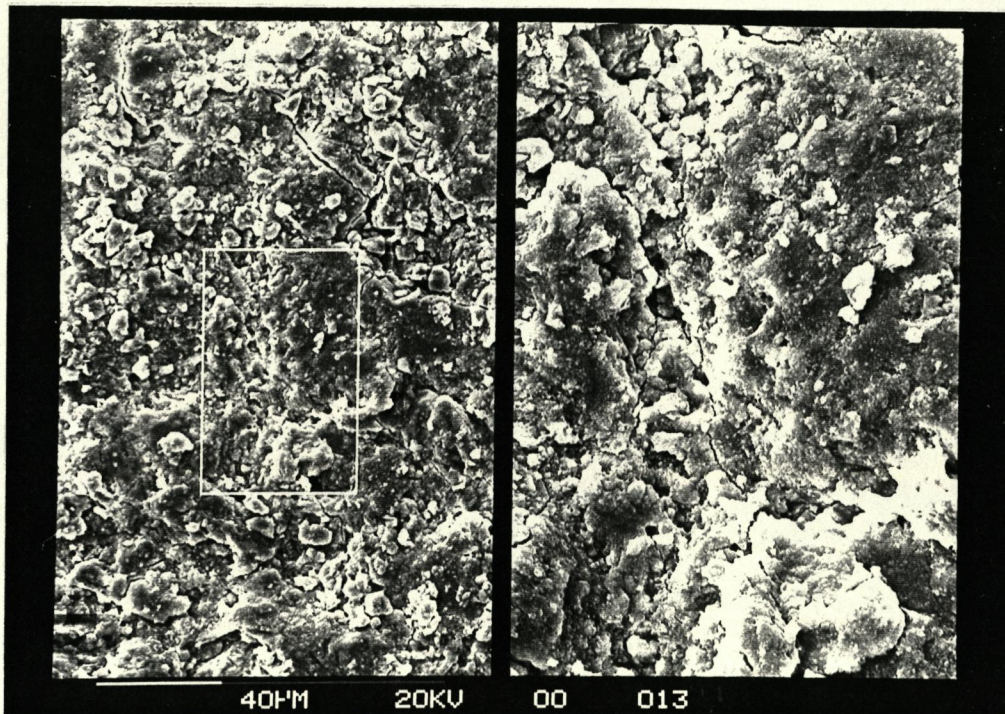
Plate 9.   Sintered Nickel Plaque Showing Light Band.

127

Table 12. XRD Analysis Data

Sample	Main Peaks d Values	Inference Main Peaks, Expected, d Values				
		Ni	Ni(OH)$_2$	ß-NiOOH	CdO	LiH
1,2,3,4	2.0(100)	2.0[100]				
	1.77(55)	1.76[42]				
	1.26(40)	1.25[21]				
	1.07(30)	1.06[20]				
	1.03(5)	1.02[7]				
5,6	2.05(100)	2.0[100]				2.0[100]
	2.35(70)		2.32[62]	2.41[80]	2.35[88]	2.36[55]
	1.7(45)	1.76[42]	1.75[29]		1.66[43]	
	1.07(30)	1.06[20]				
	1.25(25)	1.25[21]				
	1.44(25)		1.48[9]	1.40[80]	1.41[28]	1.44[40]
	4.79(20)		4.5[100]	4.8[100]		
	1.23(20)					1.23[25]
	2.76(15)		2.68[32]		2.7[100]	
	1.6(15)		1.56[29]			
	2.97(10)					
	1.18(5)		1.17[7]		1.17[5]	1.02[4]
	1.02(5)	1.02[5]				1.02[4]

128

Plate 9 shows an area representing a well defined, but narrow, band of lighter material extending, consistently, the length of the electrode. The band covers approximately 20% of the total electrode surface and lies parallel to the electrode edge.

Figures 32(a) and (b) show the S.E.M elemental analysis of the surface oxide films illustrated in Plates 8 and 9 respectively. Light element analysis showed that the two areas had approximately equal oxygen levels (Ni : O_2 = 1 : 0.29 and 1 : 0.24 for plates 8 and 9 respectively) which in comparison to the other electrodes examined, Figure 33, were at least three times higher. Table 13 shows a summary of the final equilibrium rest potentials attained after 80 hours in 0.2M NaOH. The mixed potential measurements were taken for each of the 7 electrodes over a period of 80 hours. All values are expressed with reference to the normal hydrogen scale.

Table 13   Equilibrium Rest Potential For Auxiliary Electrodes in 0.2M NaOH.

Electrode	Equilibrium Potential (V NHE)
10% H_2SO_4 Galvanostatic	-0.09
0.15M Na_2SO_4	-0.128
pH 7.6 Borate Buffer Solution	-0.139
10% H_2SO_4 Potentiostatic	0.03
Sintered Nickel Plaque	0.150
Mercury/Mercury Oxide	0.306
Blank	0.037
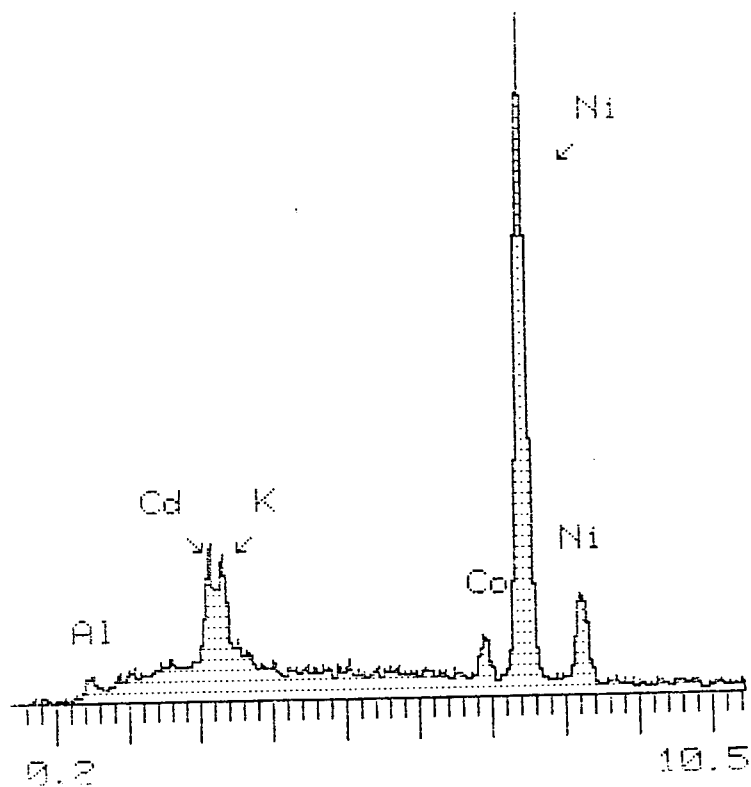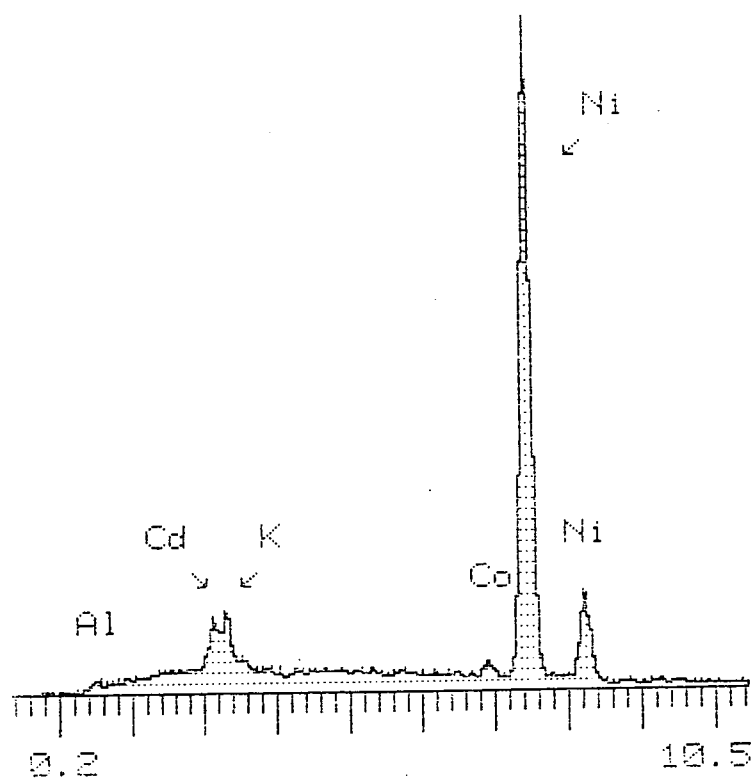
Figure 32. SEM Elemental Analysis for (a) Dark Area and (b) for Light Band.

130
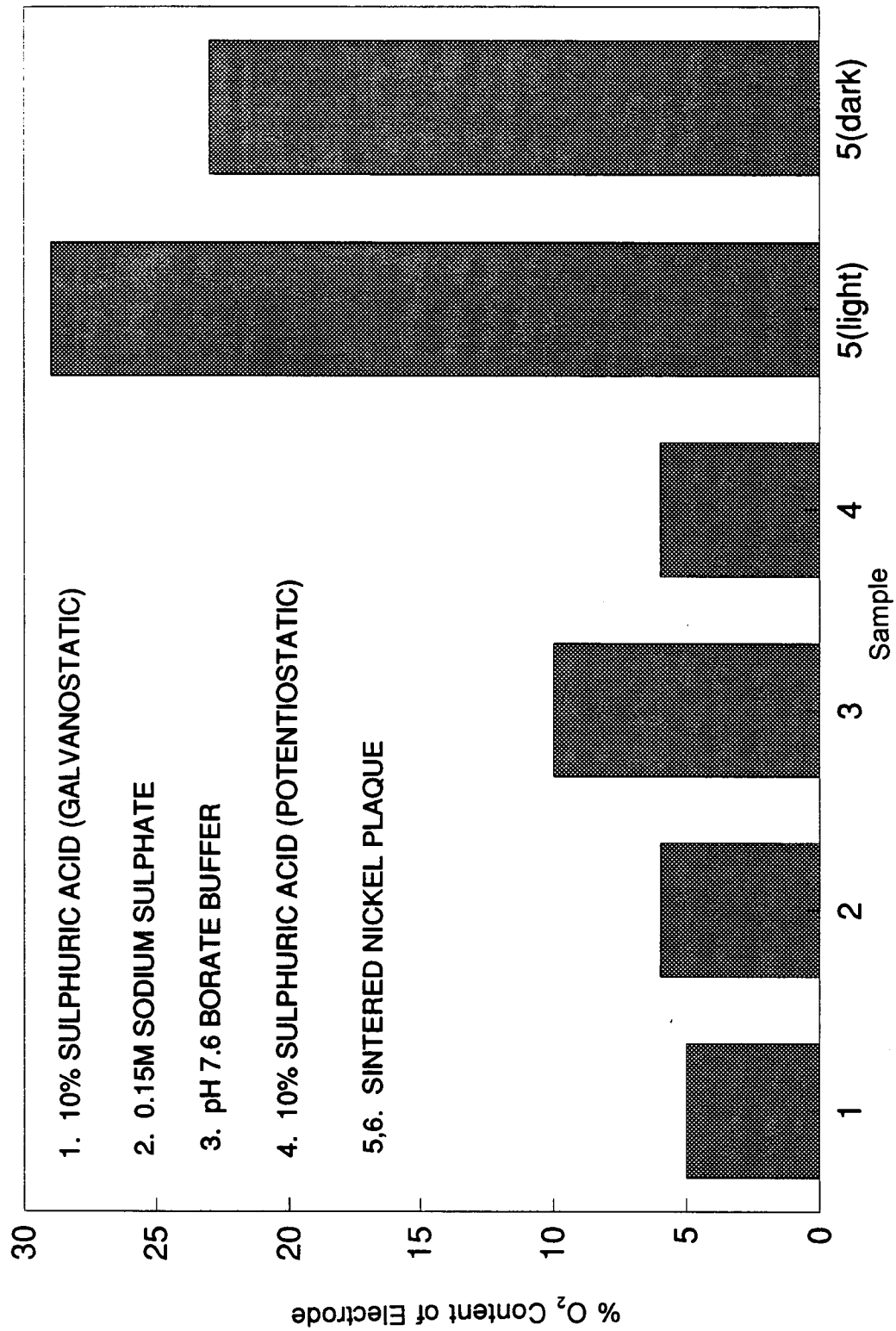
Figure 33.   Light Element Analysis for Auxiliary Electrodes.

131

4.3 The Modified Gel-Filled Hydrogen Probe.

Figure 34 shows typical gel-filled hydrogen probe readings taken over 15 minutes using the modified gel-filled hydrogen probe arrangement which incorporates a mercury/mercury oxide reference electrode and platinum auxiliary electrode. Calibration data for the probe is summarised in Figure 35. If the probe reading on the standard block conformed to the boundaries shown on the graph then the probe was functioning as expected.

4.4 Evaluation of Passive Oxide Film Formation on Steel.

Figures 36 and 37 show the results obtained from the scratch test experiments. The decaying current transients are shown on both linear and logarithmic axes respectively. Figure 38 shows the effect of a passive current on gel-filled hydrogen probe measurements for a range of surface hydrogen concentrations. The influence that the passive current had on the gel-filled hydrogen probe readings is illustrated in Figure 39. During the initial stages of the probe measurements a considerable contribution to the over all measured current was observed from the steel passivation process. However, after longer times the current associated with the passive film formation decayed to a low background value. It was after this time that, surface hydrogen concentrations were calculated from the probe measurements. Results of the delayed gel-filled probe readings are presented in Figure 40 where the surface hydrogen concentration is examined with respect to time at open circuit for the probe. Analysis of the subsequent hydrogen concentration measurements, after standing at open circuit on the specimen, still revealed a gradient which deviated from the expected value of -½ when plotted on log current / log time axes. This observation was explained by the enhanced growth of the anodic oxide film on application of the anodic potential required to oxidise the hydrogen as it reached the steel surface.

132

4.5 Preliminary Hydrogen Charging.

Figures 41 and 42 show the results of the preliminary hydrogen charging experiments for the BS Z25 and NAM specimens respectively. The graphs represent the increase in surface hydrogen concentration measured with the gel-filled hydrogen probe after successive periods of hydrogen charging. The surface hydrogen concentration recorded in these preliminary charging experiments was later found to be rather low. Development of the measuring technique through more efficient surface preparation and handling of the samples produced more reliable results as described later in section 4.9.
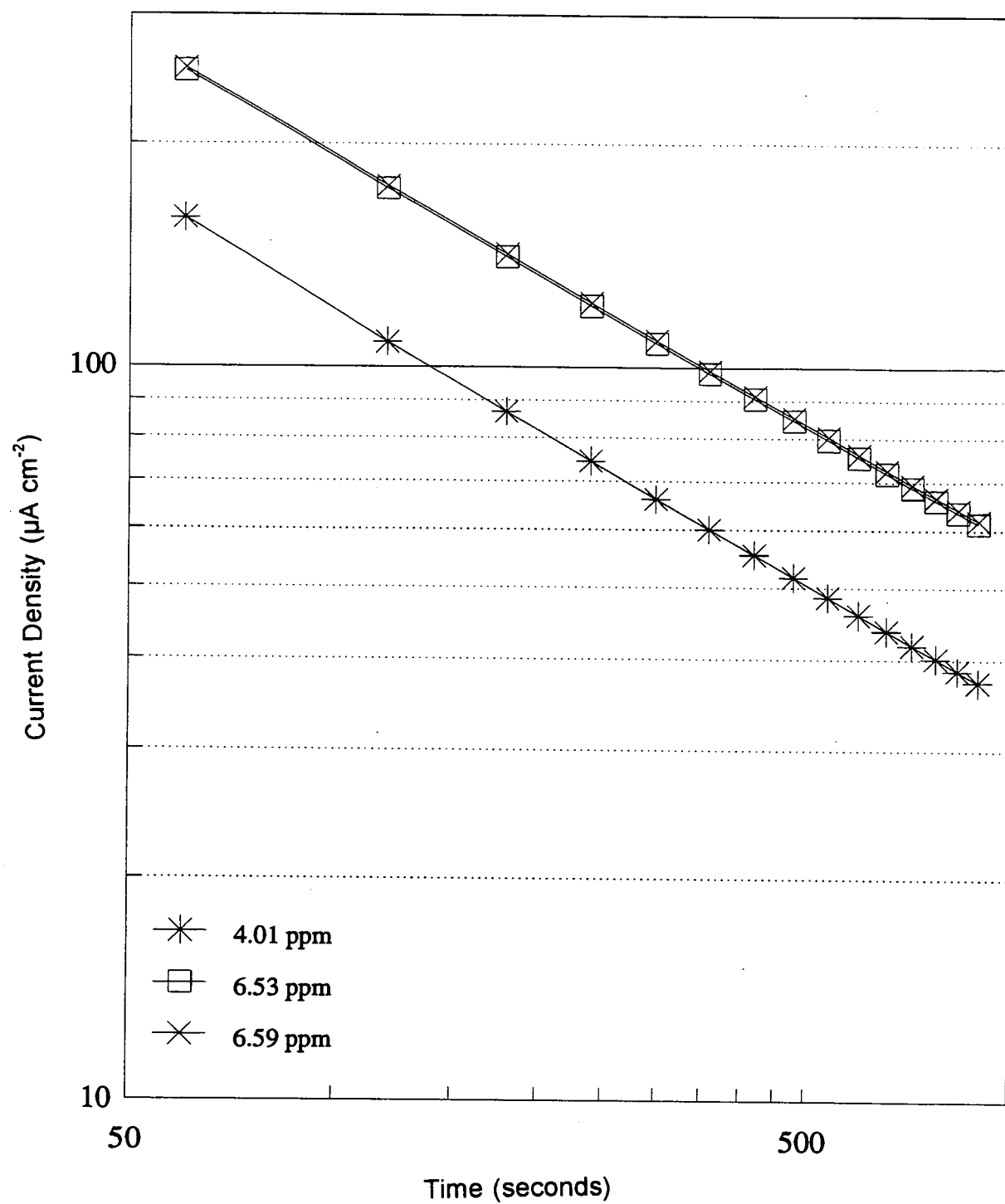
Figure 34.   Typical Current Decay Transients for the
Modified Gel-Filled Hydrogen Probe on Steel
Sample.

134

Figure 35. Plot to Show Scatter of Data on Standard Block Using the Modified Gel-Filled Probe.

135
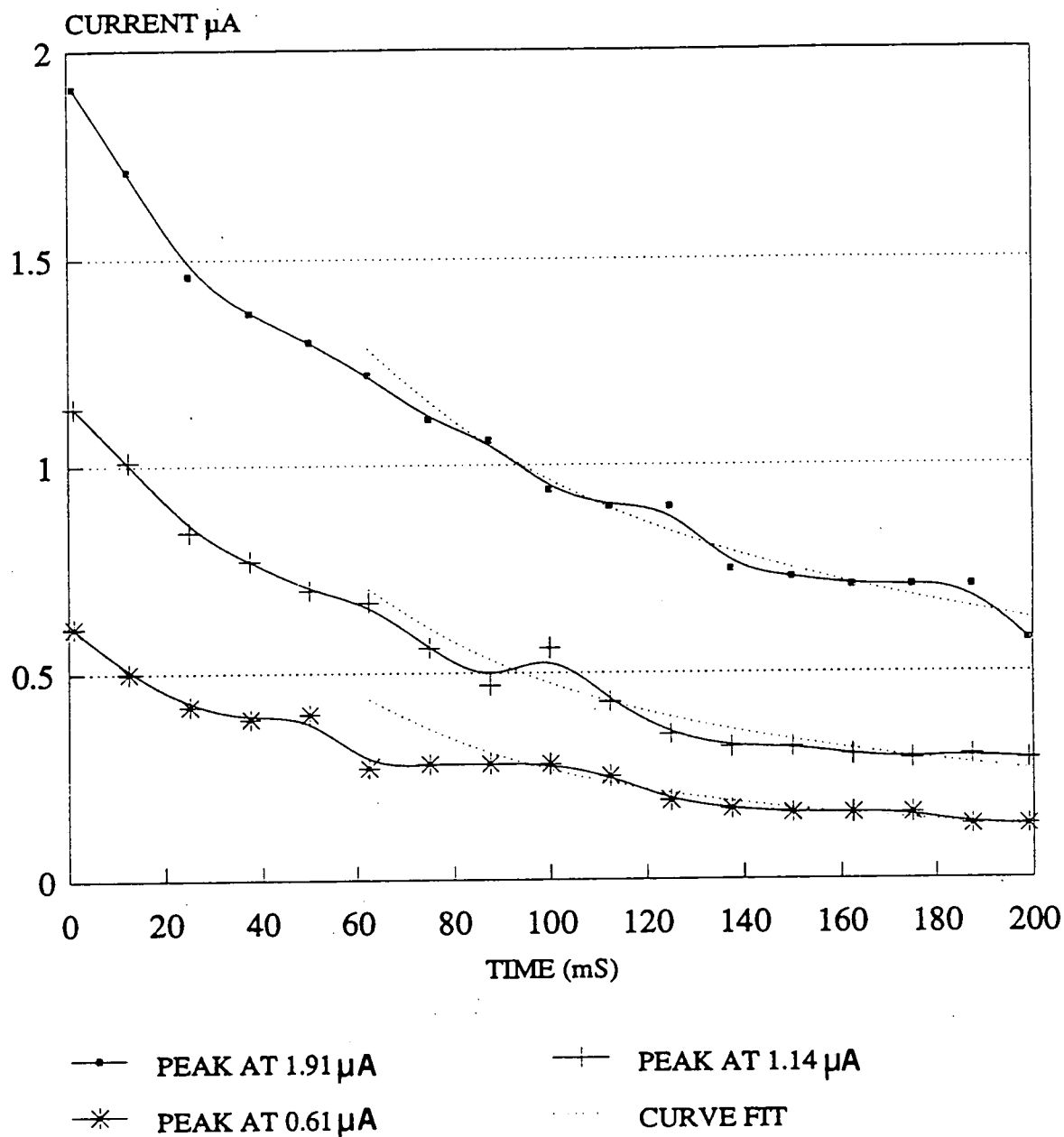
Figure 36.   Repassivation of Scratched Steel Surface
with Linear Axis.

136
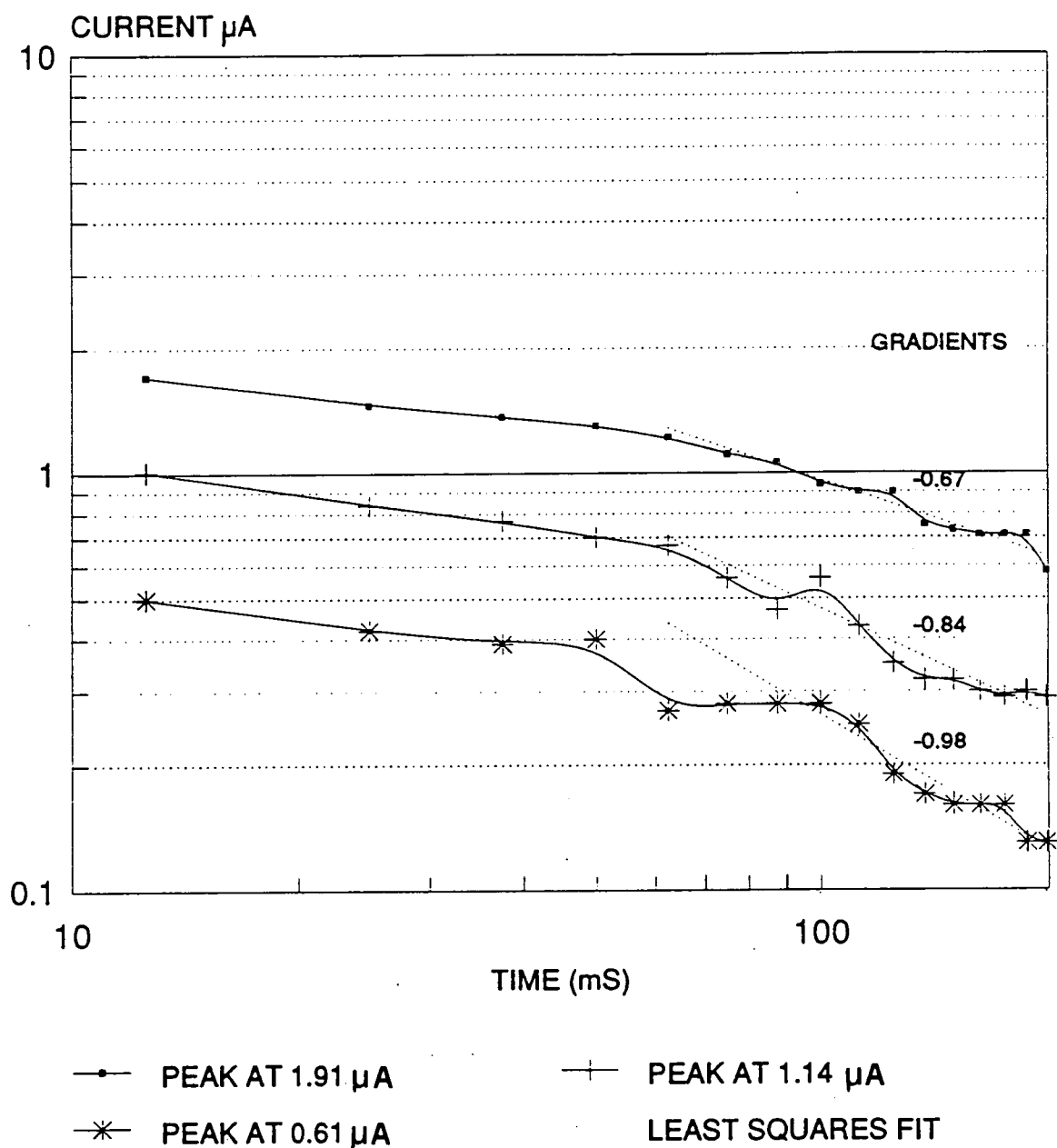
Figure 37.   Repassivation of Scratched Steel Surface
with Logarithmic Axis.

137
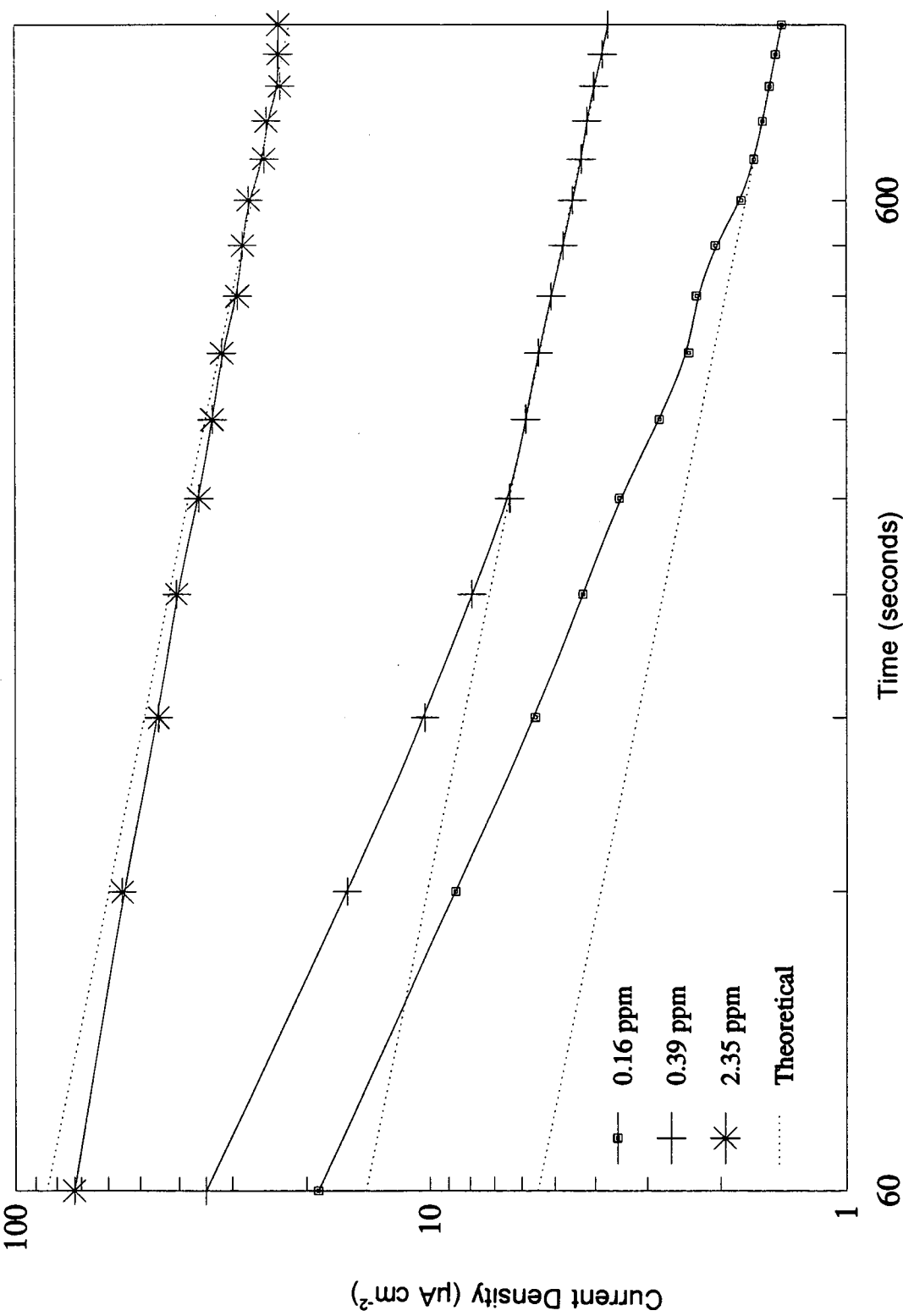
Figure 38. Gel-Filled Probe Measurements Showing the Effect of Repassivation at Low Hydrogen
Concentrations.

138

THEORETICAL GRADIENT OF -0.5

Gradient

Surface Hydrogen Concentration (ppm)
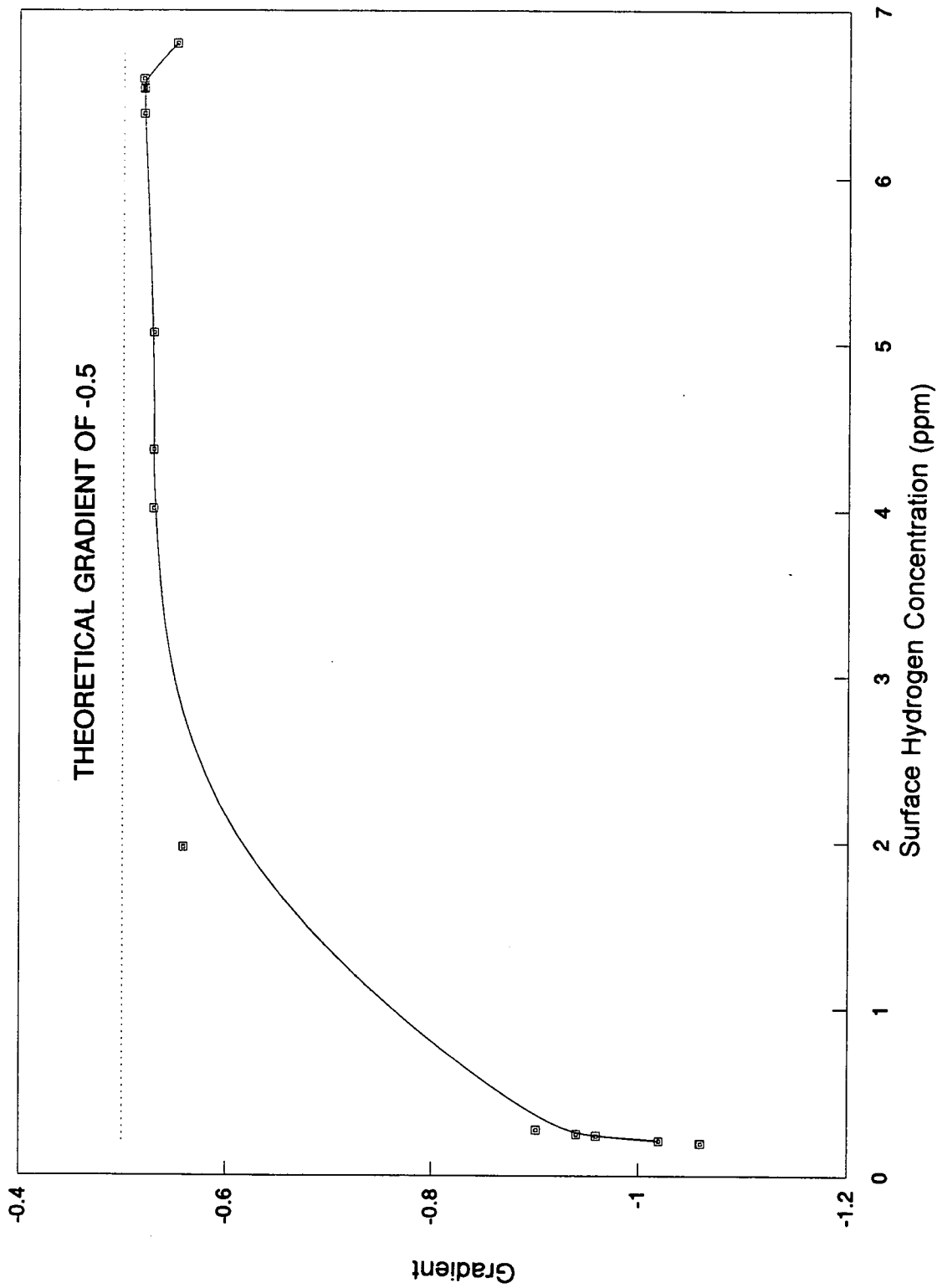
Figure 39.   Graph Showing the Effect of Hydrogen Content on the Gradient of the Current Transients.

139
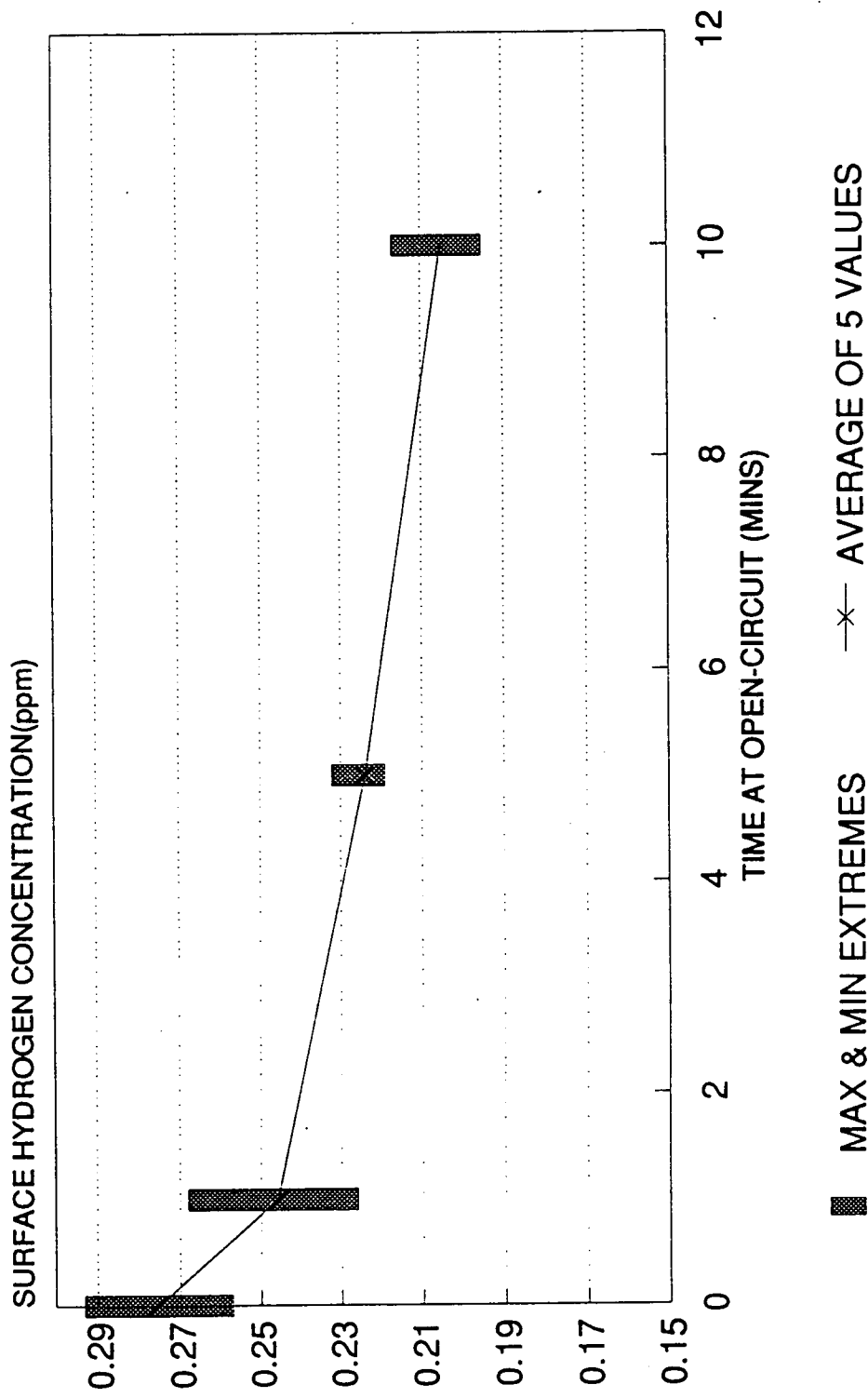
Figure 40.   Delayed Gel-Filled Hydrogen Probe Readings Illustrating the Effect of Steel Passivation.

140
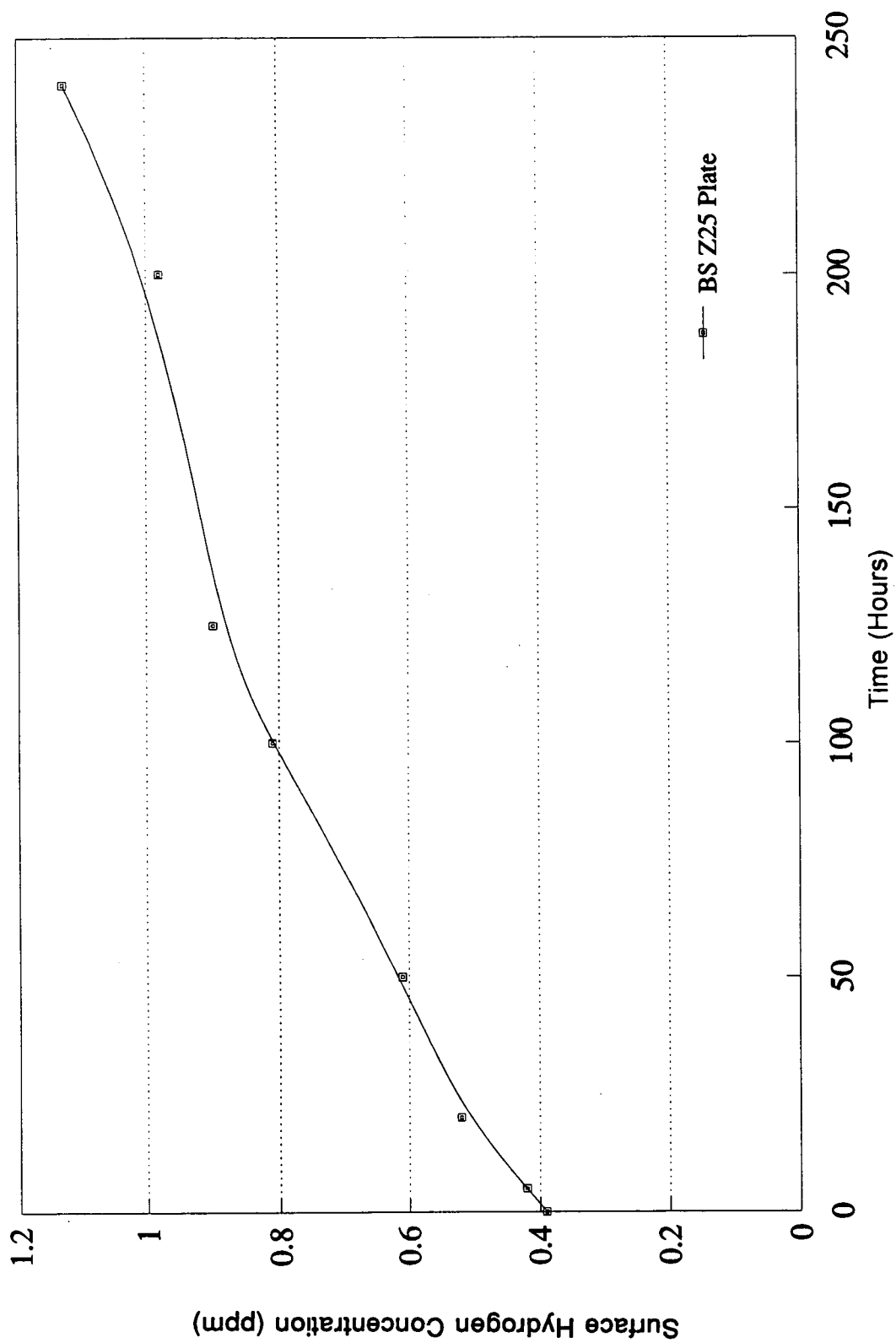
Figure 41.   Preliminary Charging Experiments for the BS Z25 Plate.

141
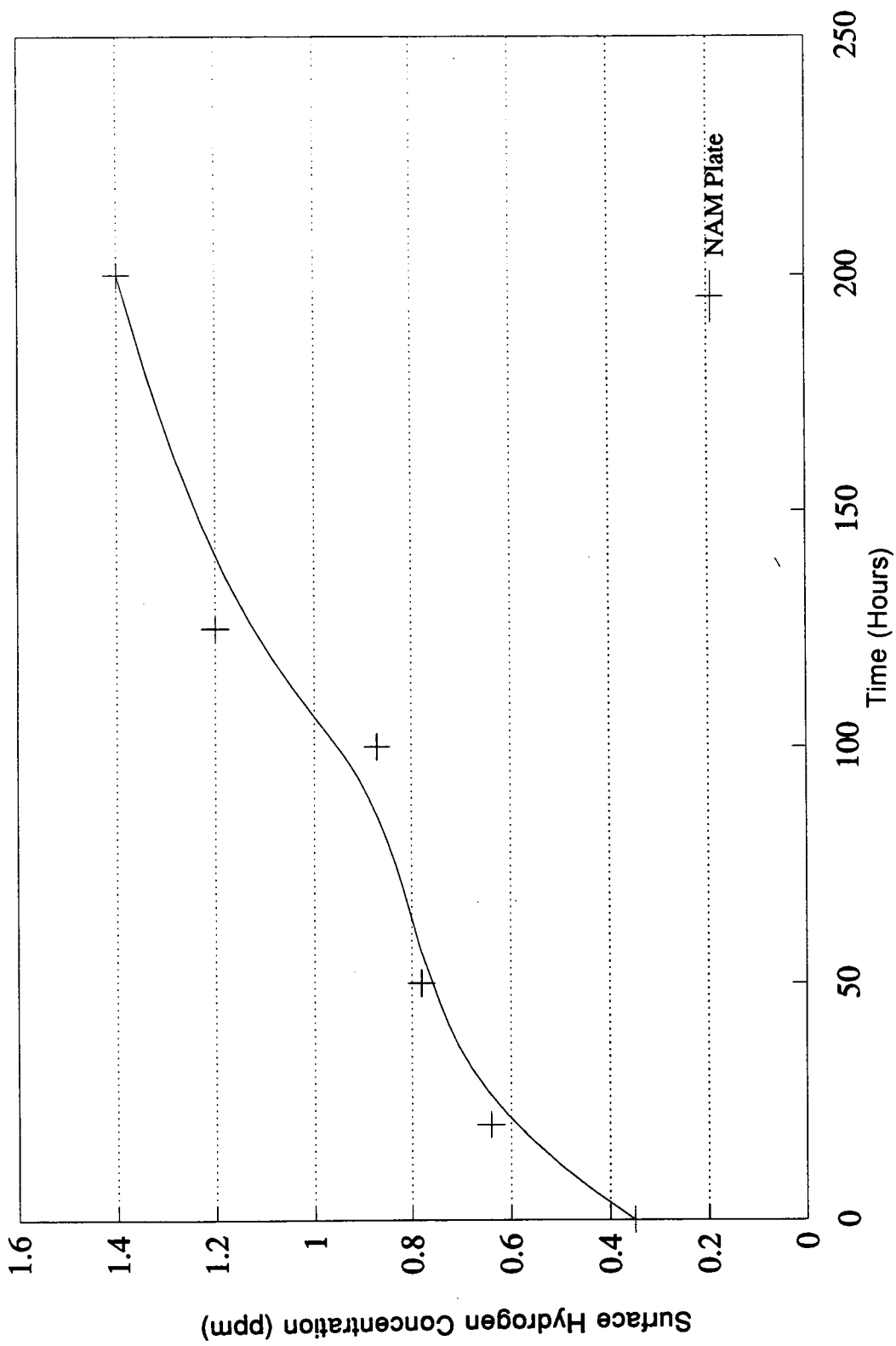
Figure 42.   Preliminary Charging Experiments for the NAM Plate.

142

4.6   The Kinetics of Hydrogen Absorption into Steel.

A series of experiments was performed to determine approximate values for the specific rate constants associated with the hydrogen absorption and hydrogen evolution reactions. Figure 43 shows the successive hydrogen permeation transients obtained with increasing cathodic charging current density. Figure 47 shows a plot of charging current against hydrogen over-voltage, used to calculate the transfer coefficient for the hydrogen evolution reaction. By manipulation of the IPZ model, the relationship between steady state permeation current and the square root of the hydrogen evolution current could be established as shown in Figure 44. The relationship between the hydrogen charging function ($i_c exp^{a\alpha\eta}$) and the adjusted steady state permeation current (i-cg/b) is shown in Figure 45. Figure 46 shows the final relationship between surface hydrogen coverage and hydrogen over-voltage. A summary of the charging currents and resulting measured parameters is shown in Table 14.

The resulting calculated coefficients appertaining to a coupled discharge mechanism for the hydrogen absorption reaction are shown in Table 15.

4.7   Conventional Glass Cell Permeation Experiments to Determine the Hydrogen Diffusion Coefficient in Steel.

Conventional glass cell permeation transients for the BS Z25 material were obtained using the apparatus adapted from that used by Devanathan and Stachurski[36] , examples of these are shown in Figures 48 and 49. Values for the time lag, Figures 50 and 51, and the time constant values, Figures 52 and 53, were also obtained by interpretation of the permeation transients shown in Figures 48 and 49. A summary of these various parameters is given in Table 16.
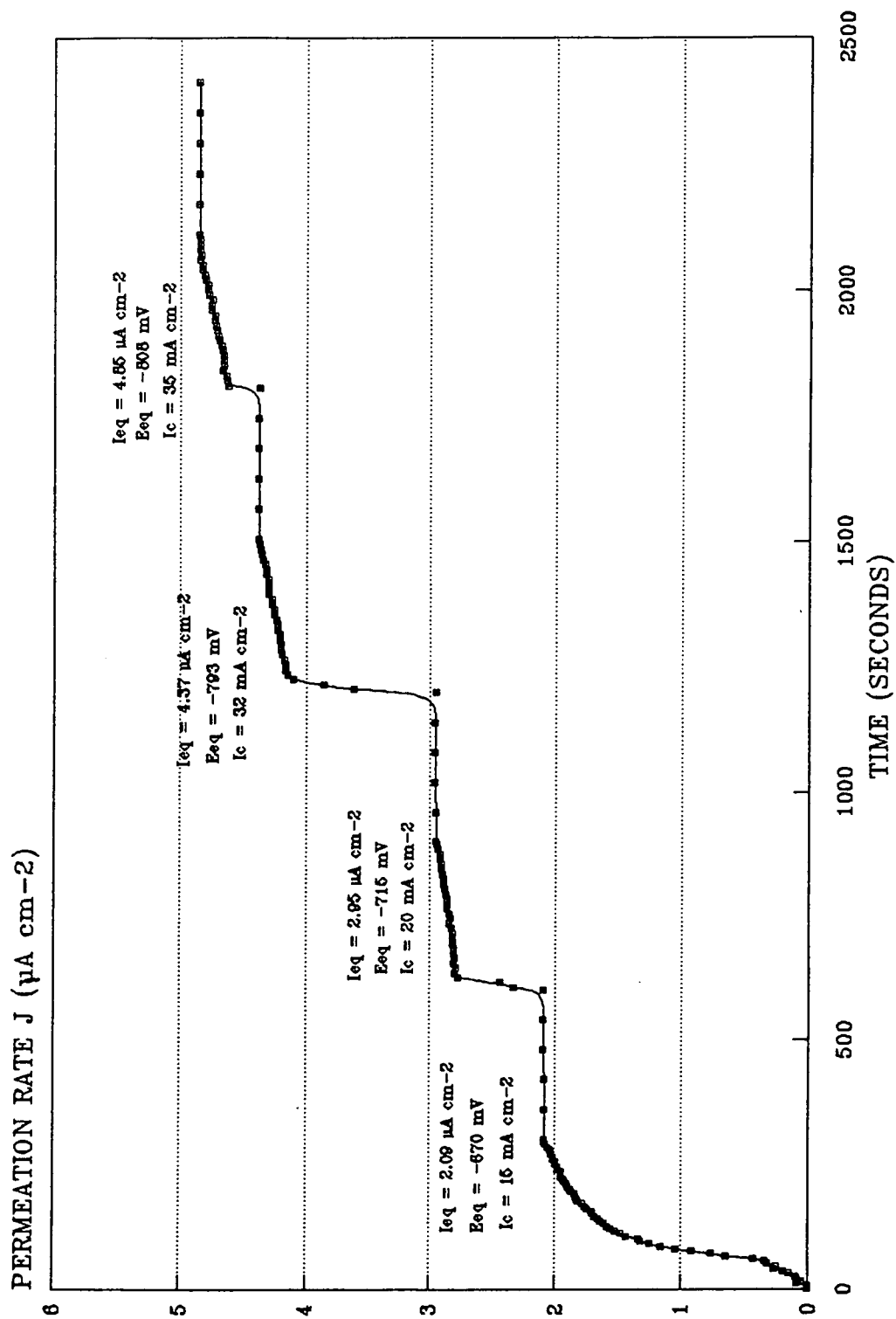
Figure 43. Successive Permeation Transients for Increasing Cathodic Current Densities.

144
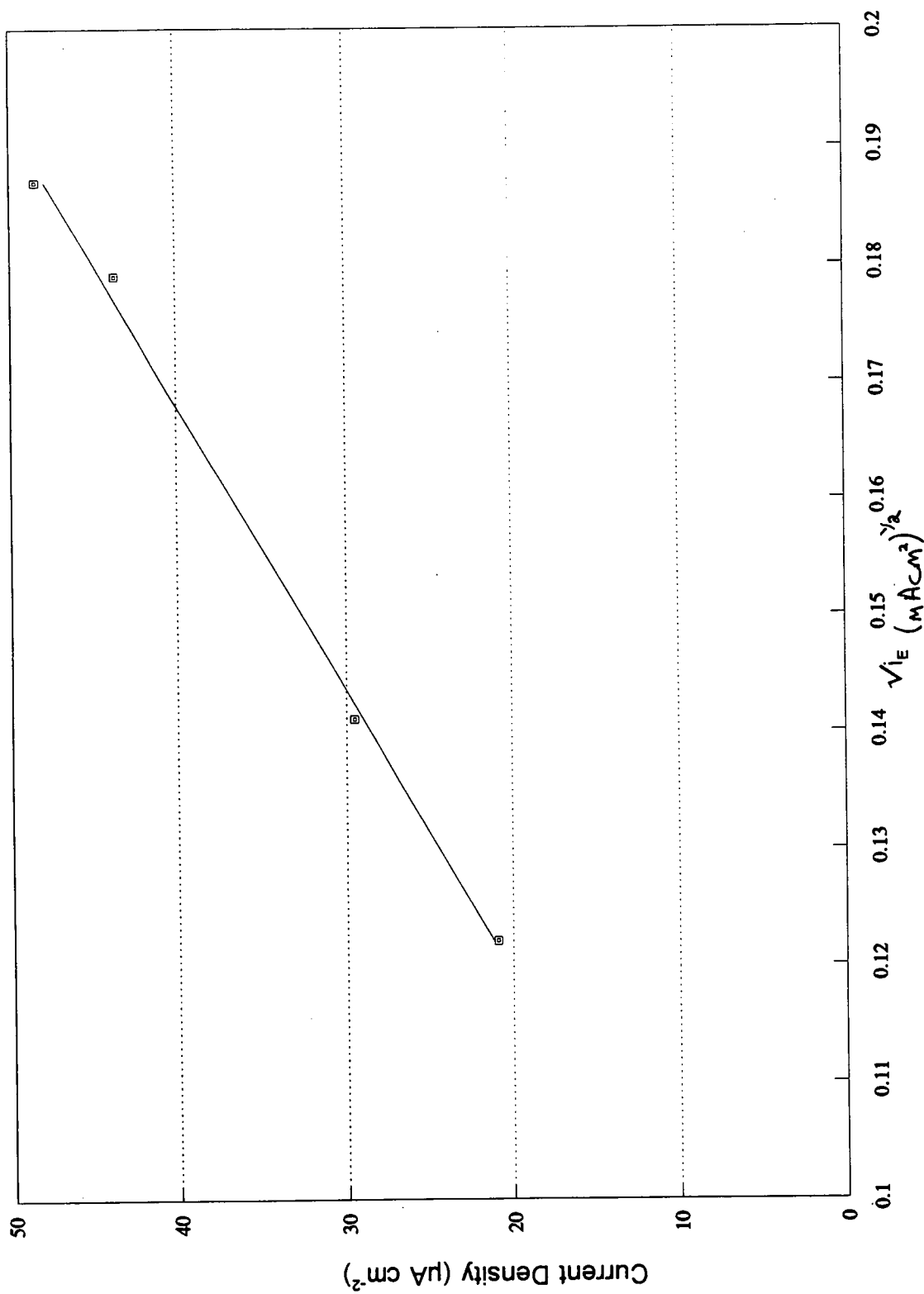
Figure 44. Steady State Permeation Current Against Square Root of Hydrogen Evolution Current.

145
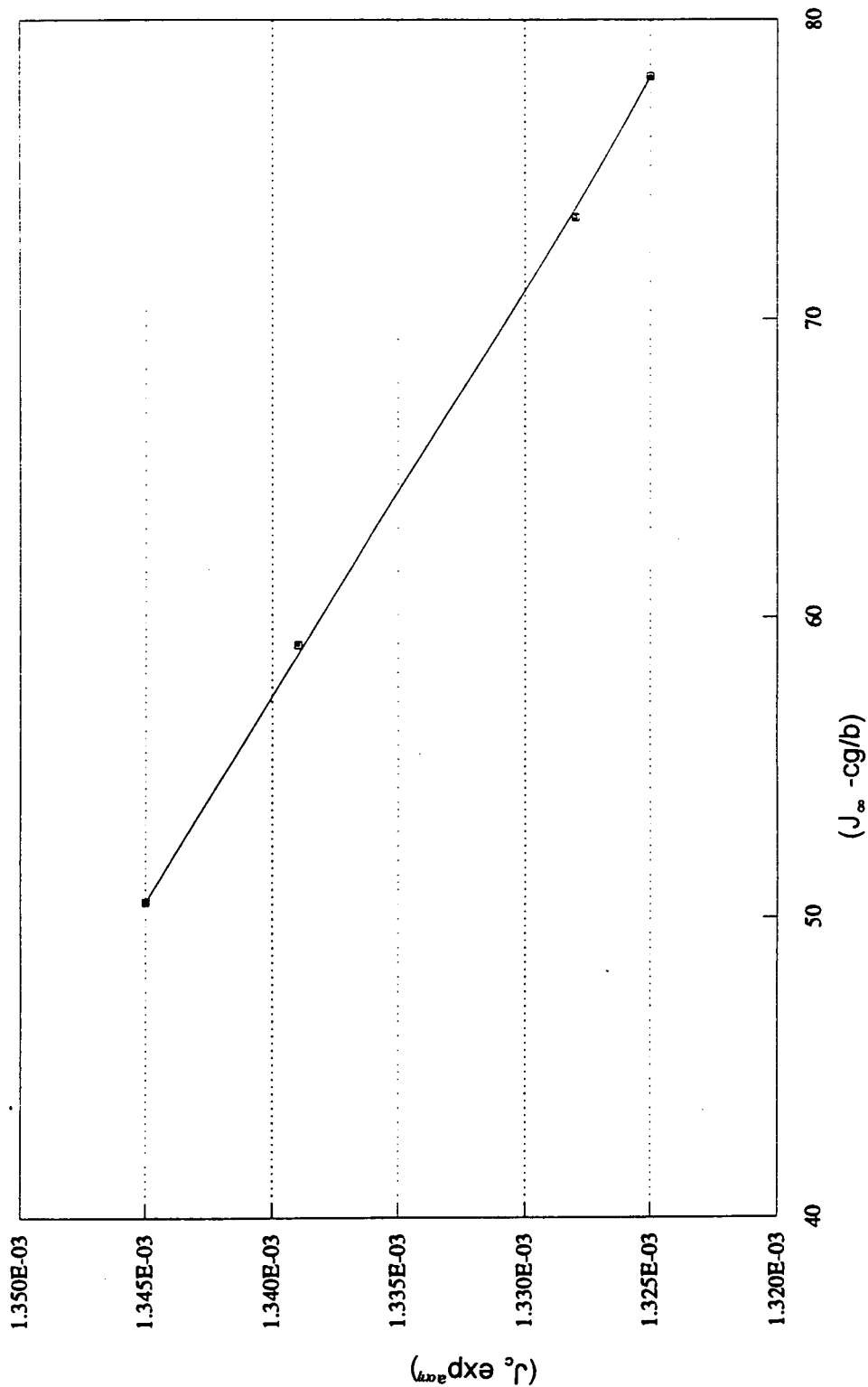
Figure 45.   Hydrogen Charging Function (I_c exp^{acm}) Against Adjusted Steady State Permeation
Current (I_∞ - cg/b).

146
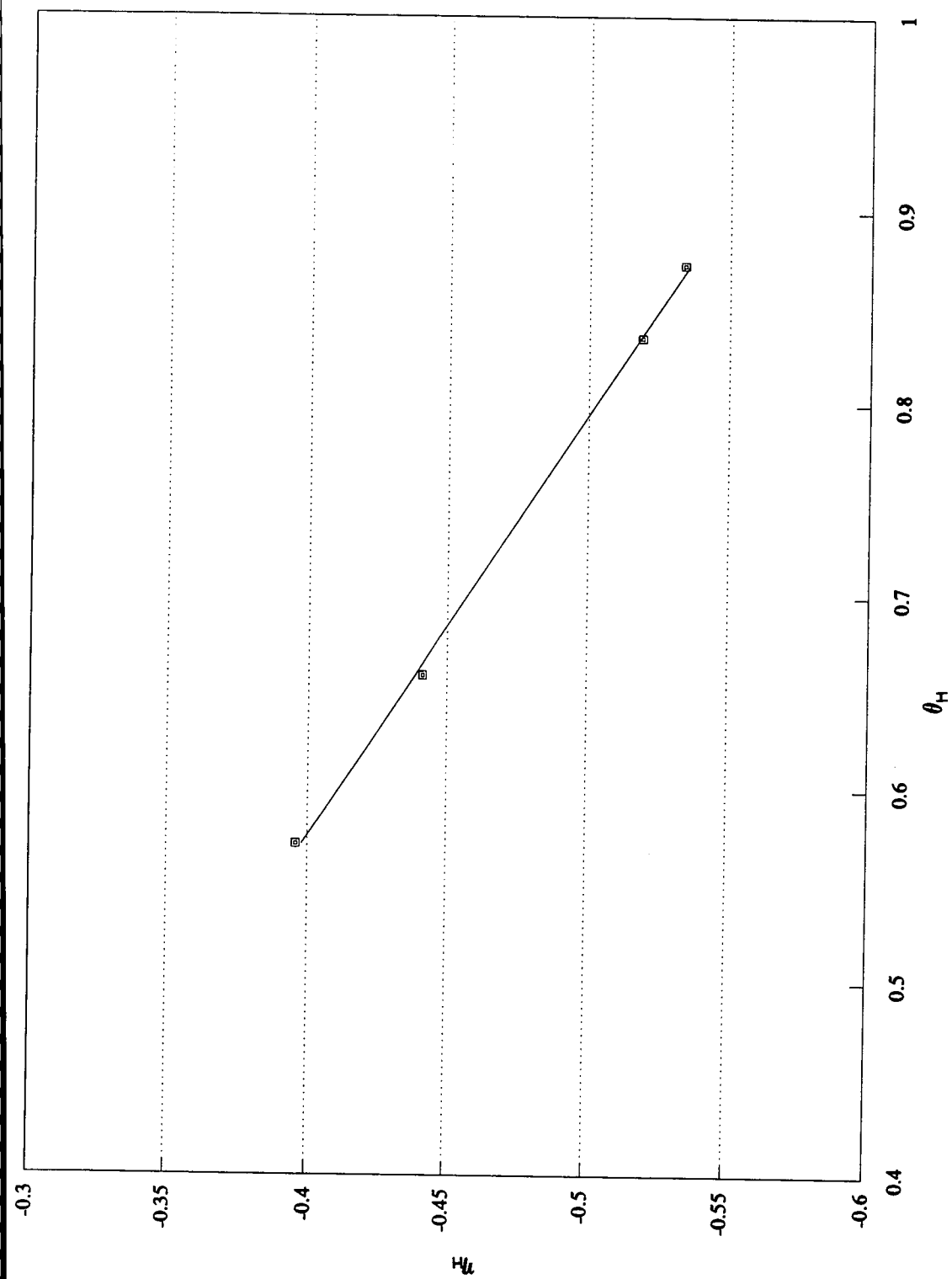
Figure 46. Surface Hydrogen Coverage Against Hydrogen Over-voltage.

147
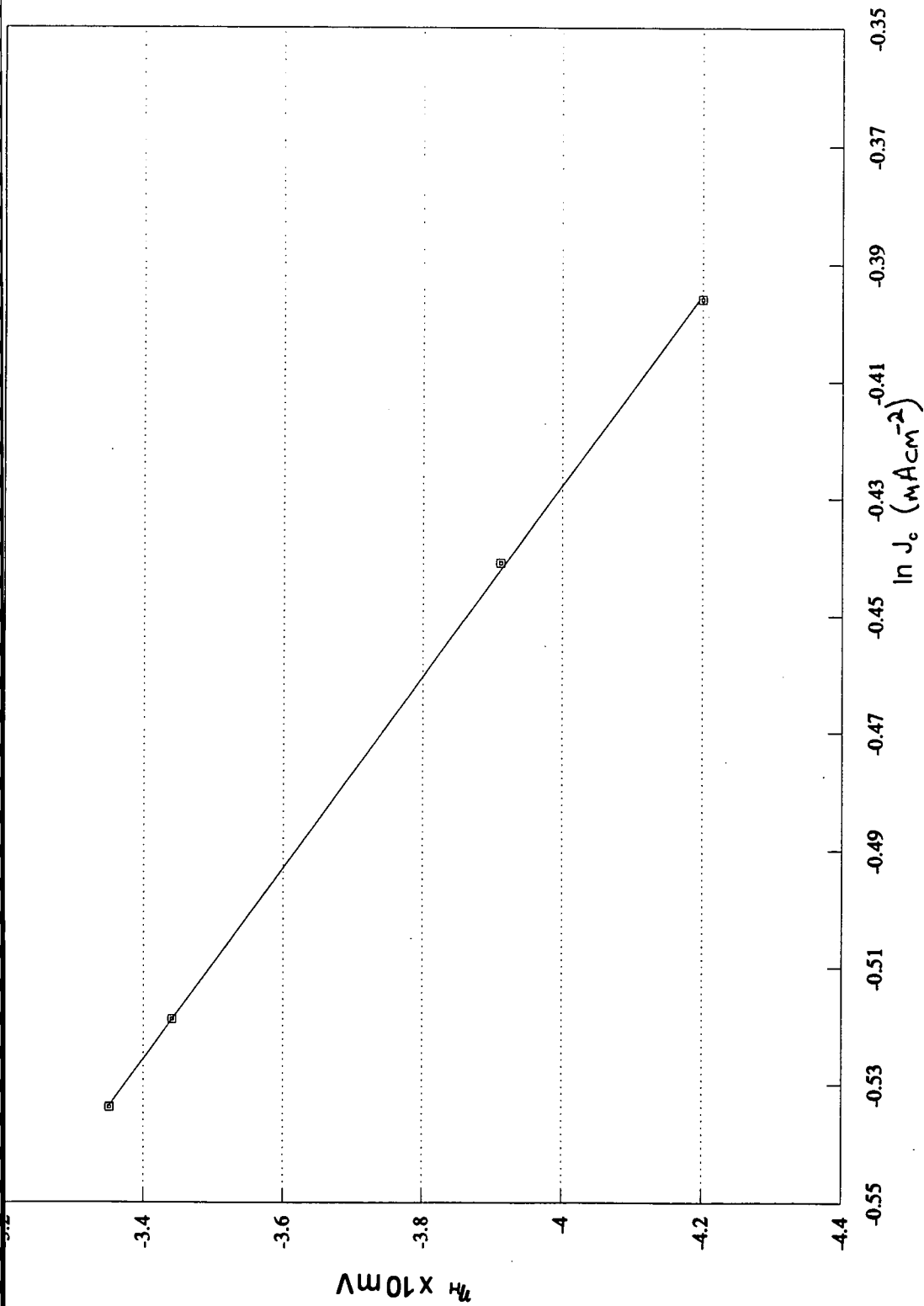
Figure 47.   Natural Logarithm of Charging Current Against Hydrogen Over-voltage to Calculate the Hydrogen Transfer Coefficient on Steel.

148

Table 14   Parameters for the Evaluation of the Kinetics of Hydrogen Absorption into Steel.

Current Density I_c (Acm^{-2} x 10^{-3})	Steady State Permeation Current I_∞ (Acm^{-2} x 10-^{6})	Steady State Potential /Volts (NHE)	Over-potential η (E^{eq}-E^0) /Volts
15	2.09	-0.67	-0.40
20	2.95	-0.72	-0.44
32	4.37	-0.79	-0.52
35	4.85	-0.81	-0.53

Table 15   Calculated Coefficients for the Coupled Discharge Mechanism.

Coefficient	Value
D	3.0×10^{-6} cm^{2}s^{-1}
L	5.5×10^{-3} cm
b	1.9 mole (Acm)$^{-1}$
α	0.316
a	19.4 V^{-1} at 25 °C
$I_0 \propto I_0'$	1.38×10^{-3} Acm^{-2}
K_1 {K_{abs}}	1.43×10^{-8} mole (cm^{2}s)$^{-1}$
K_3 {K_{des}}	2.2×10^{-4} mole (cm^{2}s)$^{-1}$
K^1	3.64×10^{-4} mole cm^{-3}
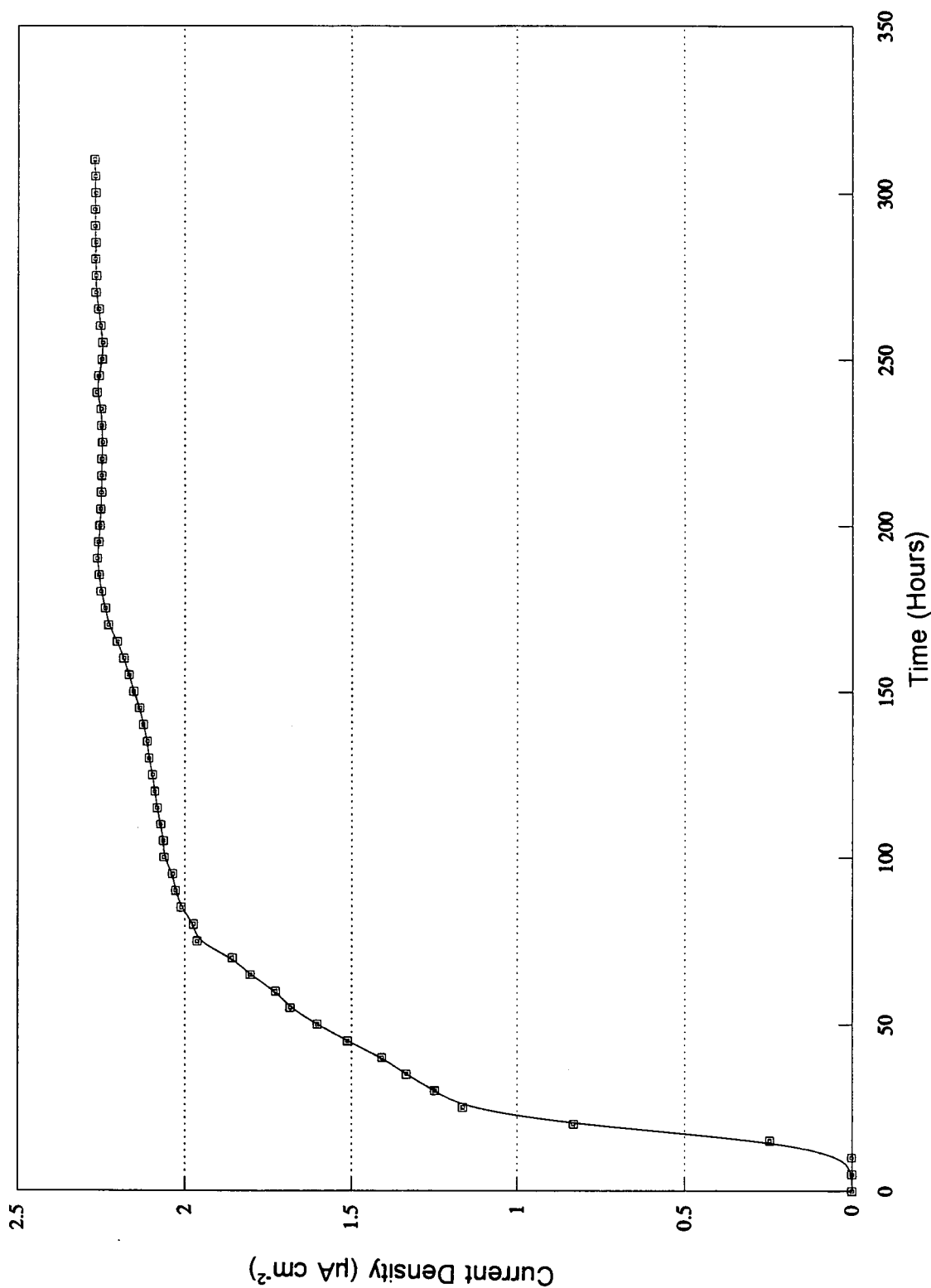
Figure 48.   Current-Time Transients for the 5 mm Thick BS Z25 Plate, Experiment 1.

150
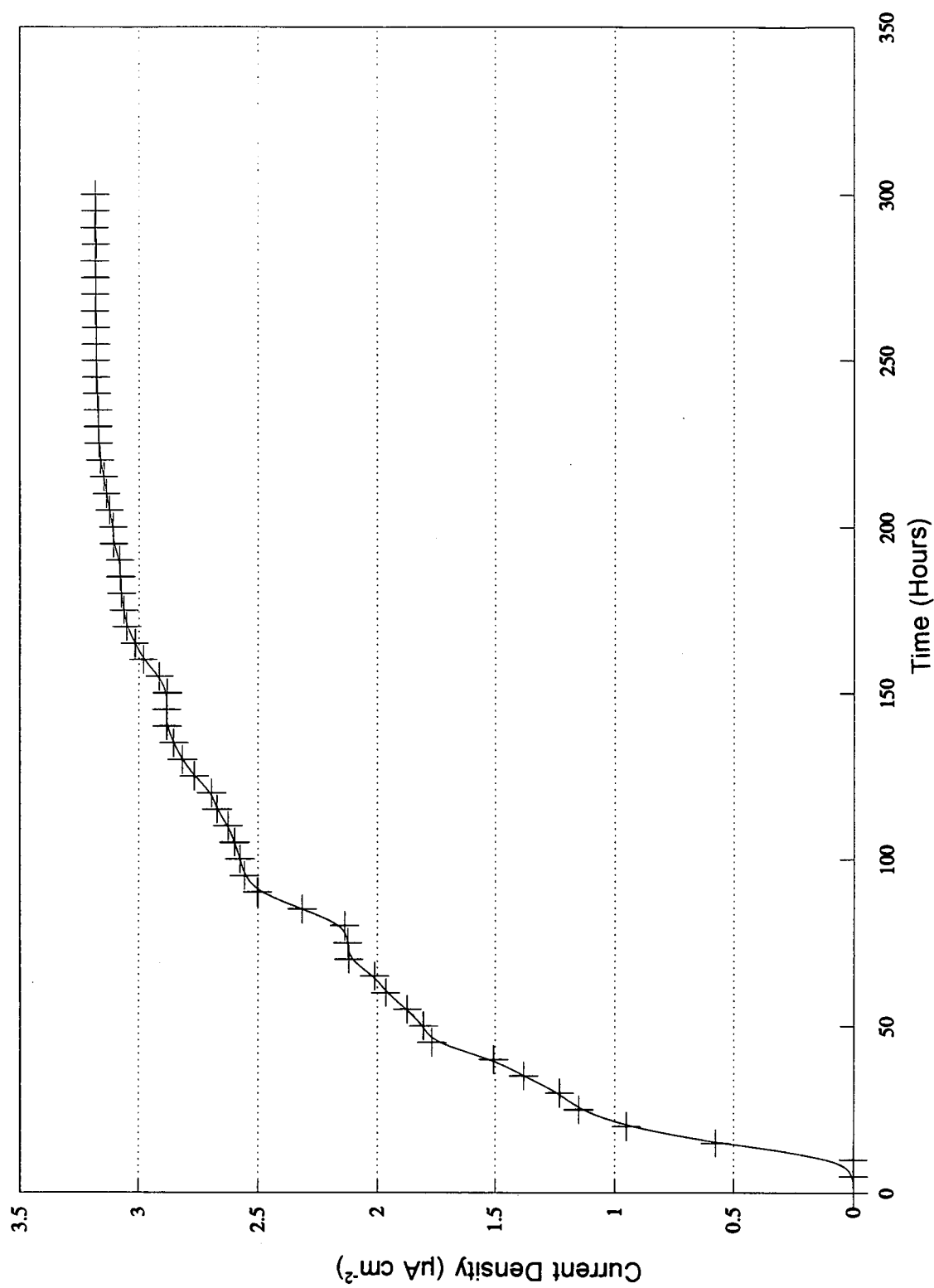
Figure 49.   Current-Time Transient for the 5 mm Thick BS Z25 Plate., Experiment 2.

151

$$\int \left[\frac{J_t - J_0}{J_\infty - J_0} \right]$$

Time (Hours)
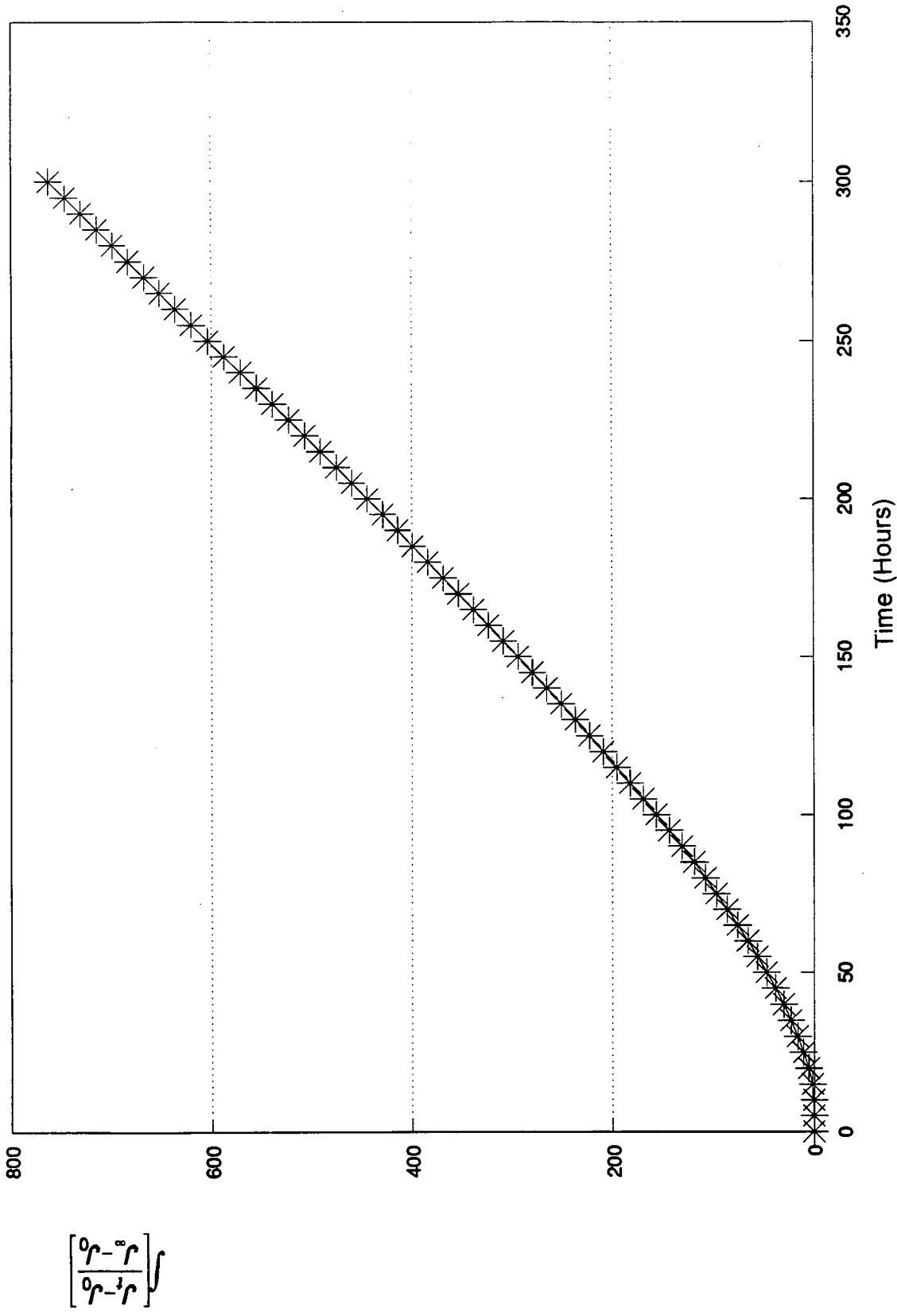
Figure 50.   Plot to Determine Time-Lag Characteristics of the 5 mm BS Z25 Plate, Experiment 1.

152

$$\int \left[\frac{J_t - J_0}{J_\infty - J_0} \right]$$

Time (Hours)
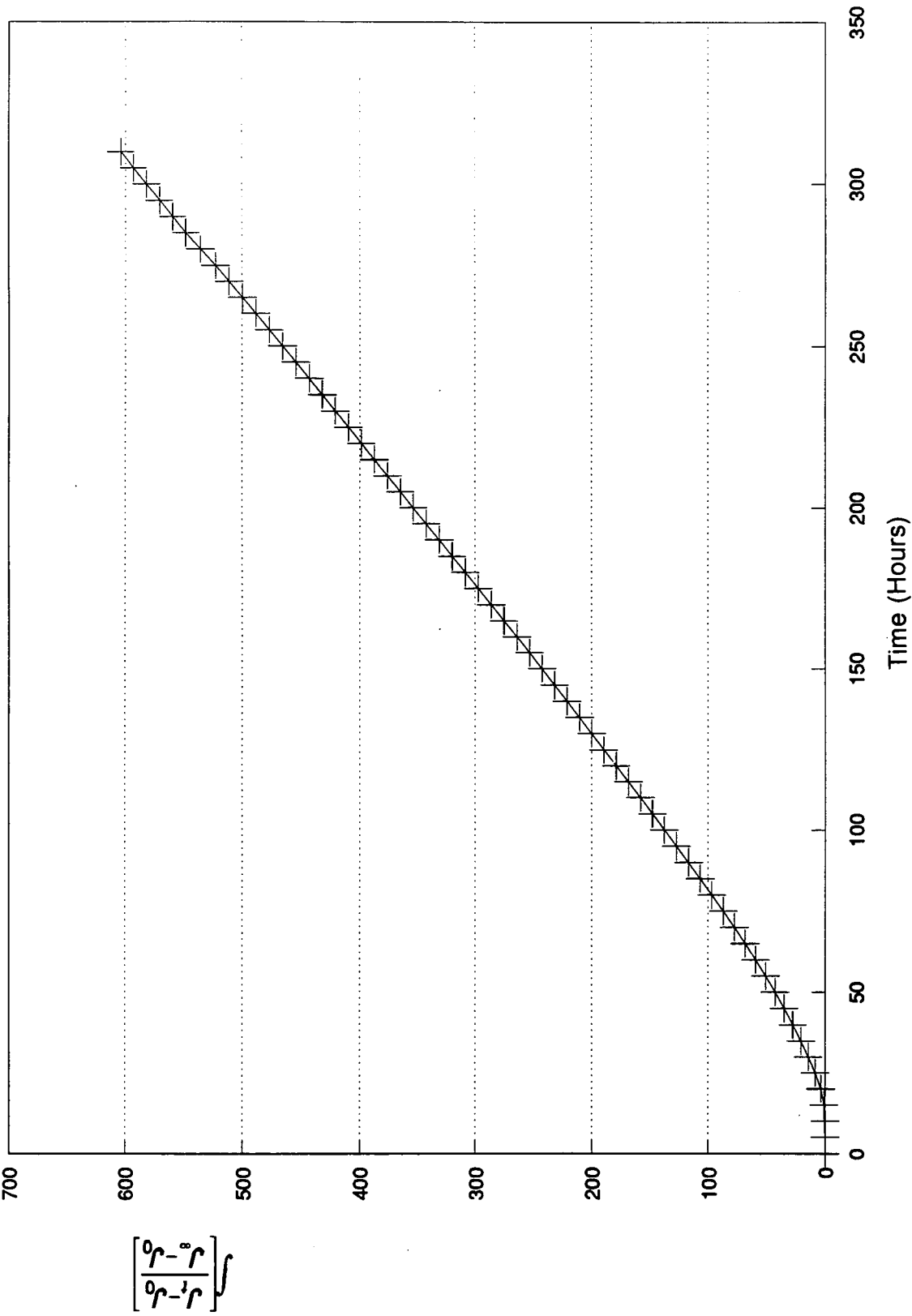
Figure 51. Plot to Determine Time-Lag Characteristics of the 5 mm BS Z25 Plate, Experiment 2.

153
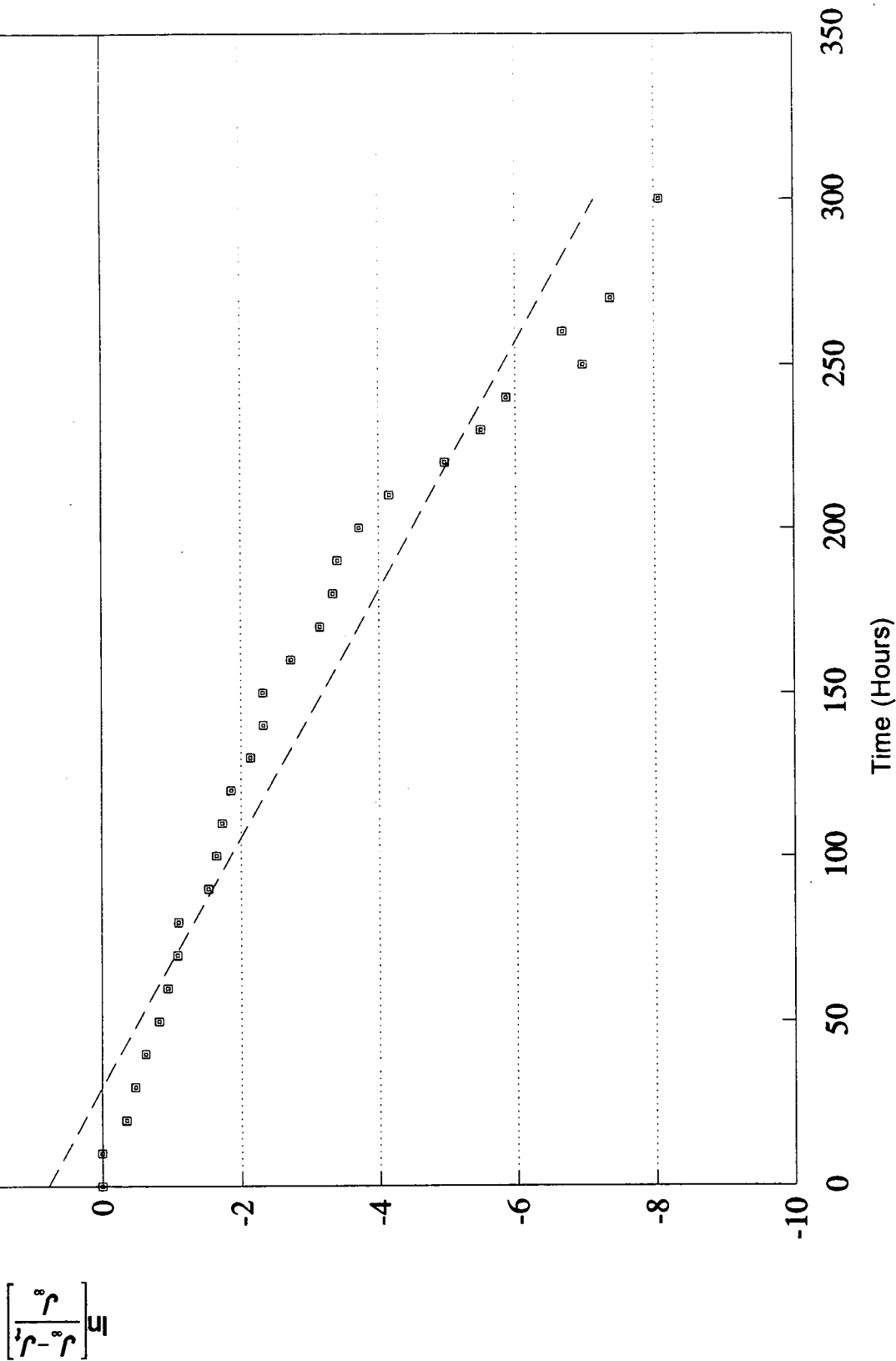
Figure 52. Plot to Determine Time-Constant (t_0) Characteristics of the 5 mm BS Z25 Plate, Experiment 1.

154
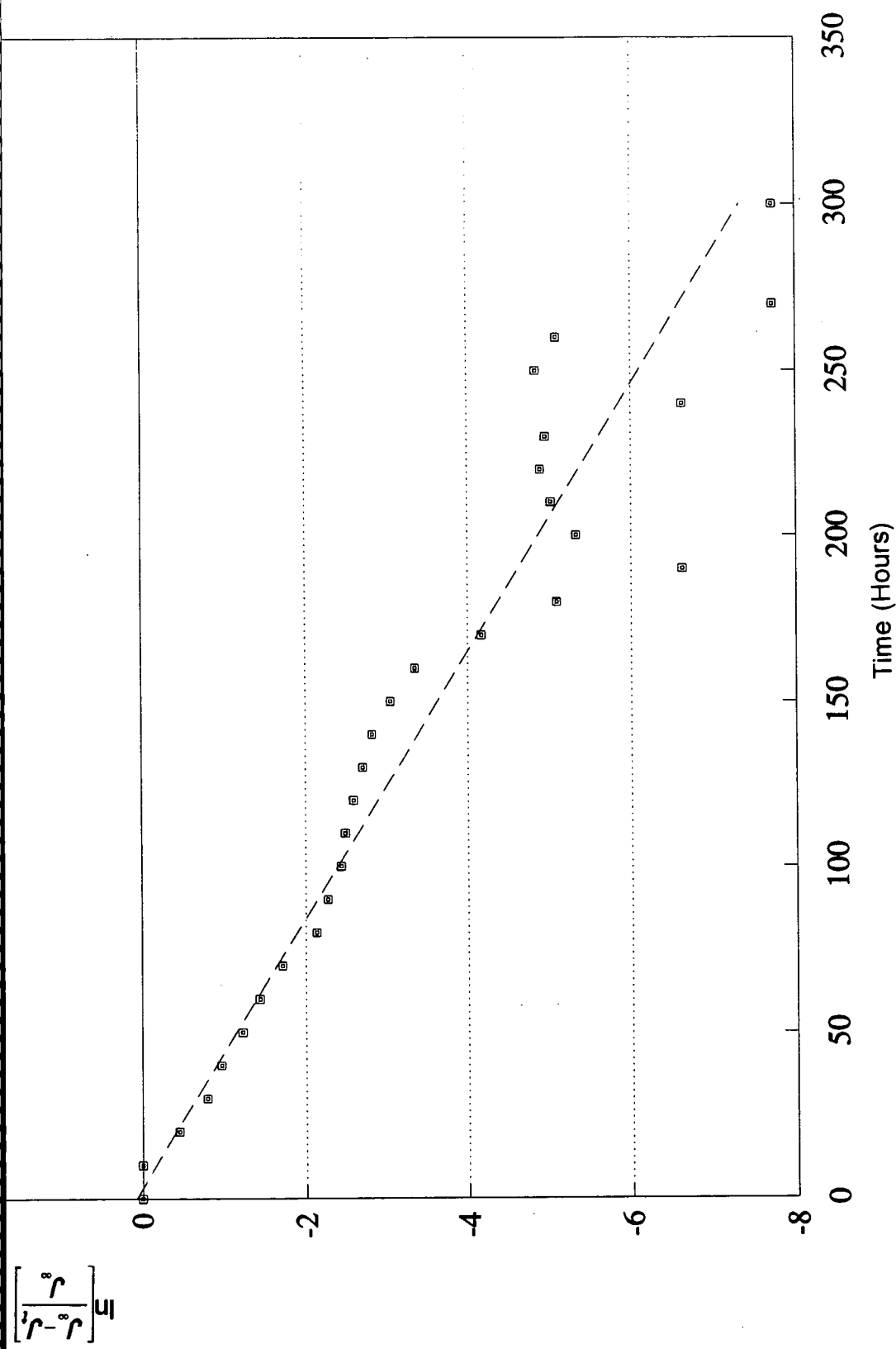
Figure 53. Plot to Determine Time-Constant (t_0) Characteristics of the 5 mm BS Z25 Plate, Experiment 1.

155

Table 16   Various Time Parameters Obtained From the Permeation Curves
for the BS Z25 Material.

Time Parameter	Experiment 1 (minutes)	Experiment 2 (minutes)
t_{lag}	40.8	57.8
t_b	13.0	14.8
$t_{1/2}$	82.4	117.5
t_0	40.5	37.9
t_i	7.41	9.26

4.8   Interpretation of Permeation Transients Using Models With Different Initial and Boundary Conditions.

Data obtained from the permeation transients, shown in Figures 48 and 49 for the BS Z25 material were used to compare possible values for the apparent diffusion coefficient. This would enable identification of the most appropriate model to be used when describing the experimental transients. A summary of the findings is given in Table 17.

4.9   Gel-Filled Hydrogen Probe Measurements on the Influx and Efflux Surfaces of a Steel Plate.

Figures 54 and 55 show replicate experiments performed to investigate the relationship between surface hydrogen concentration and time on both the charged and exit surfaces of a 5 mm BS Z25 plate during cathodic hydrogen charging. The graph shows that in the absence of continuous depletion of hydrogen from the exit surface, the surface hydrogen concentration on the efflux side apparently builds up to a value approaching that on the input surface.
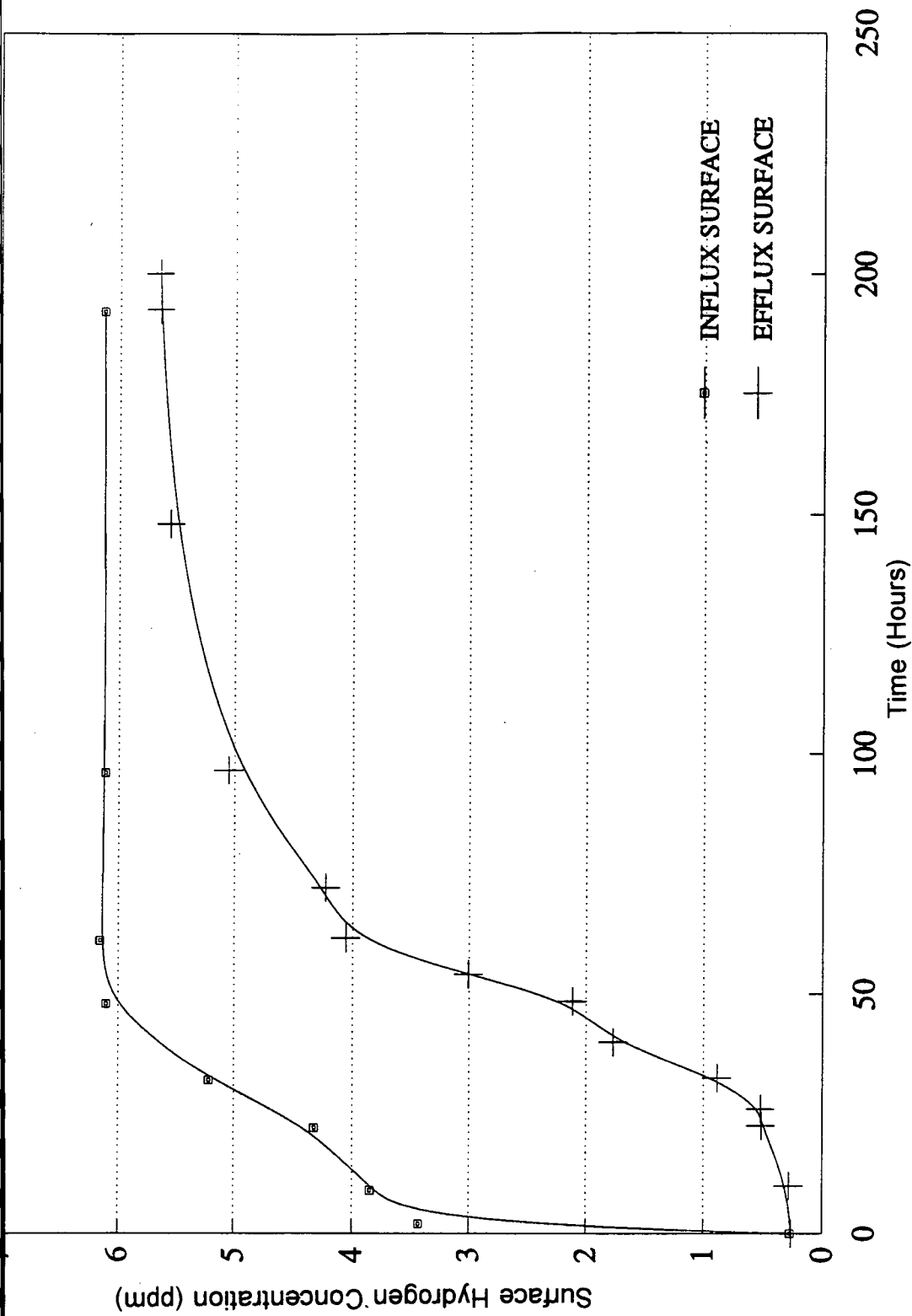
Figure 54. Gel-Filled Probe Measurements Taken on Both Sides of the 5 mm Steel Plate During Cathodic Charging Experiment 1.

157
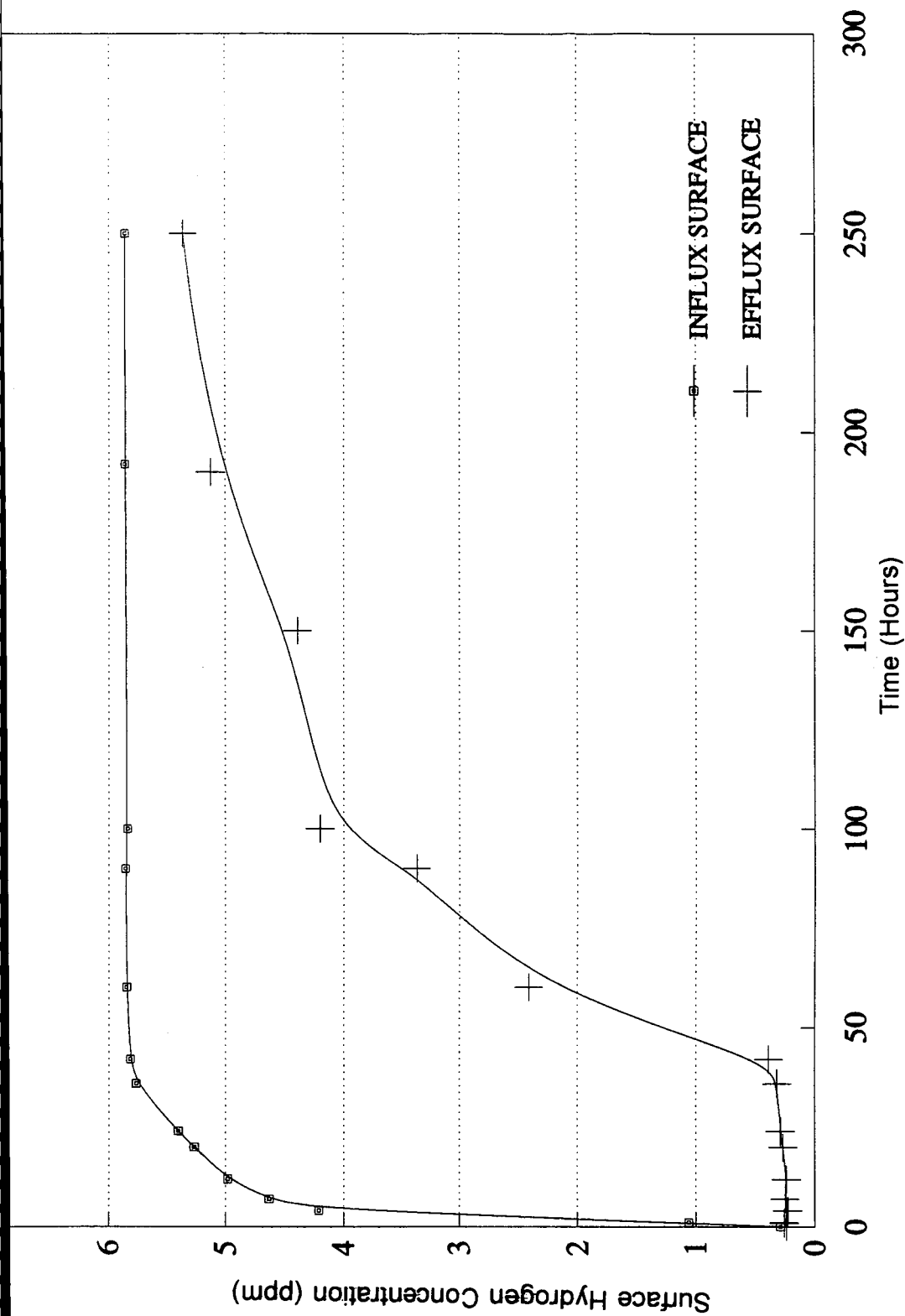
Figure 55. Gel-Filled Probe Measurements Taken on Both Sides of the 5 mm Steel Plate During Cathodic Charging. Experiment 2.

158

Table 17   Comparison of Data Using Three Different Sets of Initial and Boundary Conditions.

Model	Experiment	D From t_{lag} $(cm^2s^{-1} \times 10^{-7})$	D From t_0 $(cm^2s^{-1} \times 10^{-7})$
Constant Surface Concentration	1	3.16	1.94
	2	2.23	2.07
Constant Flux	1	7.69	76.5
	2	5.43	81.7
Constant Surface Coverage	1	----	2.49
	2	----	2.66

In both experiments a conventional permeation cell was used to compare the response of the gel-filled hydrogen probe. The permeation transients from the glass cell are shown collectively in Figure 56. The potential at the influx face was also monitored during the experiments and this is shown over a 300 hour period in Figure 57.

4.10   Determination of Hydrogen Concentrations by a Volumetric Method.

In order to qualify the observations from the gel-filled hydrogen probe readings on the influx and efflux surfaces, a definitive experiment was performed in which the hydrogen evolved from the exit surface, in the absence of an applied potential, was monitored. The volumes of hydrogen collected in the duplicate charging experiments, together with the measurements from the electrochemical permeation cell, are shown in Table 18. The low volumes of hydrogen observed were attributed to a rise in surface hydrogen concentration at the efflux surface, observed with the gel-filled hydrogen probe and the possible presence of a natural barrier to hydrogen effusion from the exit side.
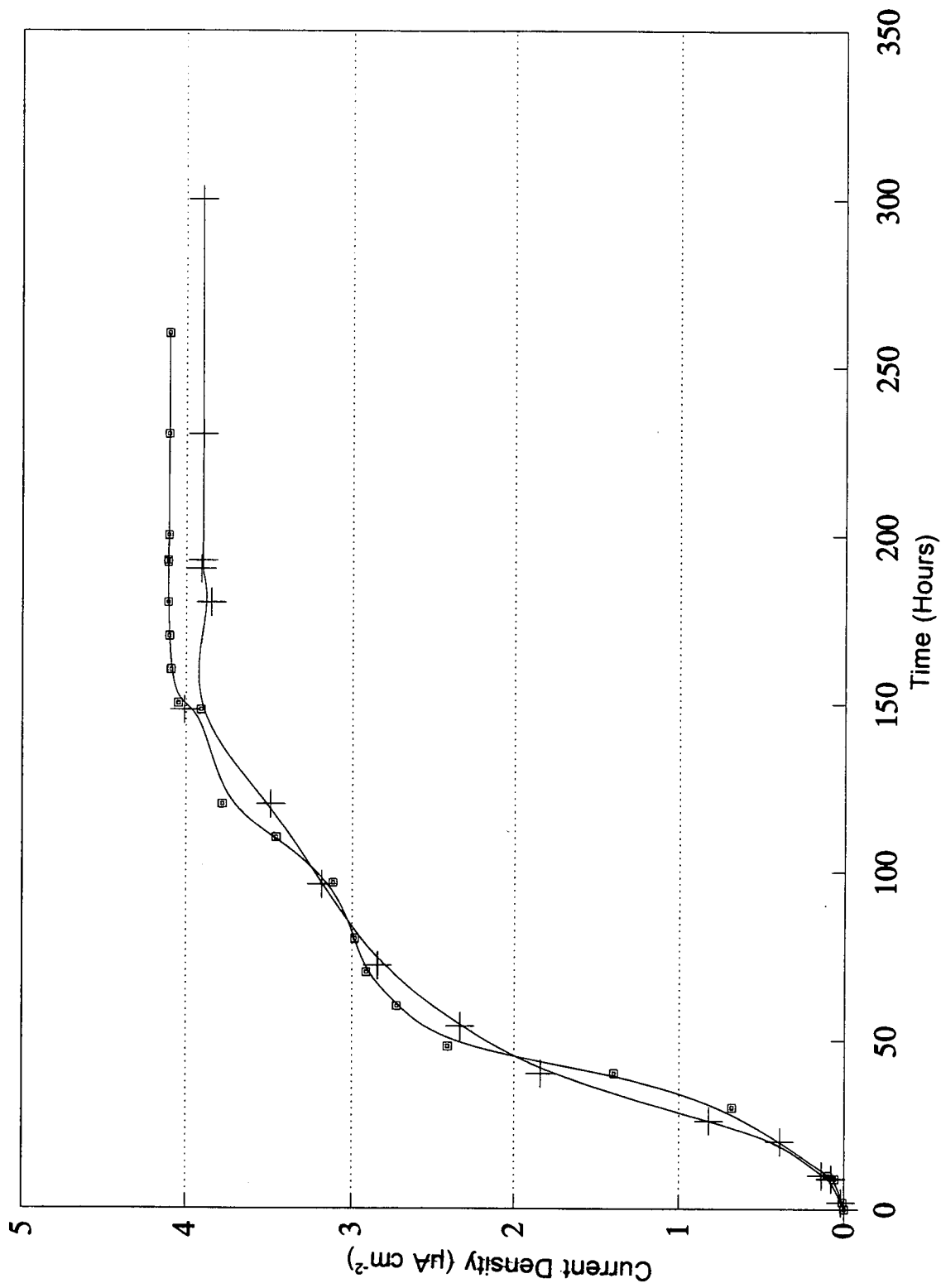
Figure 56.   Hydrogen Permeation Transients Recorded Using the Electrochemical Permeation Cell.

160
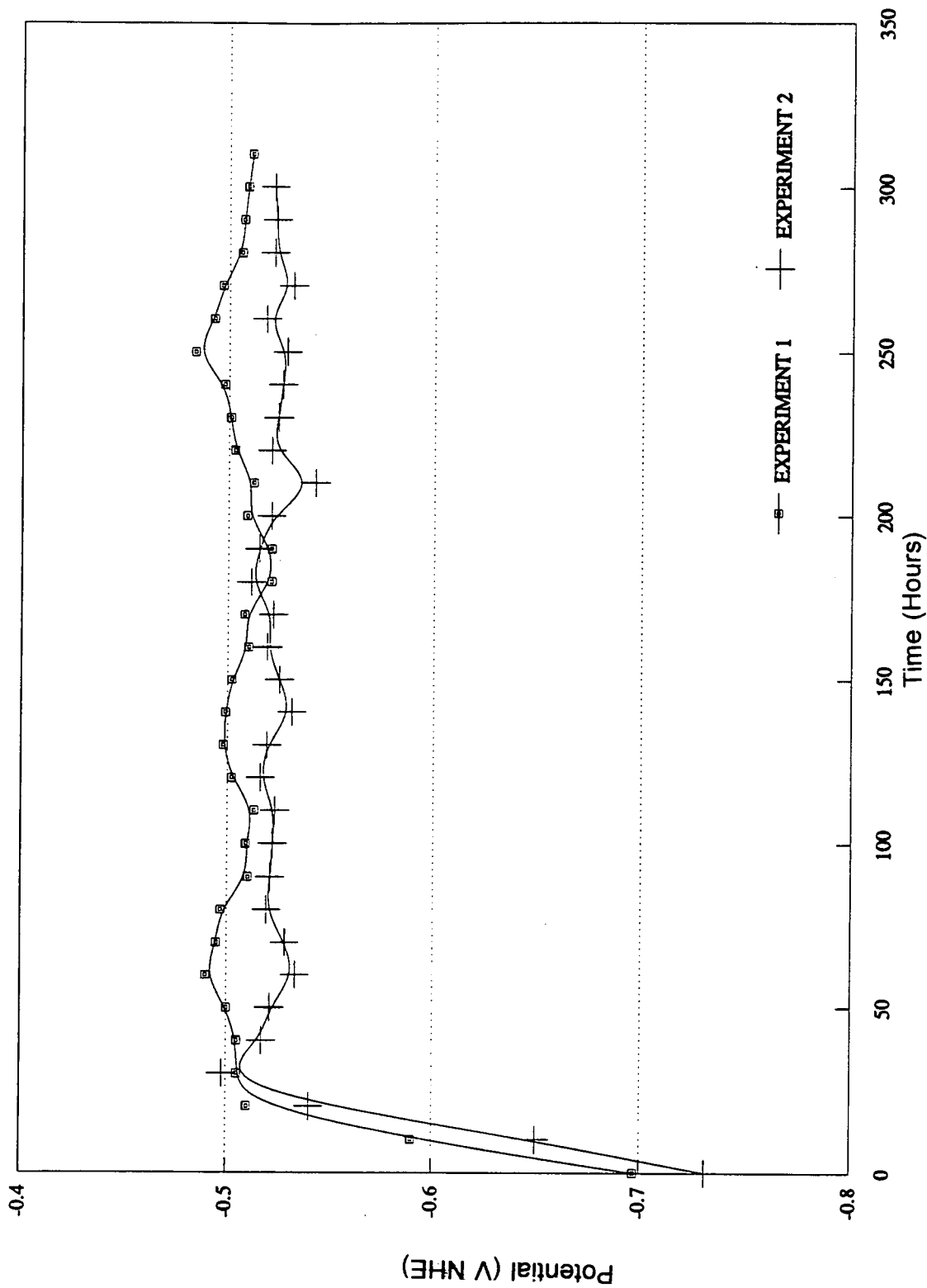
Figure 57. Potential at the Input Surface of the BS Z25 Plate During Cathodic Hydrogen Charging.

161

Table 18. Results of Volumetric and Electrochemical Permeation Measurements on 1 mm Steel Plate.

	Experiment 1	Experiment 2
Breakthrough Time (t_b)	25.2 minutes	27.9 minutes
Diffusion Coefficient D	4.32×10^{-7} cm^{2}s^{-1}	3.9×10^{-7} cm^{2}s^{-1}
Steady State Current J_∞	15.4 µA cm^{-2}	17.4 µA cm^{-2}
Surface Hydrogen Concentration C_0	4.68 ppm	5.85 ppm
Theoretical Maximum Volume of Hydrogen	0.158 ml cm^{-2} day^{-1}	0.177 ml cm^{-2} day^{-1}
Volume of Hydrogen Collected Over Silicone Fluid.	6.57×10^{-4} ml cm^{-2} day^{-1}	2.47×10^{-3} ml cm^{-2} day^{-1}
Percentage of Theoretical Maximum Volume.	0.57%	1.7%

4.11 Repeated Charging Experiments to Determine the Effect of Trapping on the Permeation of Hydrogen.

Figures 58 to 63 inclusive, show the result of potentiostatically controlled, repeated charging experiments on the BS Z25 and NAM plate materials. The steady state permeation current, corresponding surface hydrogen concentration and diffusion coefficients calculated from these experiments are summarised in Tables 19 and 20 for the BS Z25 and NAM plates respectively. The higher susceptibility of the NAM plate to hydrogen damage and the larger number of inclusions distributed inhomogeneously throughout the plate resulted in transients which deviated slightly from Fickian behaviour. This

162

manifested itself in a lowering of the steady state permeation current with respect to time. The BS Z25 plate, however, appeared to be a "cleaner" steel, which resulted in permeation transients conforming more closely to Fickian behaviour.
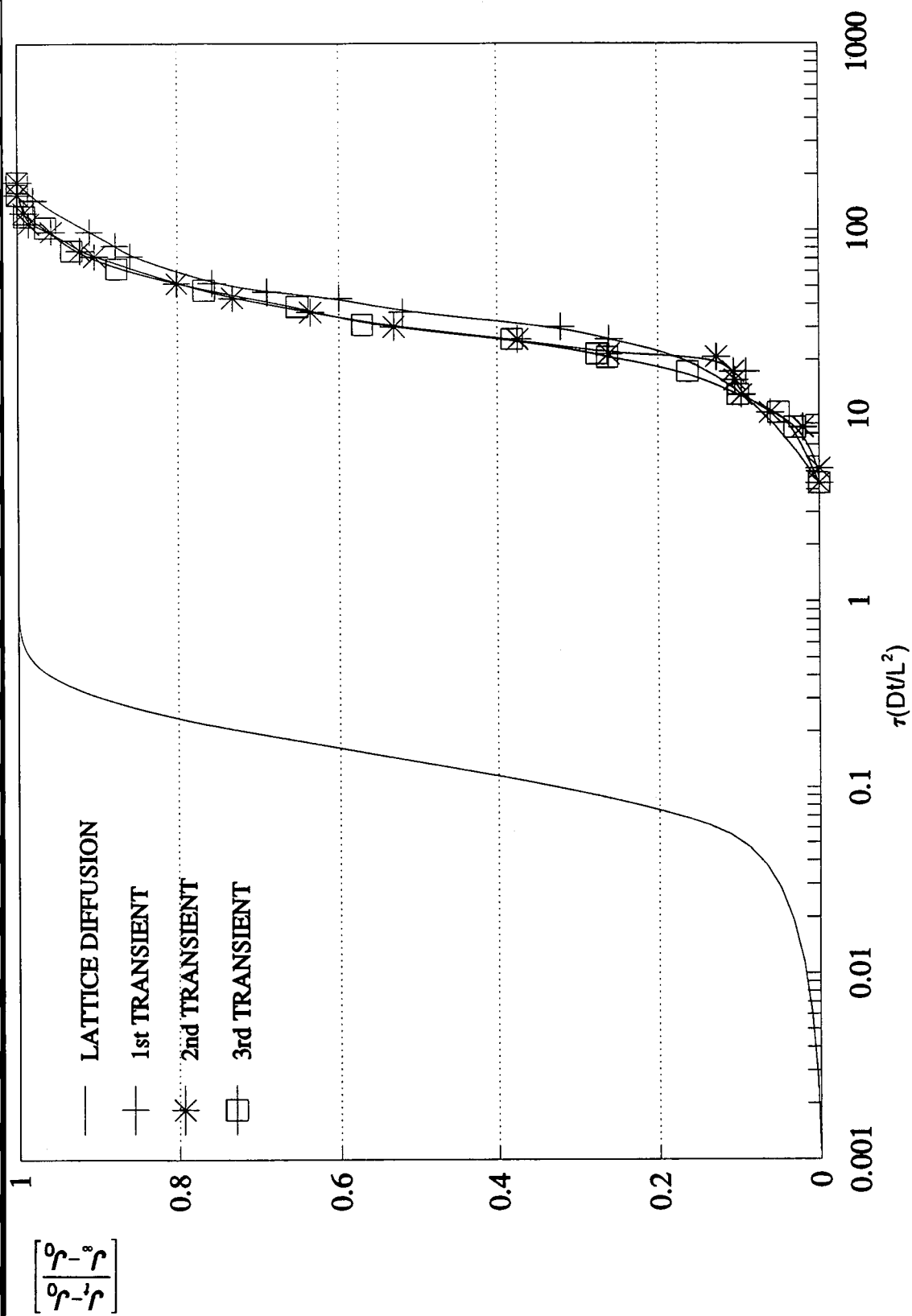
Figure 58. Rising Permeation Transient on Normalised Axis For BS Z25 Plate Experiment 1.

164
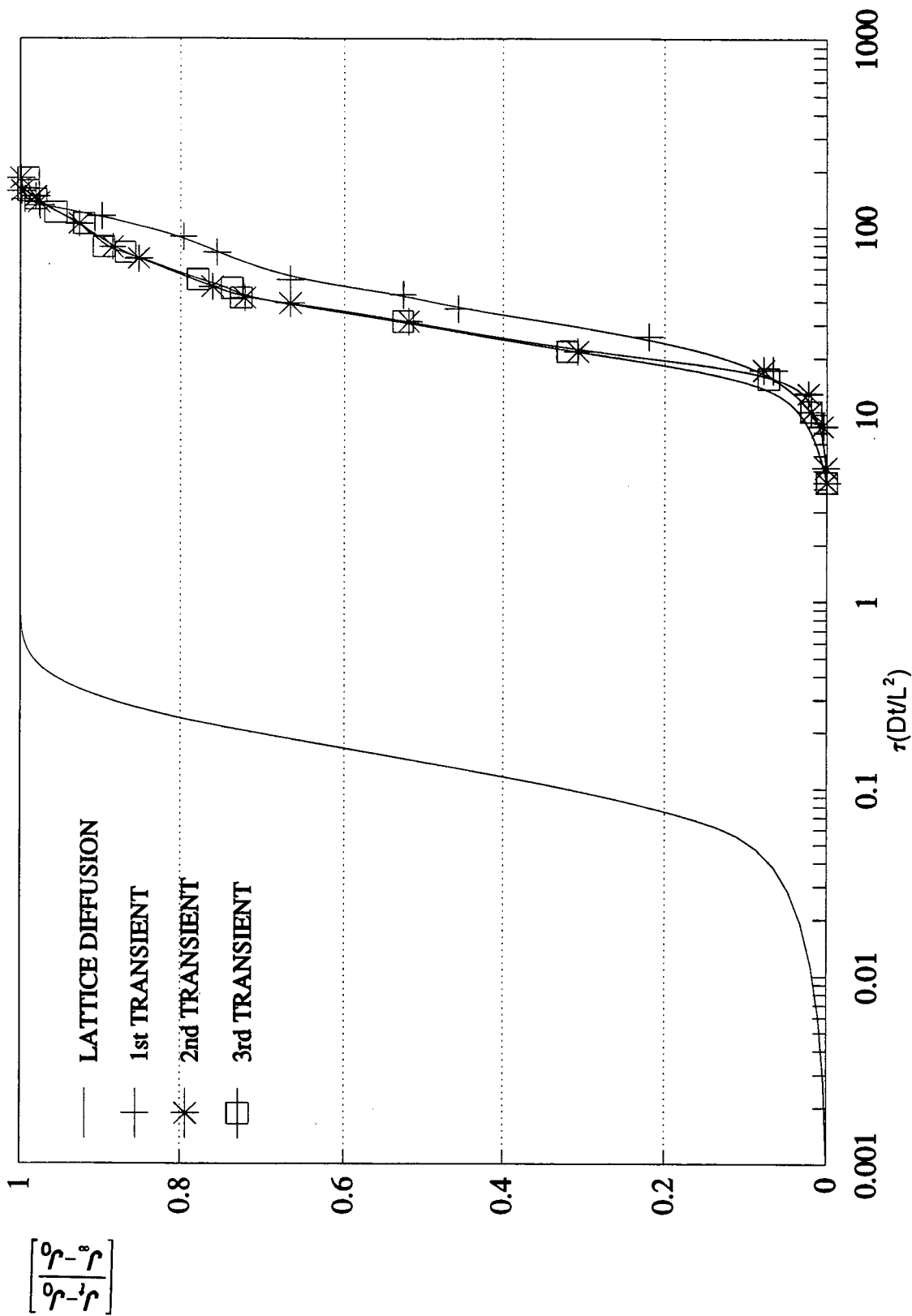
Figure 59.   Rising Permeation Transient on Normalised Axis For BS Z25 Plate Experiment 2.

165
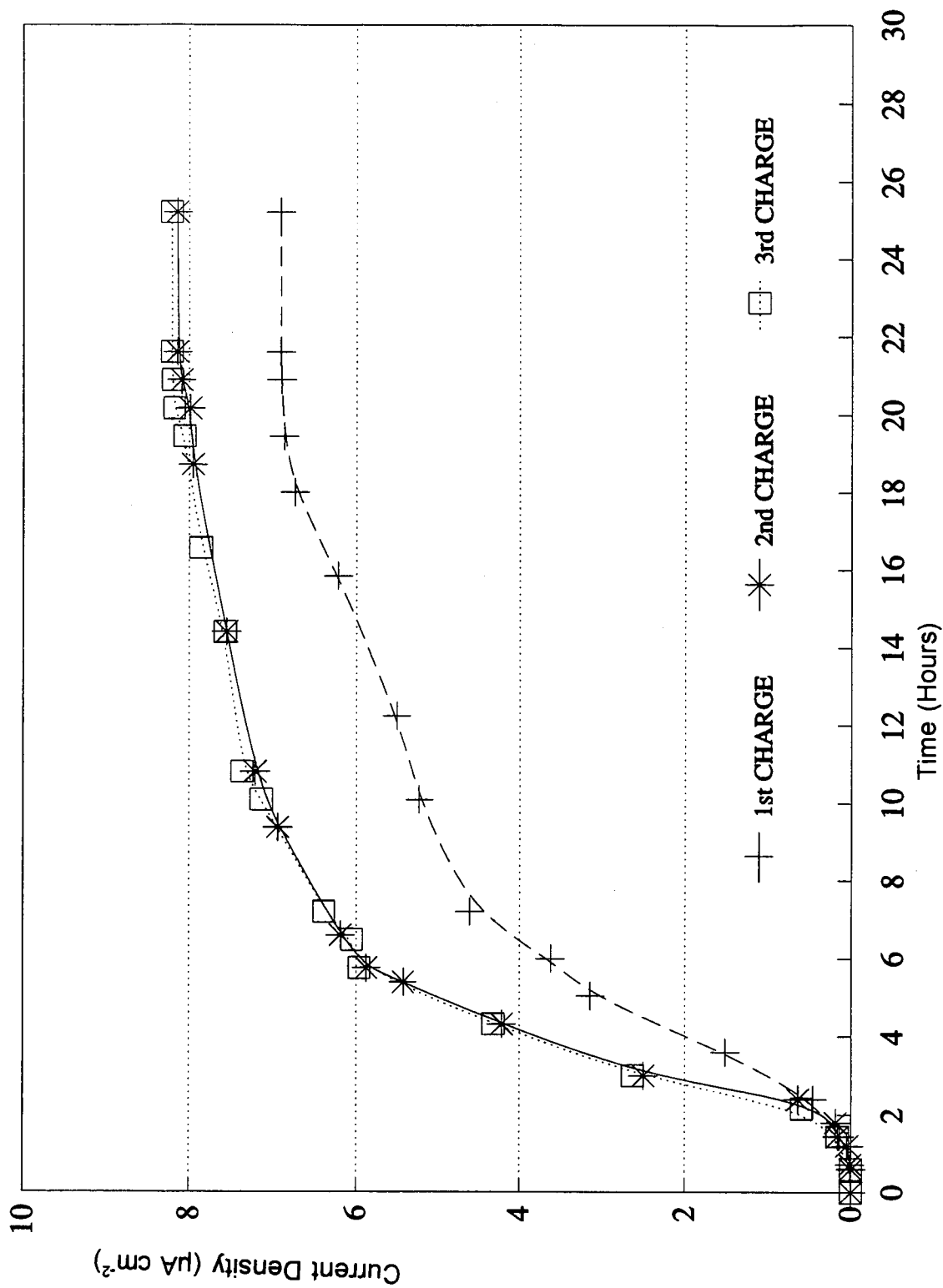
Figure 60.   Rising Permeation Transients For BS Z25 Plate.

166

$$\left[\frac{J_t - J_0}{J_\infty - J_0}\right]$$

LATTICE DIFFUSION
1st TRANSIENT
2nd TRANSIENT
3rd TRANSIENT
4th TRANSIENT

$\tau (Dt/L^2)$
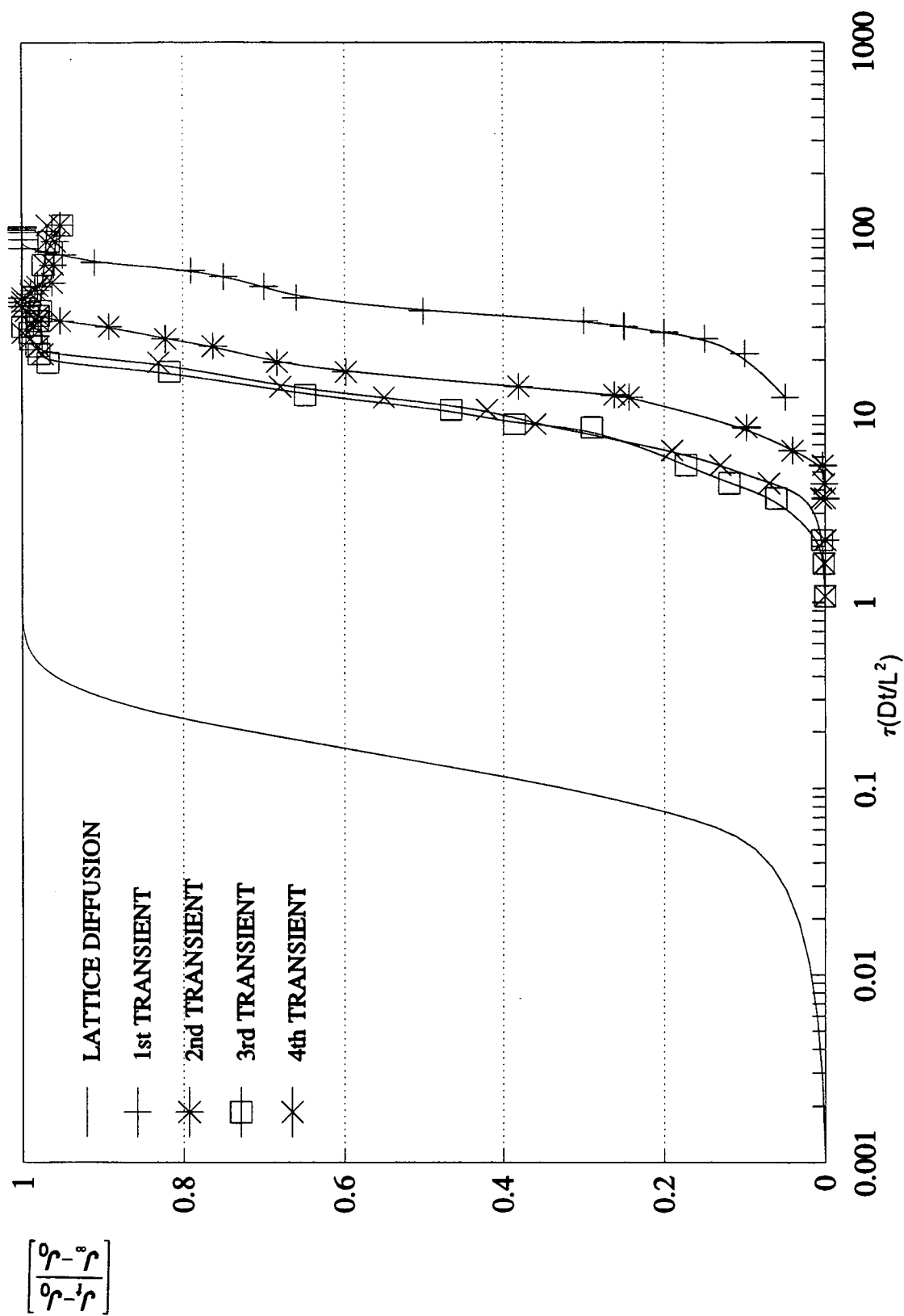
Figure 61.   Rising Permeation Transient on Normalised Axis For NAM Plate Experiment 1.

167
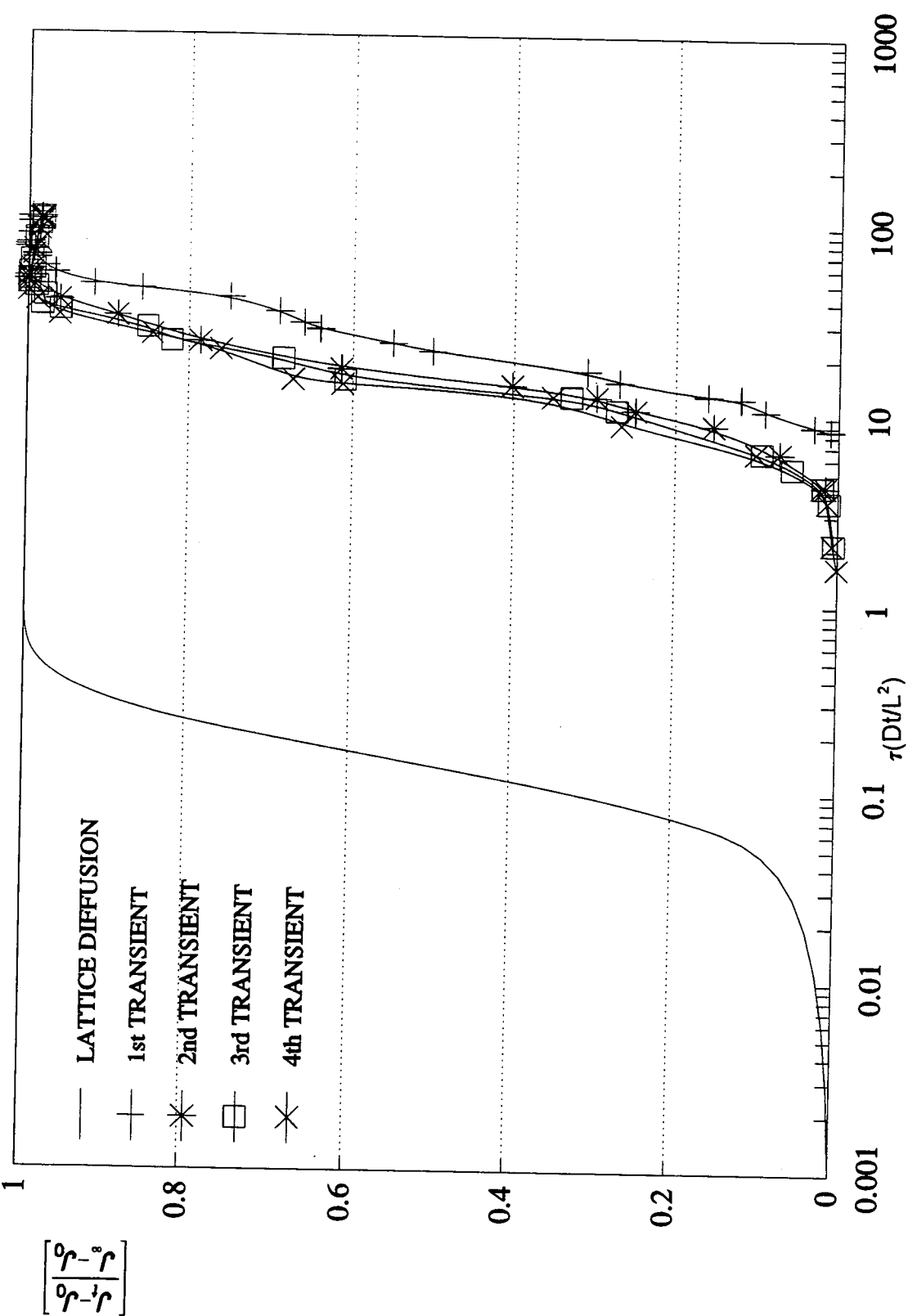
Figure 62.   Rising Permeation Transient on Normalised Axis For NAM Plate Experiment 2.

168
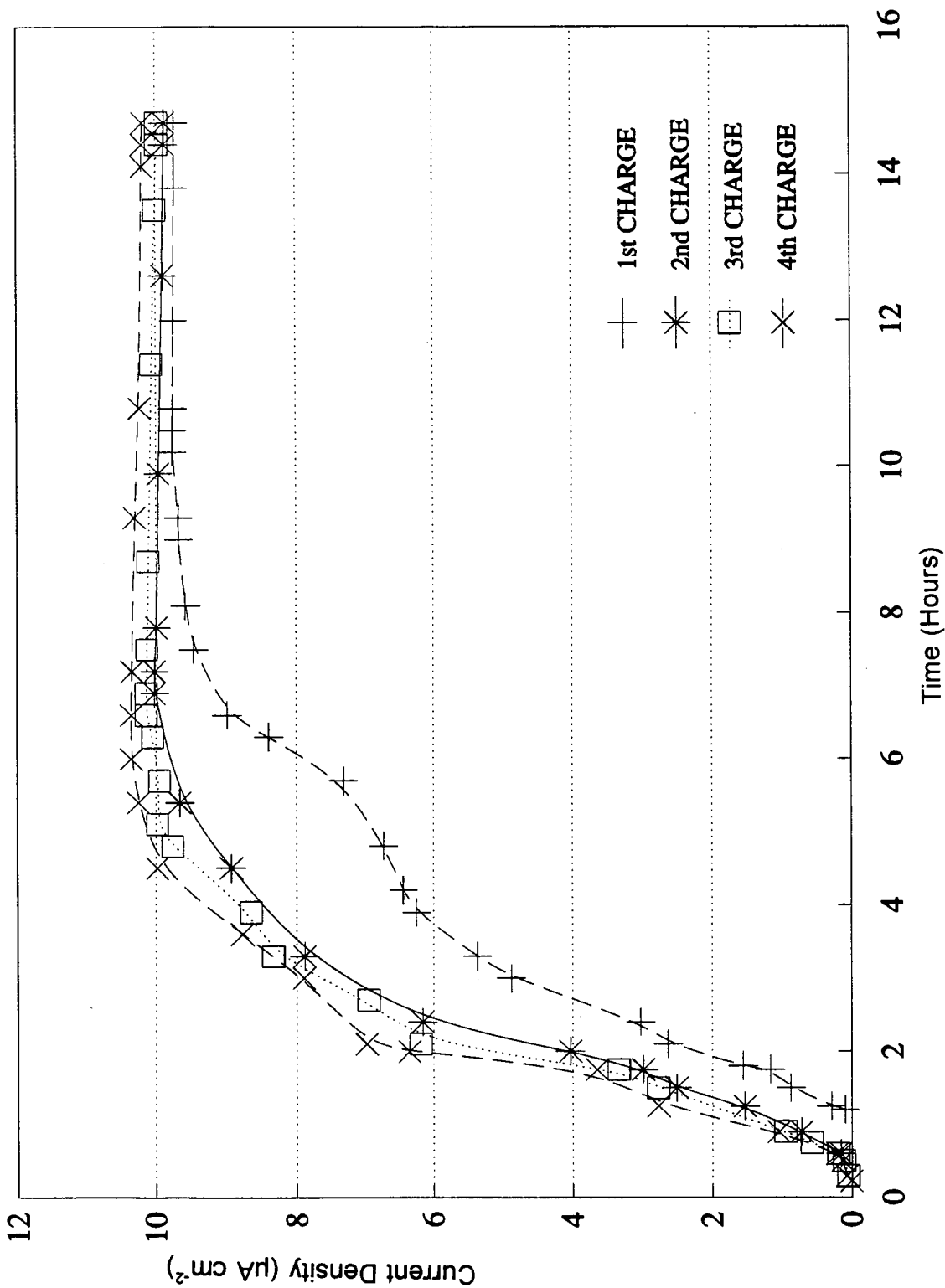
Figure 63.   Rising Permeation Transients For NAM Plate.

169

Table 19   **Results of Repeated Charging Experiments for the BS Z25 Plate.**

Experiment	BS Z25 Plate			
	J_∞ (μA cm^{-2})	C_0 (ppm)	t_b (seconds)	D (cm^{-2}s^{-1} x 10^{-7})
1A	6.33	1.97	1550	4.22
2A	8.24	1.71	1035	6.32
3A	7.69	1.53	986	6.6
1B	6.91	1.77	1280	5.11
2B	8.14	0.72	435	15
3B	8.21	0.68	411	16

Table 20   **Results of Repeated Charging Experiments for the NAM Plate.**

Experiment	NAM Plate			
	J_∞ (μA cm^{-2})	C_0 (ppm)	t_b (seconds)	D (cm^{-2}s^{-1} x 10^{-7})
1A	17.2	2.51	1533	4.27
2A	11.1	1.6	719	9.09
3A	12.7	0.57	222	2.94
4A	15.3	0.62	201	32.5
1B	9.76	2.21	1131	5.7
2B	10.03	1.17	582	11.2
3B	10.15	0.75	367	17.8
4B	10.37	0.75	359	18.2

4.12 Microstructural Hydrogen Damage.

Scanning Electron Microscopy and optical microscopy were utilised in an attempt to characterise the extent and nature of hydrogen induced damage in the NAM material. The NAM plate was chosen for its apparent susceptibility towards hydrogen damage. Samples were sectioned from the preliminary charging experiments and prepared according to section 3.9. For convenience and clarity, the resulting micrographs are reported later in section 5.14 of the Discussion.

The extent of damage observed in the NAM plate was somewhat less than expected. However, despite the apparent abundance of potential sites for hydrogen damage in the material, it is thought that this particular material was less susceptible to hydrogen induced cracking than was previously estimated for the chosen charging conditions.

5.0 DISCUSSION.

5.1 Selection of Auxiliary Electrodes.

The gel-filled hydrogen probe operates on the principle of holding a steel surface (under a given electrolyte) at a potential suitable to oxidise atomic hydrogen leaving that steel surface. This oxidation current is described by:

$$H \rightarrow H^+ + e^- \qquad [20]$$

The magnitude of the measured current is proportional to the hydrogen concentration just below the steel surface.

Devanathan and Stachurski[36] were the first investigators in this field to suggest the use of a nickel/nickel oxide electrode as a suitable auxiliary electrode to facilitate the cathodic reaction in the driven electrochemical cell. It was reported[36] that the nickel/nickel oxide electrode would maintain a potential of approximately 0 volts on the standard hydrogen scale in 0.2M NaOH. Devanathan and Stachurski utilised a sintered nickel plaque electrode obtained from the interior of a standard nickel/cadmium cell. During investigations using the gel-filled hydrogen probe, the use of such an electrode was impracticable due to the probe's construction. The sintered nickel plaque tended to be brittle and flake-like, which was prone to break up during the probe's normal operation. Consequently attempts were made to reproduce such an electrode by anodising a piece of poly-crystalline nickel foil in 10% sulphuric acid. Subsequent determinations using the arrangement cast some doubt as to the electrode's stability under the conditions dictated by the probe's alkaline electrolyte. In the light of this a series of experiments were designed to select the most suitable form of auxiliary electrode for the probe.

Macdougall, Mitchell and Graham[133] showed in their work that the film thickness produced during anodizing was hardly influenced by anodic formation conditions. It was the defect characteristics, however, of the film which determined its stability and resistance to breakdown. The defect characteristics, porosity and consequently film thickness were strongly influenced by such variables as current density or applied potential, electrolyte composition and anodizing time.

Taking these factors into consideration, 7 electrodes were selected, including a blank, un-anodised nickel foil for comparison of surface topology and electrode potentials. A mercury/mercury oxide was selected as one of the electrodes, due to its suitability to the caustic environment of the gel-electrolyte. A sintered nickel plaque electrode was also selected and was extracted from a nickel/cadmium cell. The remaining 4 electrodes were constructed from the anodising solutions and conditions as shown in Table 10. Three of these electrodes were anodised for 1 hour under constant current conditions with a current density of 150 mAcm^{-2}. The fourth electrode was anodised under constant potential conditions as a result of examining the anodic polarisation data presented in Figure 31. Accordingly, a potential in excess of +1.5 V (NHE) would be sufficient to grow an oxide layer on the nickel foil.

In the case of electrode 2, it was suggested[133] that a 0.15M sodium sulphate solution would produce a thin oxide film of between 10 and 50 Å on the nickel foil under the conditions shown in Table 10. It was suggested that thicker films were not possible in this electrolyte due to the Ni^{3+} species being soluble in this solution. Electrode 3, anodised in a borate buffer solution of pH 7.61 allegedly enabled the growth of thicker films[133], expected to be around 120 Å under the conditions shown in Table 10. It was expected that this oxide film would not be compact, but instead would behave more like a porous oxide film with a large variation in the point to point mass of oxygen[133]. The thicker film

was expected to be in a higher oxidation state than that produced on electrode 2 with an atomic concentration of oxygen in excess of 50% of the total electrode surface area directly after anodizing. The most likely interpretation of this result was that NiOOH would be produced in the O_2 evolution region of the anodic polarization plot shown in Figure 31.

On examination of the current-potential profile for this nickel foil, shown in Figure 31, anodic polarization into the oxygen evolution region (1.50 V N.H.E.) would be sufficient to establish a relatively thick, porous oxide layer on the nickel substrate. Consequently electrode 4 was produced in such a manner. Initially, the anodic current increased exponentially with increasing potential as nickel dissolved according to the overall reaction:

$$Ni \rightarrow Ni^{2+} + 2e^- \qquad [21]$$
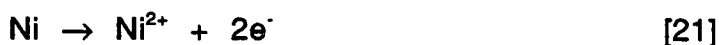
The current reached a maximum at approximately +0.3V and then decreased rapidly to a steady, low value which was maintained up to approximately +1.40V at which point it began to increase again as the potential entered the oxygen evolution region. The potential region where the surface was covered by a protective oxide film, i.e from approximately +0.60 to +1.40V, indicated the passive potential region. It was above this potential range and the resulting nature of the passive oxide film which was of interest.

Electrode 6 was taken from a standard nickel cadmium battery cell. This was chosen for the same reasoning as Berman, Beck, and DeLuccia[135] and Devanathan and Stachurski[36]. The electrodes were physically robust but tended to be brittle and the sintered nickel oxides were lost during vibration.

During the manufacture of such electrodes, porous nickel plaque is soaked in the nitrate of nickel or cadmium, formed with cathodic polarization in alkaline solutions, finally being washed and dried. A number of cycles of anodic and

cathodic polarization of the battery are then required to get the correct columbic capacity[136].

During the charging process, the active material of the positive plate is oxidised from the Ni^{2+} to the Ni^{3+} state, and the oxides of the negative plate are reduced to the free metal.

$$2NiOOH + Cd + 2H_2O \rightarrow 2Ni(OH)_2 + Cd(OH)_2 \qquad [22]$$

Under charge the cell reaction is the reverse. If any nickel is present in a higher oxidation state than 2, then it is less than 10% of the nickel present[137]. Analysis of the X-Ray patterns show that the Ni^{3+} oxide can be best described as $NiOOH$[138]. Glemser and Einerhand[139] showed that oxidation of $Ni(OH)_2$, $Ni(NO_3)_2$ or $NiSO_4$ with Br_2, $NaClO$ or $NaBrO_2$ would produce β-NiOOH.

Electrode 7 consisted of the blank, untreated nickel foil, included for comparison of topological features, molecular structure and variations in rest potential.

5.1.1 X-Ray Diffraction Analysis.

Plates 8 and 9 show the surface condition of the sintered nickel plaque at two distinct areas on the electrode surface. Plate 8 shows an area representing the bulk of the electrode surface, seen as a dark grey, ceramic finish, characteristic of a conducting oxide such as β-NiOOH[138]. At higher magnification, the surface appeared to consist of a flaky, plate like, inhomogeneous structure. The surface appeared to be very rough, with a high degree of inhomogeneity. Plate 9 shows an area representing a well defined, but narrow, band of lighter material extending, consistently, the length of the electrode. The band covered approximately 20% of the total electrode surface and lay parallel to the electrode edge. The chemical structure of this light

175

band, and that of the bulk material, appeared to be quite similar. There did, however, appear to be some minor visual differences. The lighter area, in comparison to the bulk material, appeared to have a greater abundance of smaller particles adhered to the surface. In both plates there were a large number of crevices and voids indicating a high degree of porosity.

Thin window light element analysis showed the two areas on the sintered nickel plaque electrode to have comparable oxygen levels, which compared with the other electrodes, were quite high. The two areas, dark and light, showed ratios of $Ni:O_2$ to be 1:0.29 and 1:0.24 respectively, as shown in Figure 33.

The XRD data, shown in Table 12, suggested that the sintered nickel plaque electrodes were comprised four main compounds. In addition to these peaks there are the expected peaks associated with elemental nickel. Allocation of these peaks was rather speculative, but the data obtained from XRD analysis suggested the presence of Ni^{II} oxide hydrate in a hexagonal close packed configuration ($Ni(OH)_2$); Beta-nickel oxide hydroxide, again in a hexagonal close packed configuration (ß-NiOOH); cadmium^{II} oxide (CdO) and lithium hydride (LiH).

Further evidence suggesting the presence of Cd was provided by S.E.M elemental analysis, shown in Figures 32(a) and 32(b) for electrodes 5 and 6 respectively. There appeared to be between 4 and 8% Cd in relation to total nickel content on the electrode surface (a ratio of Ni:Cd of 1:0.06 ± 0.02). Contamination of the electrode while in the Ni/Cd cell would be a probable source of cadmium.

The presence of Li^+ ions on the electrode surface was suggested from the XRD analysis. This finding was supported by Steele[136] who suggested that the impregnation of Li^+ alkali ions replaces Ni^{2+} or Ni^{3+} ions in the oxide lattice,

176

and consequently, influences the rate at which protons can diffuse through the oxide. This increases the charge capacity of the electrode. Since the presence of Li^+ increases the over-potential for oxygen evolution on nickel in alkaline solutions, it is seen as a benefit to the cycle life of an alkaline battery[136].

The presence of cadmium on the electrode surface as shown by the SEM analysis in Figure 32 (a) and (b), arises due to contamination from the cadmium electrode and most likely exists as cadmium hydroxide $Cd(OH)_2$. The presence of potassium on the electrode surface is most likely carried over from the potassium hydroxide, KOH, electrolyte within the nickel/cadmium cell.

Electrodes 1 to 4 yielded insufficient conclusive XRD data to confidently assign any peaks other than those for elemental nickel. This suggests the absence of any substantial oxide layers on the nickel foil after anodizing in the respective solutions. The SEM micro-graph shown in plate 10 is characteristic of a chemically etched nickel foil and was taken after anodizing in 10% sulphuric acid (electrodes 1 to 4). The individual grain boundaries are clearly visible after anodic dissolution of the substrate has occurred. The light elemental analysis shown in Figure 33, revealed only trace oxygen on the surface of these electrodes which was most likely to be a result of oxygen trapped in voids or between grains rather than associated with a surface oxide film. Any oxide on the electrode surface was most likely associated with the air formed oxide film of a thickness between approximately 6 and 8 $Å$[133].

5.1.2 Electrochemical Evaluation of Auxiliary Electrodes.

One of the most important aspects of the auxiliary electrode used in the gel-filled hydrogen probe is its ability to maintain a constant equilibrium potential over a period of time. The nickel/nickel oxide electrode is alleged to provide a

method by which the steel surface may be controlled to achieve an anodic potential, sufficient to oxidise the hydrogen as it leaves the surface under this applied anodic potential. For this reason, the electrode's potential should not deviate from its equilibrium potential attained in the supporting electrolyte.

The electrode potential value for the Ni/Ni^{2+} couple of -0.250 V (NHE):

$$Ni^{2+} + 2e^- \leftrightarrow Ni \qquad\qquad [23]$$

accepted by various workers, including Pourbaix[112] is difficult to maintain as the presence of oxygen in the electrolyte interferes with these measurements. The experimental difficulty experienced in obtaining the required data is reflected in the range over which the reported values of E_0, the electrode potential, are spread, generally between -0.231 V[140] and -0.248 V[141].

The standard potential of the $Ni/Ni(OH)_2$ couple:

$$Ni(OH)_2 + 2e^- \leftrightarrow Ni + 2OH^- \qquad\qquad [24]$$

is recorded as -0.72 V in alkali solutions. A number of couples may be calculated from thermal and electrochemical data, some of these which are listed by Pourbaix and co-workers[112], are shown in Table 21.
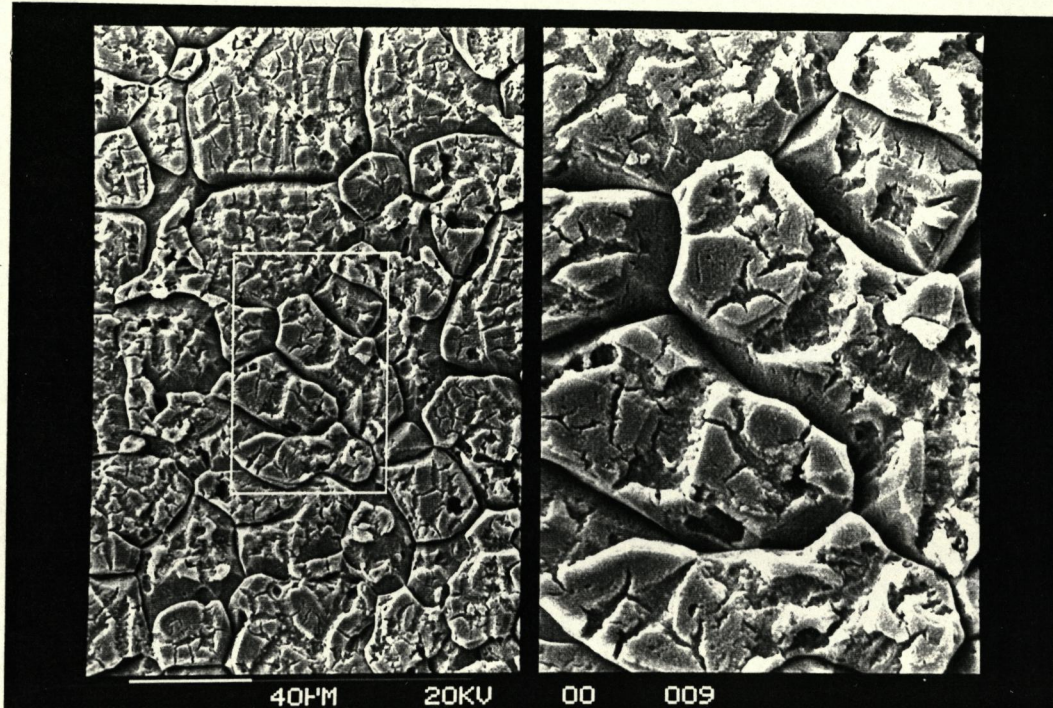
Plate 10. SEM Micro-Graph of Chemically Etched
Nickel Foil.

179

Table 21   Electrode Couple Potentials Derived From Thermal and Electrochemical Data.

Couple	E_0 Equilibrium Potential /Volts (NHE)	Calculated E_0 at pH 13 (0.2M NaOH) /Volts (NHE)
Ni/NiO	$E_0 = 0.116 - 0.059pH$	0.0393
$Ni(OH)_2/Ni_3O_2(OH)_4$	$E_0 = 0.897 - 0.059pH$	0.1300
$Ni(OH)_2/ß-NiOOH$	$E_0 = 1.032 - 0.059pH$	0.2630
$Ni_3O_2(OH)_4/ß-NiOOH$	$E_0 = 1.305 - 0.059pH$	0.5380
$ß-NiOOH/NiO_2$	$E_0 = 1.434 - 0.059pH$	0.6670

There appears to be considerable deviation between theoretical values and experimental measurement. The existence of the ß-NiOOH/NiO_2 couple is doubtful as the species NiO_2 has never been identified[133]. Accordingly, one finds in alkaline solutions, for an anodized nickel foil:

$$ß-NiOOH + H_2O + e^- \leftrightarrow Ni(OH)_2 + OH^- \quad E_0 = -0.522 \text{ V} \qquad [25]$$
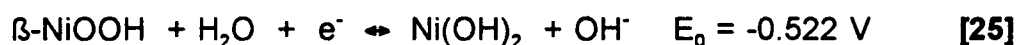
Comparing the experimental values in Table 13 with those calculated in Table 21, and coupled with SEM and XRD work, it is possible to tentatively suggest the relationship between the presence of an anodic oxide film and the electrode's equilibrium potential.

The sintered nickel plaque electrode maintains an equilibrium potential of around +0.150 V (NHE) in 0.2M NaOH solution. This would suggest the presence of $Ni(OH)_2$ and ß-NiOOH. The equilibrium potential observed for the

sintered nickel plaque is actually a mixed potential with contributions from lithium, cadmium and potassium ions. The presence of such species does not appear to affect the stability of the rest potential, shown in Table 13, and will not be considered in further detail.

With regard to electrodes 1 to 4, each have rest potentials ranging from -0.139 to -0.09 V (NHE). Taking into consideration the absence of conclusive XRD and SEM analysis, to suggest the presence of an oxide film, the most likely reactions occurring on the nickel surface in a 0.2M NaOH solution are:

$$Ni^{2+} + 2e^- \rightleftharpoons Ni \quad E_0 = -0.250 \text{ V} \qquad [26]$$

or

$$Ni + 2OH^- \rightarrow NiO + H_2O \quad E_0 = 0.116\text{-}0.059pH \quad (0.0393 \text{ pH13}) \quad [27]$$
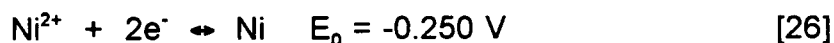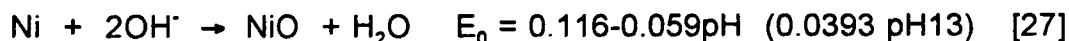
Equation [27] shows the formation of NiO, which is comparable in thickness and chemical properties to the air-formed oxide film and approximately 6-8 Å in thickness[133]. The variation in equilibrium potentials, measured for the 4 electrodes, can be explained by the varying degree of chemical etching observed in Plate 10.

The mercury/mercury oxide (Hg/HgO) element had the initial advantage of a highly reproducible standard state for the metallic phase and complete freedom from any disturbing effects due to variable valency of oxide. Precipitation reactions in which mercurous oxide, or mercurous hydroxide, might be formed yield only a mixture of mercuric oxide (HgO) and metallic mercury[142]. Although mercuric oxide is well known to exist in yellow and red forms which differ in solubility (yellow 51.3, red 48.7 mg l^{-1} at 25°C in water[142]), it appears probable that the difference is confined to particle size alone.

$$H_2, Pt \mid NaOH_{(aq)} \mid HgO \mid Hg \quad E_0 \approx +300 \text{ mV} \qquad [28]$$

Evidence shows[112] that the Hg/HgO electrode had an EMF independent of the concentration of the electrolyte except for small differences attributable to varying water activity. The calculated equilibrium potential for the mercury/mercury oxide (Hg/HgO) system in 0.2M NaOH solution was around +300 mV NHE[112,142], equation [28]. The measured equilibrium in the same solution was found to be +306 mV NHE as shown in Table 13.

It was concluded, in the light of this investigation, that due to the instability and difficulties encountered in anodizing nickel foils, a mercury/mercury oxide electrode would be used in the modified gel-filled hydrogen probe. In order to avoid polarization of the Hg/HgO element, it was decided that the probe would be controlled potentiostatically, using the Hg/HgO element as a reference electrode, a piece of platinum wire to facilitate the cathodic reaction and the steel sample would complete the circuit as working electrode. A schematic of the modified gel-filled hydrogen probe is shown in Figure 21.

5.2   Gel-Filled Hydrogen Probe.

5.2.1 Hydrogen Concentration Determination.

Having established the physical design of the probe, it was now possible to
investigate the electrochemical response of the probe during hydrogen
concentration determinations. It was assumed that the initial concentration of
hydrogen in the steel test piece was essentially uniform, as illustrated in
Figure 64(a). When the probe was attached to the steel and the anodic
potential applied, the surface hydrogen concentration of the steel in contact
with the electrolyte was lowered. Hydrogen atoms in the steel diffused from
the surface under a concentration gradient and were oxidised as they
emerged according to equation [20]:

$$H \rightarrow H^+ + e^-$$
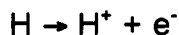
Monitoring this oxidation current led to a decaying current transient, as
illustrated in Figure 64(b) which was recorded using a data logger connected
to the potentiostat. The flux J_t, measured at a time t, for the initial and
boundary conditions shown in Figure 64(a) is described by the Laplace
transform solution to Fick's laws of diffusion[38],

$$J_t = zFC_0 \left(\frac{D}{\pi t} \right)^{\frac{1}{2}} \left[1 - e^{\frac{-L^2}{Dt}} + e^{\frac{-4L^2}{Dt}} - \ldots \right] \qquad [29]$$

where F is Faraday's constant, D is the apparent diffusion coefficient for
hydrogen in the steel and z is the number of electrons involved in the
oxidation reaction (equivalents mol^{-1}). It is possible to drop all exponential
terms and use a first term solution to equation [29] if:

$$\frac{L^2}{Dt} \geq 4$$

then:

$$t_{max} = \frac{L^2}{4D}$$
[30]

At values of $t_{max} = \frac{L^2}{4D}$, the term $e^{\frac{-L^2}{Dt}}$ << 1 and subsequent exponential

terms tend towards zero. The value of t_{max} in equation [30] is the time up to which C_0 may be calculated from the experimental value of J using the first term solution:

$$J_t = zFC_0 \left[\frac{D}{\pi t} \right]^{\frac{1}{2}}$$
[31]

For a sample of 4340 steel with a thickness of 0.1 cm and a diffusion coefficient of 2.5×10^{-7} $cm^2 s^{-1}$, t_{max} is around 10^4 seconds or approximately 3 hours[135]. For a sample of Armco Iron, with a diffusion coefficient of 2×10^{-5} $cm^2 s^{-1}$, t_{max} is around 2 minutes[135]. For practical applications where thicknesses are usually in excess of 1 mm and diffusivities are of the order of 10^{-7}, the approximation shown in equation [31] should hold true for the practical measurement time, which may be of the order of 15 to 30 minutes[135]. A plot of Log current against Log time for this duration, should yield a straight line with a gradient of -½. Values for the surface hydrogen concentration are found by substitution of J and t into equation [31].

In order to calculate C_0, however, an assumed value of the diffusion coefficient must be used. In early work, before evaluation of the diffusion coefficient through permeation transients, this was taken to be 2.5×10^{-7} $cm^2 s^{-1}$[135].
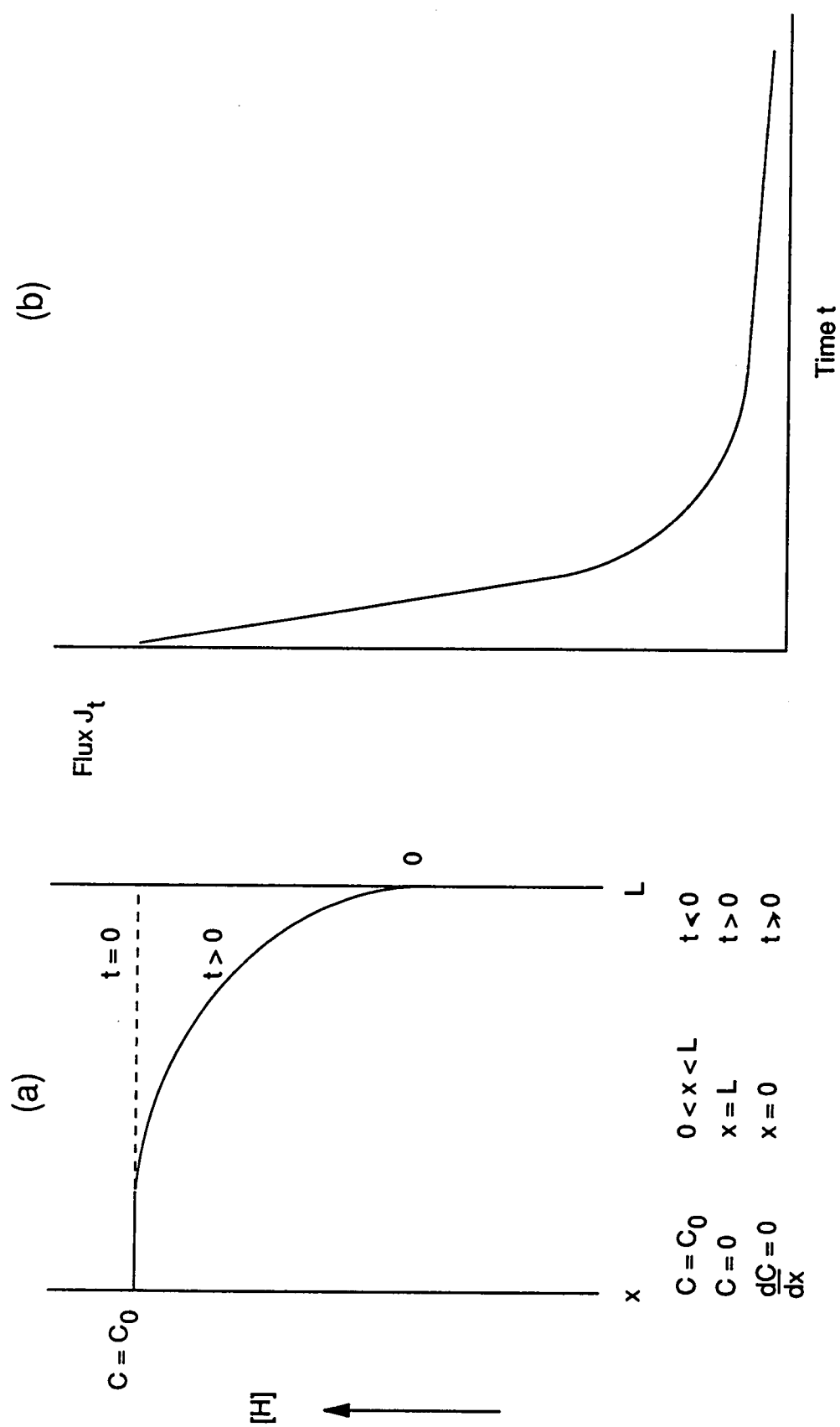
Figure 64.   Schematic Diagrams Showing (a) Concentration Gradient in Specimen During Hydrogen Determination and (b) Decaying Current Transient Resulting From Hydrogen Diffusion From Specimen Surface.

185

5.2.2 Determination of the Hydrogen Diffusion Coefficient from Non-Steady State Probe Readings.

By manipulation of the full solution shown in equation [29], it should be possible to refine the analysis to enable a true value of the diffusion coefficient to be calculated from the decaying current transient.

When the full solution is considered, the additional term:

$$Log\left[1-e^{-\frac{L^2}{Dt}}+e^{-\frac{4L^2}{Dt}}-\ldots\right] \qquad [32]$$

is introduced to the equation, thus equation [31] becomes:

$$LogJ_t=-\tfrac{1}{2}Logt+LogzFC_0\sqrt{\frac{D}{\pi}}+Log\left[1-e^{-\frac{L^2}{Dt}}+e^{-\frac{4L^2}{Dt}}-\ldots\right] \qquad [33]$$

The term shown in Equation [32] is always negative and would be expected to have the effect of lowering the current J_t progressively with time. A plot for the first term solution with a gradient of $-\tfrac{1}{2}$ and a second plot for the full solution, lowered by the additional term is shown in Figure 65.

If the experimental points can be assumed to follow the line for the full solution then a means of extracting the diffusion coefficient, D, becomes feasible. The separation between the two graphs (A) would need to be measured and D could be calculated from:

$$\frac{J_t^1}{J_t}=1-e^{-\frac{L^2}{Dt}}+e^{-\frac{4L^2}{Dt}}-\ldots \qquad [34]$$

Where J^1_t is the experimental current measurement at time t and J_t is the corresponding current from the first term solution. Although the two plots do not quite meet on a Log t graph, they can be considered to do so for times of a few seconds at the beginning of the measurements. At this stage the

magnitude of the second term $e^{\frac{-L^2}{Dt}}$ and subsequent exponential terms may

be estimated for the experimental conditions prevailing in the probe

measurements.

If the value of $L^2/Dt \geq 4$ then $e^{\frac{-L^2}{Dt}}$ is close to zero and the first term

solution is acceptable. The error introduced by this simplification is

approximately 1.8% of J_t. In practice, the probe current was recorded for 900s

and the hydrogen concentration in the steel was calculated from the value at

600s by substitution into equation [30]. The smallest value of L^2/Dt during a

900 s determination would be approximately 16000 and the value of $e^{\frac{-L^2}{Dt}}$

is essentially zero. This means that the first term solution and the full solution

would be indistinguishable. It is also interesting to note that the assumed

value of the diffusion coefficient could be reduced from 2.5×10^{-7} cm^{2}s^{-1} to 9 x

10^{-4} cm^{2}s^{-1} before the first term solution would become unacceptable.

The thickness of the steel plate used in the probe measurements have meant

that the condition for use of the first term solution has been met very easily.

Clearly, this is a factor which should be considered in applying this technique

on material with a different geometry.
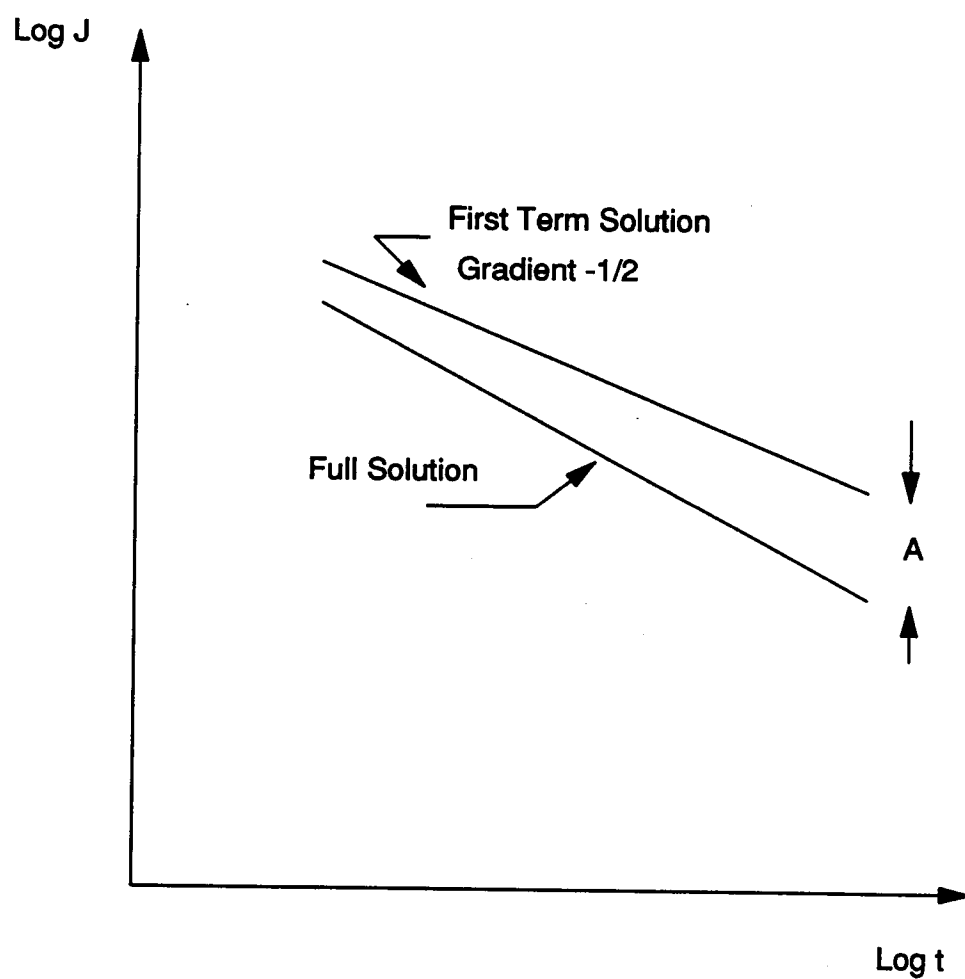
Figure 65.   Theoretical Log Current/Log Time Transient
            For First Term and Full Solution Expressions.

5.2.3 Depth of Uniform Hydrogen Concentration During Gel-Filled Hydrogen Probe Measurements.

The decaying current transient recorded by the gel-filled probe was analyzed on the assumption that the initial hydrogen concentration in the steel was uniform as illustrated in Figure 64(a). Clearly, in the early part of the charging experiments there would have been a steep concentration gradient near the influx surface and this might have been expected to influence the probe measurements at this time. However, the gradients of the experimental decay transients shown in Figure 29 for the original gel-filled hydrogen probe construction and Figure 34 for the modified gel-filled hydrogen probe, were close to the theoretical value of -½ suggesting that this was not the case. A more precise description of the initial requirement would be that the hydrogen concentration should be uniform for the distance over which diffusion would occur during the 15 minutes of the probe measurement. This may be estimated from equation [30], assuming t_{max} is the time over which diffusion occurs and by considering the distribution of hydrogen in the steel plate with respect to time.

Figure 66 shows a theoretical plot of the distribution of hydrogen within the steel plate through its thickness with respect to time[38]. A diffusion coefficient of 2.5×10^{-7} cm^2 s^{-1}, for example, would allow for a uniform concentration to a depth of approximately 0.6mm during the 15 minute probe reading.

5.2.4 Optimum Hydrogen Oxidation Potential for the Gel-Filled Hydrogen Probe.

The optimum hydrogen oxidation potential for the probe is determined by the metal substrate under test. For convenience, only the case of surface measurements on carbon-manganese steel have been considered. By examining the potential-pH diagrams of Pourbaix[112], the optimum oxidation

189

potential may be established for any metallic substrate at pH 13.3, conditions dictated by a 0.2M $NaOH_{(aq)}$ electrolyte.

From the Potential-pH diagram for the hydrogen-water system, at 25° C, shown in Figure 67[112], there are two distinct lines denoted (a) and (b). These show the thermodynamic stability limits for water. Line (a) with a slope of - 0.0591, shows the equilibrium conditions of the reduction of water (or H^+ ions) to gaseous hydrogen i.e.

$$2H^+ + 2e^- \rightleftharpoons H_{2(g)} \qquad [35]$$

Line (b), with the same slope, shows the equilibrium conditions for the oxidation of water to gaseous oxygen i.e.

$$2H_2O \rightleftharpoons O_{2(g)} + 4H^+_{(aq)} + 4e^- \qquad [36]$$
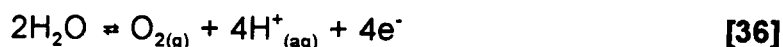
Both of these conditions are satisfied only when the partial pressure of hydrogen or oxygen is 1 atmosphere at 25° C.

The equations of these lines are obtained by equating the partial pressure of hydrogen Log $_pH_2$ and the partial pressure of oxygen Log $_pO_2$ to zero in the following expressions (where E_0 is in volts):

$$H_{2(g)} \rightleftharpoons 2H^+_{(aq)} + 2e^- \qquad E_0 = 0.000 - 0.0591pH - 0.0295 \, Log \, _pH_2 \qquad [37]$$

$$2H_2O \rightleftharpoons O_{2(g)} + 4H^+_{(aq)} + 4e^- \quad E_0 = 1.228 - 0.0591pH + 0.0147 \, Log \, O_2 \qquad [38]$$
Thus:
$$H_{2(g)} \rightleftharpoons 2H^+_{(aq)} + 2e^- \quad E_0 = 0.000 - 0.0591pH \qquad [39]$$
and
$$2H_2O \rightleftharpoons O_{2(g)} + 4H^+_{(aq)} + 4e^- \quad E_0 = 1.228 - 0.0591pH \qquad [40]$$

190
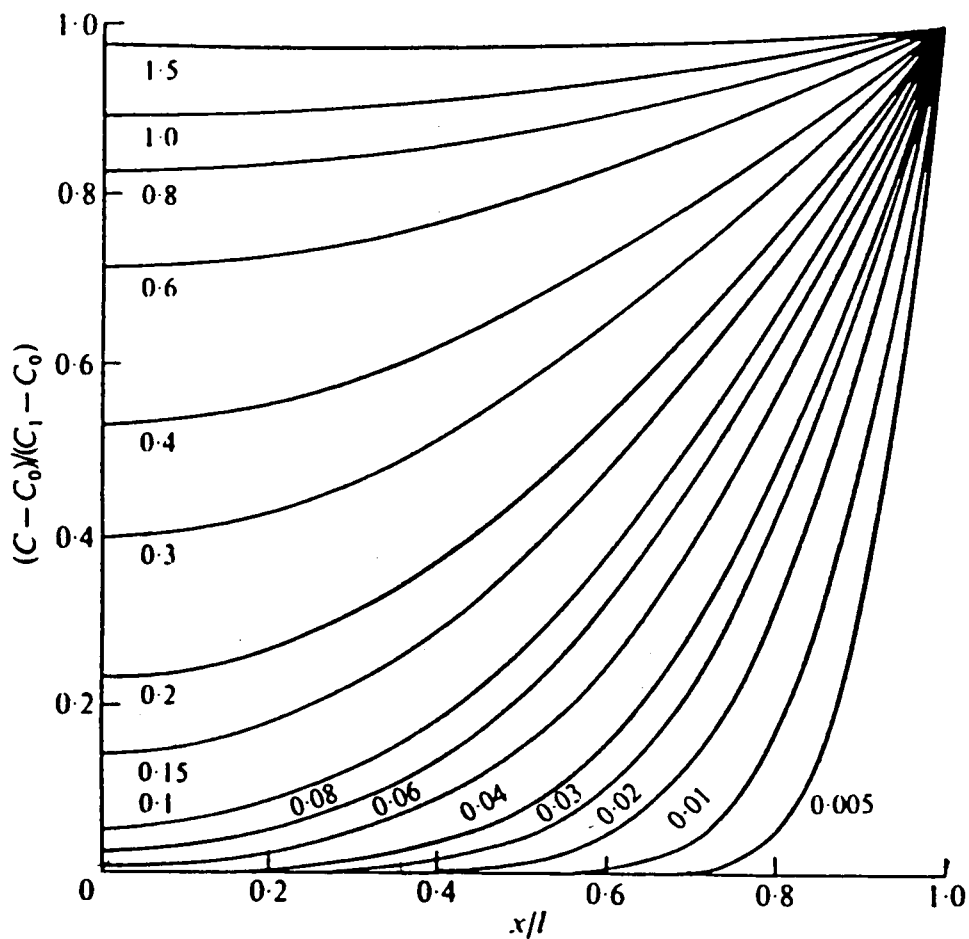
Figure 66.   Concentration Distribution at Various Times
in a Sheet With Initial Uniform Concentration
C_0 and Surface Concentration C_1. Numbers
on Curves are Values of Dt/L^2 [38].

191
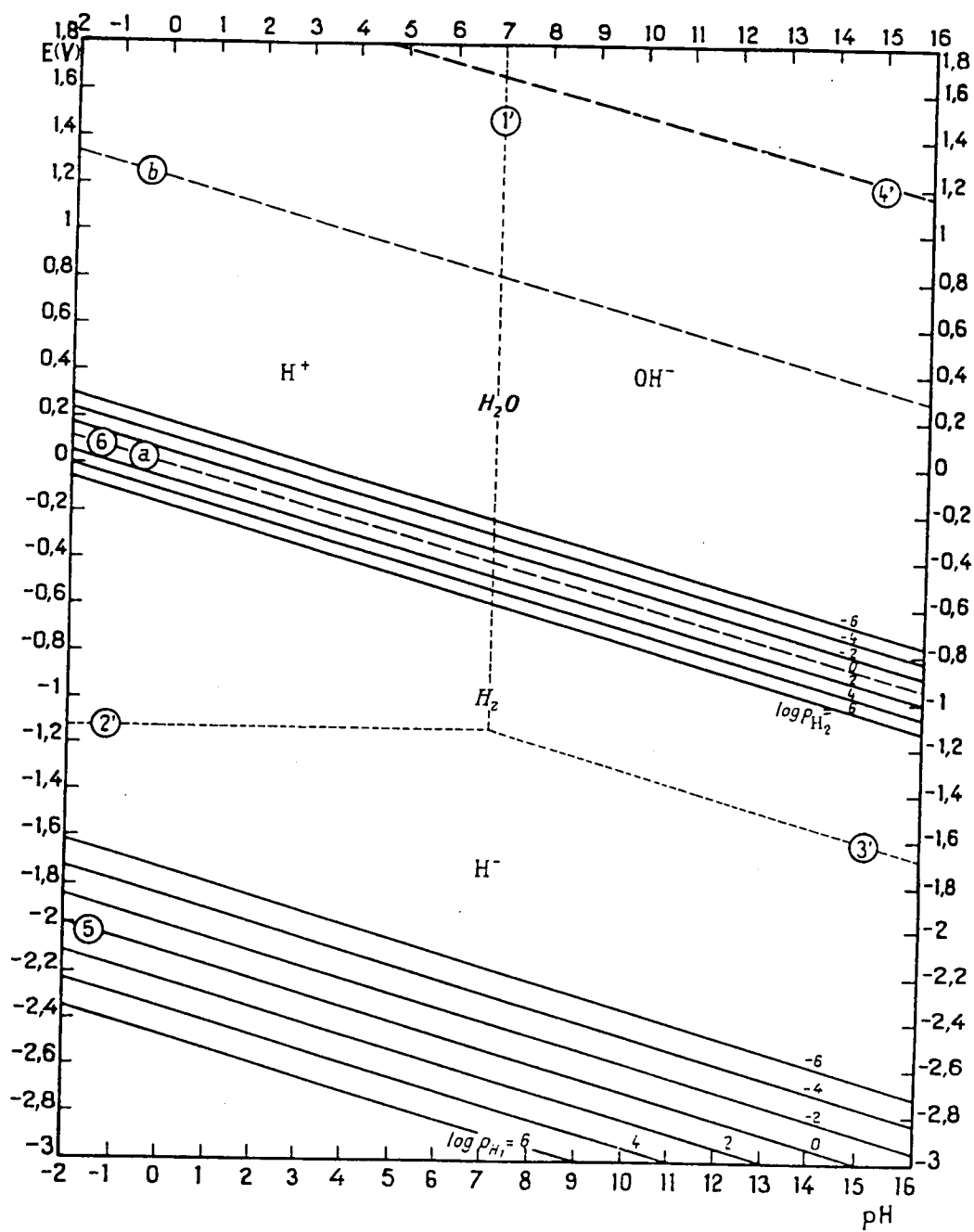
Figure 67.   Potential-pH Diagram for the Hydrogen-
              Water System[112].

192

Consequently for hydrogen evolution to occur at pH 13.3, the applied potential must be more cathodic than -0.788 V, and for oxygen evolution to occur at the steel surface, the applied potential must be more noble than +0.440 V.

Having considered the stability of water in this potential range, it is now necessary to consider the surface condition of the steel. In the presence of an aerated caustic solution (i.e. at pH's greater than 8) iron is covered with a protective film of γ-Fe_2O_3, which will, in general, be protective in the case of solutions not containing chlorides as shown in Figure 68. Above pH's of around 13, the passivation potential is given by:-

$$E_0 = +0.20 - 0.062pH \tag{41}$$

At pH 13.3 this gives a value of approximately -0.63 V. In the absence of large concentrations of oxygen and other ionic species, the range for anodic oxidation of mono-atomic hydrogen diffusing from the efflux surface is between around -0.6 V and +0.4V on the NHE. In summary an applied anodic oxidation potential within the range:

$$-0.6\ V < E < + 0.4\ V \tag{42}$$

would be suitable to oxidise any hydrogen diffusing to the efflux surface. The value of +150 mV used in the hydrogen determinations with the gel-filled hydrogen probe is sufficient to drive the electrochemical oxidation of hydrogen. Additionally, the potential is sufficiently low to avoid oxygen evolution, yet high enough to avoid hydrogen evolution.

The presence of oxygen in the solution will effectively provide a negative back ground current due to its electrochemical reduction. The higher the concentration of dissolved oxygen in solution, the larger its contribution to the observed current.
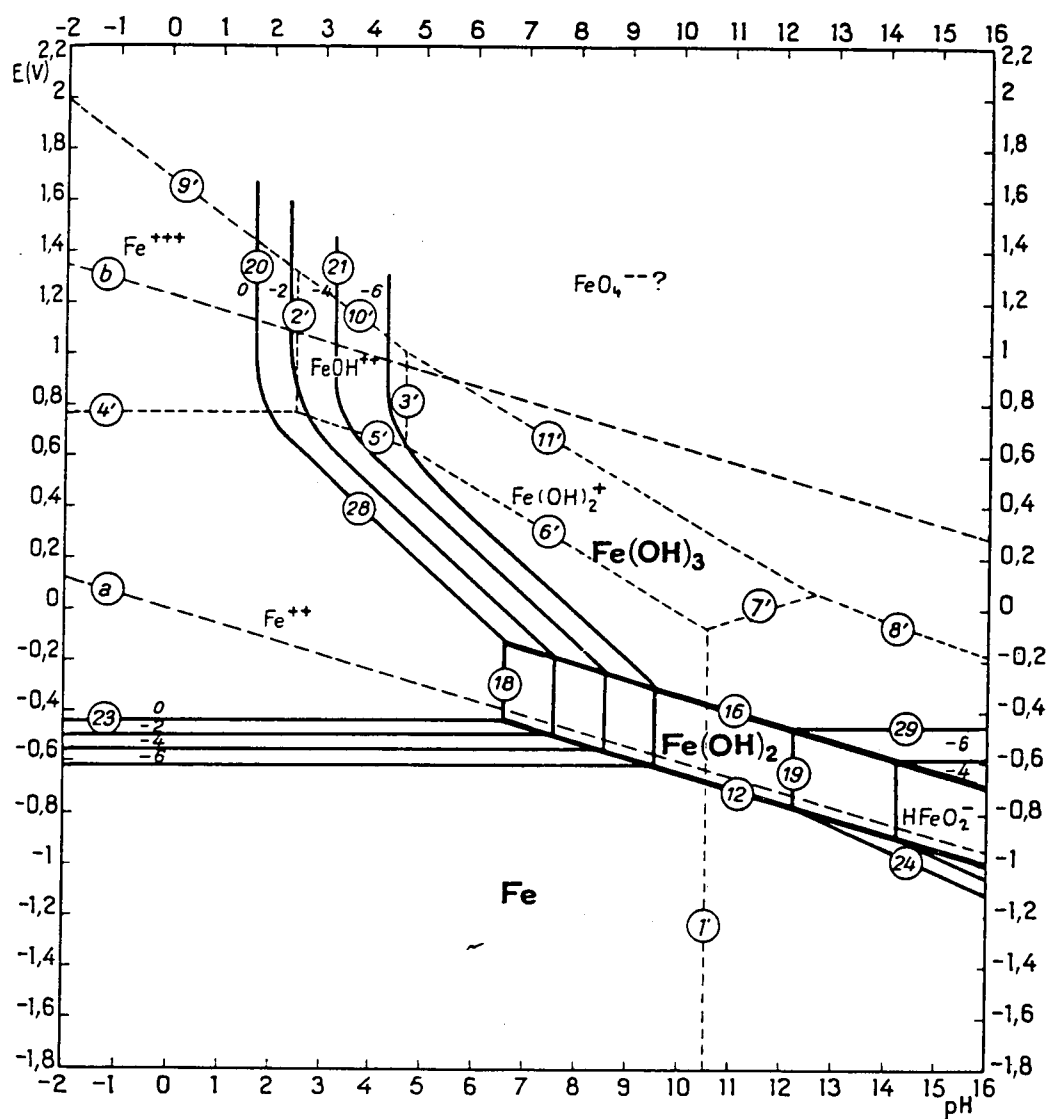
Figure 68.   Potential-pH Diagram for Iron-Water
System[112].

194

During the formation of γ-Fe_2O_3, a small current is observed which is inseparable from the total current measured. The contribution from passive film formation, however, decays logarithmically and tends toward zero after a small finite time.

5.3　The Effect of Steel Passivation on Gel-filled Hydrogen Probe Readings.

During hydrogen determinations with the gel-filled probe the steel surface was held at a potential of +150mV (NHE) in a 0.2M NaOH electrolyte with a pH of approximately 13, as described in section 5.2.4. In this condition the steel is rendered passive as shown in the potential-pH diagram[112] in Figure 68. The passive layer on the steel prevents corrosion of the surface that would contribute to the current measured by the probe, according to the oxidation reaction:-

$$Fe \rightarrow Fe^{2+} + 2e^- \qquad \text{[42]}$$

Passivation of the steel surface probably involves a combined process of steel oxidation, proposed by Evans[143] and chemisorption of oxygen to the surface proposed by Uhlig[144]. In terms of the oxidation process, the steel surface initially undergoes hydration according to:

$$Fe + 3H_2O \rightarrow Fe(OH)_3 + 3H^+ + 3e^- \qquad \text{[43]}$$
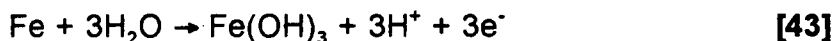
The hydrated oxide layer then undergoes rearrangement to form the passive oxide layer consisting of γFe_2O_3 according to[144]:

$$2Fe(OH)_3 \rightleftharpoons \gamma Fe_2O_3.3H_2O \qquad \text{[44]}$$

As a result of this oxidation process, the observed hydrogen oxidation current would be superficially higher than expected due to current contributions from the passive film formation. In order that the magnitude of this effect may be defined and the gel-filled hydrogen probe readings corrected, a study of the kinetics of steel passivation was made.

With careful surface preparation, subsequent anodic reactions due, for

example, to the oxidation of trace elements or surface contaminants at the steel surface can be successfully eliminated. The anodic oxidation of the steel, however, cannot be eliminated by surface preparation due to the nature of the probe's electrolyte. Consequently this secondary current must be accounted for during data analysis.

When the gel-filled probe is in operation the current transient from the oxidation of hydrogen at the metal surface decays slowly and, as described previously, a graph of Log current density plotted against Log time has a gradient of -½, Figures 29 and 34. In contrast, the kinetics of passivation on steel are thought to be much more rapid than those associated with the oxidation of hydrogen. In fact it has been shown[131] that the current associated with the passivation of the steel is inversely proportional to time i.e. $J_{Fe} \propto 1/t$, or $J_{Fe} = K/t$, where K is a constant.

As shown in section 5.2, the current associated with the oxidation of hydrogen is given by equation [29]:

$$\frac{J_t}{nF} = C_0 \left[\frac{D}{\pi t}\right]^{1/2} \left[1 - e^{\frac{-L^2}{Dt}} + e^{\frac{-4L^2}{Dt}} - \ldots\right]$$

Where J_t is the flux associated with hydrogen oxidation.

n is the number of electrons in the reaction $H \rightarrow H^+ + e^-$

F is the Faraday constant

C_0 is the surface hydrogen concentration

D is the apparent diffusion coefficient and

t is the time in seconds.

For the condition where $L^2/Dt \geq 4$ then all exponential terms may be neglected, leading to the first term approximation given by equation [31]:

$$\frac{J_t}{nF} = C_0 \left[\frac{D}{\pi t}\right]^{1/2}$$

From equation [31], it can be seen that the current associated with the oxidation of hydrogen is inversely proportional to the square root of time, i.e. $J_H \propto 1/\sqrt{t}$. A plot of Log current against Log time yields a gradient of $-\frac{1}{2}$.

In the scratch test experiments, carried out in order to evaluate the kinetics of passivation, the magnitude of the current required to reform a passive film after scratching a passivated steel surface was measured. The actual size of the scratch was not physically measured. The magnitude of the observed current, however, was indicative of the scratch size. The scratch size was not a well defined variable as this related the surface condition of the steel prior to application of the probe. If a partial anodic film existed on the steel surface, then the initial, and subsequent magnitude of the decaying current would be less.

Figures 36 and 37 show the results obtained from the scratch experiment. The results appear to be in good agreement with those of Hashimoto and co-workers[131]. They conducted a stochastic analysis of the potential fluctuation during passive film breakdown and repair on iron using a scratch technique and electrochemical noise monitoring. They used pure iron [C = 0.02, Si < 0.005, Mn < 0.01, P < 0.0005, S < 0.0005 wt%] which was annealed at 900°C for 1 hour in an Argon atmosphere. The anodic current decay curve in a 200 ppm $NaNO_2$, NaCl free solution was measured and is shown in Figure 69. The specimen was first cathodically polarised at a potential of -1.1 V against the saturated calomel electrode to remove the air-formed passive film. The potential was then changed to +0.1 V (S.C.E.). After about 1 second, the anodic current started to decrease rapidly to a final background value. The gradient of the decaying current was inversely proportional to time.

The plateau at the start of the measurement probably represents the initial, large current which appears to be dependent on the impedance of the polarization circuit. This current seems to carry mainly the actively dissolving

iron ions before the film starts to form. Wei and Geo[129], however, offered a different explanation to the presence of an initial plateau. They performed a series of experiments to investigate the distribution of initial current between bare and filmed surfaces on steel. They questioned the validity of the scratch test technique, concluding that the initial plateau was probably a result of charging of the double layer rather than a reaction on the bare metal surface. The subsequent decay, when the equilibrium between active dissolution of the iron and formation of the passive film, has shifted almost totally in favour of the film formation, was confirmed to decay inversely with respect to time[129].

The transients recorded in Figures 36 and 37 show the characteristic plateau reported by Hashimoto[131] and Wei and Geo[129]. The gradient of the subsequent decay, should in theory be close to -1. If the transients had in fact been recorded at longer times, then sufficient data points would be available to calculate the gradient of the transient without influence from the initial plateau. The measured gradient would have been close to -1.

Figure 38 compares current transients recorded for steel containing a range of hydrogen contents. It is clear that the passivation current was more significant when determining low levels of hydrogen and in these cases the initial part of the transient had a steeper gradient. In contrast, at high concentrations the contribution from passivation was masked by the larger hydrogen oxidation current and the gradient approached the theoretical value of -½. Experimental values showing the effect of hydrogen content on the initial gradient of the decay transient are summarised in Figure 39.
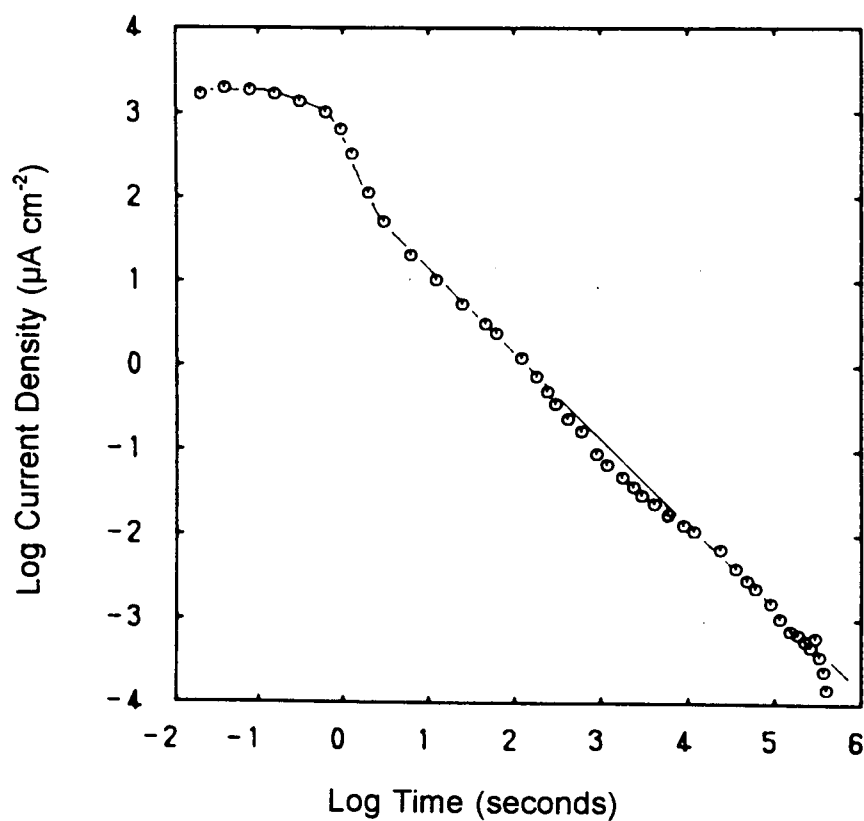
Figure 69.   The Anodic Current Decay Due to Passive
Film Growth in a NaCl Free 200ppm NaNO$_2$
Solution at a Potential of 0.1 V (SCE)[131].

200

The unknown magnitude of the passivation current appeared to present an obstacle in measuring low hydrogen contents. However, this may be overcome quite simply by recording the probe current until the contribution from passivation has decayed and the gradient has assumed a value of $-\frac{1}{2}$, as shown in Figure 38, whereupon the hydrogen concentration can be calculated in the usual way.

The magnitude of the passive current appeared to be dictated by the passive state of the steel surface prior to polarising on application of the $+150$ mV (NHE) oxidising potential. Figure 40 shows the effect of placing the probe on the steel at open circuit for a given period of time prior to gel-filled hydrogen probe determination. Although this did reduce the magnitude of the passivation current, it could not be totally eliminated at such short times, which were typically around 10 minutes at open circuit. It appeared that only when the steel was anodically polarised, the passive current decayed proportional to $1/t$.

The implication of this observation was that any contribution to the probe current caused by passivation of the steel would decay more rapidly than the current due to the detection of hydrogen and its contribution may be neglected after it has decayed to a sufficiently low value.

A more reliable method of evaluating the effect of repassivation would be simply to observe the point on the graph of log J against log t, where the gradient approaches $-\frac{1}{2}$, as shown in Figure 38. Here the influence of the repassivation process can be considered negligible.

5.4 The Kinetics of Hydrogen Absorption into Steel.

Later in this chapter, results from the conventional permeation cell experiments are analyzed with respect to three models incorporating different initial and boundary conditions. The first two models are based on constant surface hydrogen concentration at the charged surface and a constant flux of hydrogen entering the charged surface respectively. The third model is based on constant surface hydrogen coverage boundary conditions. This introduces additional parameters, such as the finite rate constants for the hydrogen adsorption and hydrogen evolution reactions on the steel surface. These influence the distribution of hydrogen within the steel. Use of this model requires approximate numerical values for these rate constants which may be obtained from a study of the kinetics of hydrogen absorption into steel.

Numerical values for the rate constants and values for the surface coverage, Θ_H, can be obtained from the experimental measurement of such parameters as the steady state hydrogen permeation current, for a series of different cathodic charging currents. Using the bi-polar cell arrangement[36], as shown in Figure 28, it was possible to evaluate the kinetic parameters involved in the Hydrogen Adsorption Reaction[23] and the Hydrogen Evolution Reaction[24,25].

The results obtained in this work were derived through manipulation of the IPZ model following the work of Iyer, Pickering and Zammanzadeh[20]. The model enables computation of the hydrogen discharge and recombination reaction rate constants and the more important hydrogen absorption and hydrogen adsorption rate constants. The later two parameters respectively, quantitatively describe the surface and sub-surface kinetic properties of the metal-hydrogen interaction leading to quantitative characterisation of the hydrogen coverage at the metal surface, Θ_H.

The scope of the project dictated that only approximate values for the various

parameters were required. This would enable an approximate solution to be evaluated for the constant surface coverage model examined later in this chapter. This work was carried out on separate material, 57μm thick, which was free of certain types of defects such as large manganese sulphide inclusions. Utilising a steel of this thickness was desirable, as the breakthrough time was particularly low, and equilibrium was rapidly established. This facilitated multiple permeation transients at various cathodic charging current densities.

The model considers a subsurface reaction (as a result of proton tunnelling) that is quite fast and constitutes a transition layer of a thickness that could range upwards from approximately 1 nm[24]. This establishes a subsurface hydrogen concentration of C_0, which allows diffusion of hydrogen to the charging and exit surfaces. An equilibrium will be established between the surface covered (adsorbed hydrogen atoms) and hydrogen just below the surface (in the absorbed state, with concentration C_0)[25]. By manipulation of equations [46] to [61] one can estimate approximate values for the finite rate constants, K_{abs} and K_{des}, for the absorption and desorption processes.

In the hydrogen permeation experiments, i_c was set to a specific current density, as shown in Table 14. A series of successive permeation rise transients were obtained as shown in Figure 45. When the permeation current was independent of time, i_∞, the steady state permeation current, was measured. From these measurements, a relationship for the hydrogen evolution current, i_r, may be established:-

$$i_r = i_c - i_\infty.$$

[45]

5.4.1 Modelling the Effects of the Hydrogen Adsorption and Hydrogen Evolution Reactions.

The charging current (i_c) was given by:

$$i_c = i^*_0 (1 - \theta_H) \exp^{-a\alpha\eta} \qquad [46]$$

Where

$$i^*_0 = Fk_1 = \frac{i_0}{(1 - \theta_e)} \qquad [47]$$

The hydrogen evolution current (i_r) (assuming chemical recombination of hydrogen atoms, which was apparent due to the plots of i_∞ against $(\sqrt{i_r})$, Figure 44, and ($i_c \exp^{a\alpha\eta}$) against ($i_\infty - C_0/b$), Figure 45, being linear) was given by:

$$i_r = Fk_3 \theta_H^2 \qquad [48]$$

The steady state hydrogen permeation current (i_∞) is given by:

$$i_\infty \cong \frac{FD_{eff}C_0}{L} \qquad [49]$$

where

i_0 = the exchange current density

θ_e = the equilibrium surface coverage of hydrogen.

k_1 = the discharge rate coefficient

$\qquad = k^0_1 c_{H+} + \exp^{-a\alpha E_{eq}}$

and

k^0_1 = rate constant for forward reaction.

c_{H+} = hydrogen ion concentration.

a = F/RT (19.4 V^{-1} at 25°C)

α = transfer coefficient

E^{eq} = equilibrium potential for the HER.

and

Θ_H = surface coverage of hydrogen

η = hydrogen overvoltage

$\quad = E_{i_\infty} - E^{eq}$

k_3 = recombination rate coefficient

D = hydrogen diffusion coefficient in the shim steel and

L = membrane thickness.

Having now defined the components which account for the charging current entering the system in terms of the permeation current and the hydrogen evolution current, it is possible to account for the effect the steady state permeation current, i_∞, has on the hydrogen evolution reaction.

$$i_\infty = \left(\frac{k^1}{b\sqrt{FK_3}}\right)\sqrt{i_r} + \frac{C_0}{b} \qquad [50]$$

and

$$i_c\, exp^{a\alpha\eta} = -\left(\frac{bi^*_0}{k^1}\right)\left(i_\infty - \frac{C_0}{b}\right) + i^*_0 \qquad [51]$$

Where b = L/(FD) = a constant for any given metal.
also[145] for the model:

$$\left(-120\,\frac{mV}{decade}\right) \sim \left(\frac{\delta\eta}{\delta\log i_c}\right) < \left(\frac{\delta\eta}{\delta\log i_\infty}\right) < 2\left(\frac{\delta\eta}{\delta\log i_c}\right) < \left(-240\,\frac{mV}{decade}\right) \qquad [52]$$

The Tafel slope for the H.E.R. and $\delta\eta/\delta\log i_\infty$ are calculated for this model from:

$$i_\infty = k^2\,\frac{\sqrt{i_r}}{(b\sqrt{FK_3})} \qquad [53]$$

Substitution leads to:

$$i_\infty = K\sqrt{i_r} = K\sqrt{(i_c - i_\infty)} \qquad [54]$$

Where **K** is a constant. Taking logarithms of equation [54] and differentiating

with respect to η:

$$\frac{\delta \ln(i_\infty)}{\delta \eta} = \frac{1}{2}\frac{\delta \ln(i_c)}{\delta \eta} + \frac{1}{2}\frac{\delta \ln\left(1-\frac{i_\infty}{i_c}\right)}{\delta \eta} \qquad [55]$$

Since the second term of the right hand side of equation [55] is equivalent to

$$\frac{\left(\frac{i_\infty}{i_c}\right)}{2\left(1-\frac{i_\infty}{i_c}\right)}\left[\frac{\delta \ln i_c}{\delta \eta} - \frac{\delta \ln i_\infty}{\delta \eta}\right] \qquad [56]$$

Equation [55] becomes:

$$\frac{\delta \eta}{\delta \log i_\infty} = \left(2 - \frac{i_\infty}{i_c}\right)\frac{\delta \eta}{\delta \log i_c} \qquad [57]$$

When $i_\infty \ll i_c$

$$S_{\infty t} = 2 S_{ct} \qquad [58]$$

where

$$S_{\infty t} = \frac{\delta \eta}{\delta \log i_\infty} \qquad\qquad S_{ct} = \frac{\delta \eta}{\delta \log i_c} \qquad [59]$$

For example, when $\alpha = 0.5$, and $\Theta \sim 0$, $S_{ct} = -120$ mV decade^{-1} ($\delta \eta / \delta \log i_c = -2.303/a\alpha$) and so $S_{\infty t} = -240$ mV decade^{-1}, which is in exact agreement with previous models and findings[146]. However, if $i_\infty \approx i_c$, equation [58] yields $S_{\infty t} = -120$ mV decade^{-1} for $S_{ct} = -120$ mV decade^{-1}. Thus, in general, the following inequality will hold for $\delta \eta / \delta \log i_\infty$

$$\left(\frac{\delta \eta}{\delta \log i_c}\right) < \left(\frac{\delta \eta}{\delta \log i_\infty}\right) < 2\left(\frac{\delta \eta}{\delta \log i_c}\right) \qquad [60]$$

It may be additionally noted from equation [60] that either the Tafel slope or $\delta \eta / \delta \log i_\infty$ or both will vary as a consequence of the dependence of Θ on η.

The transfer coefficient α may be obtained from a plot of $\ln i_c$ against hydrogen overvoltage η and is given by the expression:

$$\alpha \cong -\frac{(\frac{\delta \ln i_c}{\delta \eta})}{a} \quad [61]$$

Figure 45 shows the plot of i_∞ versus $\sqrt{i_r}$, equation [50], and Figure 46 shows the plot of $i_c \exp^{a\alpha\eta}$ versus $[i_\infty - c_0/b]$, equation [51]. As both of these plots are linear, the IPZ model suggests that the HER was taking place under a coupled-discharge mechanism[22]. From this it can be seen that the data fits the IPZ model closely and consequently, all the coefficients, k_1, k_3, c_0 and i_0' can be calculated. These values are shown in Table 22.

The value for the diffusion coefficient for the shim steel was 3.0×10^{-8} cm^2s^{-1}[147]. From equation [48], Θ_H, the fraction of surface covered with hydrogen, can be calculated using the k' and i_0' values obtained from the slope of Figure 46, k_3, the recombination rate constant, was obtained from the slope of Figure 45 and the i_r value from $i_r = i_c - i_\infty$. The surface coverage (Θ_H) versus the hydrogen over-voltage (η) plot is shown in Figure 46. It can be seen that the surface coverage is quite high in the potential range of these experiments.

The relationships summarized in the IPZ model assume that η, the hydrogen over-voltage, was much greater than (RT/F). This means that the reverse reactions, such as the transport of hydrogen from the bulk to the charged surface, can be neglected.

The present study showed that the hydrogen evolution reaction and the entry of cathodic hydrogen into mild shim steel did not follow independent reaction

paths, but proceeded in a coupled manner. The Tafel slope and also the dependence of the steady state permeation flux and hydrogen concentration on current density and over-potential were consistent with the model of coupled discharge-chemical/electrochemical desorption reaction for the hydrogen evolution reaction on shim steel.

Table 22.   Summary of Parameters

Parameter	Value	Units
D	3.0×10^{-8}	$cm^2 s^{-1}$
L	5.5×10^{-3}	cm
b	1.9	mole $(Acm)^{-1}$
α	0.316	---
a	19.4	V^{-1} @25°C
$i_0 \approx i_0'$	1.38×10^{-3}	A cm^{-2}
k_1	1.43×10^{-8}	mole $(cm^2 s)^{-1}$ (k_{abs})
k_2	2.2×10^{-4}	mole $(cm^2 s)^{-1}$ (k_{des})
k^1	3.64×10^{-4}	mole cm^{-3}

5.5   The Conventional Hydrogen Permeation Technique

In order to fully compare the measurements obtained with the gel-filled
hydrogen probe and the conventional permeation cell, it was necessary to fully
quantify these measurements. The diffusion of hydrogen through steel is best
described from solutions to Fick's laws of diffusion. Derivation from first
principles leads to the generalised diffusion equations representing Fick's first
law, equation [6] and second law, equation [7], of diffusion. In its normalised
form, equation [7] may be rewritten:-

$$\frac{\delta\sigma(\chi)}{\delta\tau} = \frac{\delta^2\sigma(\chi)}{\delta\chi^2}$$

[62]

Where the terms are defined by equations [8]-[11]. The actual solution to
these equations can only be realised after considering the initial and boundary
conditions under which a hydrogen concentration gradient is established.
From an electrochemical viewpoint, a hydrogen concentration gradient may be
established through cathodic hydrogen charging either by a constant potential
(potentiostatic) method or a constant current (galvanostatic) method.

Solution of equation **[62]** with the appropriate initial and boundary conditions
leads to the following expressions:

5.5.1 *Initial and Boundary Conditions Arising from a Constant Surface Hydrogen Concentration at the Entrance Surface.*

Assuming a slab of thickness L, which is being charged with hydrogen,
potentiostatically from one side (x = 0) with the hydrogen atoms discharged
rapidly from the exit side (x = L), the appropriate boundary conditions are:

t = 0	0 < x < L	C = 0
t > 0	x = 0	$C = C_0$
	x = L	C = 0

Where t = time, C = concentration at time t, x = distance through plate of thickness L.

The solution to equation **[62]** obtained by Fourier Transform method[38], relating the distribution of hydrogen through a slab of thickness L at a time t, expressed in dimensionless variables defined by equations [8-11], is given by:

$$\sigma(\chi, \tau) = (1-\chi) - \frac{2}{\pi} \sum_{n=1}^{\infty} \frac{1}{n} \sin n\,\pi\chi \, \exp(-n^2\pi^2\tau) \qquad [63]$$

The permeation current recorded as a result of holding the surface hydrogen concentration at the efflux surface at zero is given by[38]:

$$i(\tau) = -\left(\frac{\delta\sigma}{\delta\chi}\right)_{(\chi=1)} = 1 + 2\sum_{n=1}^{\infty} (-1)^n \exp(-n^2\pi^2\tau) \qquad [64]$$

Equation **[63]** is represented graphically in Figure 70(a) for various times of charging. The equivalent current transient is shown in Figure 70(b).

5.5.2 Initial and Boundary Conditions Arising from a Constant Hydrogen Flux at the Entrance Face.

Assuming a slab of thickness L, which is being charged with hydrogen, galvanostatically from one side (x = 0) with the hydrogen atoms discharged rapidly from the exit side (x = L), the appropriate boundary conditions are:

t = 0	0 < x < L	C = 0
t > 0	x = L	C = 0
t = ∞	x = 0	$J_t = J_\infty = C_0FD/L$
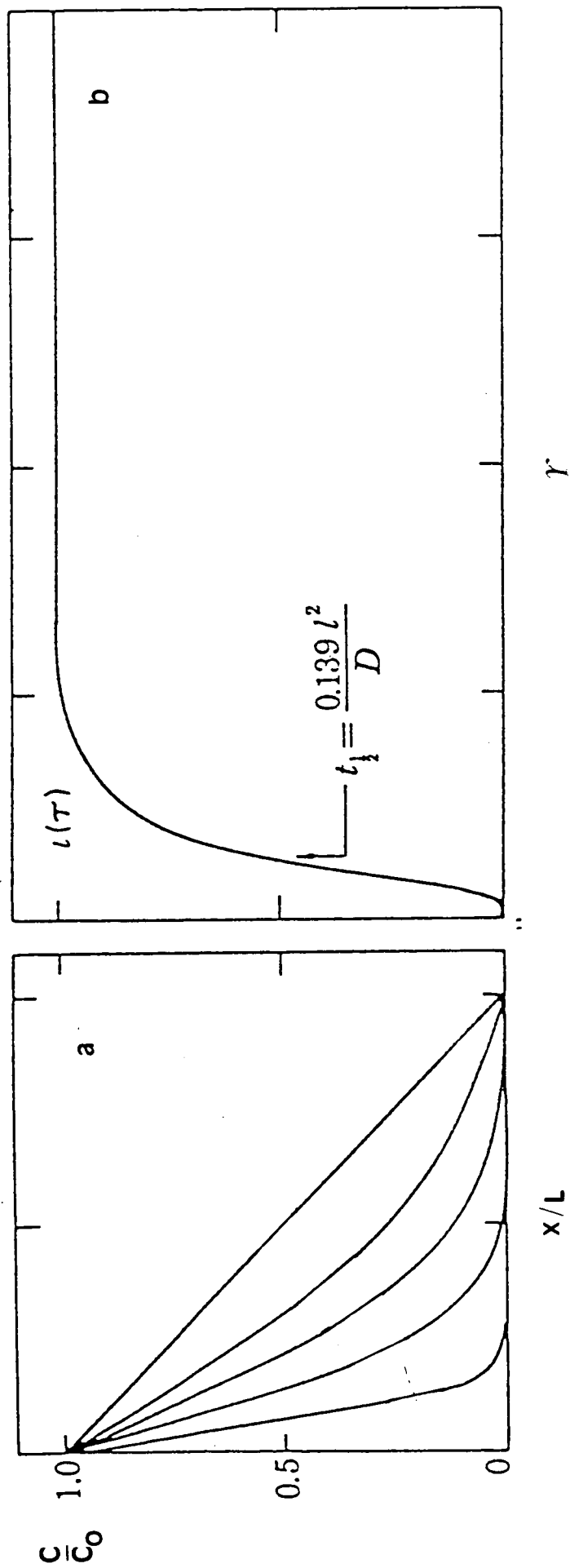
Figure 70 (a) Normalised Concentration Profile and (b) Permeation Current for Constant Surface Hydrogen Concentration Boundary Conditions[37].

211

Where J_t = flux at time t, and J_∞ = flux at steady state conditions.

The solution to equation **[62]** obtained by Fourier Transform method[38], relating the distribution of hydrogen through a slab of thickness L at a time t, expressed in dimensionless variables defined by equations [8-11], is given by:

$$\sigma(\chi, \tau) = \qquad \qquad \qquad \qquad \qquad \qquad [65]$$

$$(1-\chi) - \frac{8}{\pi^2} \sum_{n=0}^{\infty} \frac{(-1)^n}{(2n+1)^2} \sin\left[\frac{(2n+1)\pi(1-\chi)}{2}\right] \exp\left[\frac{-(2n+1)^2\pi^2\tau}{4}\right]$$

The permeation current recorded as a result of holding the surface hydrogen concentration at the efflux surface at zero is given by[38]:

$$i(\tau) = 1 - \frac{4}{\pi} \sum_{n=0}^{\infty} \frac{(-1)^n}{2n+1} \exp\left[\frac{-(2n+1)^2\pi^2\tau}{4}\right] \qquad [66]$$

Equation **[65]** is represented graphically in Figure 71(a) for various times of charging. The equivalent current transient is shown in Figure 71(b).

5.5.3 Initial and Boundary Conditions Arising from a State Where the Flux of Hydrogen Entering the Charged Surface is Limited by Surface Reaction Rates.

Assuming a slab of thickness L, which is being charged with hydrogen, either potentiostatically or galvanostatically from one side (x = 0) with the hydrogen atoms discharged rapidly from the exit side (x = L), the appropriate boundary conditions are:
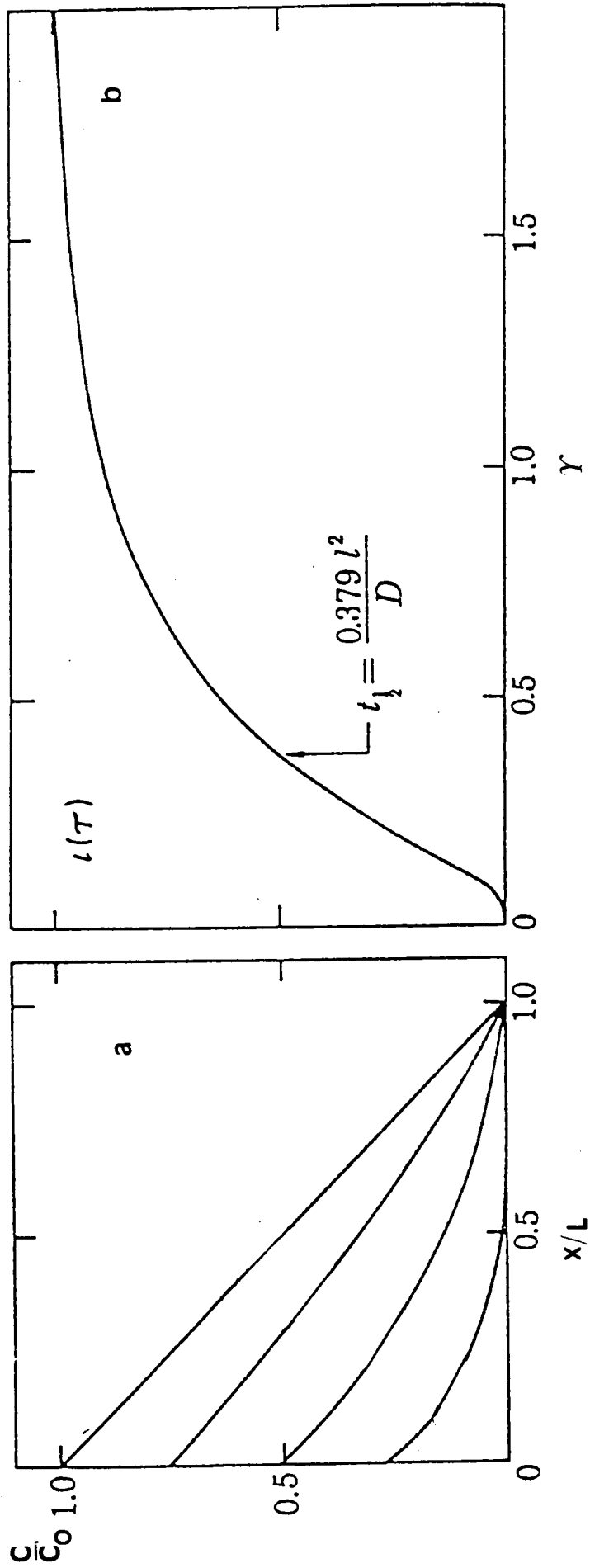
Figure 71 (a) Normalised Concentration Profile and (b) Permeation Current for Constant Hydrogen
Flux Boundary Conditions[37].

213

$$t = 0 \qquad 0 < x < L \qquad C = 0$$

$$t > 0 \qquad x = 0 \qquad J_t = K_{abs}\Theta - K_{des}C$$

$$\qquad\qquad x = L \qquad C = 0$$

$$\frac{1}{J_\infty} = \frac{L}{D}\frac{K_{des}}{K_{abs}\theta} + \frac{1}{K_{abs}\theta}$$

$$t = \infty \qquad x = 0$$

Where k_{abs} and k_{des} are the finite rate constants for the transfer of hydrogen from the surface to the bulk and from the bulk to the surface of the metal respectively, and θ is the fraction of the charged surface covered by hydrogen.

It was suggested by Chaudhari and Radhakrishnan[48] that the flux of hydrogen on the entry side decreases with time as the surface hydrogen concentration, C, increases from the initial to the steady state value.

The solution to equation [62] obtained by Fourier Transform method[38], relating the distribution of hydrogen through a slab of thickness L at a time t is given by:

$$-\sigma_{(\chi,\tau)} = \frac{K_{abs}\theta\,(-1-\chi)}{DK_{des}} - \left[\frac{2LK_{abs}\theta}{D}\right]\sum_{n=1}^{\infty}\frac{\{\sin\beta_n(-1-\chi)\}\exp^{(-\beta_n^2\tau)}}{[s+s^2+\beta_n^2]\sin\beta_n} \qquad [67]$$

where β_n, n = 1,2,3... are the positive roots of:

$$\beta\cot\beta + s = 0 \qquad\qquad [68]$$

and:

$$s = \left[\frac{LK_{des}}{D}\right]$$

Solutions to equation [68] are given in Appendix (I), Table A1 for values of s

214

between -1 and infinity[38].

The permeation current recorded as a result of holding the surface hydrogen concentration on the exit surface at zero is given by:

$$J_\tau = \frac{K_{abs}\theta}{1+s} - 2K_{abs}\theta \sum_{n=1}^{\infty} \left[\frac{\beta_n \exp^{-\beta_n^2 \tau}}{s(1+s) + \beta_n^2 \sin\beta_n} \right] \qquad [69]$$

The first term approximation to equation [35] for a value of n=1 can be written as:

$$J_\tau = \frac{1}{\sin\beta_1} \frac{2\beta_1(1+s)}{\left[s(1+s) + \beta_1^2\right]} \exp^{-\frac{t}{t_0}} \qquad [70]$$

Where:

$$t_o = \frac{L^2}{\beta_1^2 D}$$

Equations [67] and [70] are represented graphically in Figures 72 and 73 respectively for a value of s=2.

In each of the three models shown above, at infinite times, steady state conditions are achieved and the hydrogen concentration within the slab has reached a uniform linear gradient. At this time the permeation current has reached a constant steady state value which is independent of time. This steady state value for the permeation current in each case described above is given by:

$$J_\infty = \frac{DC_0 F}{L} \qquad [71]$$

Figure 74 shows a schematic representation of a generalised permeation transient outlining the major parameters which may be derived from such a graph. One of the most important parameters which may be indirectly

215

deduced from the transient is the apparent diffusion coefficient. Devanathan and Stachurski[36] documented several methods for calculating the diffusion coefficient from the shape of the hydrogen permeation transient under constant surface hydrogen concentration boundary conditions. Several of these methods have been applied to experimental transients for the BS Z25 material. The various parameters and resulting diffusion coefficients are described in section 5.6.
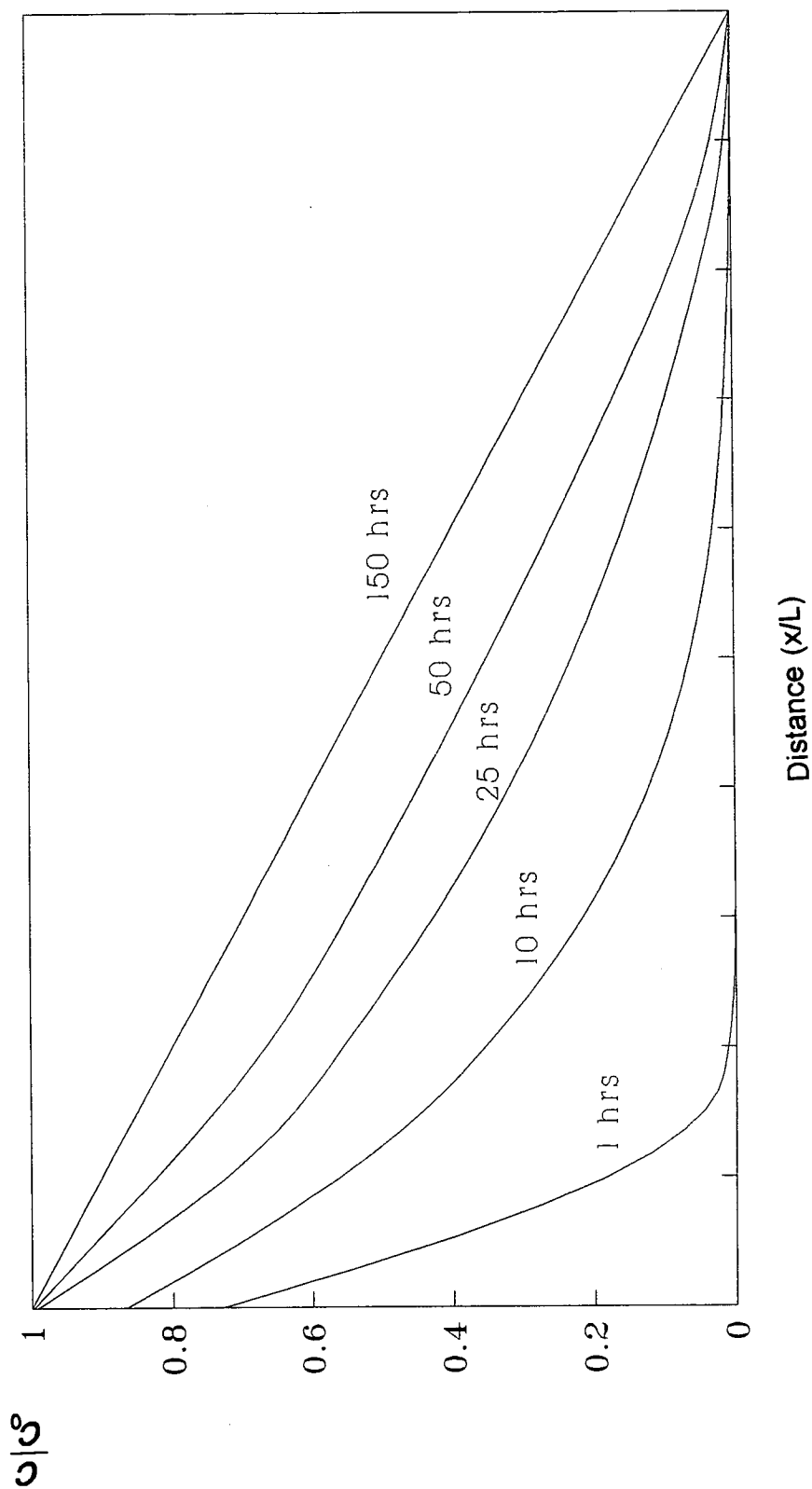
Figure 72   Normalised Concentration Profile for Boundary Conditions Where the Hydrogen Flux is Influenced by the Surface Reaction Rates[37].

217
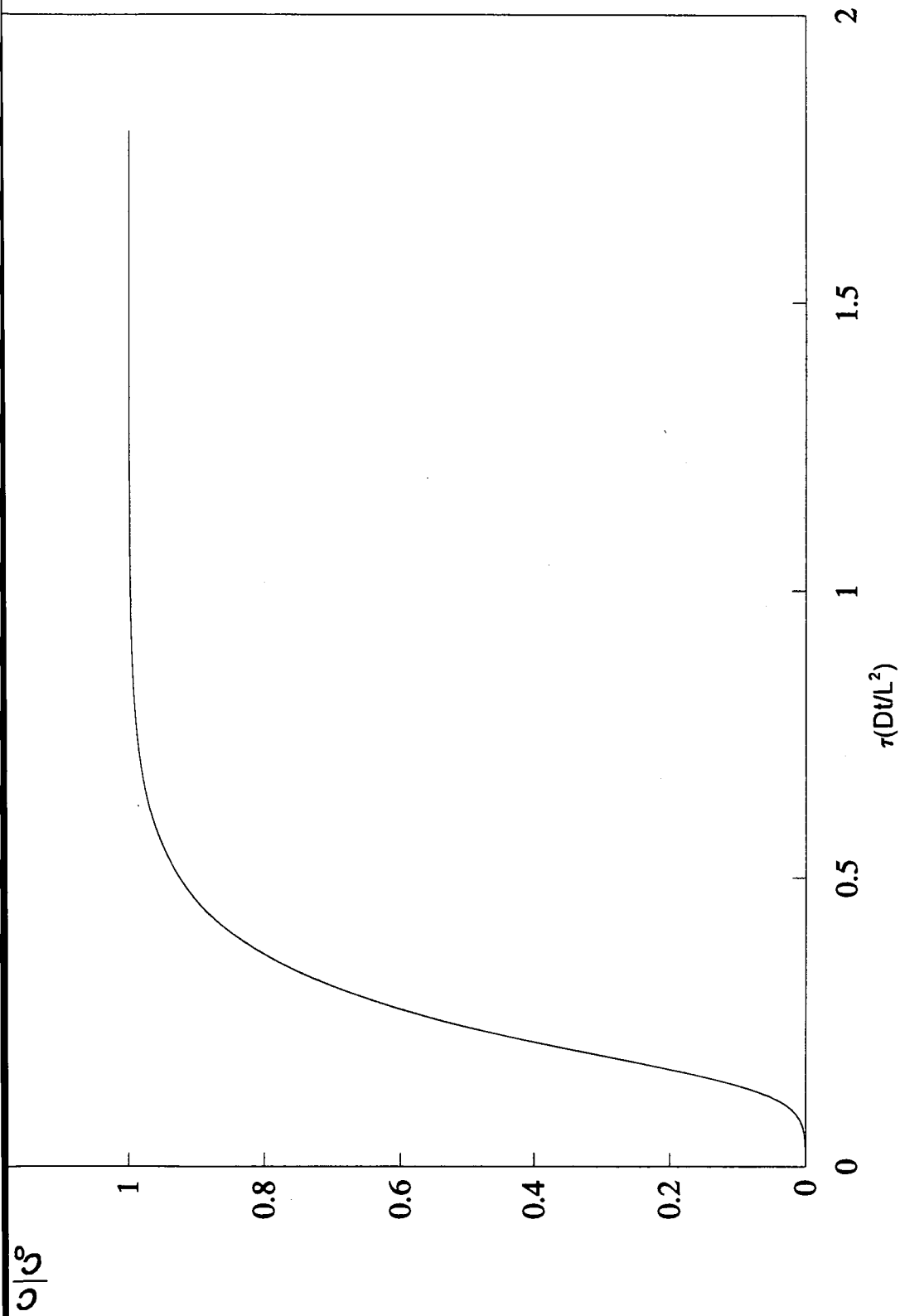
Figure 73   Normalised Permeation Transient for Boundary Conditions Where the Hydrogen Flux is Influenced by the Surface Reaction Rates[37].

218
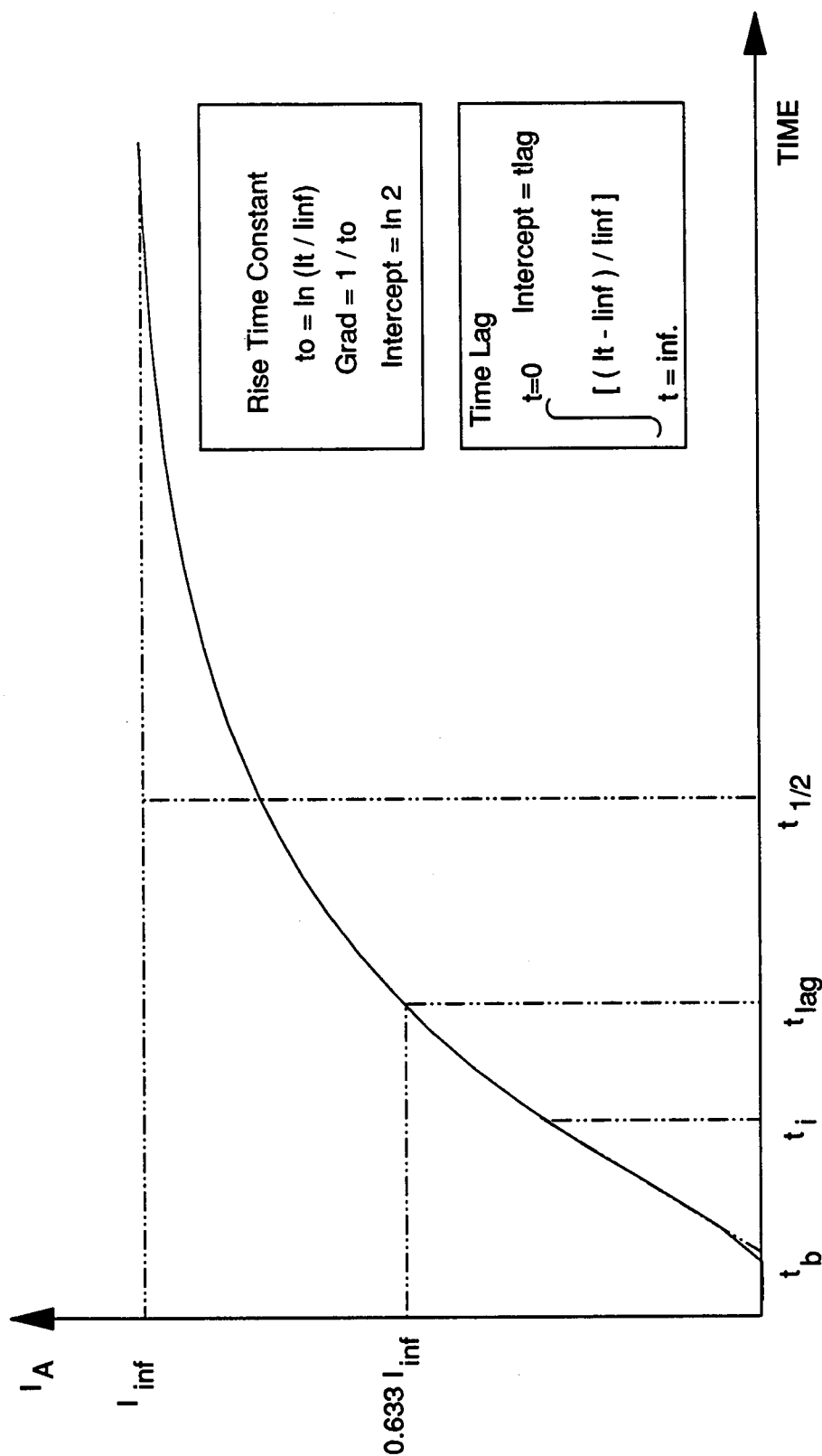
Figure 74. Generalised Hydrogen Permeation Transient Outlining the Various Parameters Employed to Determine the Effective Diffusion Coefficient of Hydrogen in Steel.

219

5.6   Determination of the Diffusion Coefficient.

The conventional glass cell permeation apparatus, or bi-polar cell arrangement, is depicted schematically in Figure 28. This particular arrangement was first described by Devanathan and Stachurski[36]. Values of the diffusion coefficient were estimated from various expressions relating the diffusion coefficient to time intervals on the permeation transient with constant surface hydrogen concentration boundary conditions. Values for t_i, the time at which the first hydrogen emerges from the efflux surface were estimated from the initial part of the transient. The half-rise time constant, $t_{\frac{1}{2}}$, was estimated as half the time taken to achieve steady state conditions, J_∞, i.e. where the permeation current became independent of time. Values for t_b, the breakthrough time, were taken by extrapolation of the linear part of the rise transient, i.e. from the first point of inflection, to the x axis. The following relationships were considered:

5.6.1 Breakthrough Time t_b.

The time lag can be shown to be equal to the sum of the rise time constant and the breakthrough time t_b[36]. Hence the diffusion coefficient is related to the breakthrough time by:

$$t_b = \frac{L^2}{D}\left(\frac{1}{6} - \frac{1}{\pi^2}\right) = \frac{L^2}{15.3D} \qquad [72]$$

Values of the diffusion coefficient were also calculated using expressions for the time lag, t_{lag} and the time constant, t_0 shown in Figure 74.

5.6.2 Time Lag Method T_{lag}.

By integrating the rising curve shown in Figure 74 and assuming the surface hydrogen concentration to be constant, the quantity of hydrogen which has permeated through the steel can be obtained at various times. An extrapolation of the plot of quantity against time gives the time lag, T_{lag}, which is related to the diffusion coefficient by:

$$T_{lag} = \frac{L^2}{6D} \qquad [73]$$

It has also been shown that the T_{lag} method may be simply obtained by spotting the time at which the rate of permeation is 0.633 times the steady state value, J_∞[23].

5.6.3 The Rise Time Constant t_0.

It can be shown that the equation to the rising transient is given by[36]:

$$\ln\left(\frac{J_t - J_\infty}{J_\infty}\right)_{x=0} = \ln\left[1 - e^{-3\frac{t}{t_0}} + e^{-8\frac{t}{t_0}} \dots\right] + \ln 2 - \frac{t}{t_0} \qquad [74]$$

where t_0, the rise time constant is related to the diffusion coefficient by the equation:

$$t_0 = \frac{L^2}{\pi^2 D} \qquad [75]$$

The first term on the right-hand side of equation [74] is indeterminate at t = 0 but rapidly decreases to zero, so that for times which are greater than zero a plot of $\ln\left[\frac{J_t - J_\infty}{J_\infty}\right]_{x=0}$ against t should have an intercept of ln 2 and a gradient of $1/t_0$.

5.6.4 The Decay Time Constant

If we consider time, t, as zero from the instant at which permeation begins to decrease for the decay transient it can be shown that[36]:

$$J_{(x=0)\,t} = J_{(x=0)\,(t=0)}\, e^{-\frac{t}{t_0}} \qquad [76]$$

where t_0 is given by equation [75]. Hence a logarithmic plot of $(J_t/J_{t=0})_{x=0}$ against time should have the same gradient as the logarithmic plot for the rising transient but would have zero intercept.

The methods used to determine values for the t_{lag} and t_0 expressions seem to be the most reliable as they take into account the overall distribution of the rise transient. Expressions such as t_i and t_b only utilise the first part of the rise transient which may be erroneous if in the initial stages of permeation the transport of hydrogen is not completely diffusion controlled. This is particularly apparent in very thin plates where, there may be a contributory influence from surface reaction rates or secondary oxidation processes due to trace impurities in the charging electrolyte.

Figures 48 and 49 show experimental rise transients obtained with the glass cell arrangement shown in Figure 26 for the BS Z25 plate. From this graph, values for the various time constants were obtained and are given in Table 23.

The values for t_i were taken at the point where the transient began to rise. The values of t_b were obtained by extrapolation of the linear part of the rise transient i.e. from the first point of inflection, to the x axis. The half-rise time constant, $t_{1/2}$, was calculated as half the value of the point where the permeation current became independent of time, i.e. when J_∞ was established.

222

Table 23. Summary of Parameters Derived From the Hydrogen Permeation Transient.

Boundary Condition Models	t_b	t_i	t_{lag}	t_0	$t_{\frac{1}{2}}$
Constant Surface Hydrogen Concentration.	$0.5L^2/\pi^2 D$	$0.924L^2/\pi^2 D$	$L^2/6D$	$L^2/\pi^2 D$	$0.138L^2/D$
Constant Flux.	$0.76L^2/\pi^2 D$	$1.65L^2/\pi^2 D$	$L^2/2D$	$4L^2/\pi^2 D$	$0.38L^2/D$
Constant Surface Coverage.				$0.13L^2/D$	

Values for the time lag, t_{lag} were established graphically and are shown in Figures 50 and 51. Values for the time constant, t_0, were also found graphically and are shown in Figures 52 and 53. The values for t_0 were established from the relationship shown in equation [74]. The t_{lag} constant was determined as the integral flux, i.e. $\int(J_t/J_\infty)$ between the limits $t = 0$ and $t = \infty$. At longer times the plot became linear, hence from a linear least squares analysis and extrapolation to the x axis, values of t_{lag} were found.

Table 24   Summary of Time Constants.

Time Constants	t_{lag} / hours	t_b / hours	$t_{1/2}$ / hours	t_0 / hours	t_i / hours
Experiment 1	40.8	13.0	82.4	40.5	7.41
Experiment 2	57.8	14.8	117.5	37.9	9.26

Between the two experiments, in the case of the t_0 values, there was a maximum deviation of 7%, and in the case of the t_{lag} method there was a maximum deviation of 29%. Corresponding values of the apparent diffusion coefficient were calculated for each model and are given in Table 25. Their relationships with D are shown in Table 23.

Table 25   Summary of Apparent Diffusion Coefficients Calculated for the BS Z25 Material Using the Three Models for Hydrogen Diffusion.

Model	Experiment	$D_{app.}$ From t_{lag} cm^2 s^{-1} x 10^{-7}	$D_{app.}$ From t_0 cm^2 s^{-1} x 10^{-7}
Constant Concentration.	1	3.16	1.94
	2	2.23	2.07
Constant Flux	1	7.69	76.5
	2	5.43	81.7
Constant Surface Coverage	1		2.49
	2		2.66

5.7 The Conventional Permeation Cell, Interpretation of Experimental Results.

Figure 75 shows the theoretical transients derived from equations [64, 66, 70] and are shown in their normalised form i.e $[(J_t-J_0)/(J_\infty-J_0)]$, where J_t is the flux of hydrogen at time t, J_∞ is the steady state flux of hydrogen and J_0 is a small background value of hydrogen which exists in the material.

In the case of the constant hydrogen concentration boundary conditions, the permeation transient rises sharply because the concentration gradient is very high at short times, representing a step function in hydrogen concentration. In the case of the constant flux boundary conditions, the permeation current rises more slowly than that in the constant hydrogen concentration boundary conditions because the flux of hydrogen entering the membrane is constant and remains at that value rather than being initially high and decreasing with respect to time. In the situation, where hydrogen entering the surface is limited by the surface reaction rates, the flux of hydrogen on the entry side decreases with time as the surface hydrogen concentration, C_0, increases from the initial to the steady state value.

The theoretical permeation transients for these three types of boundary condition[37] are compared with the experimental transients in Figure 76. It is apparent that the experimental case was not uniquely defined by any one of the theoretical conditions but that it was intermediate between constant surface coverage and constant flux conditions. It is worth commenting, however, that while the theoretical boundary conditions affect the assumed rise in the surface hydrogen concentration, once steady state conditions have become established the C_0 value calculated from equation [77] will be independent of the model chosen.
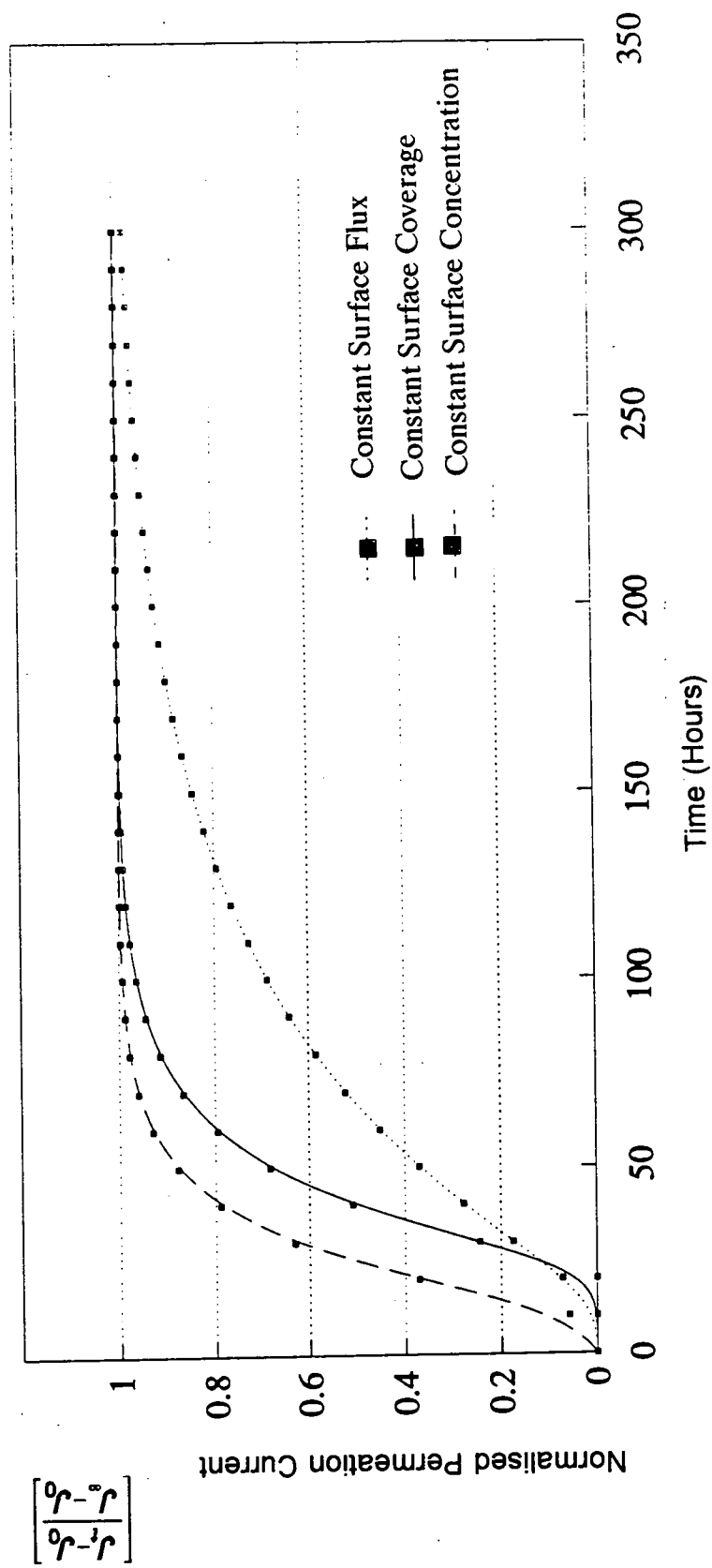
Figure 75. Theoretical Permeation Transients Derived for the Three Different Boundary Conditions.

226
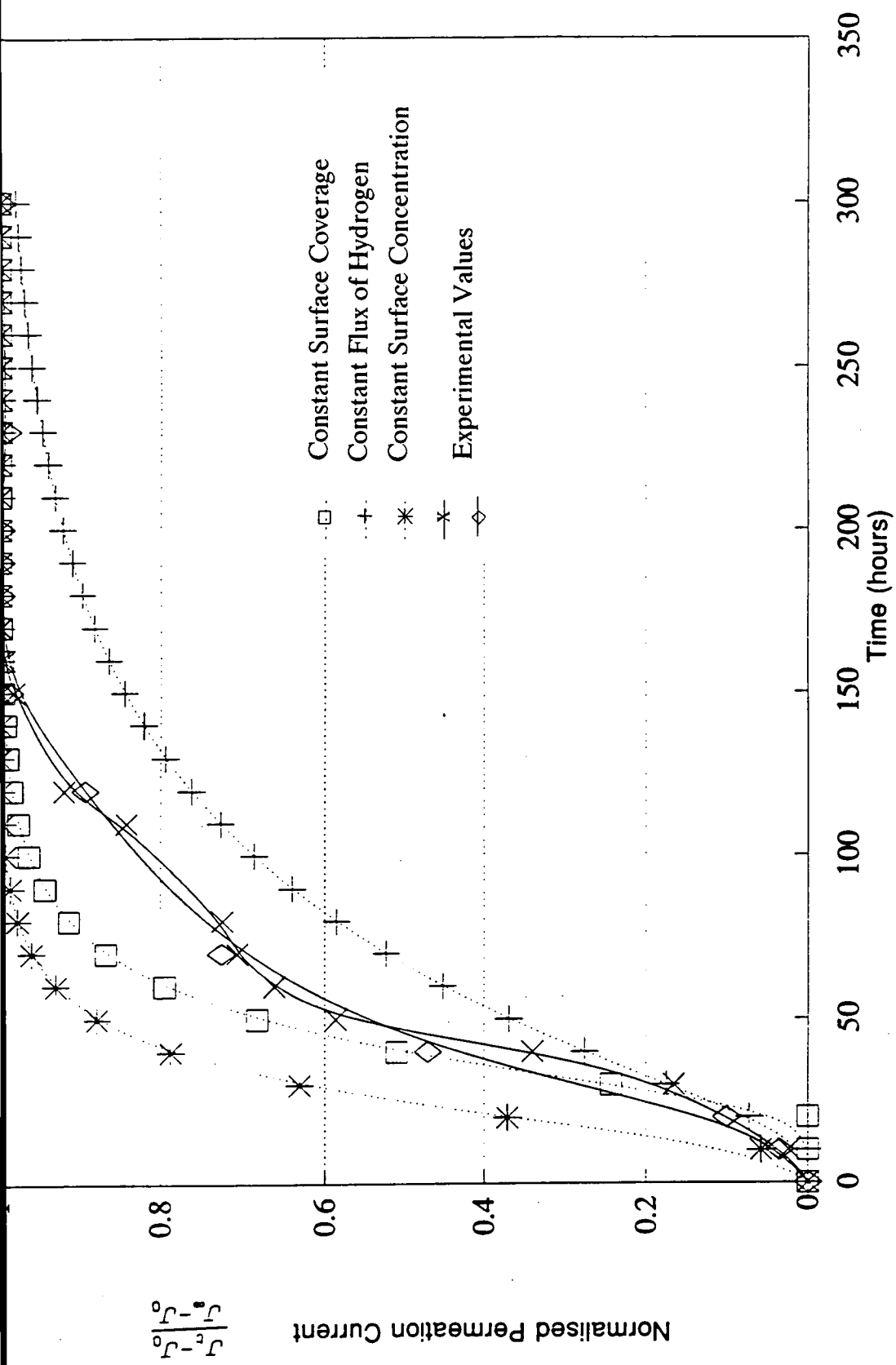
Figure 76. Comparison Between Experimental and Theoretically Predicted Permeation Transients for the Three Different Boundary Conditions.

227

$$C_0 = \frac{J_\infty L}{FD}$$ [77]

Through the duration of the experiments, the potential at the influx surface, cathodic compartment, was monitored using a mercury/mercury sulphate reference electrode. The values obtained are shown graphically in Figure 77 with respect to the normal hydrogen scale. After approximately 40 hours of charging, the potential reached a steady state value in each case between approximately -0.53 V and -0.5 V (NHE). From this value an approximate indication of the hydrogen overvoltage could be obtained by manipulation of the IPZ model[25] consequently an estimation of the hydrogen surface coverage, θ, was established from extrapolation of the hydrogen overvoltage versus surface coverage plot as shown in Figure 46.

Figure 78 shows the theoretical distribution of hydrogen through a 5 mm slab described by equation [63]. The boundary conditions at the efflux surface are such that the hydrogen concentration is held at zero. Consequently at infinite times the concentration gradient across the plate is essentially linear.

The profile taken after around 10 hours shows the breakthrough of hydrogen at the efflux surface. This time is calculated from equation [78], i.e.:

$$t_b = \frac{L^2}{15.3D}$$ [78]

Equations [64, 66, 70], describing the flux of hydrogen through the steel, represented in Figure 75, and equations [63, 65, 67], describing the distribution of hydrogen throughout the slab, shown for equation [63] in Figure 78, are essentially the same. When examining the flux at the charging surface, however, the boundary conditions are set at x=0 and the flux is

monitored with respect to time. In the case of the hydrogen distribution through the slab, the time is fixed and the distance x from the charging surface is varied between 0 and L, the slab thickness.
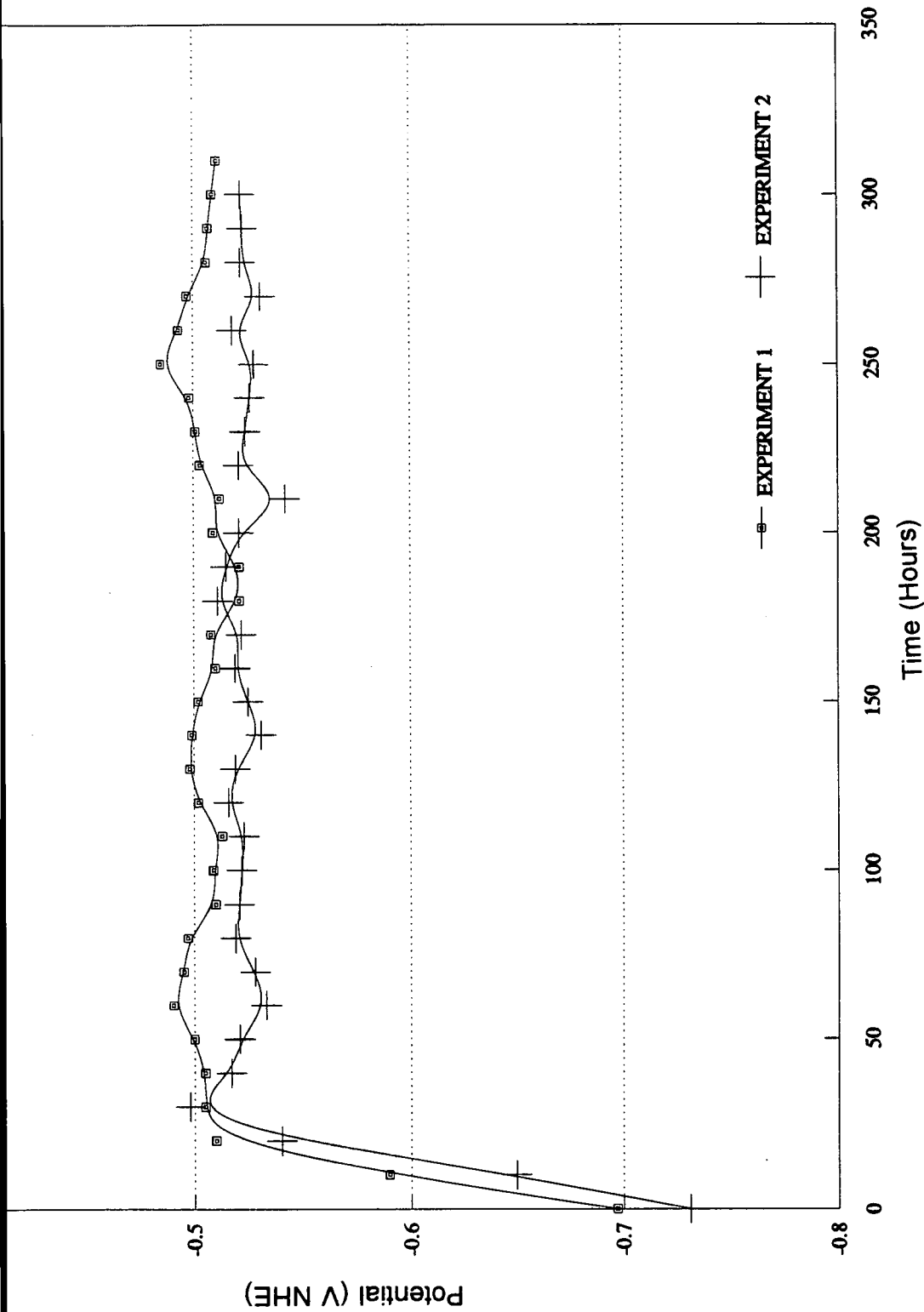
Figure 77.   Potential Fluctuations at the Influx Surface of the Steel Plate During Galvanostatic Cathodic Hydrogen Charging.

230
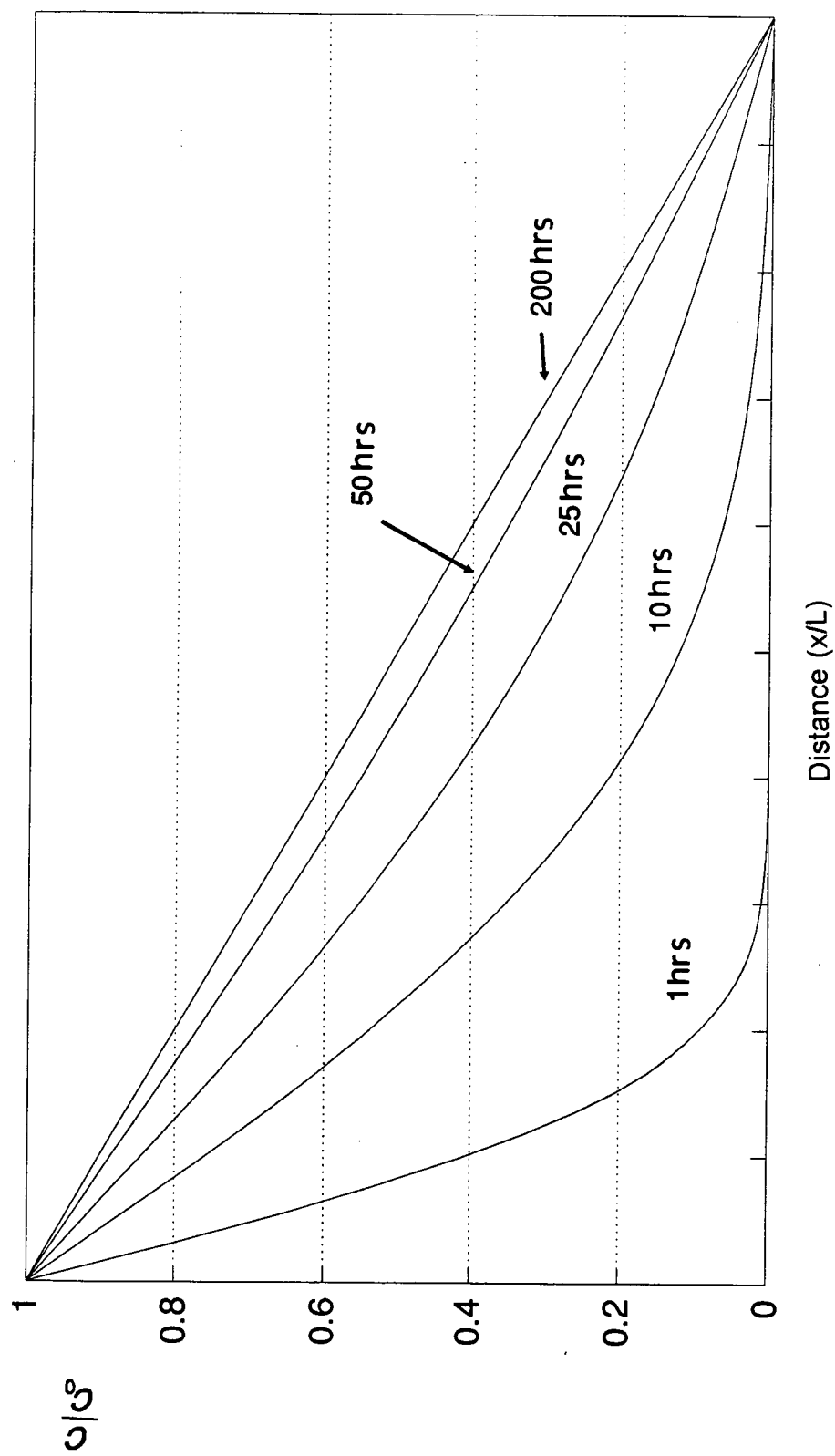
Figure 78.   Theoretical Hydrogen Concentration Profiles for a Steel Plate With Constant Influx Surface Hydrogen Concentration Conditions Assuming the Efflux Concentration is Maintained at Zero.

231

5.8 Gel-filled Hydrogen Probe, Interpretation of Experimental Results from the Influx Surface.

The expected changes in hydrogen concentration on the influx surface for each of the three boundary conditions are shown in Figure 79 and were derived from equations [63, 65, 67] expressed in terms of C/C_0 for the condition $x/L = 0$. For the potentiostatic (constant surface concentration) boundary conditions, the full solution is of the form[38]:

$$\frac{C_{(x,t)}}{C_0} = (1-\chi) - \frac{2}{\pi}\sum_1^{\infty} \frac{1}{n} \sin n\ \pi\chi\ \exp(-n^2\pi^2\tau) \qquad [79]$$

The experimental measurements on the influx surface using the gel-filled probe, expressed as the fractional change C/C_0, are compared in Figure 80 with the theoretical values for the constant surface coverage and constant flux boundary conditions.

The increase in surface hydrogen concentration recorded by the gel-filled probe was in broad agreement with that predicted by the diffusion equations. More detailed examination shows that the increase occurred more slowly than that calculated for the constant surface coverage model yet more rapidly than suggested by the constant flux boundary conditions.

It appeared that when the power supply was switched on and charging commenced, there was an initial jump in surface hydrogen concentration at the steel surface. This was observed in the experimental probe readings after 1 hour of charging. During the first 40 hours of charging, the concentration on the input surface appeared to rise to a steady state value which then remained constant.

Figure 81 shows the experimental results for the probe readings on the influx surface up to 60 hours of charging. In the first experiment, the final value of
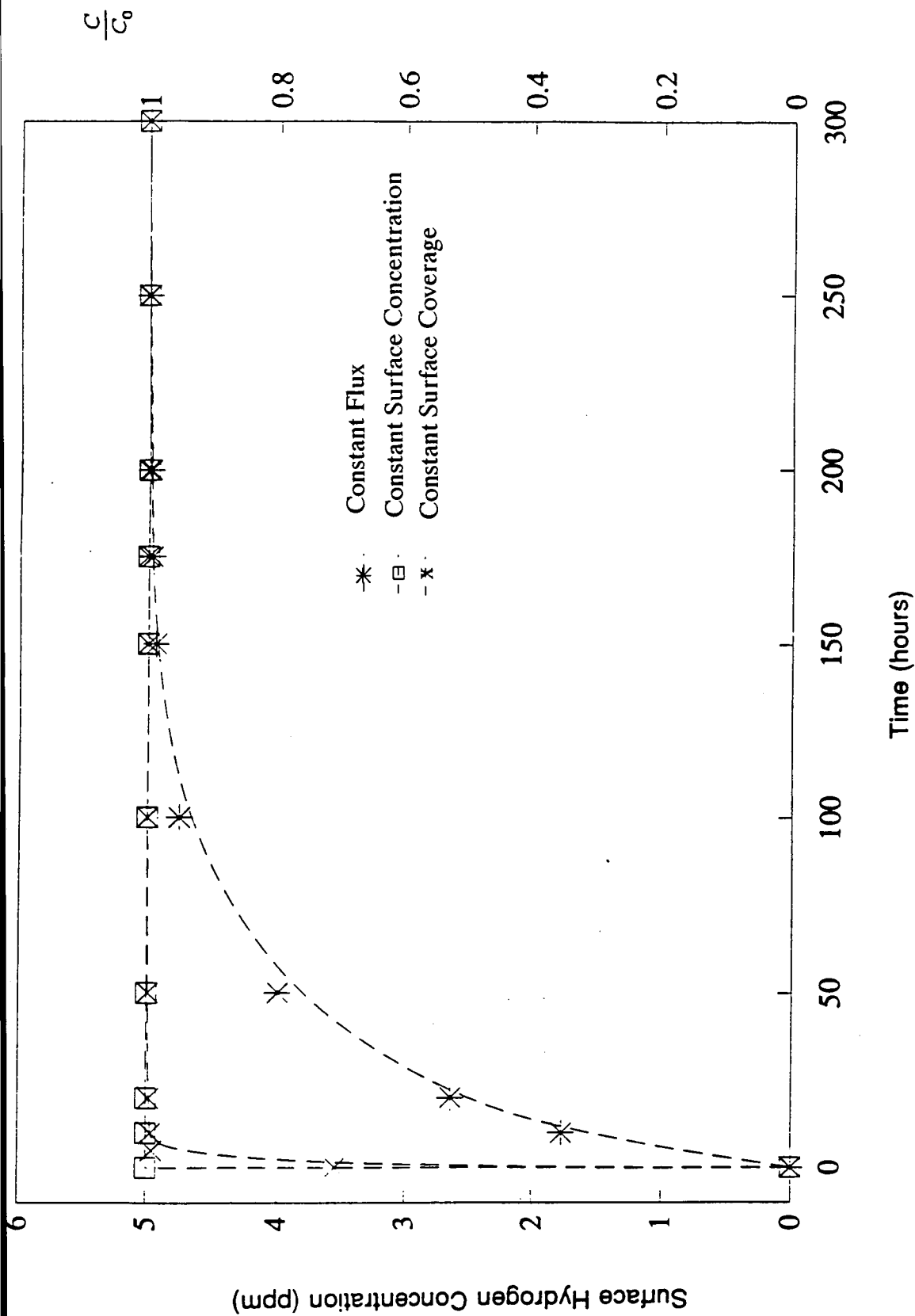
Figure 79.   Predicted Hydrogen Concentrations on the Influx Surface for Each of the Three Boundary Conditions.

233
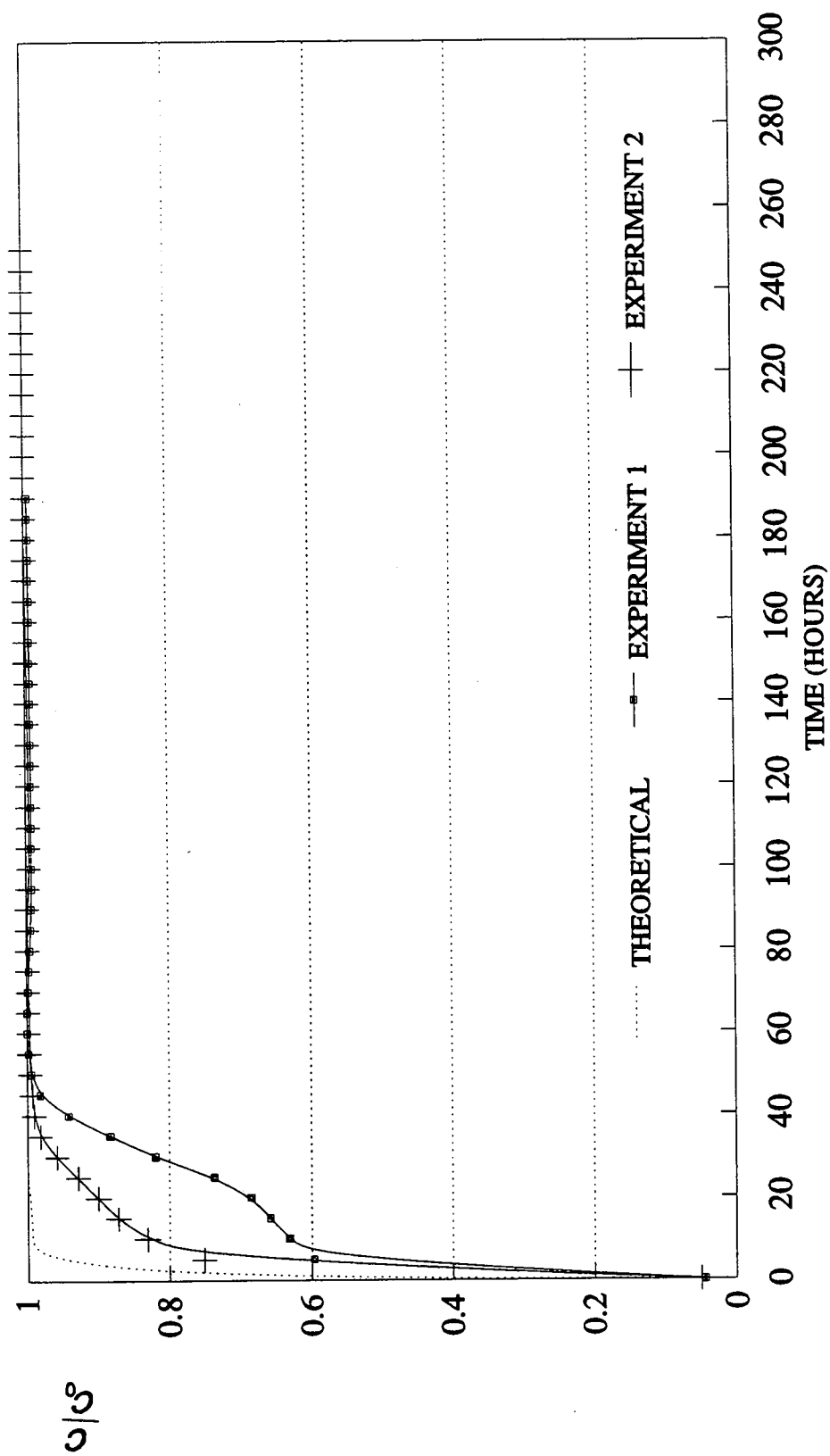
Figure 80.   Comparison Between Gel-Filled Probe Readings and Predicted Values on the Influx Surface.

234
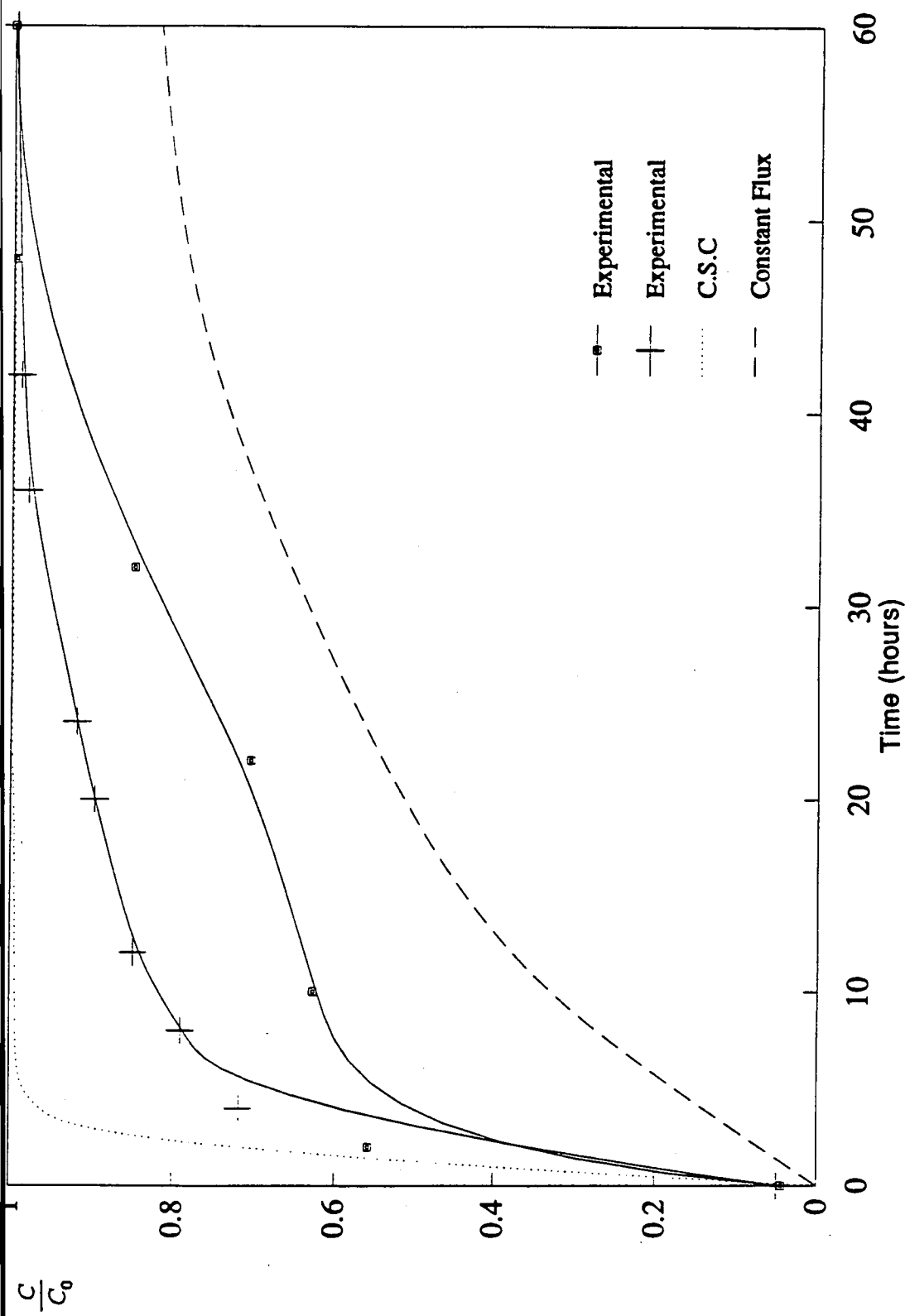
Figure 81.   Comparison Between Gel-Filled Probe Readings and Predicted Values on the Influx Surface During the First 60 Hours of Charging.

235

the steady state surface hydrogen concentration was slightly higher than that observed in the second experiment, 6.13 ppm compared to 5.86 ppm. This ultimately affected the relationship of C/C_0 for each transient and altered the final shape of the curve. There appears to be an approximate 10 fold increase in the time to establish a steady state surface hydrogen concentration for the experimental curves compared to the theoretical. This could be attributed to some loss in hydrogen from the charging surface during or just prior to probe readings. The surface preparation involved vigorous polishing which may have generated sufficient heat to encourage diffusion of hydrogen to the environment close to the input surface.

The differences in steady state surface hydrogen concentrations may be due to some extent to the formation of blisters on the input surface. This could have led to superficially high concentrations of hydrogen being recorded.

In a later chapter, the concept of hydrogen trapping will be considered. From the experimental findings, it would appear that the apparent diffusion coefficient of the material may be significantly affected by different numbers and distribution of trapping sites within the same material. An explanation for the different recorded surface hydrogen concentrations will be offered from a trapping theory point of view.

5.9   Comparison of the Gel-Filled Hydrogen Probe and the Conventional Permeation Cell.

5.9.1   The Two Probes.

Figure 82 shows a schematic of the gel-filled hydrogen probe and conventional permeation cell, highlighting the differences in operation and interpretation of results. The principal mode of operation is essentially the same, i.e. both devices maintain a constant potential at the steel surface in a suitable electrolyte which then oxidises hydrogen leaving that surface.

The conventional cell, holds the hydrogen concentration at the efflux surface at zero and maintains an essentially linear gradient at times when steady state conditions are established. The gel-filled hydrogen probe temporarily disturbs the hydrogen concentration gradient at the surface, to a depth of up to 0.6mm. Consequently, the conventional cell requires that comparatively long term experiments are performed to produce a transient similar to that shown in Figure 82b(ii) from which the steady state permeation current J_∞ is given and C_0 is calculated from:

$$J_\infty = \frac{nC_0FD}{L} \qquad\qquad [80]$$

The gel-filled hydrogen probe functions under non-steady state conditions. Provided the criteria specified in section 5.1 are met, a series of readings can be made within around 15 minutes, giving the flux at time t, J_t, as in Figure 82a(ii) leading to the surface hydrogen concentration, C_0, calculated from:

$$J_t = nFC_0\sqrt{\frac{D}{\pi t}} \qquad\qquad [81]$$

In summary, the conventional permeation cell relies on the flux being independent of time and the gel-filled hydrogen probe functions under time
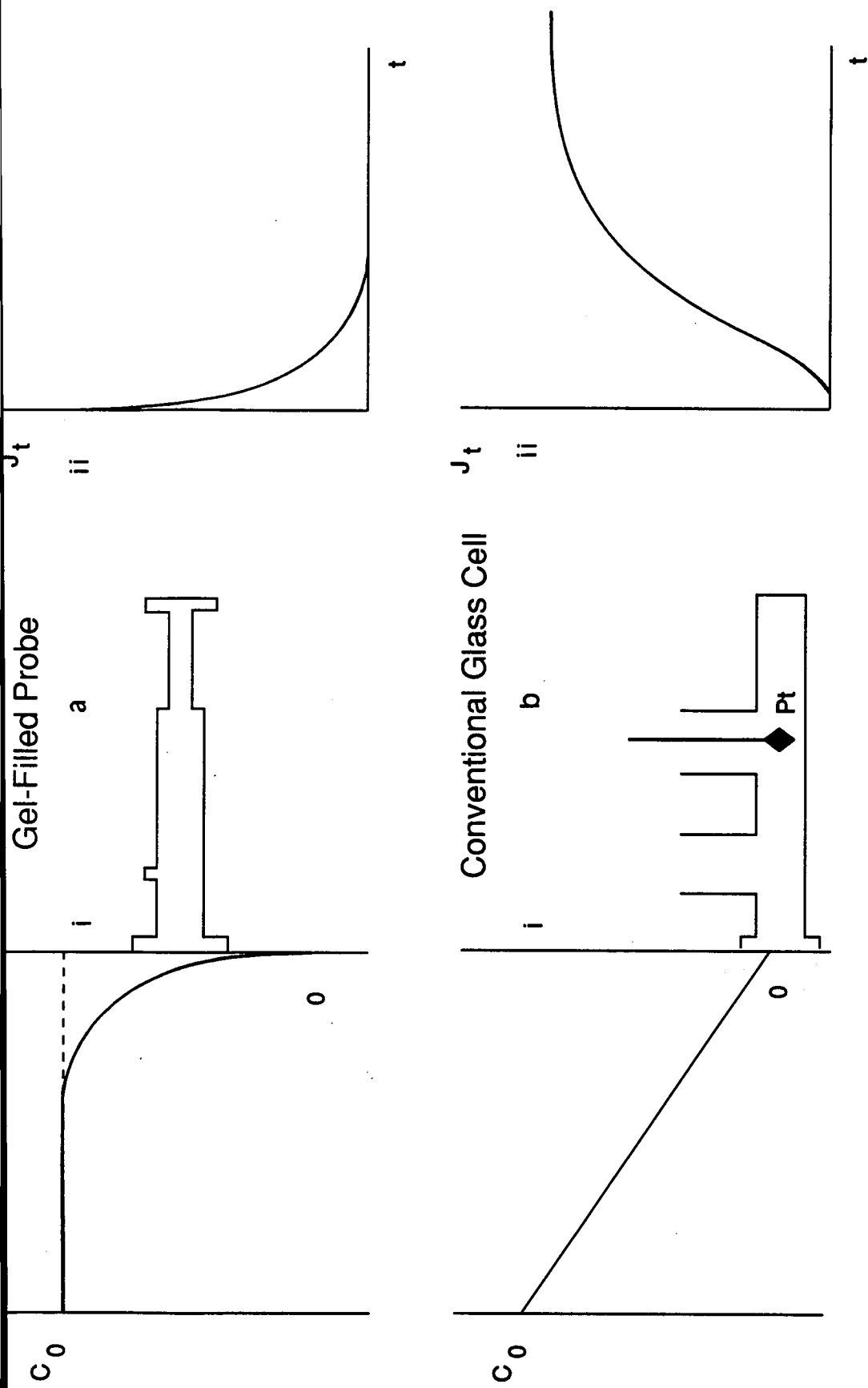
Figure 82. (a{i}) Gel-Filled Hydrogen Probe and (b{i}) Conventional Permeation Cell With Associated Boundary Conditions and Resulting Transients {ii}.

238

dependent non-steady state conditions.

One of the limitations of the conventional permeation cell is that surface hydrogen concentrations on the influx surface can only be inferred from the experimental permeation transients. This, however, does allow a direct comparison with the gel-filled hydrogen probe, as this device can record, directly the surface hydrogen concentration on both charging and exit surfaces. In comparing the experimental results from the conventional permeation cell with the theoretical transients given by equations [64, 66, 70], shown in Figure 76, and comparing the experimental results obtained with the gel-filled hydrogen probe with transients obtained from equations [63, 65, 67], at the influx surface (x=0), shown in Figure 80, it is evident that neither method conforms exactly to the theory.

As the constant surface coverage model was thought to give the closest description of the charging conditions[37] the reasons for this apparent discrepancy should be considered. The gel-filled probe readings and the permeation rise transient recorded independently by the electrochemical cell both lie between values predicted for the constant surface coverage and the constant flux boundary conditions. It appears that the two techniques were responding to the changing surface hydrogen concentrations in a similar manner and it may be assumed that both sets of measurements gave a good representation of the true surface condition.

To support this finding, a comparison between hydrogen concentrations measured on the influx surface using the gel-filled hydrogen probe were in good agreement with those derived from the permeation measurements as shown in Table 26.

Table 26. Comparison of Hydrogen Concentrations Measured on the Influx Surface Using the Permeation Technique and the Gel-Filled Probe

Surface Hydrogen Concentration, C_0 (ppm)	
Permeation Method	Gel-Filled Probe
6.7	6.1
6.6	5.9

5.10 Experimental Gel-Filled Hydrogen Probe Readings on the Efflux Surface.

Figure 83 represents the expected hydrogen concentration profiles through a 5 mm plate after a range of times assuming that the surface hydrogen concentration C_0 on the charging side remained constant and that there was no loss of hydrogen from the efflux side. These assumptions may, however, not hold true during the first 40 hours of charging as shown in Figure 81. At times greater than 40 hours, however, the value of C_0 appears to be constant. Provided the loss of hydrogen to the environment is minimal, then the assumptions are essentially valid.

The hydrogen concentration profiles were calculated using the Laplace Transform solution to Fick's Law of diffusion as given by Crank[38] and are represented by equations [63, 65, 67]. In the case of the gel-filled probe, the variation of permeation current with respect to time is of less importance as the probe measures a surface concentration rather than a distribution dependent on bulk properties of the material. The model used here to describe the distribution of hydrogen through a 5 mm slab assumes the plate to be 2L in thickness, (i.e. with a 5 mm slab, 2L is 10 mm). The charging is assumed to take place uniformly from both faces, i.e at L=0 and L=2L. Consequently, observation of the hydrogen distribution at L, (half the complete slab thickness), displays a situation where the hydrogen is allowed to top up at this new exit surface and no loss of hydrogen occurs. At infinite times, the distribution of hydrogen through the plate is essentially uniform and the surface hydrogen concentration on both sides is the same.

From these assumptions, while the predicted breakthrough time, equation [72], was estimated at approximately 14 hours, a time of 500 hours would be required for the hydrogen to reach an approximately uniform concentration through the material, according to the theoretical transient. By taking the

hydrogen concentrations on the efflux surface (expressed as C/C_0, where $x/l = 1$) for a range of times, a graph of the predicted probe readings was plotted as shown in Figure 84.

Figure 85 shows the probe's response as recorded on the efflux or exit surface together with a theoretical curve showing the predicted increase in surface hydrogen concentration.

The hydrogen concentrations could be expressed in ppm instead of C/C_0 provided the surface concentration, C_0, on the charging side of the plate was known. Having measured this value during cathodic hydrogen charging, plots of surface hydrogen concentration with respect to time were constructed.

The initial background hydrogen concentration of the steel was taken to be around 0.24 ppm for both of the experiments. The presence of a substantial background surface hydrogen concentration in the case of gel-filled probe measurements dictated different boundary conditions from those for the conventional glass cell. In the case of the glass cell, the initial background hydrogen concentration was reduced to a very low value and then maintained at this value. In the case of the gel-filled probe the surface hydrogen concentration was allowed to build up on the efflux surface. During the initial stages of the experiment the gel-filled probe readings appear to be in good agreement with the theory, possibly because C_0 was increasing at this stage. At times in excess of around 60 hours, however, there is considerable deviation from the theory and the surface hydrogen concentration appears to rise more rapidly. This time of 60 hours appears to correspond to the time for steady state conditions to be achieved at the input side, around 40 hours, with an additional time of around 20 hours or less, which approximates to the time for hydrogen to diffuse through the material.
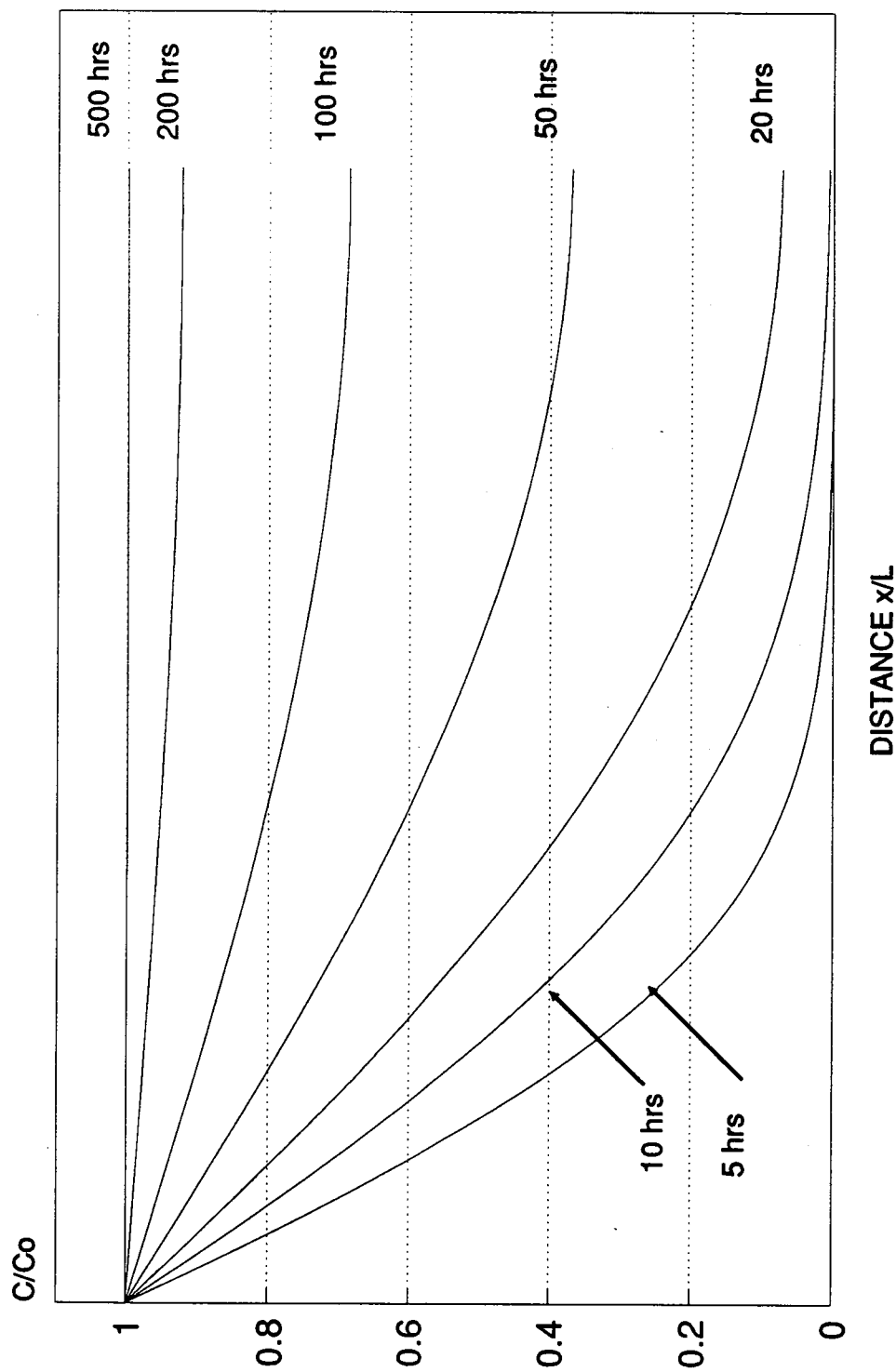
Figure 83.   Theoretical Hydrogen Concentration Profile for a Plate With Constant Influx Surface Hydrogen Concentration Boundary Conditions Assuming no Hydrogen Loss from the Efflux Surface.

243
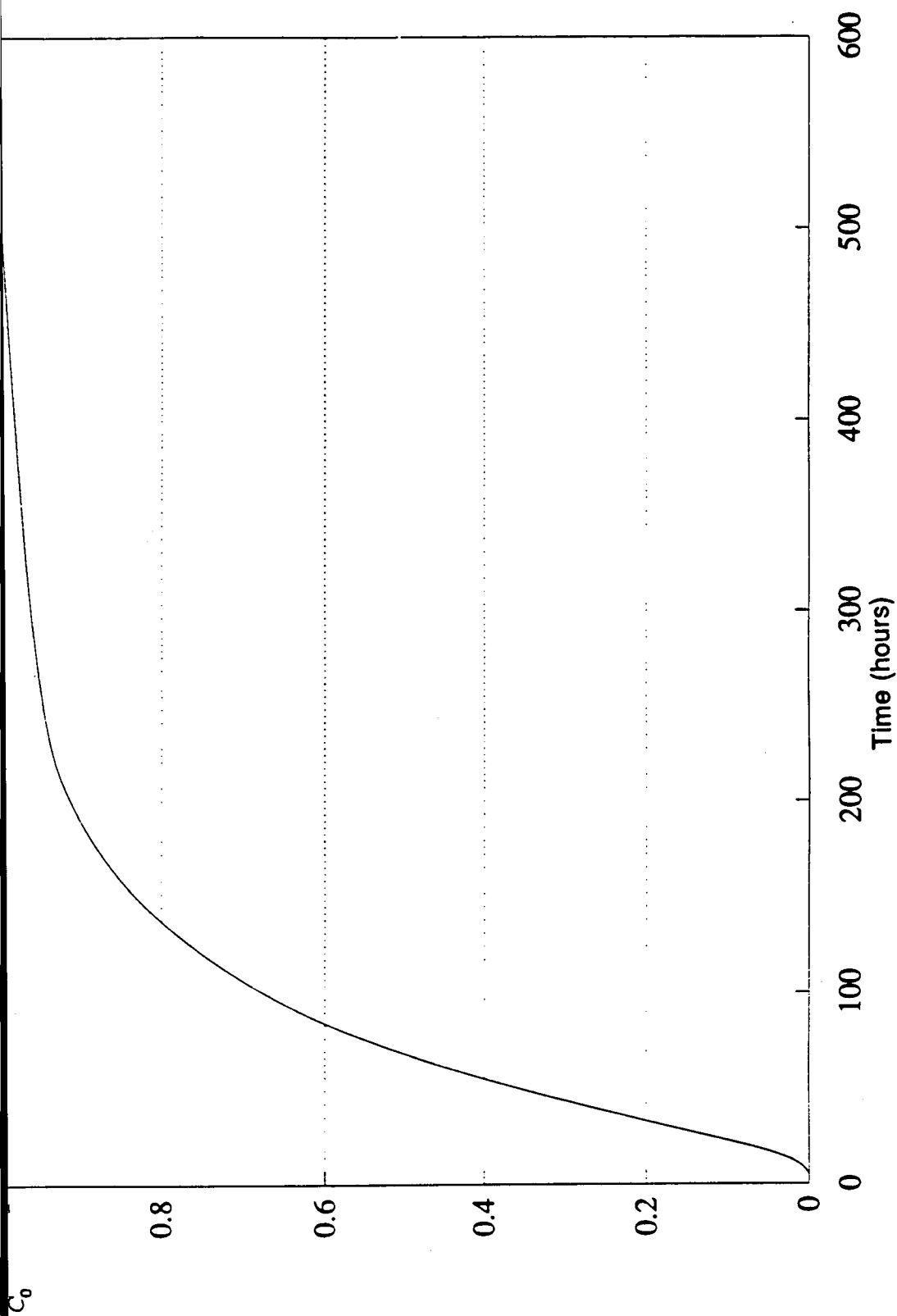
Figure 84. Theoretical Efflux Hydrogen Concentrations for Constant Concentration Boundary Conditions on the Influx Surface.

244
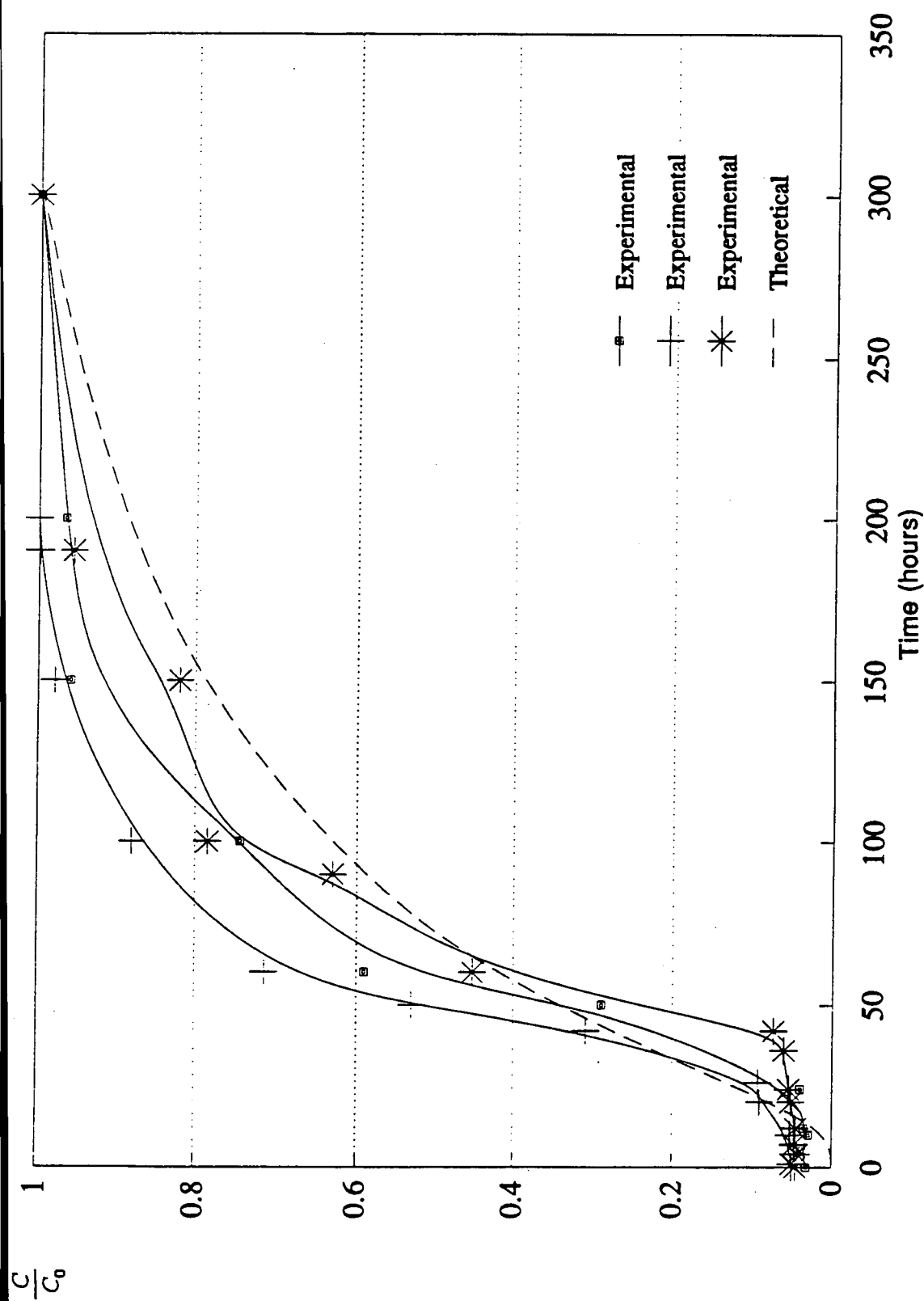
Figure 85.   Comparison of Experimental and Theoretical Efflux Concentrations for no Hydrogen Loss Conditions.

245

5.11 Hydrogen Concentration Gradient Across the Steel Plate.

It has been widely assumed that lattice hydrogen, once diffused through a steel plate, from the charging surface, escapes rapidly from uncoated steel at the opposite face. Consequently the concentration at a free surface is close to zero. In this situation, the distribution of hydrogen across a plate, charged continuously on one side, would approach the steady state condition shown in Figure 83, with the highest concentration at the influx surface. This assumption is supported by the fact that, in general, the walls of steel pipes and vessels in service display most microstructural hydrogen damage close to the surface that was exposed to the hydrogen charging environment[149].

The results of the gel-filled probe measurements, however, taken on both sides of the steel plate, shown in Figures 86 and 87, indicate that the hydrogen concentration on the efflux surface was not zero but after a long period of charging (approximately 20 times the breakthrough time) approached the concentration on the influx side. After 200 hours, the efflux concentration on the 5mm plate was approximately 90% of the influx value. The inference is that only a small proportion of the hydrogen that diffused through the plate was lost from the uncharged surface and an almost uniform hydrogen distribution was established as shown in Figure 83.
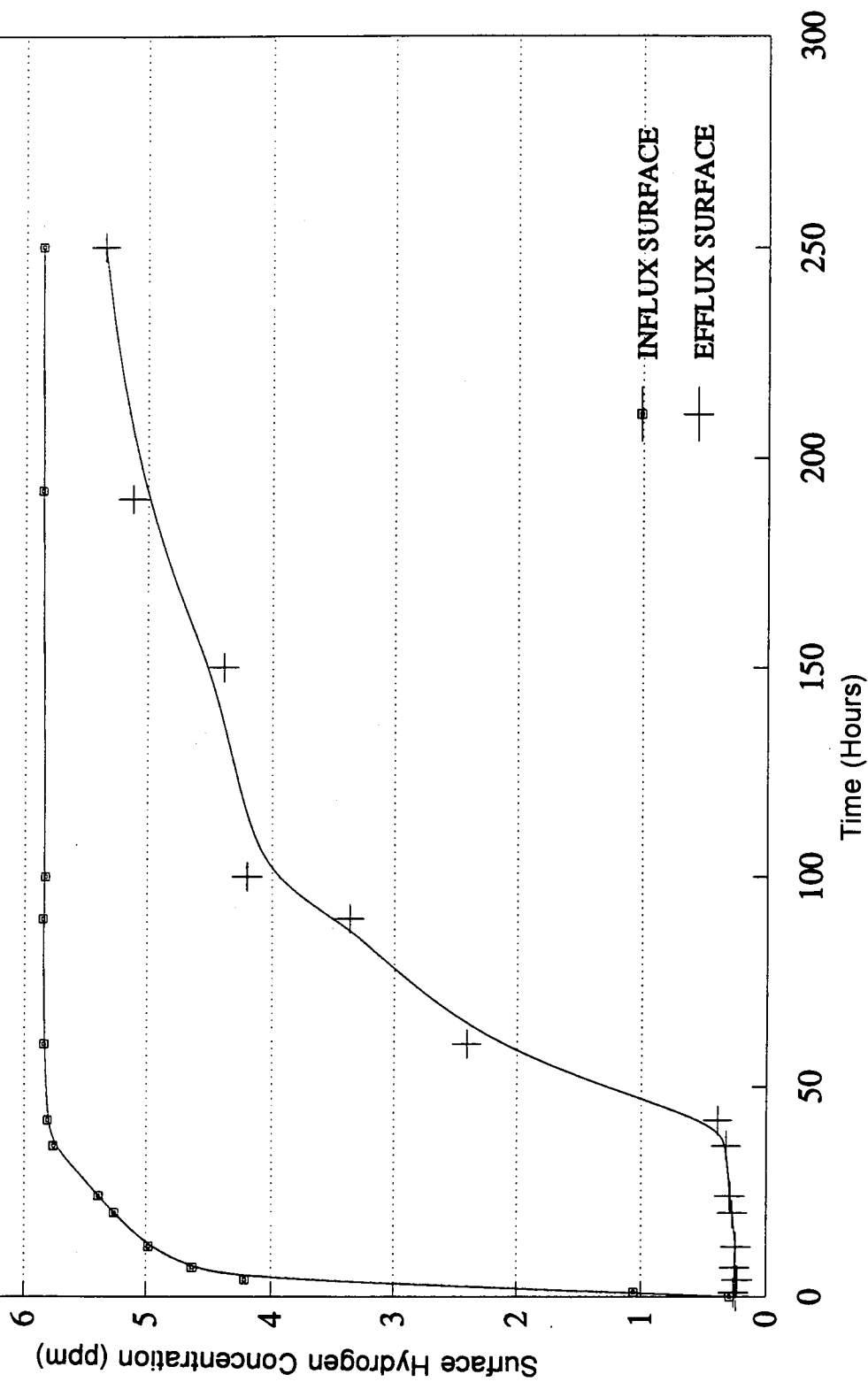
Figure 86.   Gel-Filled Probe Measurements Taken on Both Sides of the BS Z25 Steel Plate During Cathodic Hydrogen Charging, Experiment 1.

247
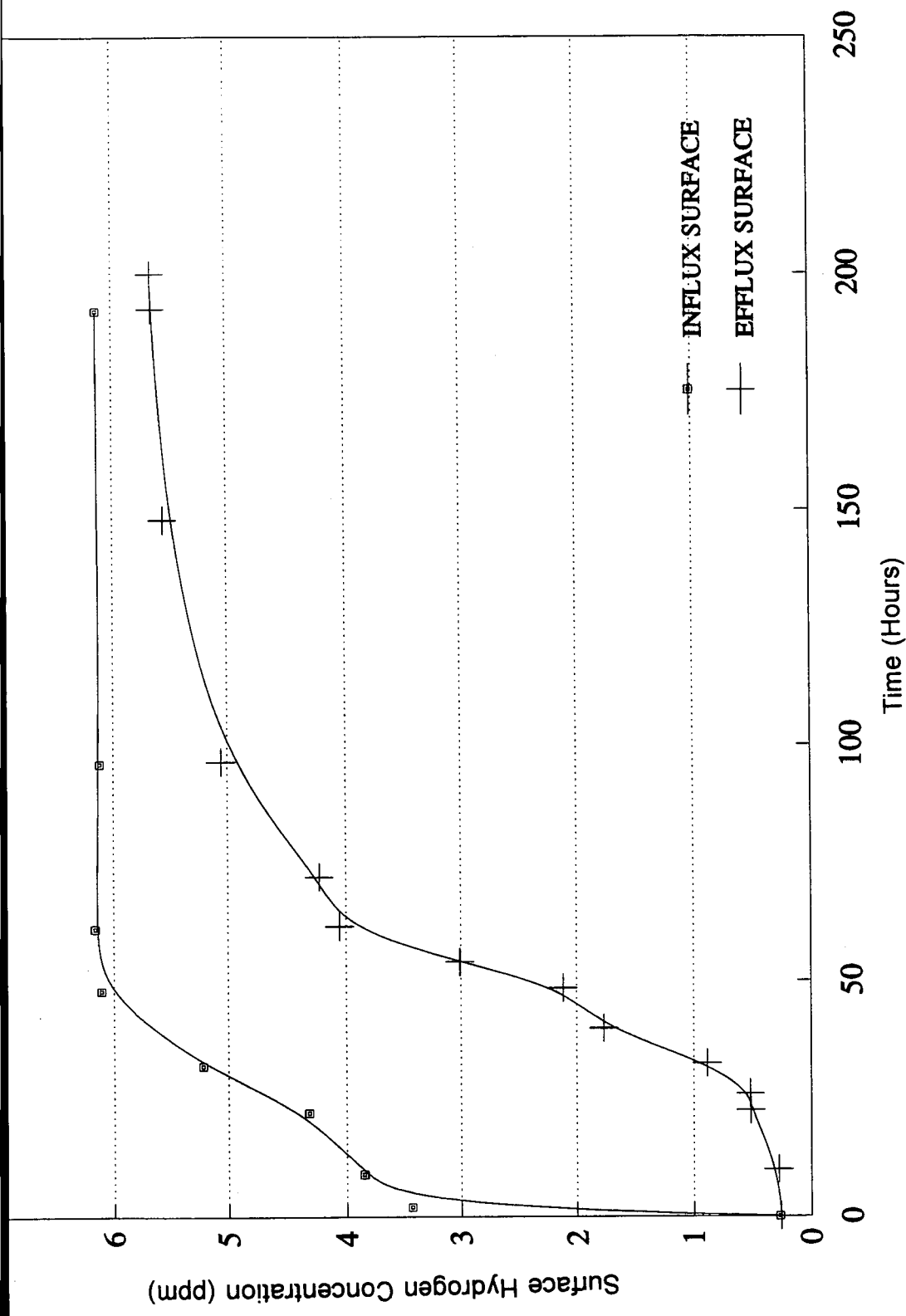
Figure 87. Gel-Filled Probe Measurements Taken on Both Sides of the BS Z25 Steel Plate During Cathodic Hydrogen Charging, Experiment 2.

248

5.12   Volumetric Permeation Measurements

The purpose of these experiments was to compare the results of the electrochemical methods of hydrogen determination with those of an established volumetric technique. The method was adapted from the British Standards 6693: Parts 1-5: 1988[108] using the apparatus shown in Figure 28.

1mm samples were machined from the same parent material as that used in the previous determinations, i.e. with the BS Z25, 5 mm samples. The hydrogen that diffused through the steel plate (thickness 1mm) was collected at ambient temperature in a glass cell, 35 cm^2 in surface area, containing a chemically inert silicone oil (dimethicone polydimethylsiloxane). After 24 hours the volume of hydrogen in the cell was determined by measuring the length of the gas column in the 1mm diameter capillary tube with a travelling microscope and correcting to standard temperature and pressure. The electrochemical cell was also used on the efflux surface to record the total amount of hydrogen that permeated the plate, which enabled a value to be inferred for the surface hydrogen concentration on the influx surface.

In the British Standards report, B.S.6693 Parts 1-5: 1988[108], it was suggested that mercury be used as a collection medium for the evolved hydrogen. It was considered, however, that there was a possibility of an amalgam forming between the steel and mercury, or the manganese sulphide inclusions and the mercury. Also the possibility of an immersion deposit forming on the steel surface was apparent which may have affected the volume or rate of hydrogen evolution. In addition this material is unpleasant to work with from a safety point of view. Glycerol was initially used as a collection medium, however, little success was achieved. It was thought that the glycerol could be reduced, in the presence of hydrogen, to an unsaturated aldehyde such as acrolein:-

$$CH_2\text{-}CH\text{-}CH_2 \rightarrow CH_2\text{=}CH\text{-}CHO + 2H_2O$$
$$OH \quad OH \quad OH$$
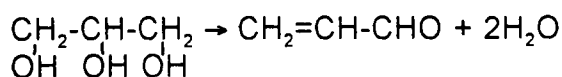
glycerol   acrolein

This would provide a soluble medium for any evolved hydrogen. Consequently the inert silicone oil, dimethicone polydimethylsiloxane, was used, which according to available literature[150], did not undergo any physical or chemical reactions with hydrogen at ambient temperature or pressure.

The volumes of hydrogen collected in duplicate charging experiments, together with the measurements from the electrochemical permeation cell, are shown in Table 27.

As described in section 5.11, the gel-filled hydrogen probe readings suggested that there was a build up of hydrogen on the efflux surface with little or no loss from that surface. The resulting hydrogen concentration gradient was essentially uniform across the plate. The maximum hydrogen permeated through the plate would have occurred if the efflux concentration had been artificially maintained at zero, corresponding to the boundary conditions imposed by the electrochemical permeation cell (Figure 83). The two experimental current transients indicated that the theoretical maximum volumes of hydrogen permeating the 1mm plate would have been 0.158 and 0.177 ml cm^{-2} day^{-1} as shown in Table 27. In contrast, the volumes of hydrogen collected were 6.57×10^{-4} and 2.47×10^{-3} ml cm^{-2} day^{-1} respectively. These represent only 0.42% and 1.4% of the maximum possible values.

The clear implication of all these results is that after long charging times the concentration gradients across the steel plates were very shallow and the efflux concentrations were almost equal to those on the influx side. The hydrogen appeared to have been more uniformly distributed in the 1mm plates, used for the volumetric measurements, as these were charged for 50

times the breakthrough time, t_b, compared to 20 x t_b for the 5mm material. Rather than hydrogen being lost rapidly from the free surface, it appears that even after careful preparation to remove contamination and surface films there was a large resistance to transport across the metal/air interface.

Table 27. Results of Volumetric and Electrochemical Permeation Measurements on 1mm Steel Plate

	Experiment 1	Experiment 2
Break through time t_b	25.2 minutes	27.9 minutes
Diffusion coefficient D	4.32×10^{-7} cm^2 s^{-1}	3.9×10^{-7} cm^2 s^{-1}
Steady state current density J_∞	15.4 µA cm^{-2}	17.4 µA cm^{-2}
Surface hydrogen concentration C_0	4.68 ppm	5.85 ppm
Theoretical Maximum Hydrogen Volume	0.158 ml cm^{-2} day^{-1}	0.177 ml cm^{-2} day^{-1}
Volume of hydrogen measured over silicone fluid	6.57×10^{-4} ml cm^{-2} day^{-1}	2.47×10^{-3} ml cm^{-2} day^{-1}
Percentage of theoretical maximum volume	0.57 %	1.7 %

5.13 Hydrogen Trapping.

Introduction.

The solubility of hydrogen in an iron matrix at room temperature is very low and most of the hydrogen is located not in normal lattice interstices but in other sites in the steel refered to as traps. These sites can act as traps for hydrogen atoms because of a deepening of the associated potential well. These obstacles, present in the material, affect several important parameters which are fundamental to the research programme:-

a)   The hydrogen distribution in the microstructure.

b)   The hydrogen diffusion coefficient.

c)   The quantity of hydrogen desorbed from the steel at room temperature.

d)   The hydrogen embrittlement susceptibility of the material.

There are two distinct kinds of traps, present to a varying extent in the materials under investigation. These are reversible and irreversible traps. A reversible trap is one at which hydrogen has a short residence time at the temperature of interest with an equivalent low interaction energy. On the other hand for the same conditions an irreversible trap is a one with a negligible probability of releasing its hydrogen. A schematic representation of these traps is shown in Figure 7 with their associated potential wells.

The consequence of trapping is to decrease the rate of transport of hydrogen through the metal because there is a finite probability of the hydrogen atoms jumping into trap sites and because the residence time in the trap site will be longer than in a normal lattice diffusion site.

Most of the earlier work conducted during the investigation of trapping effects

253

on the transport of hydrogen through steel[64-68] involved complex theoretical models which tried to embrace a complete description of all types of trapping sites; the number and distribution of these sites; and the average time of transfer between such sites. This problem is almost intractable. An extensive mathematical solution to the problem of trapping in the steels investigated at Cranfield were beyond the scope of this work. Consequently a semi-quantitative interpretation of the observed variance in hydrogen permeation from that associated with the pure trap free lattice was made.

THE MODEL

Turnbull et al.[70] suggested that if the diffusion coefficient and the solubility of hydrogen are assumed uniform throughout the metal, the continuity equations described by Fick's laws of diffusion could be rewritten taking into account the presence of traps.

$$\frac{\delta C}{\delta t} = D\frac{\delta^2 C}{\delta x^2} - N_r\frac{\delta\theta_r}{\delta t} - N_i\frac{\delta\theta_i}{\delta t} \qquad [82]$$

$$\frac{\delta\theta_r}{\delta t} = k_r C(1-\theta_r) - p\theta_r \qquad [83]$$

$$\frac{\delta\theta_i}{\delta t} = k_i C(1-\theta_i) \qquad [84]$$

Where
C is the number of diffusing atoms per unit volume,

N is the number of traps per unit volume,

Θ is the fraction occupied of N traps,

k is the capture rate ,

p is the release rate of hydrogen atoms,

t is the time and

D is the lattice diffusion coefficient.

The subscripts r and i represent reversible and irreversible traps respectively.

Equation [82] indicates that the rate of change of concentration of diffusing atoms depends on diffusion and the net rate of loss of hydrogen atoms into reversible and irreversible traps. The second and third equations relate to reversible and irreversible traps respectively and contain no diffusion terms because the traps are assumed to be isolated, and hence, there is no direct path between the trap sites. Saturation of traps occurs as Θ_r and Θ_i, approach 1.

Assuming a slab of thickness L, which is being charged with hydrogen from one side (x=L) with the hydrogen atoms being discharged rapidly from the exit side, the appropriate boundary conditions are:

t = 0	all x,	C = 0	[85]
t > 0	x = 0	C = 0	[86]
	x = L	$C = C_0$.	[87]

A more generalised form of the boundary conditions at x=L would involve the kinetics of absorption and desorption which are reported in section 5.4.

It is more convenient from a mathematical point of view to express equations [82] to [87] in non-dimensional form such as:

$$\tau = Dt/L^2 \qquad\qquad X = x/L$$
$$u = C/C_0 \qquad\qquad \upsilon = N_r\Theta_r/C_0$$
$$w = N_i\Theta_i/C_0 \qquad\qquad \lambda = N_r k_r L^2/D$$
$$\mu = pL^2/D \qquad\qquad \kappa = N_i k_i L^2/D$$
$$\rho = C_0/N_r \qquad\qquad v = C_0/N_i$$

Equations [82] to [87] may be rewritten as equations [88] to [93].
With initial boundary conditions

$$\frac{\delta u}{\delta \tau} = \frac{\delta^2 u}{\delta \chi^2} - \frac{\delta \upsilon}{\delta \tau} - \frac{\delta w}{\delta \tau} \qquad [88]$$

$$\frac{\delta \upsilon}{\delta \tau} = \lambda u(1-\rho \upsilon) - \mu \upsilon \qquad [89]$$

$$\frac{\delta w}{\delta \tau} = \kappa u(1-\nu w) \qquad [90]$$

$\tau = 0$	$u = \upsilon = w = 0$		[91]
$\tau > 0$	$X = 0$	$u = 0$	[92]
	$X = 0$	$u = 1.0.$	[93]

The solution to equations [88] to [90] and conditions [91] to [93] furnish the time dependent distribution of u, υ, and w[70]. Values of the time independent flux at the exit side of the slab were determined as described in the experimental procedure. J_∞ was independent of trapping and is given by

$$J_\infty = \frac{FC_0 D}{L} \qquad [94]$$

In interpreting the results of the repeated charging experiments, utilization of the various trapping parameters, described by Turnbull et al[70] has been made to describe the effects trapping has on the diffusion of hydrogen through mild steel. Use of such parameters necessitates the identification of their limitations. Firstly it is assumed that the diffusion coefficient and solubility of hydrogen are uniform throughout the material. In the case of the steels investigated at Cranfield, this may not be strictly true. The presence of large numbers of MnS inclusions and their susceptibility to subsequent void growth in this material suggests the number of trap sites may increase during charging which may not be completely accountable. Secondly, it is assumed that in the presence of a large number of reversible traps, the number of irreversible traps is low and vice versa. In steels where there are large numbers of inclusions or defects, this assumption may not be strictly true. Considering, however, the nature of this investigation, the conclusions which

may be derived in terms of the various trapping parameters are somewhat tentative.

Figures 58 to 63 show the hydrogen permeation transients obtained for the BS Z25 and NAM materials respectively, by repeated cathodic charging. The similarities of the initial gradients in each of the first transients, where the thickness of the material is both equal and constant, suggest that the permeation transients may be determined by mass transport within the volume of the material. Consequently the assumption of a boundary condition of C_0 at the reacting surface is experimentally justified. A slight increase in the steepness of the first permeation transient, however, may be expected with increasing permeation thickness due to the thickness dependence of the trapping parameter κ ($N_i k_i a^2/D$).

Permeation transients obtained for the BS Z25 material appeared to reach steady state conditions leading to a constant value of J_∞ well within the experimental duration, this being in excess of 15 times the expected breakthrough time. The NAM plate, on the other hand, appeared to reach a maximum value of J_∞ after around 7 hours. Beyond this time, there was a very slow, but steady decrease in the final value of J_∞. This phenomenon is often observed with carbon - manganese steels. The relative decrease in J_∞ exhibited by the NAM plate may be attributed to the extensive population of manganese sulphide (MnS) inclusions distributed in the matrix. MnS inclusions are well-recognised as strong hydrogen traps[151,152] and a thermal analysis study[152] of AISI 4340 steel showed that the temperature for hydrogen release increases in the following order:-

ferrite-carbide interface < dislocations < micro-void < MnS interface

Accordingly, MnS inclusions are likely to be principal irreversible trapping sites in such steels. The BS Z25 plate did not show such a variance in J_∞. This

may be due to the fact that the BS Z25 plate was a much *"cleaner"* steel than the NAM plate. This correlates with the metallurgical observations reported in the following section. By comparing the initial transient with subsequent transients, for the two materials, one can postulate the influence that the various trapping parameters may exert on the diffusion of hydrogen through the plate whilst being cathodically charged.

In the case of the BS Z25 plate, Figures 58 and 59, the second and subsequent transients are almost superimposed on one another. This suggests that there is no increase in the apparent diffusion coefficient. This may be attributed to the saturation of irreversible traps after the first experimental charge. Consequently the effect of κ ($N_i k_i a^2/D$) may be neglected for the second and third charges.

In the case of the NAM plate, Figures 61 and 62, there appears to be a gradual increase in the rate of diffusion. This is most likely due to the participating number of irreversible traps decreasing as they become filled with hydrogen. New irreversible traps are however being continuously created due to void growth around manganese sulphide inclusions. It would appear, however, that the rate of filling of the existing traps with hydrogen is faster than the rate of creation of new trapping sites. Consequently at infinite times it is probable that the effective diffusion coefficient would achieve an almost constnt value. For each set of permeation data there are essentially three parameters, including the lattice diffusion coefficient, involved with interpreting the experimental data.

Evaluation of the lattice diffusion coefficient from permeation studies is not readily possible for steels with such a significant degree of trapping. Kiuchi and McLellan[153] have reviewed a large body of data for the lattice diffusion coefficient of iron. For temperatures between -40° and 80°C, the best representation for $D_{lattice}$ in a body centred cubic iron was[153]:

258

$$D = 7.23 \times 10^{-4} \exp^{\frac{E_a}{RT}} \ cm^2 s^{-1} \qquad [95]$$

where E_a = 5.69 kJmol^{-1} and this yields a value of D = 7.2 x 10^{-5} cm^2 s^{-1} at 23°C.

For reversible traps, when the loss of hydrogen diffusing into traps is very low (low λ or low N_r and low k_r), diffusion through the slab takes place before significant loss to traps can develop and the transient is similar to that for the trap-free lattice. With increasing λ (i.e. higher values of N_r or k_r) steady state diffusion is not achieved before trapping becomes effective and deviation from trap free behaviour occurs with the transient showing an apparent intermediate plateau prior to steady state. The effects of varying λ at a constant ratio of λ/μ, where ρ = 0 and κ = 0 are shown in Figure 88. The permeation transient, in the absence of trapping, i.e. when λ = 0 is also shown. For very high values of λ, the transient is identical in shape to that for the trap-free lattice but is displaced in time. This corresponds to an equilibrium between mobile and reversibly trapped hydrogen.

When the number of irreversible sites per unit volume exceeds the number of hydrogen atoms per unit volume by about an order of magnitude the effect of irreversible trapping becomes significant in relation to the time evolution of the flux. As κ increases, deviation from the transient in the lattice free of irreversible traps occurs at increasingly shorter times until the transient is dominated by the irreversible trapping process. If the capture rate is very high, (large k) filling of the traps is very efficient and almost all of the trap sites are predicted to be filled prior to hydrogen breakthrough. The subsequent transport is unhindered (with the exception of reversible trapping) with a consequent very rapid rise in flux at the exit surface. The effect of κ on the permeation transient, for fixed values of v, λ/μ, μ and ρ is shown in Figure 89.
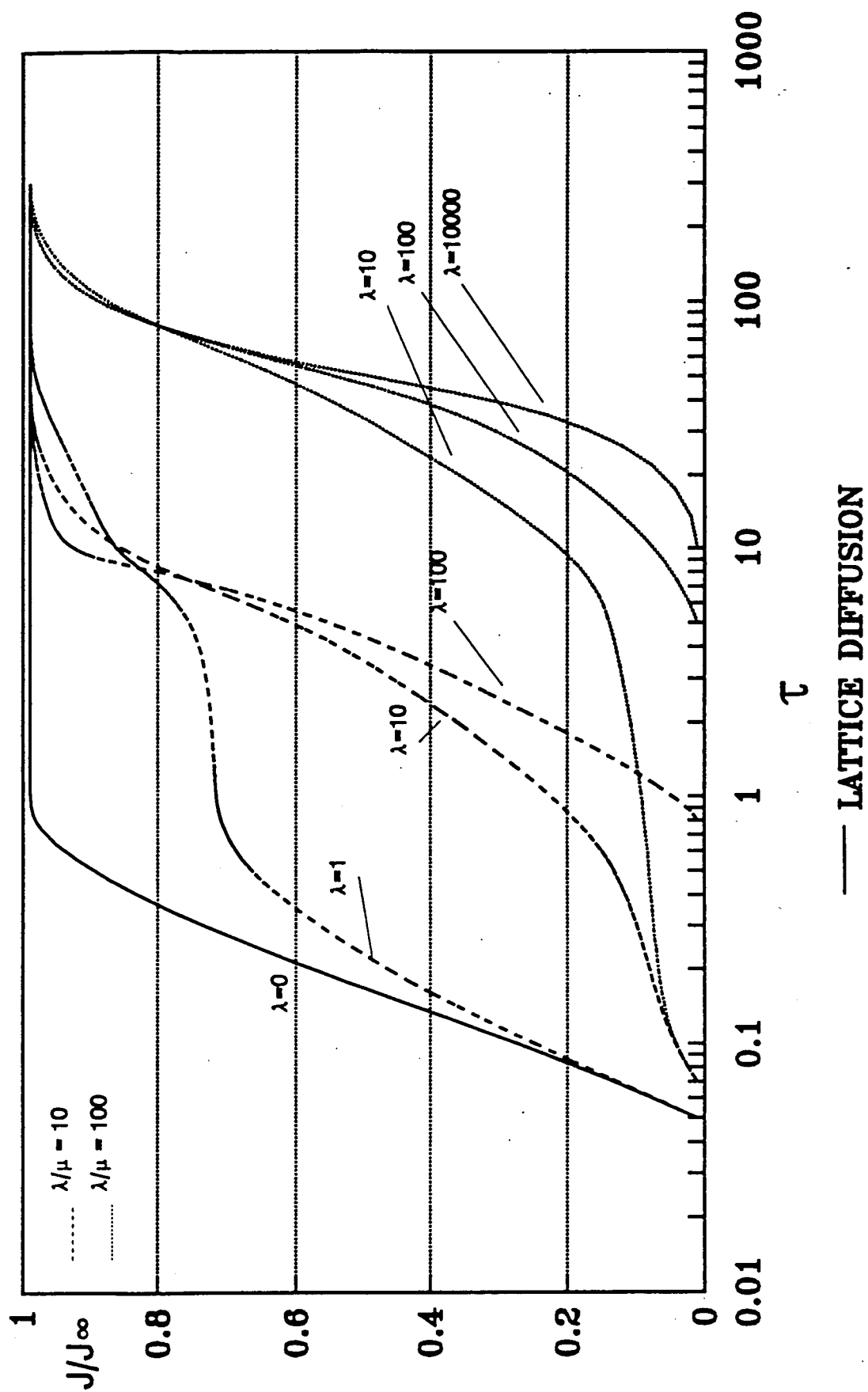
Figure 88.   Effect of Varying λ With a Constant Ratio of λ/μ, ρ=0, κ=0.[70]

260
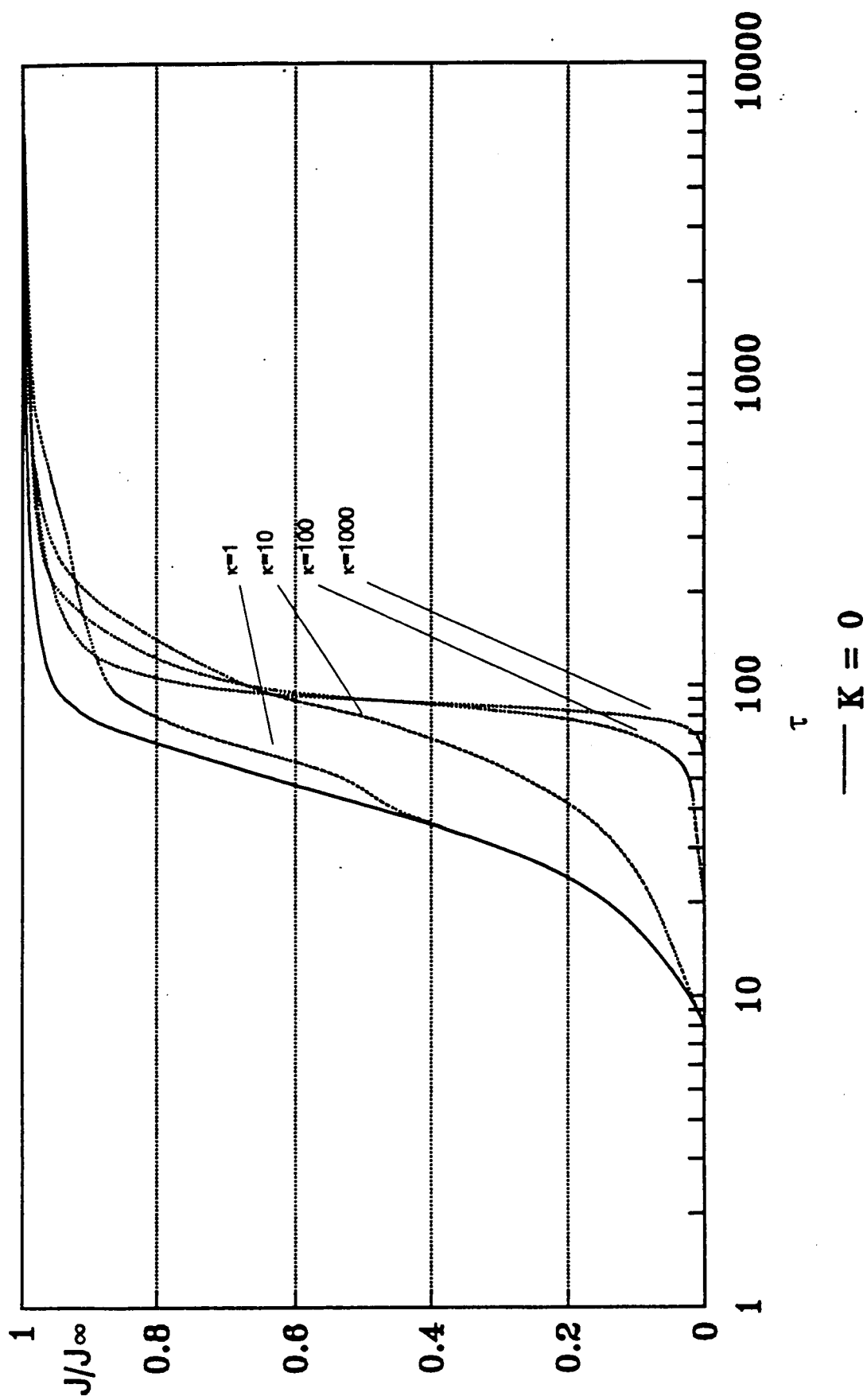
Figure 89.   Effect of κ on the Permeation Transient for $\upsilon=0.01$, $\lambda/\mu=2.3\times10^2$, $\mu=10^2$, $\rho=0$.[70]

261
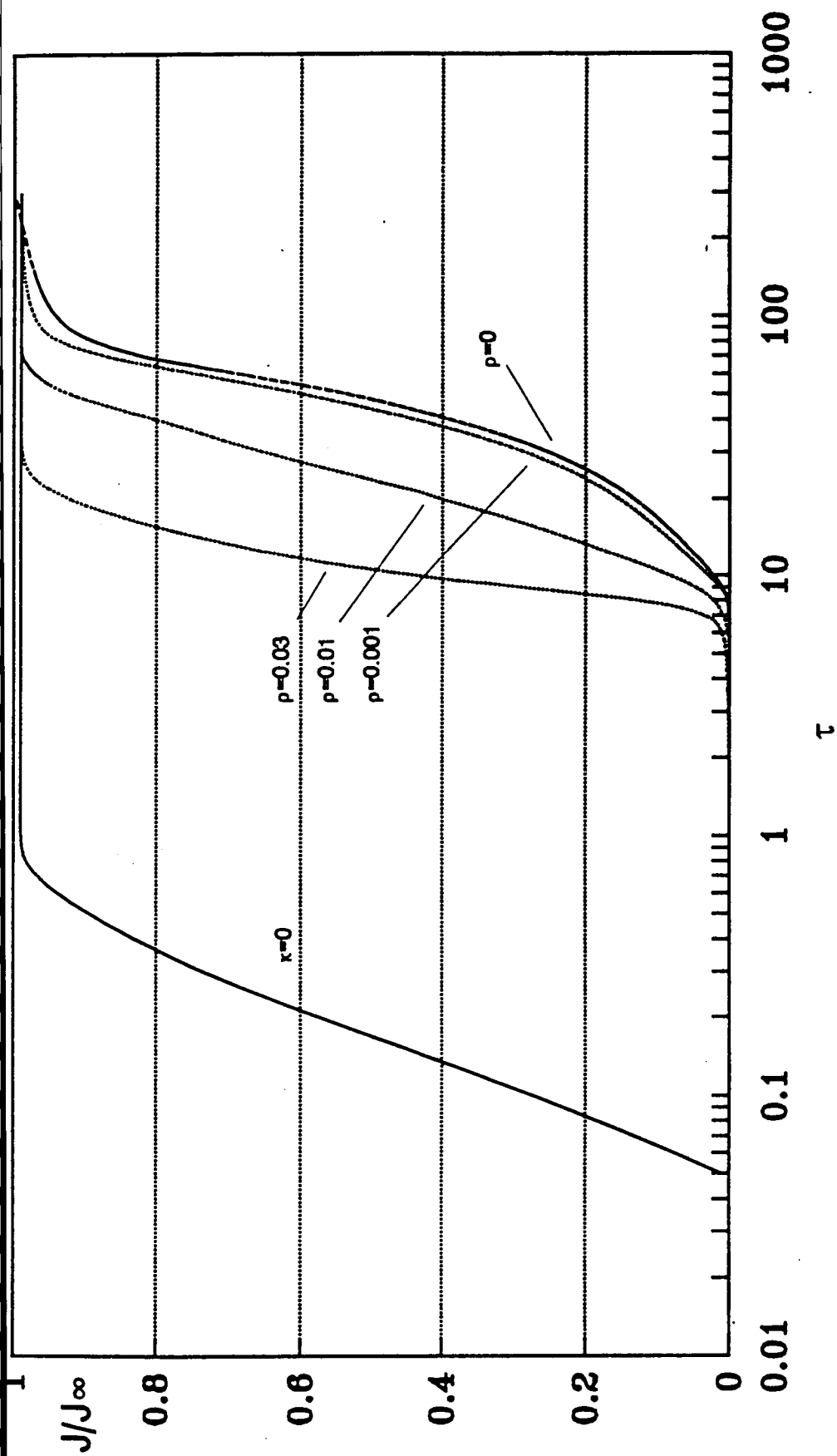
Figure 90. Effect of Varying ρ (C_o/N_r) on the Permeation Transient for Reversible Trapping ($\kappa=0$) with $\lambda/\mu=2.3\times10^2$ [70].

With no release of hydrogen from the traps to counter balance the filling of the traps the permeation transient simply gets steeper with increasing κ.

It has been shown[58,59,154] that the effect of trapping on the apparent diffusion coefficient can be described by Fick's second law but with the lattice diffusion coefficient replaced by an effective value given by:-

$$D_{eff} = \frac{D}{\left[1 + \frac{N_r k_r}{p}\right]} = \frac{D}{\left[1 + \frac{\lambda}{\mu}\right]} \qquad [96]$$

Provided that equilibrium conditions are maintained, i.e. when the exchange between diffusion site and trap site is rapid, the effect of increasing the ratio λ/μ should be equivalent to displacing the normalised flux for an ideal lattice to longer times.

Under severe charging conditions it may not be valid to assume a low occupancy of the reversible trapping sites in relation to equation [89]. This implies a non-zero value for p (C_0/N_r). The effect of varying p on the normalised flux is shown in Figure 90 for a constant value of λ/μ, with μ and λ assumed large so that the diffusing and trapped hydrogen is at equilibrium. The effect of continually increasing p, for example above 10^{-3}, is to steepen the permeation transient. This can be explained by a decrease in the efficiency of trapping as time progresses with the consequent effect that transport of the diffusing hydrogen atoms becomes less restrained.

Figure 91 shows the effect of ν (C_0/N_i) on the permeation transients. For simplicity in constructing such transients, it is assumed that the fractional occupancy of reversible traps is low. This assumption, however, may not be correct if during charging, the volume or number of irreversible traps N_i, is increasing due to high populations of MnS inclusions or subsequent void growth.
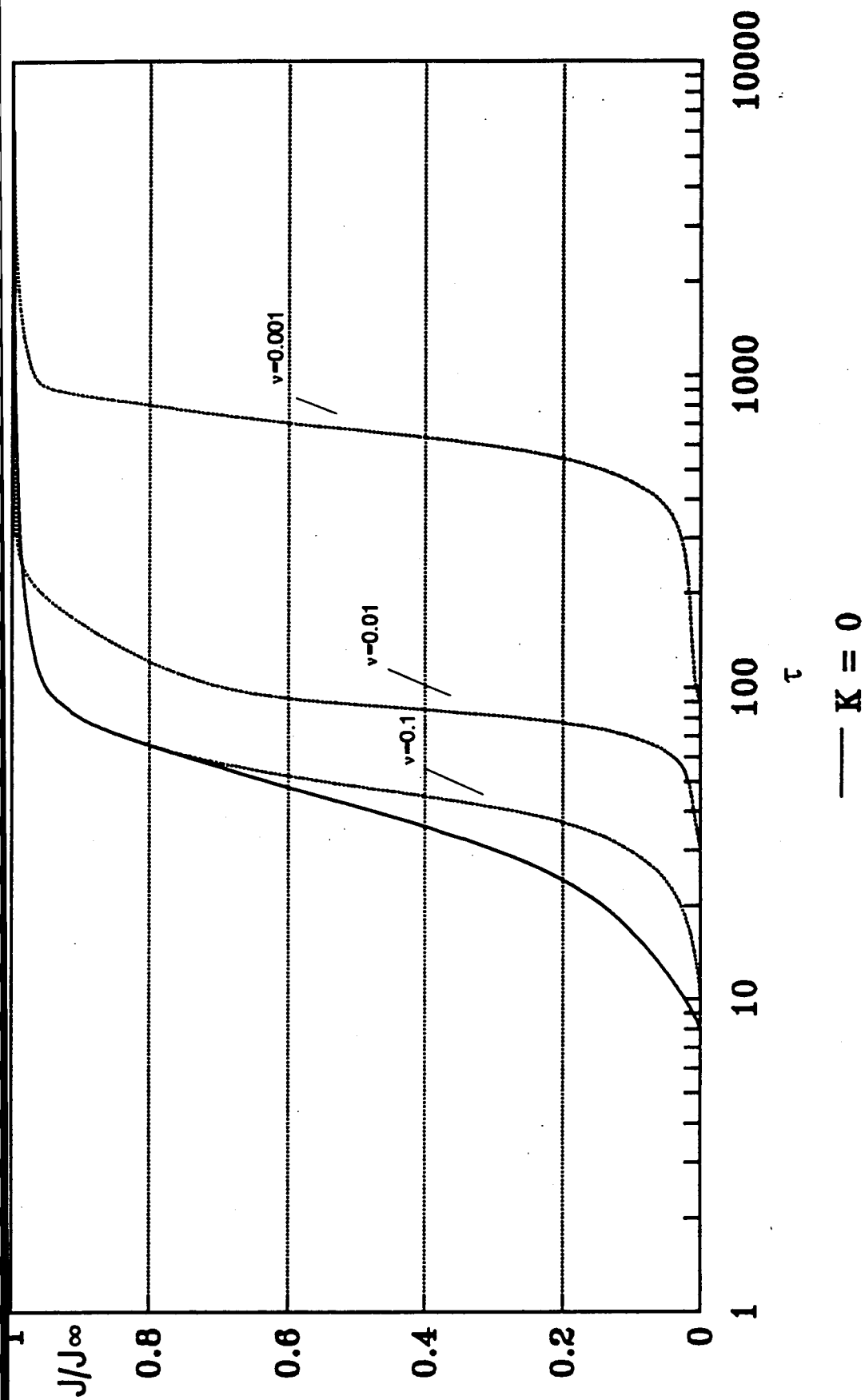
Figure 91. Effect of Varying υ (C_o/N_l) on the Permeation Transient for $\lambda/\mu=2.3\times10^2$, $\mu=10^2$, $\rho=0$, $\kappa=10^2$ [70].

264

When the concentration of irreversible traps is low, i.e. κ approaches 0, then there is little or no influence on the permeation transient from irreversible trapping and only reversible trapping sites need be considered. However, assuming a constant, larger value of κ, then the effect of decreasing ν is to displace the permeation transient to longer times. Over a range of small values of ν, the permeation transient tends to become steeper in appearance. At values of $\nu \leq 0.01$, the shape of the transient is little influenced.

Irreversible traps can be measured through evaluation of the parameter ν (C_0/N_i), which represents the displacement in time of the first and second transients. The value of C_0 can be derived from the value of the steady state flux ($J_\infty = FDC_0/L$), provided D is known. An order of magnitude estimate of the capture rate per trap (k_i) is feasible by analysis of the shape of the permeation transient. In calculating D it is favourable to use the initial stages of the permeation, however surface effects are most likely to exert an influence at shorter times. Approximate values or an indication of the magnitude of ρ (C_0/N_r), can only be made with tests in environments generating varying values of C_0. At low fractional occupancy resolution situations, realisation of this parameter is not realistically possible. Absolute values of λ ($N_r k_r a^2/D$) and μ (pa^2/D) are also unobtainable unless there is a marked difference in shape of the transient from that of the equilibrium case. If the transient is similar in shape to that for the equilibrium case then only the ratio is essential for describing the transients.

Tables 28 and 29 list the experimental parameters derived from the repeated charging experiments. Values of the diffusion coefficient are shown as calculated from the breakthrough time[36]. In the case of the BS Z25 plate, the value of D has increased by a factor of approximately 3 in the second experiment. In the case of the NAM plate, however, D has increased by factors of 6 and 4 for experiments 1 and 2 respectively.

Table 28. Experimental results for BS Z25 plate.

	J_∞ µA cm^{-2}	C_0 ppm	t_b s	$D_{(tb)}$ cm^{-2} s^{-1}
	BS Z25 Plate			
1A	6.33	1.97	1550	4.22 x 10^{-7}
2A	8.24	1.71	1035	6.32 x 10^{-7}
3A	7.69	1.53	986	6.6 x 10^{-7}
1B	6.91	1.77	1280	5.11 x 10^{-7}
2B	8.14	0.72	435	15 x 10^{-7}
3B	8.21	0.68	411	16 x 10^{-7}

Table 29. Experimental results for NAM plate.

	J_∞ µA cm^{-2}	C_0 ppm	t_b s	$D_{(tb)}$ cm^{-2} s^{-1}
	NAM Plate			
1A	17.2	2.51	1533	4.27 x 10^{-7}
2A	11.1	1.6	719	9.09 x 10^{-7}
3A	12.7	0.57	222	2.94 x 10^{-7}
4A	15.3	0.62	201	32.5 x 10^{-7}
1B	9.76	2.21	1131	5.7 x 10^{-7}
2B	10.03	1.17	582	11.2 x 10^{-7}
3B	10.15	0.75	367	17.8 x 10^{-7}
4B	10.37	0.75	359	18.2 x 10^{-7}

5.13.1 Interpretation of Results in Terms of Trapping Parameters.

1. λ $(N_t k_t a^2/D)$ AND (λ/μ) $(N_t k_t/p)$

In the case of the BS Z25 material, there is a small but significant displacement between first and subsequent transients which suggests that λ is quite small, for a relatively small ratio of λ/μ, i.e. μ has an intermediate value approaching an order of 10^2. Between the second and subsequent transients, there is virtually no increase in the diffusion coefficient and the transients are superimposed on one another. Consequently for the same ratio of λ/μ, μ is much smaller and approaches a value of around 10^0.

In the case of the NAM specimen, the first transient appears to deviate quite substantially from Fickian diffusion. There appears to be a slight plateau which suggests an intermediate value of λ. For a small ratio of λ/μ, μ has an approximate magnitude of 10^1. Consequently there is a substantial influence from trapping before steady state conditions have been achieved. The apparent differences between second and subsequent transients in the NAM plate indicate λ to be very large, of the order 10^4 resulting in a very low value of μ, of the order of 10^{-3}.

2. κ $(N_t k_t a^2/D)$

In the case of the NAM material, there appears to be a very slight increase in steepness of the later transients, Figure 61. This suggests that κ may be increasing slightly, possibly due to void growth. The BS Z25 material has a lower concentration of MnS inclusions per unit volume than the NAM plate and consequently, after the first transient, when all the irreversible traps appear to be saturated, κ appears to have little or no subsequent effect on the transients.

3. ν (C_0/N_i)

Initially the ratio of (C_0/N_i) is very small as the number of irreversible traps, N_i, is much larger than the value of C_0 or the relative rate of diffusion. In the case of the BS Z25 material, after the first transient, N_i approaches zero and ν is much larger. Large values of ν are favourable as this does not substantially affect the shape of the transient and displacement in time is small relative to λ.

4. ρ (C_0/N_r)

In the case of both materials for the first transient values of ρ are very small due to the fact that trapping is dominated by irreversible traps. Any increase in steepness of the subsequent transients during charging may be due to an increase in ρ. This may be accompanied by a subsequent increase in the apparent diffusion coefficient.

In general, it may be concluded that the parameter λ and the ratio of (λ/μ) are of most significance when interpreting the effect of trapping on the transport of hydrogen through the two materials under investigation. It is these parameters that directly affect the magnitude of the apparent diffusion coefficient as shown by equation [96]. The parameter ν has little effect on the shape of the transients and is not as sensitive to time displacement as the λ parameter. ρ is also of little importance as the number of reversible trap sites, or those with low associated potential wells and residence times are not increasing during the charging. It appears that, certainly in the case of the NAM material, κ may play an important role in describing the influence of traps on the hydrogen permeation transients.

5.14   Hydrogen Related Microstructural Damage.

Introduction

In this section the physical damage produced by hydrogen diffusing in a steel plate is examined in some detail.   In order to observe the effects hydrogen had on the microstructure, the NAM steel was utilised for its known susceptibility to hydrogen damage.   The abundance of elongated type III manganese sulphide and mixed oxide inclusions in the metal matrix provided ideal sites for void nucleation and hydrogen induced crack propagation.

It is widely accepted that the susceptibility of a steel to the reversible and irreversible micro-structural damage caused by hydrogen depends on the steel's composition and structure.   Preliminary studies of the effects of electrolytic charging with hydrogen on the mechanical properties of carbon-manganese steels revealed a significant part played by non-metallic inclusions which may initiate the micro-cracks and contribute to their development. Consequently a systematic investigation was undertaken to evaluate the combined effect of non-metallic inclusions and of hydrogen.

5.9.1   The NAM Steel.

Plate 11 shows a micrograph of the uncharged NAM plate etched in 2% nital to reveal a banded microstructure of pearlite and ferrite.   Elongated manganese sulphide inclusions were found to lie parallel to the banding predominantly in the ferrite phase.   The elemental analysis for these inclusions is shown in Figure 92.

Plate 12 shows an inclusion found in the NAM material which was based on a type III manganese sulphide inclusion with a large aluminium oxide particle embedded in it.   The elemental analysis for this inclusion is shown in Figures

93(a) and 93(b).

Apparent hydrogen damage was observed in the charged material up to a depth of around 100 μm below the charged surface. The damage appeared to initiate at the steel/inclusion interface and manifested itself as a widening of the void due to hydrogen pressure build up. This is shown in Plate 13. It was apparent that separation of the two materials had taken place, initially due to the formation of small approximately hemispherical voids. As the concentration of hydrogen increased these voids coalesced to form one large void encompassing the original site of the manganese sulphide inclusion. Elemental analysis of the defect revealed the manganese sulphide inclusion was still present at the bottom of the void. This process is illustrated schematically in Figure 94. At a depth of around 225 μm below the surface, the large elongated single phase manganese sulphide inclusion appears to be unaffected by hydrogen damage.

These observations are supported by Smialowski[149] who showed that when voids formed near the charging surface they acted to trap hydrogen and prevent its entry into the interior so that damage tended to remain localised near the surface.

From the results obtained with the gel-filled hydrogen probe it was suggested that after long periods of charging, a uniform hydrogen concentration would develop throughout the thickness of the steel plate. Consequently it would be expected that microstructural damage would be observed almost uniformly throughout the cross-section of the material. Indeed, when in service, a pipe or vessel is generally exposed to hydrogen charging for sufficient time to establish such uniform gradients.

Plate 11   Uncharged, Etched micrograph of NAM plate
            showing Manganese sulphide inclusion.
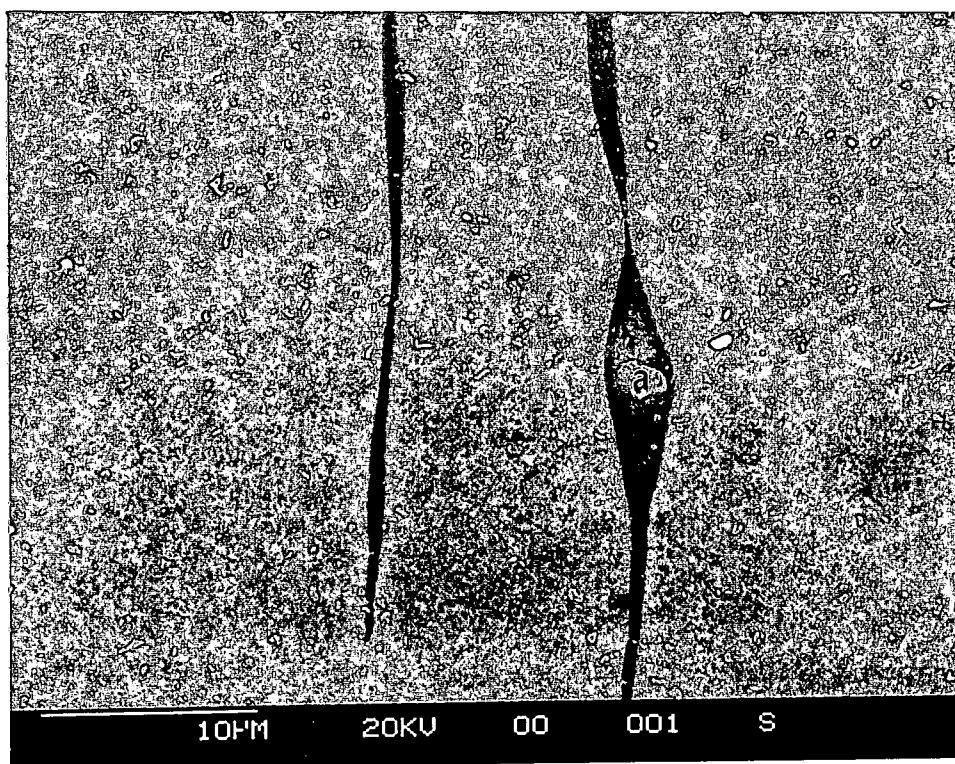
Plate 12   SEM Micrograph in the uncharged condition
            showing a mixed oxide inclusion.

271
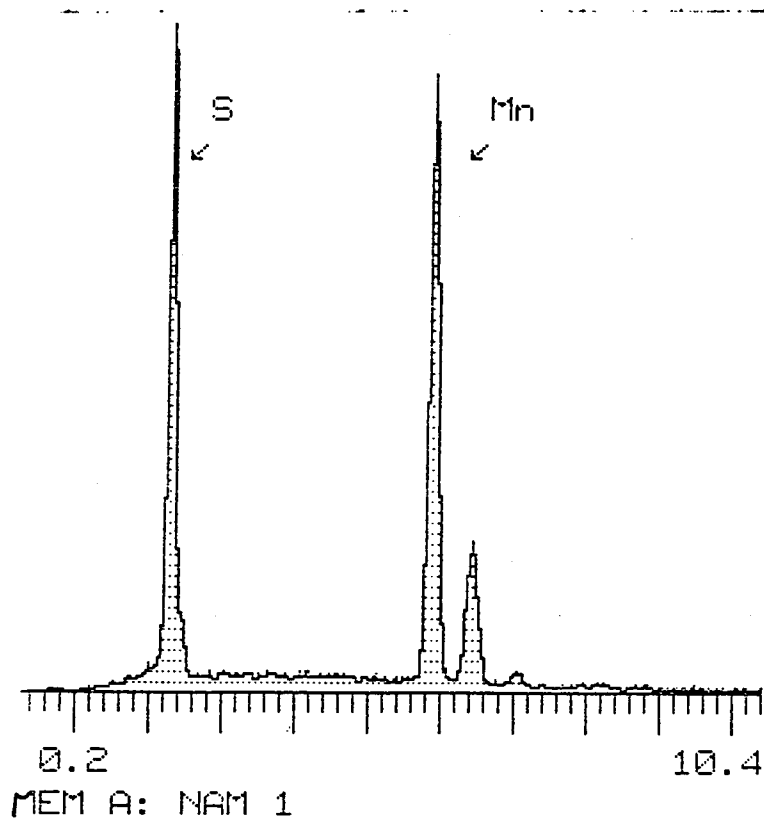
Figure 92.   SEM Elemental analysis for the

inclusion shown in Plate 11.
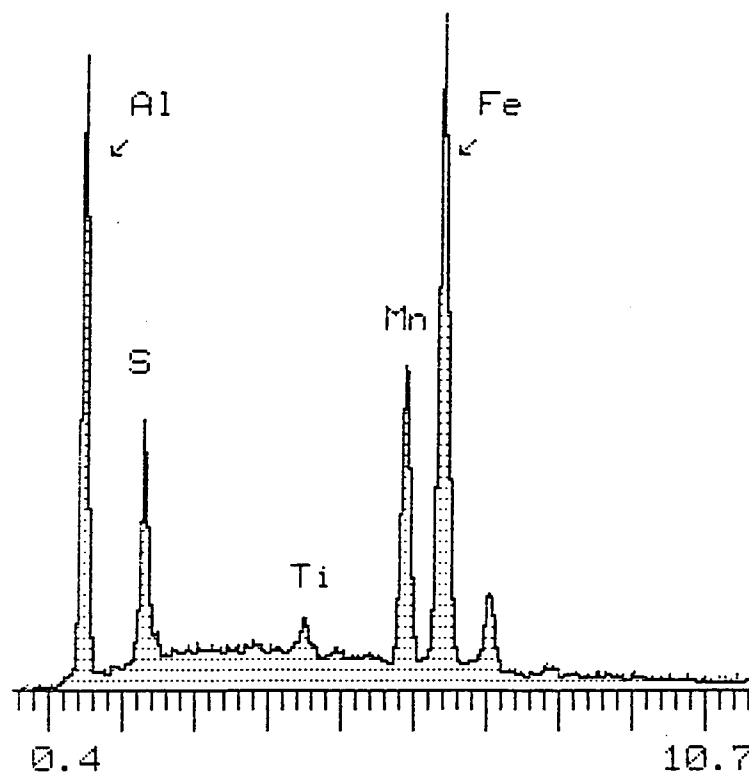
Figure 93(a). SEM Elemental analysis for the mixed oxide inclusion shown in
Plate 12 Spot a.
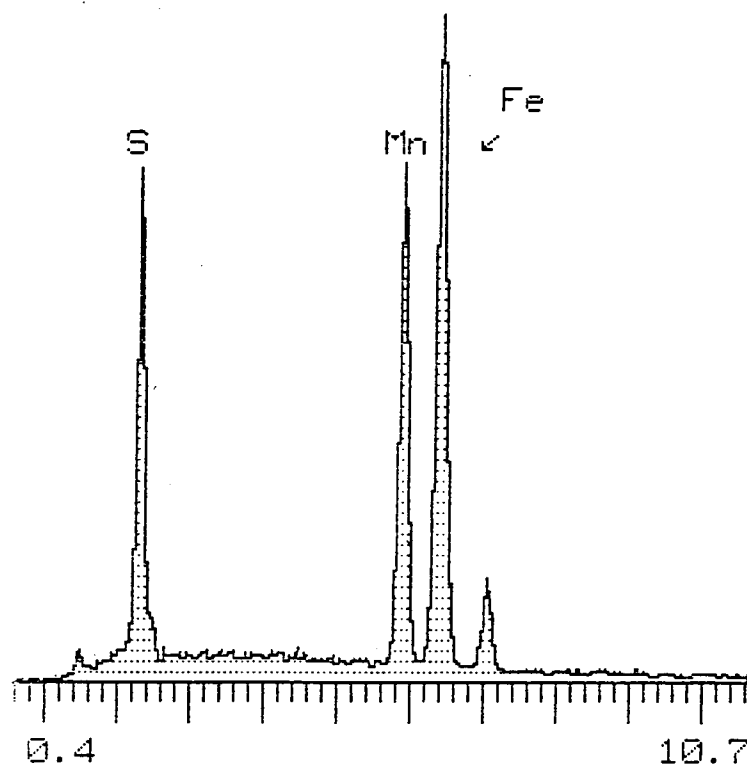
Figure 93(b). SEM Elemental analysis for the mixed oxide inclusion shown in
Plate 12 Spot b.
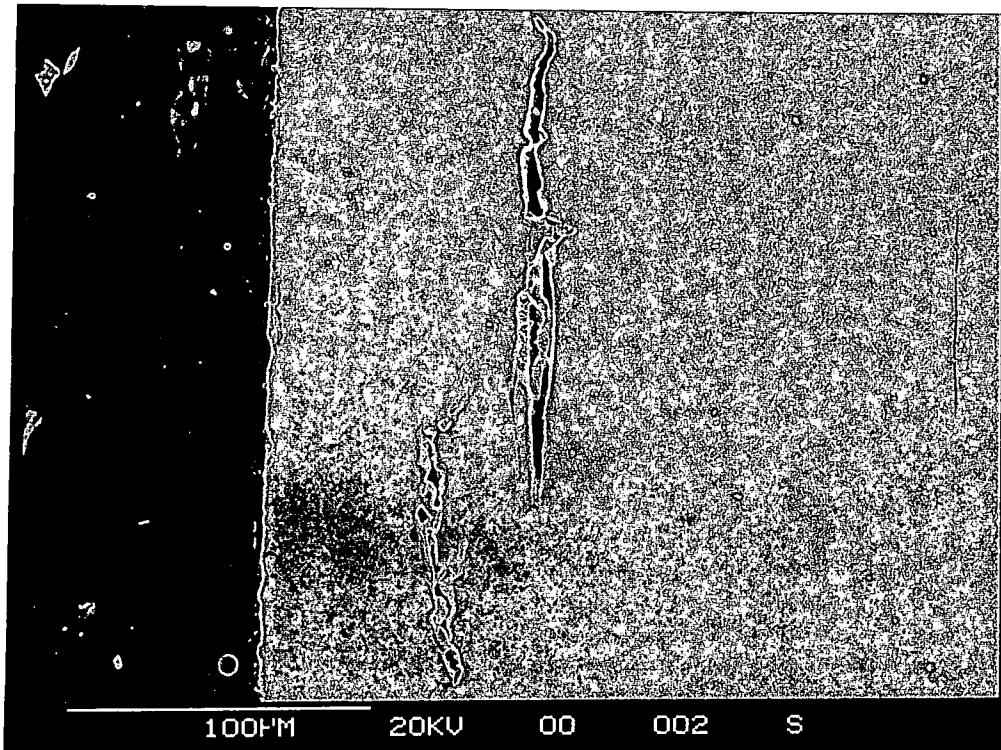
Plate 13.   Apparent Hydrogen Damage Situated Near
the Charged Surface.

274
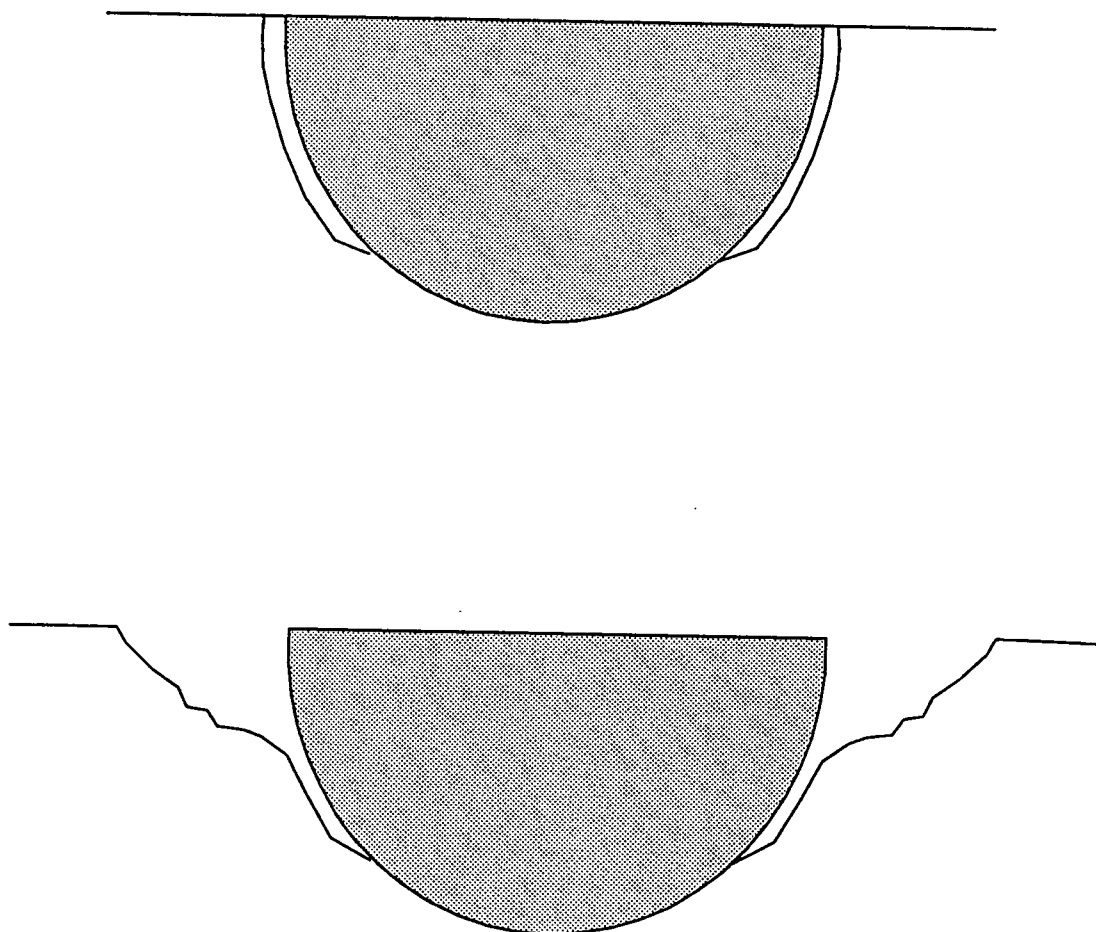
Manganese Sulphide Inclusion

Crack

Figure 94. Development of micro-voids around manganese sulphide inclusions as a result of hydrogen pressure build up.

The fact that hydrogen damage is not observed uniformly through the plate thickness but appears to be concentrated near the charging surface[149] suggests that damage results not from the steady state hydrogen concentration in the steel but from events of relatively short duration which may cause particularly high rates of hydrogen charging. A transient flux of absorbed hydrogen could be sufficiently large to induce damage near the metal surface, whereas it would then disperse into the metal without affecting the material further away. Clearly, the size and distribution of the hydrogen flux, the thickness of the steel and the threshold concentration to cause microstructural damage are all important factors that would influence the outcome.

The source of these short duration events remains unclear and requires further investigation. However, it seems probable that an acidic process could provide sufficiently high surface hydrogen concentrations, particularly if this occurred in the presence of a cathodic poison. Acid cleaning to remove a sulphide film is one likely example. A systematic examination of the procedures employed on a particular item of equipment may reveal a possible cause of the high hydrogen fluxes and this could then be examined in detail by appropriate permeation measurements.

Further into the interior of the metal, where inclusions have seen less hydrogen and for a shorter time than those near the charging surface some apparent hydrogen damage was observed around inclusions containing large oxidic particles such as Al_2O_3.

This suggested that cracking, or even less developed hydrogen damage might be due to the summing up of stresses produced by the precipitating hydrogen with those stresses occurring around some inclusions in the steel. This observation may be due to the differences in thermal contraction of the two materials involved.

The problem of the so called summing up of stresses associated with non-metallic inclusions in carbon manganese steels was the subject of a systematic study by Brooksbank and Andrew[155,156]. As derived from their calculations, the magnitude of stresses is determined by the differences in thermal expansion coefficients and in elastic constants. The highest stresses are obtained with alumina inclusions, while manganese sulphide, due to its high coefficient of thermal expansion, does not produce these particularly large stresses.

Brooksbank and Andrew[155,156] estimated critical values of hydrogen pressure for various types of non-metallic inclusions. Mean coefficients of linear expansion for some inclusions are shown in Table 30[156]. This suggests, for inclusions situated well within the metal interior and under the given charging conditions, 10% sulphuric acid with 50 ppm arsenic trioxide and a current density of 150 mAcm^{-2}, the pressure of hydrogen precipitated within the steel matrix attained sufficient values to produce micro-cracks at oxidic inclusion/steel interfaces. This hydrogen pressure did not, however, appear high enough to develop cracks or blisters at pure manganese sulphide inclusions. From these observations, it is apparent that the pressure of hydrogen generated from electrochemical cathodic hydrogen charging would attain a value in the metal matrix in the range of 3000 to 8000 atms[155]. This value would, however, not reach 12,000 atms[155] indicated by the fact that no cracks were initiated at the sites of pure manganese sulphide inclusions at these depths below the charging surface.

Table 30. Thermal Expansion Coefficients of Inclusions[156]

Material		Mean Linear Coefficient of Thermal Expansion. (0 to 800°C)x10⁻⁶/°C
Type	Composition	
Inclusion		
Calcium Aluminate	$CaO.2Al_2O_3$	5.0
Calcium Aluminate	$CaO.Al_2O_3$	6.5
Calcium Aluminate	$12CaO.7Al_2O_3$	7.6
Calcium Aluminate	$CaO.6Al_2O_3$	8.8
Alumina	Al_2O_3	8.0
Spinel	$MgO.Al_2O_3$	8.4
Silica	SiO_2	0.58
Silicate (mullite)	$3Al_2O_3.2SiO_2$	5.0
Manganese Sulphide	MnS	18.1
Steel		
Steel	0.4% C, 1% Cr	12.5

6.0   Conclusions

1.   Gel-Filled Hydrogen Probe.

Modifications to the existing gel-filled hydrogen probe containing a Nickel/Nickel Oxide reference/auxiliary electrode have led to a more stable and reliable device which operates at a constant potential using a Mercury/Mercury Oxide reference electrode and a platinum auxiliary electrode.

Immobilising the electrolyte in the form of a gel provides an essentially leak free device which is considerably more versatile than previous hydrogen probes[101].

The probe, however, is sensitive to surface conditions and the presence of a passive film on the steel test sample shows contributory effects to the measured oxidation current. This phenomenon is easily overcome as the passivation current decays rapidly compared with the hydrogen oxidation current. At longer times the effect of the passive current may be regarded as negligible and a true value for the hydrogen oxidation current may be found. By using Fick's laws of diffusion under non-steady state conditions and with a knowledge of the diffusion coefficient for the test specimen, a value for the surface hydrogen concentration may be established at the point of contact of the gel-filled hydrogen probe.

2.   Comparison of Gel-Filled Hydrogen Probe and Conventional Permeation Technique.

The hydrogen concentrations measured with the gel-filled probe were in good general agreement with those from the conventional permeation and volumetric techniques and those predicted by the diffusion equations. The probe measurements and the permeation transients both indicated that the

influx boundary conditions for galvanostatic charging lay between those of the constant surface coverage and the constant hydrogen flux models.

3. Hydrogen concentration gradients

After long charging times the hydrogen concentration on the efflux surface approached that on the influx side, indicating an almost uniform distribution of hydrogen in the steel. It was clear that even after careful preparation to remove contamination and surface films there was a large resistance to hydrogen transport across the metal/air interface.

4. Trapping

By repeated charging of a specimen it is possible to arrive at semi-quantitative expressions showing the effect reversible and irreversible trapping has on the diffusion of hydrogen in steel. The present model breaks down, however, in the presence of a very high population of traps and the resulting permeation curve deviates substantially from Fickian type behaviour. The model allows semi-quantitative description of the effect traps have on the shape of the permeation transient with respect to the trap free case of body centred cubic single crystal iron. Predictions for the real case, i.e. in the presence of reversible traps, show a displacement of the permeation curve on the time axis and a steepening of the curve's gradient.

5. Microstructural Hydrogen Damage.

In carbon-manganese steel, electrochemical hydrogen charging appears to provoke hydrogen damage in the absence of applied stress. This is assumed to be due to a joint action of hydrogen and of micro-stresses which may have developed around individual inclusions during manufacture or working.

The damage appears to extend from one inclusion to another. Some oxide inclusions with low coefficients of thermal expansion appear to have a particularly deleterious effect. On the contrary, the presence of sulphides with high coefficients of thermal expansion (e.g manganese sulphide) have a less detrimental effect since contraction of such a particle gives rise to the formation of a micro-void at the inclusion/matrix interface which may accommodate significant amounts of hydrogen. Provided the amount of hydrogen accumulated does not cause the internal pressure to exceed values which would result in crack initiation at MnS inclusions, the combination of such inclusions and relatively low concentrations of hydrogen does not appear to result in catastrophic failure.

Microstructural damage, observed only near the hydrogen charged wall of pipes and vessels, cannot be explained by a uniform steady state hydrogen distribution. It is thought that this damage results from short duration events which generate a particularly high hydrogen flux, during which the threshold concentration is exceeded near the surface. This hydrogen disperses as it diffuses deeper into the material and therefore damage is restricted to the surface regions.

6.1 Further Work.

In the light of the present research and the continuing demand for cumulative data on the effects hydrogen has on ferrous alloys, there appears to be scope for further work in this field. In order to qualify the work further, particular attention must be focused on the structural damage within the material. This could be emphasised using a particularly susceptible material possibly one which is heavily segregated providing extensive damage on hydrogen charging.

The observations made in this work are in general contrary to the beliefs of previous workers. Further, confirmatory work providing more evidence for the existence of an almost uniform hydrogen concentration gradient is therefore essential. In an attempt to explain this controversial phenomenon, it was proposed that a natural barrier may exist on the exit surface, possibly in the form of an oxide film. This barrier may not be totally impervious to hydrogen diffusion. However, literature suggests there to be a difference in the diffusion coefficients between the base metal and the oxide film of approximately 10 orders of magnitude[152].

In light of this, an investigation to identify and characterise the nature of the oxide films formed on pipe-line steels in various process environments should be conducted. It would then be possible to model the permeation of hydrogen through the oxide films in terms of Fickian diffusion, treating the system as a composite material.

Table A1[(38)] showing the first Six roots (all real if C > -1), B_n, of:-

$$\beta \cot \beta + C = 0$$

C	α_1	α_2	α_3	α_4	α_5	α_6
−1·0	0	4·4934	7·7253	10·9041	14·0662	17·2208
−0·995	0·1224	4·4945	7·7259	10·9046	14·0666	17·2210
−0·99	0·1730	4·4956	7·7265	10·9050	14·0669	17·2213
−0·98	0·2445	4·4979	7·7278	10·9060	14·0676	17·2219
−0·97	0·2991	4·5001	7·7291	10·9069	14·0683	17·2225
−0·96	0·3450	4·5023	7·7304	10·9078	14·0690	17·2231
−0·95	0·3854	4·5045	7·7317	10·9087	14·0697	17·2237
−0·94	0·4217	4·5068	7·7330	10·9096	14·0705	17·2242
−0·93	0·4551	4·5090	7·7343	10·9105	14·0712	17·2248
−0·92	0·4860	4·5112	7·7356	10·9115	14·0719	17·2254
−0·91	0·5150	4·5134	7·7369	10·9124	14·0726	17·2260
−0·90	0·5423	4·5157	7·7382	10·9133	14·0733	17·2266
−0·85	0·6609	4·5268	7·7447	10·9179	14·0769	17·2295
−0·8	0·7593	4·5379	7·7511	10·9225	14·0804	17·2324
−0·7	0·9208	4·5601	7·7641	10·9316	14·0875	17·2382
−0·6	1·0528	4·5822	7·7770	10·9408	14·0946	17·2440
−0·5	1·1656	4·6042	7·7899	10·9499	14·1017	17·2498
−0·4	1·2644	4·6261	7·8028	10·9591	14·1088	17·2556
−0·3	1·3525	4·6479	7·8156	10·9682	14·1159	17·2614
−0·2	1·4320	4·6696	7·8284	10·9774	14·1230	17·2672
−0·1	1·5044	4·6911	7·8412	10·9865	14·1301	17·2730
0	1·5708	4·7124	7·8540	10·9956	14·1372	17·2788
0·1	1·6320	4·7335	7·8667	11·0047	14·1443	17·2845
0·2	1·6887	4·7544	7·8794	11·0137	14·1513	17·2903
0·3	1·7414	4·7751	7·8920	11·0228	14·1584	17·2961
0·4	1·7906	4·7956	7·9046	11·0318	14·1654	17·3019
0·5	1·8366	4·8158	7·9171	11·0409	14·1724	17·3076
0·6	1·8798	4·8358	7·9295	11·0498	14·1795	17·3134
0·7	1·9203	4·8556	7·9419	11·0588	14·1865	17·3192
0·8	1·9586	4·8751	7·9542	11·0677	14·1935	17·3249
0·9	1·9947	4·8943	7·9665	11·0767	14·2005	17·3306
1·0	2·0288	4·9132	7·9787	11·0856	14·2075	17·3364
1·5	2·1746	5·0037	8·0385	11·1296	14·2421	17·3649
2·0	2·2889	5·0870	8·0962	11·1727	14·2764	17·3932
3·0	2·4557	5·2329	8·2045	11·2560	14·3434	17·4490
4·0	2·5704	5·3540	8·3029	11·3349	14·4080	17·5034
5·0	2·6537	5·4544	8·3914	11·4086	14·4699	17·5562
6·0	2·7165	5·5378	8·4703	11·4773	14·5288	17·6072
7·0	2·7654	5·6078	8·5406	11·5408	14·5847	17·6562
8·0	2·8044	5·6669	8·6031	11·5994	14·6374	17·7032
9·0	2·8363	5·7172	8·6587	11·6532	14·6870	17·7481
10·0	2·8628	5·7606	8·7083	11·7027	14·7335	17·7908
15·0	2·9476	5·9080	8·8898	11·8959	14·9251	17·9742
20·0	2·9930	5·9921	9·0019	12·0250	15·0625	18·1136
30·0	3·0406	6·0831	9·1294	12·1807	15·2380	18·3018
40·0	3·0651	6·1311	9·1987	12·2688	15·3417	18·4180
50·0	3·0801	6·1606	9·2420	12·3247	15·4090	18·4953
60·0	3·0901	6·1805	9·2715	12·3632	15·4559	18·5497
80·0	3·1028	6·2058	9·3089	12·4124	15·5164	18·6209
100·0	3·1105	6·2211	9·3317	12·4426	15·5537	18·6650
∞	3·1416	6·2832	9·4248	12·5664	15·7080	18·8496

REFFERENCES.

1.   A. J. Turnell. Metal Construction, November (1977). Pages 516-520.

2.   A. J. Turnell. Metal Construction, December (1977). Pages 552-559.

3.   R. A. Oriani, Proceedings of the Conference on "Fundamental Aspects of Stress Corrosion Cracking. (1967)", Columbia Ohio, NACE, Houston Texas, (1969).

4.   P. H. Pumphrey. Corrosion Vol. 36 No. 10 October. (1980). Pages 537-543.

5.   F. P. Ford and P. L. Anderson. Corrosion 89 April 17-21, (1989) Paper 498 New Orleans, Louisiana.

6.   B. G. Ateya and H. W. Pickering. NACE Corrosion 6 Houston Texas (1986) Pages 1183-1188.

7.   P. H. Pumphrey, Scripta Metallurgica, Vol. 14, No. 7. (1980) Pages 695-701.

8.   E. Sunami, S. Tanimira, and G. Tennyo. 5th International Congress on Mettalic corrosion, Toklo, Pages 493. (1974).

9.   D. L. Dull. PhD Thesis, University of California, Los Angeles, (1976).

10.   P. Amiott, A. Bernard and G. Pinard-Lengry. 2nd International Congress, Hydrogen in Metals, Paris. Paper 3E8. (1977).

11.   B. S. Chaudhari and T. P. Radhakrishnan, Corrosion Science, 30, 12, pp 1219-1234 (1990).

12.   N. Boes and H. Zuchner, Journal of the Less Common Metals, 49 (1976) pp 223-240.

13.   J. Brogan, I. M. Austin and E. F. Walker, Mthod of Calculating the Hydrogen Diffusion Coefficient in Steel from Hydrogen Permeation Data. Report from British Steel Corporation, EM/R/S1189/3/87/B. 24 March (1987).

14.   L. Nanis and T. K. G. Namboodhiri, NACE Corrosion 6 Houston Texas (1986) pp 432-444.

15.   M. G. Hay. Petroleum Society Of CIM. Paper 88-39-115 39th

Annual Technical Meeting of the Petrochemical Society, Calgary (1988).

16. D. Noël, C. P. Vijayan and J. J. Hechler. Surface and Coatings Technology, 28 (1986) pp 225-237.

17. T. Zakroczymski. Corrosion, Vol 38 No. 4, (1982). pp 218-223.

18. W. H. Thompson. Metal Protection. July (1988). Pages 63-69.

19. J O'M Bockris and D. F. A. Koch, J. Phys. Chem, 64, p. 1941 (1961).

20. R. N. Iyer, H. W. Pickering and M. Zammanzadeh, Scripta Metallurgica, Vol 22, pp. 911-916, (1988).

21. W. Beck and P. Fischer, Corrosion Science, vol 15, pp. 757-766 (1975).

22. R. D. McCright NACE 5 (1985) Houston Texas.

23 M. A. V. Devanathan and Z. Stachurski, J. Electrochemical Soc. Vol 111, No.5 May 1964 pp. 619-623.

24. C. D. Kim and B. E. Wilde. J Electrochem Soc. Vol 118. No 2. February 1971 pp. 202-206.

25. R. N. Iyer, I. Takeuchi, M. Zamanzadeh and H. W. Pickering, Corrosion Vol 46. No. 6. June (1990).

26. R. D. McCright and R. W. Stahle, J. Electrochem Soc. Vol 121 No. 5, May 1974, pp609-618.

27. J. F. Newman and L. L. Shreir, Corrosion Science, 1969. Vol9. pp 631-641.

28. Y. Saito and K. Nobe, Corrosion Vol 36 No.4 April 1980 pp 178-182.

29. D. L. Dull and K. Nobe, Corrosion, Vol 35 No.12 December 1979 pp 535-540.

30. P. Kedzierzawski, Z. Szklarska-smialowski and M. Smialowski. "Hydrogen Effects in Metals". New York, AIME. (1987). Eds. I. M. Bernstein and A. W. Thompson. pp 153-157.

31. M. Enyo. Electrochim Acta, 18 155 (1973).

32. J. P. Frazer and R. S. Tresedar. Corrosion. Vol 18, p342 (1952).

33. A. E. Schuetz and W. D. Robertson. Corrosion, Vol13, p437t (1957).

34. A. Kawashima, K. Hashimoto and S. Shimodaria. Corrosion Vol32, p321

(1976).

35.   C. M. Hudgins, R. L. McGlasson, P. Mehdizadeh and W. M. Rosborough. Corrosion 22, 238. August (1966).

36.   M. A. V. Devanathan and Z. Stachurski. Proceedings of the Royal Society of London. Series A. Vol. 270 (1962). Pages 90-102.

37.   M. D. Archer and N. C. Grant, Proc. R. Soc. Lond. A395, 165 - 183 (1984).

38.   J. Crank. "The Mathematics of Diffusion" 2nd. Edition (1975). Clarendon Press, Oxford.

39.   P. McIntyre. "Corrosion Fatigue" Proceedings of the first USSR-UK Seminar on Corrosion Fatigue of Metals. Held in Luov, USSR. 19-22 May (1980) P.60-73.

40.   Metals Handbook, 8th Edition (Eds. H. E. Boyer) Vol.10, "Failure Analysis and Prevention". (1975) ASM. P.230-235.

41.   R. P. Gangloff. "Corrosion Prevention and Control" Proceedings 33rd Sagamore Army Materials Research Conference, (Eds. S. Isserow) U.S. Art Materials Laboratory, Watertown, MA. (1986).

42.   A. Ciszewski, T. Radomski and M. Smialowski. Corrosion '86 NACE, Houston Texas (1986). P.671-679.

43.   J. P. Hirth. Metallurgical Transactions A. Vol. 11A, June (1980). Pages 861-890.

44.   C. A. Zapffe and C. E. Sims. Transactions AIME Vol.145 (1941) P.225-61.

45.   A. P. Moidownik. Corrosion '86 NACE, Houston Texas (1986). P.272-285.

46.   H. I. McHenry, P. T. Purtscher and T. R. Shives. Corrosion Science, Vol. 27, No. 10/11, pp. 1041-1057 (1987).

47.   P. Hancock. Cranfield Institute of Technology Bedford. (1993).

48.   R. D. Kane and W. K. Boyd. Metal Progress. February (1981). Pages 54-65.

49.   S. A. Golovanenko, V. N. Zikeev, E. B. Serbry-anaya and L. V. Popova. Corrosion '86 NACE, Houston Texas (1986). P.198-204.

50.   T. R. Allmand. "Microscopic identification of inclusions in steel" British Iron

and Steel Research Association. (1962) Pages 51-58.

51. Sulphide Inclusions in Steel (Eds. J. J. Barbadill and E. Snape). ASM Vol. 1 (1974).

52. F. B. Pickering. Physical Metallury and the Design of Steels, Applied Sciences, (1978).

53. J. Garland and J. Plateu. Trans ASM 56 (1963) p.442.

54. Sulphide Inclusions in Steel (Eds. J. J. Barbadill and E. Snape). ASM Vol. 2 (1974).

55. Sims, C. E. Transactions AIME, Vol 215, P 367 (1959).

56. E. Myoshi, T. Tanaka, F. Terasciki, and J. Ikeda. 30th annual meeting ASME (Pet Div), Tulsa, Oklahoma, September 1975.

57. J. L. Lee and J. Y. Lee. Metal Science. Vol. 17 September (1983). Pages 426-432.

58. A. McNabb and P. K. Foster. Trans AIME. 227, 619 (1963).

59. R. A. Oriani. Acta Metallurgica 18, 147 (1970).

60. M. Koiwa. Acta Metallurgica 22, 1259 (1974).

61. M. I. Luppo and J. Ovejero-Garcia. Corrosion Science. Vol. 32, No. 10. (1991). Pages 1125-1136.

62. H. G. Von Ellerbrook, G. Vibrans, H. P. Stüwe. Acta Metallurgica 20, 53 (1972).

63. A. J. Kumnick, H. H. Johnson. Metallurgical Transactions, 5, 1199 (1974).

64. A. W. Cochardt, G. Schoek, and H. Wiedersich. Acta. Met. 3, 533 (1955).

65. H. H. Podgurski and R. A. Oriani. Metallurgical Transactions. 3 2055 (1972).

66. I. M. Bernstein and A. W. Thompson. International Metals Review, 21, 269 (1976).

67. O. D. Gonzales. Trans AIME 24 5, 607 (1969).

68. J. A. Donovan. Met. Trans. 7A, 1677 (1975).

69. M. Iino. Metallurgical Transactions A. Vol.18A. September (1987). Pages 1559-1564.

70. A. Turnbull, M. W. Carroll and D. H. Ferriss. Acta Metallurgica, Vol. 37,

No. 7, 1989 p2039-2046.

71. A. Turnbull. Corrosion Science. Vol. 34, No. 6. (1993). Pages 421-460.

72. H. K. Birnbaum. "Environmenta-Induced Cracking of Metals." (Eds. R. P. Gangloff and M. B. Ives), NACE, Houston. (1990). Pages 21-30.

73. D. G. Westlake. Trans ASM Vol.62 (1969) P. 1000-1006.

74. J. J. Gilman. Proceedings NACE Confrence. France. June (1973). (Eds. Staehle, Hochman, McRight and Slater). Published (1977). P. 57-60.

75. E. D. Beacham. Metallurgical Transactions Vol.3, (1972). P. 437-451).

76. E. D. Beachman. Proceedings NACE Confrence. France. June (1973). (Eds. Staehle, Hochman, McRight and Slater). Published (1977). P. 376-381.

77. J. C. Dingman, D. L. Allen and T. F. Moore. Hydrogen Carbon Processes. Vol. 45 No. 9. (1966) p.285-290.

78. Metals Handbook. 9th Edition Vol. 13 "Corrosion". (1977) A.S.M.

79. R. A. Oriani. "Environmental-Induced Cracking of Metals." (Eds. R. P. Gangloff and M. B. Ives), NACE, Houston. (1990). Pages 439-448.

80. A. R. Troiano. Corrosion 15 (1959). 207t.

81. A. R. Troiano. Trans ASM. Vol. 52 p.54. (1960).

82. R. A. Oriani. NACE 5. NACE Publications (1977). p.351-358.

83. H. Vehoff and W. Rothe. Acta Met. Vol. 31. (1983). p.1781-1793.

84. N. J. Petch and P. Stables. Nature Vol. 69. (1952). p. 842.

85. S. P. Lynch. "Hydrogen Effects in Metals " (Editors: Bernstein and Thompson.) Met. Soc. AIME. New York. p. 863-871.

86. P. Bastien and P. Azou. Proc. First World Met. Congr. A.S.M. Cleveland, Ohio (1951).

87. J. K. Tien, A. W. Thompson, I. M. Bernstein and R. S. Richards. Met. Trans. A. Vol. 7A. June (1976). p. 821-829.

88. H. H. Johnson and J. P. Hirth. Met. Trans. A. Vol. 7A. (1976). p. 1543-1548.

89. S. V. Nair, R. R. Jenson and J. K. Tien. Met. Trans. A. Vol. 14A. (1983). p. 385

90. L. Aver and F. W. Hewes. Materials Performance. Vol. 3, No.8. (1964). p.10.

91. W. H. Thomason. Materials Performance. Vol. 23, No.5. (1984). p.24-29.

92. A. Eagles and J. Fray. Proc. Conf. U.K. Corrosion (1984), Wembley Conference Centre, 12-14. Novemmber. 1984. p.199.

93. D. R. Fincher, A. C. Nestle and J. J. Murr. Materials Performance, Vol. 15, No. 1. (1976). p. 34.

94. S. C. Lawrence Jr., Corrosion 74. Pre-print No. 96, NACE, Houston Texas. (1974).

95. G. Lawrence, Presentation at NACE T-1c Committee meeting, Corrosion 82 Houston Texas. (1982)

96. F. J. Radd and D. H. Oertle, Corrosion 71, Preprint No. 37, NACE, Houston Texas. (1971)

97. F. J. Radd and D. H. Oertle, U.S. Patent No. 3,498,900. (1970)

98. R. M. Vennett, Materials Performance, Vol16, No. 8 page 34. (1977)

99. K. B. Das. General Keynote Lecture in Hydrogen In Metals. (Editors: Bernstein and Thompson) A.S.M. (1974). p. 610.

100. R. L. Martin and E. C. French, Journal of Petroleum Technology, vol. 30, p1556 (November 1978).

101. D. A. Berman, J. J. De Luccia and F. Mansfield. Metal Progress. May (1979)

102. M. Meron, W. Reginiano, B. Triguboff and M. Ungarish, Metal Progress. July (1981)

103. F. Mansfield, S. Jeanjaquet and D. K. Roe, Materials Performance. February (1982)

104. M. J. Robinson and D. R. J. Hudson, British Corrosion Journal. Vol. 25, No. 4. pages 279 - 284. (1990)

105. G. M. Padawer and E. J. Schneid. Trans. A.M.S., Vol. 12. (1969). p. 493.

106. S. B. Lyon and D. J. Fray. British Corrosion Journal. Vol. 19, No. 1. (1984). Pages 23-29.

107. S. B. Lyon, D. J. Fray, "Hydrogen Measurements Using Hydrogen Uranyl Tetraphosphate", 4th International Conference on Solid State Ionics, Grenoble. (1983)

108. "Diffusible Hydrogen" British Standards BS 6693 Parts 1-5 1986. British Standards Institute.

109. N. Christenson and G. M. Evans. Metal Construction. 20(5). (1988). Pages 228-231.

110. Private Communications with International Welding Institute. April (1993) Cambridge.

111. "Hydrogen in Metals I" (Editors: G. Alefeld and J. Völkl). Chapter 8. Spriner-Verlag Berlin (1978).

112. M. Pourbaix. "Atlas of Electrochemical Equilibrium in Aqueous Solutions". 2nd English Edition. (1974).

113. J. J. DeLuccia and D. A. Berman. Electrochemical Corrosion Testing. ASTM. STD727. (1981). Pages 256-273.

114. J. Brogan, M. Austen and E. F. Walker. British Steel Corporation Research Organisation. Report No. EM/R/S1189/3/87/B. March (1987).

115. M. G. Hay. Petrochemical Society of SIM. Calgary. June (1988). Paper No. 88-39-115.

116. D. Noël, C. P. Vijatan and J. J. Hechler. Surface and Coatings Technology, 28 (1986). Pages 225-237.

117. T. K. G. Namboodhari and L Nanis. Acta Metallurgica. Vol. 39, No. 6. (1991). Pages 1091-1099.

118. C. L. Yu and T. P. Perng. Acta Metallurgica Material. Vol. 39, No. 6. (1991). Pages 1091-1099.

119. B. S. Chaudhari and T. P. Radhakrishnan. Corrosion Science 30, 12. (1990). Pages 1219-1234.

120. T. Zakroczymski. Corrosion. Vol. 38, No. 4. April (1982). Pages 218-223.

121. P.Mandatos and C. Duret. Hydrogen and Materials, Tsinghua University, Beijing, China. May (1988).

122. K. Van Gelder. Paper 235, Corrosion 85 NACE, Boston, Massachusetts. (1985).

123. P.Mandatos and C. Duret. Hydrogen and Materials, Tsinghua University, Beijing, China. May (1988).

124. J. O'M. Bockris. NACE Corrosion 86. Houston, Texas. (1986). Pages 286-305.

125. S. Pyun and R. A. Oriani. Corrosion Science. Vol. 29, No. 5. (1989). Pages 485-495.

126. T. Zakroczymski. Corrosion. Vol. 38, No. 4. April (1982). Pages 218-223.

127. R. C. Newman. Procdeedings of Conference on Corrosion Chemistry Within Pits, Crevices and Cracks. (Editor: A. Turnbull) HMSO, (1987). p.317-356.

128. F. P. Ford, G. T. Burnstein and T. P. Hoar. Journal Electrochemical Society. Vol. 128. (1980). Pages 1325.

129. R. P. Wei and M. Geo. Corrosion Vol. 47, No. 12. Dec. (1991). p.948-951.

130. G. Song and C. Cao. Corrosion Science. Vol. 33, No. 3. (1992). p. 413-423.

131. M. Hashimoto, S. Miyajima and T. Murata. Corrosion Science. Vol. 33, No. 6. (1992). Pages 885-904.

132. J. A. Bardwell. Corrosion Science. Vol. 30, No. 10. (1990). Pages 1009-1017.

133. B. MacDougall, D. F. Mitchell and M. J. Graham. Corrosion. Vol. 38, No. 2. February (1982). p. 85-91.

134. "Index (Inorganic) To The Powder Diffraction File" (Editors: J. V. Smith.) A.S.T.M. 48-M2. (1963).

135. Berman, Beck and DeLuccia. "Hydrogen in Metals". (Editors: I. M. Bernstein and I. W. Thompson.) A.S.M. Metals Park Ohio. (1974). p. 595-607.

136. B. C. H. Steele. Phil. Trans. R. Soc. London. A302. (1981). p. 361-374.

137. B. E. Conway and E. Gileadi. Canadian Journal of Electro-chemistry. Vol.

40. (1962). p. 1933-1942.

138. P. Oliva, J. Leonardi and J. F. Lavtent. Journal of Power Sources. 8. (1982). p. 229-255.

139. O. Glenser and J. Einerhand. Z. Electro-chemistry. 54, 302. (1950).

140. D. S. Carr and C. F. Bonilla. Journal of the Electrochemical Society. 999, 475 (1952).

141. M. M. Haring and E. G. Van den Bosche. Journal Physical Chemistry. Vol. 33, No. 161. (1929).

142. N. V. Sidgwick. "The Chemical Elements and Their Compounds." p. 292. Oxford University Press. London and New York. (1950).

143. U. R. Evans. Journal of the Chemistry Society. (1927). p. 1024.

144. H. H. Uhlig. Journal of the Electrochemical Society, 100, 216. (1953).

145. R. N. Iyer and H. W. Pickering. J. Electrochem. Soc. Vol. 136. No 9. (September 1989).

146. R. N. Iyer and H. W. Pickering. Scripta Metallurgica. Vol22, pp 911-916 (1988).

147. M. J. Carr. Cranfield Institute of Technology (personnel communication). (1991-1994).

148. B. S. Chaudhari and T. P. Radhakrishnan. Corrosion Science. Vol. 30, 12. (1990). Pages 1219-1234.

149. M. Smialowski. Scripta Metallurgica. Vol. 13. (1979). p. 393-395.

150. Dow Corning Data Sheet No. 22-0691-01. (1991).

151. T. Asaoka. Proc. J.I.M.I.S.-2. On Hydrogen in Metals, Minakami, Japan Institute of Metals. (1980). p. 161.

152. B. G. Pond. Corrosion Science. Vol. 45, No. 1. January (1989). p. 18-25.

153. K. Kiuchi and R. B. McLellan. Acta Metallurgica. Vol. 31. (1986). p. 961.

154. A. Turnbull, M. Saenz de Santa Maria and N. D. Thomas. NPL Report. DMA(A) 148, (1987).

155. D. Brooksbank and K. W. Andrews. J. Iron and Steel Inst. Vol. 207. (1969). p. 474.

156. D. Brooksbank and K. W. Andrews. J. Iron and Steel Inst. Vol. 210.

(1971). p. 246.

157. A. H. Cotterall and B. A. Bilby. Proceedings of the Physics Society. A62, 49, (1949).